

First-Principles Investigation of Trends in High-Temperature Thermochemistry of Perovskite Oxides

Krishna Kamol GHOSE BSc (Hons); MSc (France)

A thesis submitted in fulfilment of the requirements for the degree of Doctor of
Philosophy in Chemistry

June 2020

This research was supported by the University of Newcastle International Postgraduate Research Scholarship (UNIPRS) and the University of Newcastle Research Scholarship External (UNRSE) supported by Australian Solar Thermal Research Initiative, CSIRO Energy Technology, Australia.

Statement of Originality

I hereby certify that the work embodied in the thesis is my own work, conducted under normal supervision. The thesis contains no material which has been accepted, or is being examined, for the award of any other degree or diploma in any university or other tertiary institution and, to the best of my knowledge and belief, contains no material previously published or written by another person, except where due reference has been made. I give consent to the final version of my thesis being made available worldwide when deposited in the University's Digital Repository, subject to the provisions of the Copyright Act 1968 and any approved embargo.

.....

Krishna Kamol GHOSE

(Date: 02/06/2020)

Acknowledgement of Authorship

I hereby certify that the work embodied in this thesis contains scholarly work for which I am a joint author. I have included a written declaration below endorsed in writing by my primary supervisor, attesting to my contribution to the scholarly work.

By signing below I, Associated Prof. Alister Page confirm that Krishna Kamol GHOSE contributed to the following scholarly works:

1. Electronic Structure and High-Temperature Thermochemistry of BaZrO_{3-δ} Perovskite from First-Principles Calculations.

Ghose KK, Bayon A, Hinkley J, Page AJ. *Physical Chemistry Chemical Physics*. 2019;21(23):12468-76. DOI: 10.1039/C9CP02505G.

As leading author, Krishna Kamol GHOSE;

- Performed all calculations presented in the publication.
- Performed data analysis and figure formatting in the publication.
- Wrote initial manuscript draft.
- Collaborated with co-authors on manuscript revisions, submission and reviewer comments.
- Provided corrections and proofs prior to publication.

2. Experimental, Computational and Thermodynamic Studies in Perovskites Metal Oxides for Thermochemical Fuel Production: A Review.

Bayon A, de la Calle A, **Ghose KK**, Page A, McNaughton R. *International Journal of Hydrogen Energy*. 2020; 45(23):12653-79. DOI: 10.1016/j.ijhydene.2020.02.126.

As co-author, Krishna Kamol GHOSE;

- Wrote initial manuscript section “First-principles studies”.
- Collaborated with co-authors on initial manuscript draft.
- Collaborated with co-authors on manuscript revisions, submission and reviewer comments.
- Provided corrections and proofs prior to publication.

Signed,

Associated Prof. Alister Page (Date: 02/06/2020)

By signing below I, Dr Alicia Bayon confirm that Krishna Kamol GHOSE contributed to the following scholarly works:

1. Electronic Structure and High-Temperature Thermochemistry of BaZrO_{3-δ} Perovskite from First-Principles Calculations.

Ghose KK, Bayon A, Hinkley J, Page AJ. *Physical Chemistry Chemical Physics*. 2019;21(23):12468-76. DOI: 10.1039/C9CP02505G.

As leading author, Krishna Kamol GHOSE;

- Performed all calculations presented in the publication.
- Performed data analysis and figure formatting in the publication.
- Wrote initial manuscript draft.
- Collaborated with co-authors on manuscript revisions, submission and reviewer comments.
- Provided corrections and proofs prior to publication.

2. Experimental, Computational and Thermodynamic Studies in Perovskites Metal Oxides for Thermochemical Fuel Production: A Review.

Bayon A, de la Calle A, **Ghose KK**, Page A, McNaughton R. *International Journal of Hydrogen Energy*. 2020; 45(23):12653-79. DOI: 10.1016/j.ijhydene.2020.02.126.

As co-author, Krishna Kamol GHOSE;

- Wrote initial manuscript section “First-principles studies”.

- Collaborated with co-authors on initial manuscript draft.
- Collaborated with co-authors on manuscript revisions, submission and reviewer comments.
- Provided corrections and proofs prior to publication.

Signed,

Dr Alicia Bayon (Date: 02/06/2020)

By signing below I, Dr Jim Hinkley confirm that Krishna Kamol GHOSE contributed to the following scholarly works:

Electronic Structure and High-Temperature Thermochemistry of BaZrO_{3-δ} Perovskite from First-Principles Calculations.

Ghose KK, Bayon A, Hinkley J, Page AJ. *Physical Chemistry Chemical Physics*. 2019;21(23):12468-76. DOI: 10.1039/C9CP02505G.

As leading author, Krishna Kamol GHOSE:

- Performed all calculations presented in the publication.
- Performed data analysis and figure formatting in the publication.
- Wrote initial manuscript draft.
- Collaborated with co-authors on manuscript revisions, submission and reviewer comments.
- Provided corrections and proofs prior to publication.

Signed,

Dr Jim Hinkley (Date: 02/06/2020)

By signing below, I, Dr. Alberto de la Calle, confirm that Krishna Kamol GHOSE contributed to the following scholarly works:

Experimental, Computational and Thermodynamic Studies in Perovskites Metal Oxides for Thermochemical Fuel Production: A Review.

A. Bayon, A. de la Calle A, **K.K. Ghose**, A. Page & R. McNaughton. *International Journal of Hydrogen Energy*. 2020; 45(23):12653-79. DOI: 10.1016/j.ijhydene.2020.02.126.

As co-author, Krishna Kamol GHOSE;

- Wrote initial manuscript section “First-principles studies”.
- Collaborated with co-authors on initial manuscript draft.
- Collaborated with co-authors on manuscript revisions, submission and reviewer comments.
- Provided corrections and proofs prior to publication.

Signed,

Dr. Alberto de la Calle (Date: 09/06/2020)

By signing below I, Robbie McNaughton confirm that Krishna Kamol GHOSE contributed to the following scholarly works:

Experimental, Computational and Thermodynamic Studies in Perovskites Metal Oxides for Thermochemical Fuel Production: A Review.

Bayon A, de la Calle A, **Ghose KK**, Page A, McNaughton R. *International Journal of Hydrogen Energy*. 2020; 45(23):12653-79. DOI: 10.1016/j.ijhydene.2020.02.126.

As co-author, Krishna Kamol GHOSE;

- Wrote initial manuscript section “First-principles studies”.
- Collaborated with co-authors on initial manuscript draft.
- Collaborated with co-authors on manuscript revisions, submission and reviewer comments.
- Provided corrections and proofs prior to publication.

Signed,

Robbie McNaughton (Date: 02/06/2020)

Acknowledgements

First and foremost, I would like to acknowledge and sincerely thank my supervisors, Associate Professor Alister Page, Dr Alicia Bayon for their guidance, insight, and support over these past four years. I would like to thank Dr Jim Hinkley for useful scientific discussions during the first year of my PhD research.

I would like to thank Mr Aaron Scott for his assistance in using the RCG Grid at UON high capacity computing, NCI and Intersect help desks and all staffs associated with SELS School office.

I would like to thank all members of CompChem group at the University of Newcastle; Ben McLean, Clothilde Eveleens, Enis Yusof, Gareth Elliot, Izaac Mitchell, Jacob Johnston, Jemma Lawrence, Josh Brown, Kasimir Gregory, Parishudda Babu Moova, Simone Waite, Supriya Saha, Thomas Bourke, Xinyu Li, and all other present and past members. Working with you has been a great pleasure.

I would like to thank my family; my father Subash Ghosh, my mother Manju Ghosh, my elder sister Jhumur Ghosh, my younger brother Haripada Ghosh, my younger sister Nupur Ghosh. I would like to thank my friend Sukanta Sen Gupta. All of you have shown me nothing but support and patience for which I am eternally grateful.

Finally, I dedicate this thesis to parents; my mother Manju Ghosh and my father Subash Ghosh. Your unconditional love and support have driven me to make this academic journey successful.

Publications Arising from this Thesis

1. **Ghose KK**, Bayon A, Hinkley J, Page AJ. Electronic Structure and High-Temperature Thermochemistry of $\text{BaZrO}_{3-\delta}$ Perovskite from First-Principles Calculations. *Physical Chemistry Chemical Physics*. 2019;21(23):12468-76. DOI: 10.1039/C9CP02505G.
2. Bayon A, de la Calle A, **Ghose KK**, Page A, McNaughton R. Experimental, Computational and Thermodynamic Studies in Perovskites Metal Oxides for Thermochemical Fuel Production: A Review. *International Journal of Hydrogen Energy*. 2020; 45(23):12653-79. DOI: 10.1016/j.ijhydene.2020.02.126.
3. **Ghose KK**, Bayon A, Page AJ. Electronic Structure and High-Temperature Thermochemistry of Oxygen-Deficient BaMO_3 (M = Ti - Cu) Perovskites. (Manuscript Submitted at Journal of Physical Chemistry)
4. **Ghose KK**, Bayon A, Page AJ. Trends in High-Temperature Reduction Thermochemistry of RCO_3 (R = La, Ce, Nd, Sm) Perovskites: Effects of A-site cation. (Manuscript in Preparation)
5. **Ghose KK**, Bayon A, Page AJ. A Systematic Evaluation of Common GGA Exchange-Correlation Functionals on Prediction of Thermochemical Properties of Hexagonal and Cubic BaMnO_3 Perovskite. (Manuscript in Preparation)
6. **Ghose KK**, Bayon A, Page AJ. First-Principle High-Temperature Redox Thermochemistry of $\text{BaCeO}_{3-\delta}$ Perovskite for Solar Hydrogen Production. (Manuscript in Preparation).

Conference Talks Related to this Thesis

1. **Ghose KK**, Bayon A, Page AJ. Trends in High-Temperature Thermochemistry of BaMO_3 ($M = \text{Ti} - \text{Cu}$) and RCoO_3 ($R = \text{La}, \text{Ce}, \text{Nd}, \text{Sm}$) Perovskites from First-Principles Calculations. *Computational Chemistry Conference 2020*, Bowral, Australia.
2. **Ghose KK**, Bayon A, Hinkley J, Page AJ. Electronic Structure and High-Temperature Thermochemistry of $\text{BaZrO}_{3-\delta}$ Perovskite from First-Principles Calculations. *Asia-Pacific Solar Research Conference 2019*, Canberra, Australia.
3. **Ghose KK**, Bayon A, Hinkley J, Page AJ. Thermochemical Properties of BaXO_3 ($X = \text{Zr}, \text{Mn}$) Perovskites using First Principles Phonon Calculations. *International Conference on Emerging Advanced Nanomaterials 2018*, Newcastle, Australia.
4. **Ghose KK**, Bayon A, Hinkley J, Page AJ. High-Temperature Redox Thermochemistry of $\text{BaZrO}_{3-\delta}$ Perovskite from First-Principles Calculations. *Asia-Pacific Solar Research Conference 2018*, Sydney, Australia.
5. **Ghose KK**, Bayon A, Hinkley J, Page AJ. Thermochemical Properties of BaXO_3 ($X = \text{Ce}, \text{Zr}, \text{Mn}$) Perovskites from First-Principles Calculations. *RACI Physical Chemistry Student Conference 2016*, Katoomba, Australia.

Conference Posters Related to this Thesis

1. **Ghose KK**, Bayon A, Page AJ. BaZrO₃ Perovskite for Solar Thermal Water Splitting Applications - Temperature-Dependent Redox Properties. *Australian Symposium on Computational Enhanced Materials Design 2018*, Sydney, Australia.
2. **Ghose KK**, Bayon A, Hinkley J, Page AJ. Thermochemical Properties of BaXO₃ (X = Ce, Mn) Perovskites using First Principles Phonon Calculations. *World Association of Theoretical and Computational Chemists 2017*, Munich, Germany.
3. **Ghose KK**, Bayon A, Hinkley J, Page AJ. Thermochemical Properties of BaZrO₃ Perovskite using First Principles Phonon Calculations. *Workshop on Hands-on DFT and beyond 2017*, Berlin, Germany.

Table of Acronyms

AFLOW	Automatic-FLOW for Materials Discovery
BM EOS	Birch-Murnaghan equation of state
BO	Born-Oppenheimer
BS	Band Structures
BLYP	Becke-Lee-Yang-Parr
BZ	Brillouin Zone
CDD	Charge Density Distributions
CV	Cross-Validation
DFPT	Density Functional Perturbation Theory
DFT	Density Functional Theory
DFT-CH	DFT-based Convex Hull
FERE	Fitted Elemental-phase References Energy
GDC	Gadolinium-Doped Ceria
GGA	Generalized Gradient Approximation
HF	Hartree and Fock
HK	Hohenberg-Kohn
HS	High-spin State
HT-SOFC	High Temperature Solid Oxide Fuel Cell
IS	Intermediate-spin State
IT-SOFC	Intermediate Temperature Solid Oxide Fuel Cell
JARVIS	Joint Automated Repository for Various Integrated Simulations
KS	Kohn-Sham

LDA	Local Density Approximation
LSDA	Local Spin Density Approximation
LS	Low-spin State
LSM	$\text{La}_{1-x}\text{Sr}_x\text{MnO}_{3-\delta}$
LT-SOFC	Low Temperature Solid Oxide Fuel Cell
MIEC	Mixed Ionic and Electronic Conduction
ML	Machine Learning
NIST-	National Institute of Standards and Technology-
JANAF	Joint Army, Navy and Air Force
NOMAD	Novel Materials Discovery Laboratory
NREL-	National Renewable Energy Laboratory's-
MatDB	computational Materials Database
OER	Oxygen Evolution Reaction
OQMD	Open Quantum Materials Database
ORR	Oxygen Reduction Reaction
PAW	Projector Augmented Wave
PBE	Perdew Burke Ernzerhof
PBEsol	Perdew Burke Ernzerhof revised for solids and surfaces
PDOS	Partial Density of States
PP	Pseudo-Potentials
PW91	Perdew-Wang 1991
RPBE	Revised Perdew Burke Ernzerhof
RR	Reduction Reaction

SCF	Self-Consistent Field
ScSz	Scandia-Stabilized Zirconia
SLMA	$\text{La}_x\text{Sr}_{1-x}\text{Al}_y\text{Mn}_{1-y}\text{O}_{3-\delta}$
SOFC	Solid Oxide Fuel Cell
STWS	Solar Thermal Water Splitting
TF	Thomas-Fermi
US-PP	Ultra-Soft Pseudo-Potentials
VASP	Vienna <i>ab initio</i> Simulation Package
VDOS	Vibrational Density of States
XC	Exchange-Correlational
XRD	X-Ray Diffraction
YSZ	Yttria-Stabilized Zirconia
ZPE	Zero-Point vibrational Energy

Abstract

ABO_3 perovskite oxides containing cations of mixed and identical oxidation states at A- and B-sites are attractive candidates for high-temperature thermochemical energy conversion processes. The structural and thermochemical properties, and hence defect thermochemistry of such perovskites strongly depend on the identity of their A-site and B-site cations. Analyzing their temperature-dependent thermochemical and reduction properties can reveal their applicability for high-temperature energy applications, including solar thermal water splitting, solid oxide fuel cells, mixed ionic and electronic conduction processes etc. Since the typical A-site cations are comprised mainly of alkaline, alkaline-earth or rare-earth elements, and B-site cations mostly 3d, 4d, and 5d transition metals from the periodic table can form ABO_3 perovskite structure, thus identifying the generalized trends in the physical and chemical properties of ABO_3 perovskite could reveal a way to estimate the similar properties for other perovskite oxides that have not yet been investigated.

Towards understanding the generalized trends in the structural, thermochemical and reduction properties of ABO_3 perovskite with cations of mixed oxidation states at A- and B-sites, cubic $BaMO_3$ ($M = Ti - Cu$) perovskites have been investigated by first-principles calculations. Similar analysis has been accomplished for cations of identical oxidation states at A- and B-sites with cubic $RCoO_3$ ($R = La, Ce, Nd, Sm$). The structural and thermochemical properties of $BaMO_3$ and $RCoO_3$ perovskites have been characterized by first-principles calculations to reveal the influence of A-/B-site cations among the respective group of perovskites. In addition, the effect of oxygen vacancies and temperatures on reduction properties of $BaMO_3$ and $RCoO_3$ have been studied. The following conclusions have been drawn from the identified generalized trends in $BaMO_3$ and $RCoO_3$.

The formation energies of ABO_3 cations have a linear correlation with their atomic number of A-/B-site cations, whereas the formation energies have a significant inclination with the increasing atomic number of B-site cation for a given period in $BaMO_3$ series, but have minor increases with the increasing atomic number of A-site cation in $RCoO_3$ series. Similar to the formation energies, the oxygen vacancy formation energies increase to the greater extent with the increasing atomic number at B-site in $BaMO_{3-\delta}$, but to a lesser extent with the increasing atomic number at A-site in $RCoO_{3-\delta}$. However, the incorporation of thermal corrections into reduction free energies of $BaMO_{3-\delta}$ and $RCoO_{3-\delta}$, led to a significant deviation from their reduction properties without thermal contributions. A comparison of calculated entropic contributions into oxygen-deficient- and defect-free- ABO_3 perovskites demonstrate that the oxygen vacancies have substantial effects on the entropic contributions, which ultimately influence the temperature-dependent reduction properties of $BaMO_3$ and $RCoO_3$. On the other hand, at an equivalent temperature the thermochemical properties such as entropy, specific heat and relative molar enthalpy, show a consistent increase from Ti to Cu at B-site in defect-free $BaMO_3$, while reverse trends are observed from La to Sm at A-site in $RCoO_3$. The physical origins of all these generalized trends are elucidated via the electronic structure analysis and phonon mode analysis. Rationalizing the role of A-site and B-site cations in $BaMO_3$ and $RCoO_3$ perovskite series reveal that, the B-site cation has dominant effects on the structural, thermochemical and reduction properties of ABO_3 perovskites.

Table of Contents

Statement of Originality.....	i
Acknowledgement of Authorship.....	ii
Acknowledgements.....	ix
Publications Arising from this Thesis.....	x
Conference Talks Related to this Thesis.....	xi
Conference Posters Related to this Thesis.....	xii
Table of Acronyms.....	xiii
Abstract.....	xvi
Table of Contents.....	xviii
Chapter 1: Perovskite Oxides for High-Temperature Energy Conversion Processes.....	1
1.1 Introduction.....	1
1.2 Structure of ABO ₃ -Type Perovskite Oxides.....	2
1.3 ABO ₃ Perovskites in High-Temperature Energy Applications.....	3
1.3.1 High-Temperature STWS.....	4
1.3.1.1 Principles of STWS.....	4
1.3.1.2 Traditional STWS Redox Materials.....	5
1.3.1.3 Perovskite Oxides for STWS.....	7
1.3.2 High-Temperature SOFC.....	10
1.3.2.1 Principles of SOFC.....	10
1.3.2.2 Traditional SOFC Materials.....	12
1.3.2.3 Perovskite Oxides for SOFC Components.....	15
1.4 First-Principles Studies of Perovskite Oxides.....	19
1.4.1 Effect of A-site and B-site Cations in ABO ₃ Perovskites.....	20
1.4.2 Effect of Doping Both A-site and B-site Cations in ABO ₃ Perovskites.....	24

1.4.3 High-Throughput Screening Studies.....	28
1.4.4 Ab-Initio Databases and Machine-Learning Approaches	30
1.5 Knowledge Gap, Project Aims and Chapter Outline	37
1.6 References.....	40
Chapter 2: First-Principles Methodology for Electronic Structures and Thermochemical Properties of ABO ₃ Perovskites.....	
2.1 Introduction.....	58
2.2 Electronic Structure Methods	58
2.2.1 Time-Independent Schrödinger Equation	58
2.2.2 Born-Oppenheimer Approximation	59
2.2.3 Hartree-Fock Theory	60
2.2.4 Electron Correlation Methods	61
2.2.5 Thomas-Fermi and Thomas-Fermi-Dirac Models	62
2.2.6 Hohenberg-Kohn Theorem	63
2.2.7 Kohn-Sham Density Functional Theory	64
2.2.8 Exchange-Correlation Functionals.....	65
2.2.8.1 Local Density Approximation	66
2.2.8.2 Local Spin Density Approximation.....	66
2.2.8.3 Generalized Gradient Approximation	67
2.2.8.4 Strong Electron Correlation and the Hubbard Correction	68
2.2.9 Periodicity, Plane-Wave Basis Sets and Pseudopotentials	70
2.3 Modelling Thermochemistry with DFT via Phonon Dispersions.....	72
2.4 Phonon Structures and Thermochemical Properties of Ba-based ABO ₃ Perovskites.....	76
2.4.1 Computational Methods.....	77
2.4.2 BaCeO ₃	79

2.4.3 BaZrO ₃	85
2.4.4 BaMnO ₃	90
2.5 Conclusion	98
2.6 References.....	99
Chapter 3: Trends in High-Temperature Reduction Thermochemistry of BaMO ₃ (M = Ti – Cu): Effects of B-site Cation.....	
109	109
3.1 Introduction.....	109
3.2 Computational Methods.....	112
3.2.1 Electronic Structure Methods.....	112
3.2.2 Model Cubic BaMO ₃ Structures	112
3.2.3 First-Principles Thermochemical Properties of Cubic BaMO ₃ (M = Ti – Cu).....	113
3.2.4 Reduction Thermochemistry of Cubic BaMO _{3-δ} (M = Ti – Cu)	114
3.3 Results and Discussion	115
3.3.1 Trends in Formation Energies of Cubic BaMO ₃	115
3.3.2 Reduction Thermochemistry of Cubic BaMO _{3-δ} at 0 K	117
3.3.2.1 Oxygen Vacancy Formation Energies	117
3.3.2.2 Electronic Structures Analysis: Effect of Oxygen Vacancy and B-site Cation.....	119
3.3.3 Reduction Thermochemistry of Cubic BaMO _{3-δ} with Thermal Corrections.....	131
3.3.3.1 Temperature-Dependent Reduction Free Energies.....	131
3.3.3.2 Phonon Analysis: Effect of B-site Cation and Oxygen Vacancy	135
3.3.4 Thermochemical Properties and Phonon Dispersions of Cubic BaMO ₃	137
3.3.4.1 Effect of B-site Cation on Thermochemical Properties.....	137
3.3.4.2 Effect of B-site Cation on Phonon Dispersions and VDOS	140
3.4 Conclusion	144
3.5 References.....	145

Chapter 4: Trends in High-Temperature Reduction Thermochemistry of RCoO_3 (R = La, Ce, Nd, Sm): Effects of A-site Cation.....	153
4.1 Introduction.....	153
4.2 Computational Methods.....	155
4.3 Results and Discussion	156
4.3.1 Trends in Lattice Structures and Formation Energies of Cubic RCoO_3	156
4.3.2 Reduction Thermochemistry of Cubic $\text{RCoO}_{3-\delta}$ at 0 K.....	158
4.3.2.1 Oxygen Vacancy Formation Energies.....	158
4.3.2.2 Electronic Structures Analysis: Effect of Oxygen Vacancy and A-site Cation	159
4.3.3 Reduction Thermochemistry of Cubic $\text{RCoO}_{3-\delta}$ with Thermal Corrections.....	168
4.3.3.1 Temperature-Dependent Reduction Free Energies.....	168
4.3.3.2 Phonon Analysis: Effect of A-site Cation and Oxygen Vacancy	171
4.3.4 Thermochemical Properties and Phonon Dispersions of Cubic RCoO_3	174
4.3.4.1 Effect of A-site Cation on Thermochemical Properties	174
4.3.4.2 Effect of A-site Cation on Phonon Dispersions and VDOS.....	176
4.4 Conclusion	180
4.5 References.....	181
Chapter 5: Conclusions and Future Work.....	187
5.1 Conclusions.....	187
5.2 Future Work	189
5.2.1 Altering A- and B-site Cation in ABO_3 Perovskites	190
5.2.2 Doping A-site Cation in ABO_3 Perovskites	190
5.2.3 Doping B-site Cation in ABO_3 Perovskites	191
5.2.4 The Combination of A- and B-site Doping in ABO_3 Perovskites.....	191
5.3 References.....	192

Chapter 6: Appendix	195
Chapter 7: Copyright Permissions	197

Chapter 1: Perovskite Oxides for High-Temperature Energy Conversion Processes

1.1 Introduction

The development of new energy technologies to produce sustainable and clean energy have been gaining more importance over the last few decades. Worldwide strong economic growth, population expansion in the developing nations, and uncertainty and shortage of oil production drive the global energy crisis at an alarming rate. Therefore, the exploration of new energy resources is crucial to meet the current global energy demand and produce energy sustainably into the future. Ongoing research aims to achieve an efficient conversion of chemical energy in the form fossil fuel resources and derivatives by a broad range of energy applications such as solar thermochemical water splitting (STWS), solid oxide fuel cell (SOFC), and thermochemical heat storage. High-temperature routes are of particular interest because of its increased efficiency and accelerated chemical reaction rates. This thesis proposes a novel computational methodology to obtain structural, thermochemical and reduction properties of stoichiometric and nonstoichiometric perovskite metal oxides related to high-temperature alternative energy conversion processes.

In this context, the structural properties of ABO_3 -type perovskite oxides are discussed. Additionally, the basic principles of the two most relevant high-temperature energy applications, STWS and SOFC, are highlighted by considering their energy conversion efficiencies and production rates. Furthermore, materials conventionally used for STWS and SOFC are also discussed in terms of their performances, efficiencies and limitations. In addition, ABO_3 -type perovskite oxides are reviewed and shown to overcome these limitations in certain cases. Moreover, first-principle studies of perovskite thermochemical properties are summarized and

critically discussed. This chapter concludes with a statement of the knowledge gap addressed in this thesis and an overview of the project aims.

1.2 Structure of ABO₃-Type Perovskite Oxides

Perovskite materials have gathered a great deal of attention over the last ten years due to their tunable structure-property relationships. The first reported perovskite was calcium titanate (CaTiO₃), discovered as a natural mineral in 1839 by the Russian mineralogist Lev Perovski. The perovskite structure contains two cations of very different sizes, with an anion that bonds to both (Fig. 1.1). The A cation is 12-fold coordinated with oxygens while the B atom is 6-fold coordinated.^[1] Ideal perovskite oxides are cubic (Fig. 1.1(a)) but can exhibit orthorhombic (Fig. 1.1(b)), rhombohedral (Fig. 1.1(c)) and hexagonal (Fig. 1.1(d)) crystal structures. Different elements can occupy the A and B sites of the perovskite according to their ionic radius. Perovskites featuring multiple A-site or B-site cations in the same sublattice (e.g. (AA')(BB')O₃ or AA'BB'O₆) are called doped perovskite or double perovskites. The radii of A-site cations are generally larger (typically falls between 1.10 and 1.80 Å) than those of B-site cations (between 0.62 and 1.00 Å) due to their respective valence states.^[1] The crystalline structure of ABO₃ perovskites can be predicted using the Goldschmidt tolerance factor (t),

$$t = \frac{(r_A + r_O)}{\sqrt{2}(r_B + r_O)} \quad (1.1)$$

where, r_A , r_B , r_O are the relative ionic radii of the A-site cations, B-site cations and the O²⁻ anions respectively. The most stable perovskite structures are generally found in the range of $0.85 < t < 1.10$.^[2, 3] When $0.9 < t < 1.0$, perovskites are cubic in structure at ambient conditions. If the cation radius of A decreases and/or B increases (i.e. $0.71 < t < 0.9$), the perovskite crystal structure will form an orthorhombic/rhombohedral phase at ambient conditions, whereas hexagonal phases are

formed for $1.0 < t < 1.10$. It is noted that at temperatures relevant to high-temperature SOFC and STWS operating conditions, the most stable perovskite phase is cubic.^[2]

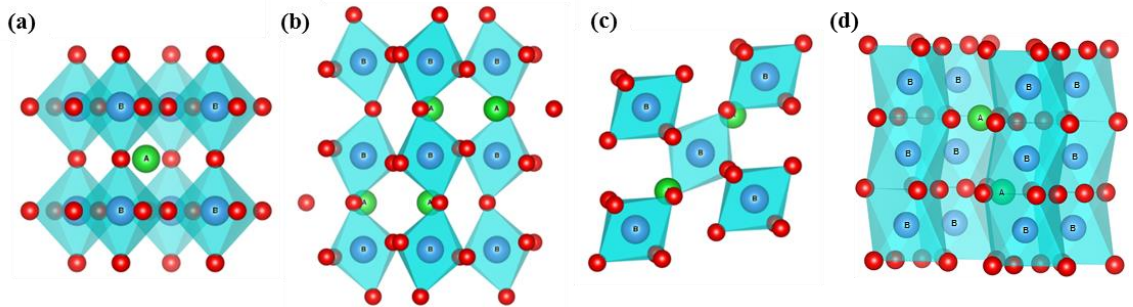


Fig. 1.1 Schematic of ABO₃ perovskite structures in (a) cubic, (b) orthorhombic, (c) rhombohedral and (d) hexagonal phases. Atoms: A (green), B (blue) and O (red).

1.3 ABO₃ Perovskites in High-Temperature Energy Applications

ABO₃ perovskites have great diversity in their properties, making them attractive candidates for important high-temperature energy applications such as STWS,^[4-6] SOFC as cathode, anode and electrolyte materials,^[3, 7-15] mixed ionic and electronic conductors (MIEC),^[16] solid-state gas sensors,^[17, 18] membrane separation,^[19] oxidation of CO, hydrogen, hydrocarbon and NO_x decomposition.^[20-23] Regarding this Thesis, the two that are most relevant are arguably STWS and SOFC, for which comparably fast energy conversion efficiency with higher production rates are demonstrated.^[24, 25] For this reason, these technologies, and the materials underpinning them, are first reviewed before the more technical aspects of perovskite materials are considered below.

1.3.1 High-Temperature STWS

1.3.1.1 Principles of STWS

Hydrogen can be produced using concentrated solar radiation via single-step, two-step and multi-step pathways. In single-step water splitting, solar heat energy is used to thermally dissociate water, producing H₂ and O₂ at high-temperature (>2500 K).^[26]

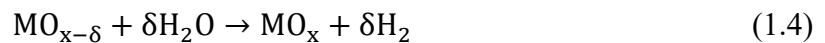


Although one-step direct thermolysis of water has the potential of high theoretical hydrogen conversion efficiency,^[27] this process is impractical due to the required temperature. Additionally, separating H₂ and O₂ gases at this temperature is thermodynamically unfavorable. The latter problem can be averted by using rapid cooling separation techniques. However, cooling will introduce a large temperature swing between reaction and separation steps, ultimately leading to the irreversibility of the operation cycle.

An alternative strategy that circumvents these issues is the production of H₂ and O₂ via a two-step thermochemical redox reaction (Fig. 1.2). In two-step STWS processes, water is decomposed thermally in the presence of sunlight, typically using a metal oxide.^[28-30] In the first step, a reducible metal oxide is heated to high temperature via an endothermic reaction,



In the second step, exothermic oxidation of the reduced metal oxide MO_{x-δ} with water produces H₂,



For the initial endothermic reduction, the metal oxide must be heated (>1250 K) by sunlight, thus halving the temperature required compared to direct thermolysis of water using concentrated solar

radiation.^[26, 31-33] In both the reduction and oxidation reactions equations, (1.3) and (1.4) respectively, the single factor limiting efficiency is the metal oxide itself, which determines how efficiently the solar spectrum can be captured and converted.^[34-38] In multi-step STWS cycles, the reduction temperature can be lowered significantly compared to single and two-step processes. A brief overview of several 3-step water splitting cycles can be found in references.^[39-42]

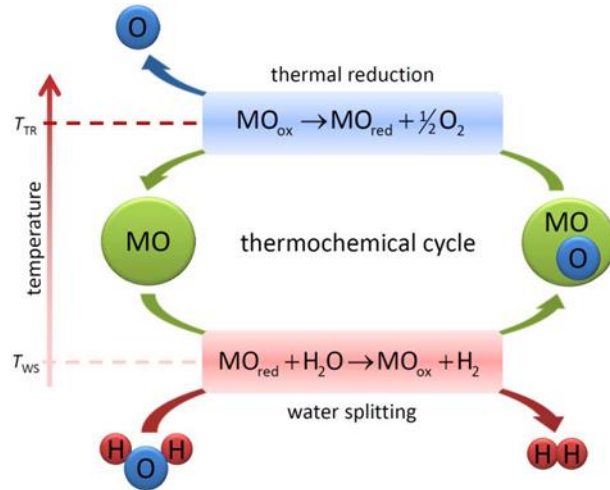


Fig. 1.2 Conceptual scheme of a generic two-step STWS cycle, where metal oxide is heated with concentrated solar energy to some elevated temperature, and then reduced metal oxide is quenched to a lower temperature and exposed to steam.^[43] Reprinted under the open-access license by MDPI.

1.3.1.2 Traditional STWS Redox Materials

The redox materials traditionally used for driving STWS (equations (1.3 – 1.4)) have been transition metal oxides such as ceria, iron oxide and hercynite (FeAl_2O_4). In this context, an “ideal” STWS metal oxide need to reach the following properties:^[44]

- (i) The optimum redox temperature range in between 1200-1800 K and minimum ΔT ($0 < \Delta T < 400 \text{ K}$).^[45]
- (ii) High redox capability and corresponding production capacity.

- (iii) Fast redox kinetics and maintain consistent redox cycles.
- (iv) Chemical and physical stability at operational temperatures/pressures.
- (v) Large abundance, low toxicity and low cost.

In this respect, $\text{CeO}_2/\text{CeO}_{2-\delta}$ based STWS represents the current state-of-the-art (with an overall solar-to-fuel efficiency $\sim 11\%$); however, it requires high operating temperature ($>1700\text{ K}$).^[46] Doping ceria with other metals such as Zr, lower the reduction temperature between $1400 - 1700\text{ K}$ and increase H_2 production,^[47, 48] however, the hydrogen production capacity of ceria is still insufficient for commercial applications.^[44, 49] $\text{Fe}_3\text{O}_4/\text{FeO}$ redox materials are generally promising due to their high theoretical solar-to- H_2 conversion capability. Nevertheless, the reduction temperature of Fe_3O_4 implies a partial melting of the iron oxide that impedes its use for extended cycles.^[50] The thermal reduction of ZnO using concentrated solar energy requires high temperature ($\sim 2300\text{ K}$).^[51] While this temperature could be lowered to $\sim 1573\text{ K}$ ^[52] by operating the endothermic step (equation (1.3)) under a N_2 flow of 100 ml/min , the product Zn in the gas phase and oxygen of this reduction reaction requires further separation to avoid recombination. For the SnO_2/SnO redox cycle, SnO_2 is reduced at $\sim 1573\text{ K}$ but tends to form SnO via partial reduction, instead of Sn, ultimately reducing H_2 production.^[53] W/WO_3 , CaO/CaSO_4 , SrO/SrO_4 , Cd/CdO , $\text{In}/\text{In}_2\text{O}_3$ and their corresponding hybrid cycles (involving electrochemical step) undergo reduction at comparatively low temperatures, but the high temperature difference between reduction and oxidation reactions cause the active metal oxides to experience thermal fatigue due to frequent heating and cooling, ultimately limiting the utility of these materials.^[39]

1.3.1.3 Perovskite Oxides for STWS

The traditional metal oxides utilized in STWS commonly require excessive reduction temperatures, or relatively low non-stoichiometries (and hence lower yields). Additionally, in some other cases, there are large temperature swings between the reduction and oxidation reactions, further lowering H_2 yields due to energy loss.^[45, 54] These shortcomings have driven the search for new redox materials with a potential to provide more favorable thermochemistry, and ultimately more H_2 fuel.^[44]

ABO_3 perovskites show great potential as STWS redox materials, due to their unique structural features, high chemical/thermal stabilities and ionic conductivities.^[2, 3, 55-57] Their chemical and electronic properties can easily be modified via chemical doping at either the A or B sites or both. Fig. 1.3 shows a schematic of STWS based on ABO_3 perovskite materials. ABO_3 can be reduced under solar-driven, high-temperature conditions, to produce oxygen ($\delta/2 O_2$) and reduced metal oxide ($ABO_{3-\delta}$). This reduced metal oxide can subsequently be oxidized by water, to release heat and hydrogen (H_2) via an exothermic reaction.

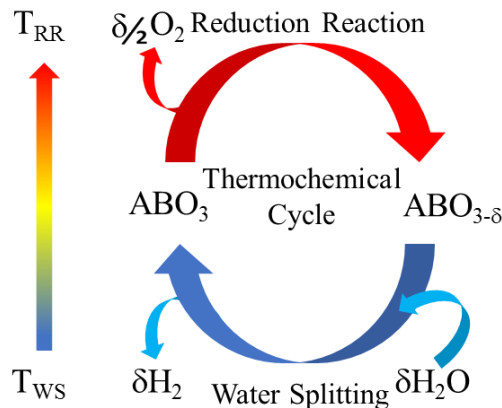


Fig. 1.3 Conceptual scheme of STWS reduction and oxidation reactions using ABO_3 perovskite.

The structurally stable ABO_3 perovskite-type oxide can tolerate defects at the A- ($A_{1-x}BO_3$), B- ($AB_{1-x}O_3$), and oxygen- ($ABO_{3-\delta}$) -lattice sites to considerable extents. Partial substitution of A or B cation with higher or lower valence state also introduces lattice defects, such that charge neutrality is maintained in the crystal structure. In order to compensate for electrical neutrality, some ions diffuse from one site to another through the defects in the crystal lattice, provided they have sufficient energies to overcome the associated diffusion barriers. Notably, oxide ions migrate to the vacant lattice sites from their original sites at elevated temperature. For example, partial substitutions of Ca^{2+} on $LaAlO_3$ and Al^{3+} on $CaTiO_3$ formed $La_{1-x}Ca_xAlO_{3-\delta}$ and $CaTi_{1-x}Al_xO_{3-\delta}$ compositions respectively, which lead to oxygen ion vacancy formation in order to maintain charge neutrality in the crystal.^[58, 59] At various cation concentrations, oxide ion conductivity was dominant at elevated temperatures.^[60]

La-based perovskites ($LaXO_{3-\delta}$ with $X = Mn, Al, Co$ or mix of them) have been extensively studied for solar-driven thermochemical water splitting. For instance, Scheffe et al.^[61] first investigated Sr-doped $LaMnO_{3-\delta}$ perovskites (LSM) such as $La_{1-x}Sr_xMnO_{3-\delta}$ ($x=0.3, 0.35, 0.4$) for H_2O splitting and demonstrated that LSM has thermodynamically favorable reduction compared to ceria at temperature ranges 1523-1923 K. McDaniel et al.^[62] used $LaAlO_3$ with additional doping of Sr^{2+} on the La-site and $Mn^{2+}/Mn^{3+}/Mn^{4+}$ on the Al-site for STWS cycles. They found that $La_xSr_{1-x}Al_yMn_{1-y}O_{3-\delta}$ (SLMA) materials gave even better H_2 yields than LSM perovskites. Unlike the LSM compositions, SLMA compositions produce nine times greater H_2 yields compared to ceria at reduction temperature of 1623 K and re-oxidation temperature of 1273 K (see Fig. 1.4(a)). Demont et al.^[56] also reported LSM materials with 35% and 50% Sr doping at the A-site (see Fig. 1.4(b)). However, these perovskites exhibited slower kinetics compared to ceria, possibly due to the lower enthalpies of oxidation.

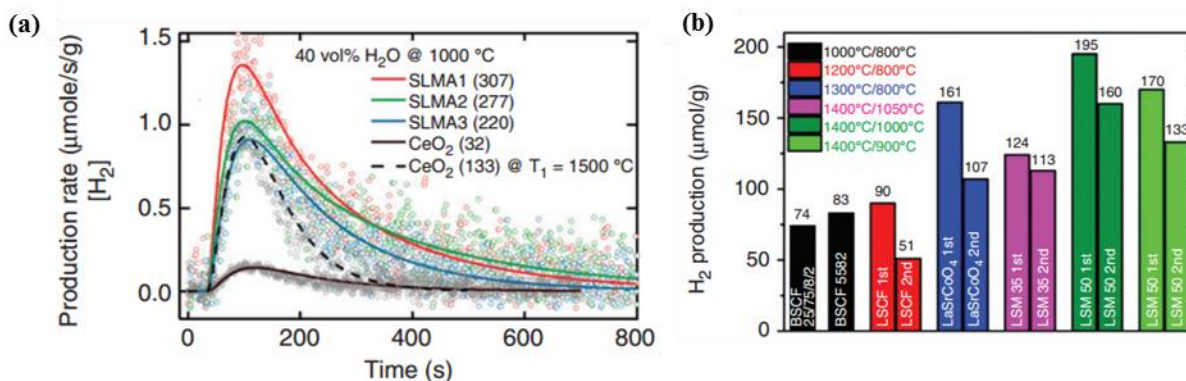


Fig. 1.4 (a) SLMA perovskites produce higher H₂ than ceria at reduction temperature 1623 K and oxidation temperature 1273 K.^[57] Reprinted with permission from Elsevier[®]. (b) H₂ production capacities by perovskites in STWS cycles.^[63] The green bars indicate the maximum fuel production by La_{0.5}Sr_{0.5}MnO₃ under operating conditions. Reprinted with permission from ACS Publications[®].

A further study of LSM by substituting Mn³⁺ with trivalent cations Al³⁺, Sc³⁺ or Ga³⁺ revealed that 5% Sc-doped LSM (La_{0.5}Sr_{0.5}Mn_{0.95}Sc_{0.05}O_{3-δ}) outperforms the other two dopants in fuel production, even during multiple cycles due to the size of Sc³⁺, which enhances O²⁻ mobility and the oxygen vacancy ratio.^[64] Furthermore, Dey et al.^[65] showed that replacing Sr²⁺ with Ca²⁺ on the A-site in LaMnO_{3-δ} (La_{0.5}Ca_{0.5}MnO_{3-δ}) can enable greater O₂ evolution compared to LSM, and subsequent superior H₂ fuel production. The orthorhombic crystal structure of La_{0.5}Ca_{0.5}MnO_{3-δ} enhanced the catalytic activity more than the rhombohedral LSM, due to the distortion of MnO₆ octahedra. Sr- and Ca-doped RMnO₃ (R=Y, La, Nd, Sm, Gd, Dy) have also been investigated for thermochemical H₂O and CO₂ splitting,^[65] where Y_{0.5}Sr_{0.5}MnO₃ have been found to produce fuel remarkably at low redox temperature (reduction at ~1473 K and oxidation at ~1173 K), which was attributed to the high distortion and mismatch between the radii of R³⁺

and Sr^{2+} . Furthermore, Cooper et al.^[66] revealed that doping the A-site of $\text{LaMnO}_{3-\delta}$ by $\text{Sr}^{2+}/\text{Ca}^{2+}$, and the B-site by Al^{3+} increased the reduction capacity by up to a factor of 13 times at temperatures between 1473 and 1673 K. Sr- and Cr-doped LaCoO_3 perovskites, such as $\text{La}_{0.6}\text{Sr}_{0.4}\text{Cr}_{0.8}\text{Co}_{0.2}\text{O}_{3-\delta}$ were also identified as strong candidates, outperforming CeO_3 by a factor of ~25 in terms of fuel production.^[67]

More recently, Wang et al. experimented with Ca-doped La-based perovskites, such as, $\text{La}_{1-x}\text{Ca}_x\text{CoO}_3$ ($x=0.2-0.8$),^[68] $\text{La}_{1-x}\text{Ca}_x\text{MnO}_3$ ($x=0.2-0.8$),^[68] and $\text{La}_{1-x}\text{Ca}_x\text{Mn}_{1-y}\text{Al}_y\text{O}_3$ ($x, y=0.2-0.8$),^[69] and, respectively found that $\text{La}_{0.6}\text{Ca}_{0.4}\text{CoO}_3$, $\text{La}_{0.6}\text{Ca}_{0.4}\text{MnO}_3$, and $\text{La}_{0.6}\text{Ca}_{0.4}\text{Mn}_{0.6}\text{Al}_{0.4}\text{O}_3$, have lower reduction temperature compared to ceria, still maintaining the higher H_2 production rates under certain experimental conditions. Other La-based perovskites, such as $\text{La}_{0.6}\text{Sr}_{0.4}\text{BO}_3$ ($\text{B}=\text{Cr}, \text{Mn}, \text{Fe}, \text{Co}, \text{Ni}$),^[70] and $\text{La}_{1-x}\text{A}_x\text{Mn}_{1-y}\text{B}_y\text{O}_3$ ($\text{A}=\text{Ca}, \text{Sr}, \text{Ba}$; $\text{B}=\text{Al}, \text{Ga}$; and $x=0, 0.4$; $y=0, 0.2$)^[71] have also been systematically investigated. The highest production capacities were obtained with $\text{La}_{0.6}\text{Sr}_{0.4}\text{CoO}_3$ and $\text{La}_{0.6}\text{Ca}_{0.4}\text{Mn}_{0.8}\text{Ga}_{0.2}\text{O}_3$ compositions.

Although several doped ABO_3 perovskite materials are identified as promising candidates for solar-driven thermochemical fuel production (as detailed above), very few undoped perovskites are reported in the literature as STWS materials.

1.3.2 High-Temperature SOFC

1.3.2.1 Principles of SOFC

SOFC converts chemical energy directly to electric energy at high temperature with high efficiency (50-60%) while maintaining environmental compatibility.^[72] Due to a simple functional design, long-life times (40, 000 – 80, 000 h), ability to tolerate impurities to enhance performance and overall efficiency, SOFC is considered an emerging technology for power generation from

fuel. SOFC consists of three layers of functional materials where an anode and a cathode are separated by an electrolyte (Fig. 1.5).

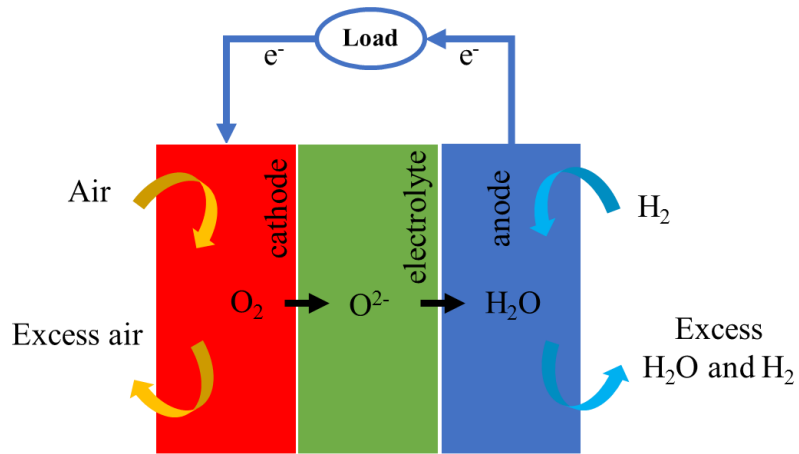
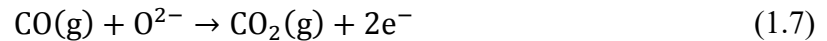
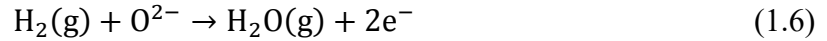


Fig. 1.5 Scheme of a solid oxide fuel cell composed of a cathode, an anode and an electrolyte.

The cathode side typically contains air or oxygen, and the anode is fed by fuel. When power is applied externally to the cell, the air in the cathode side combines with electrons returning from the load by forming O²⁻,



O²⁻ then migrates through the dense electrolyte to the anode side, where they react with entering fuel at the anode. The electrolyte only allows the flow of charged ions from the cathode to anode but prevents electron conduction. Commonly, if the entered fuel is H₂ or CO at the anode side, then it becomes positively charged ions and combines with O²⁻ to produce H₂O or CO₂ respectively which drains from the cell. During the oxidation reaction at the anode side, electrons are released and flow via the external load to the cathode side, which further reacts there in oxygen reduction. In this way, electrical power can be generated throughout the cell.



SOFC can be categorised into three types based on their operational temperature: high-temperature SOFC (HT-SOFC, $T > \sim 1,300$ K), intermediate-temperature SOFC (IT-SOFC, $\sim 900 < T < \sim 1,300$ K), and low-temperature SOFC (LT-SOFC, $T < \sim 900$ K).^[73-75] While high operational temperature is beneficial for overall SOFC performance, it results in higher thermal fatigue to the cell components. Thermal stresses could be reduced by choosing SOFC components with similar thermal expansion characteristics. On the other hand, while lowering the operation temperature reduces thermal degradation, it decreases oxide ion conductivity significantly. Thus, more active electrode materials, possessing higher conductivity and electrocatalytic activity at these temperature ranges are desirable.

1.3.2.2 Traditional SOFC Materials

The choice of the anode, cathode and electrolyte are the most important factors influencing SOFC performance.^[74] Each SOFC component has several functions to perform during redox reaction in the cell and therefore must meet certain requirements. For instance, cathode materials facilitate O_2 adsorption, O^{2-} formation, and O^{2-} transport to the electrolyte in an oxidising environment. Therefore, an ideal cathode material for SOFC must exhibit the following physical and chemical properties:^[25, 76, 77]

- (i) Superior electronic conductivity and significant ionic conductivity to assure both electron and oxygen ion transport.
- (ii) High catalytic activity for oxygen reduction reactions.
- (iii) Compatible thermal expansion coefficient with typical electrolyte and interconnect.

(iv) Adequate porosity to allow mass transport of oxygen from the gas phase to the cathode-electrolyte interface.

(v) Morphological, chemical and thermal stability under operating conditions.

The oxidation of fuel takes place in the anode material, which facilitates fuel access along with product removal. Thus, an effective anode of SOFC must meet several criteria:^[78, 79]

(i) Excellent electrocatalytic activity.

(ii) High electronic and ionic conductivity.

(iii) Stability under strong reducing environment.

(iv) Proper porosity to allow fuel transportation and drainage of oxidation by-products.

(v) Compatibility with electrolytes and interconnect.

The electrolyte plays the most important role in SOFC by flowing ion conduction between cathode and anode and simultaneously blocking electronic conduction. Therefore, the following important characteristics are required for an efficient SOFC electrolyte:^[77, 80]

(i) It should have a strong, thin and dense membrane to reduce ionic resistance.

(ii) High ionic conductivity.

(iii) Low electronic conductivity.

(iv) Good mechanical and chemical stability in both oxidizing and reducing environments.

(v) Matching thermal expansion coefficients with electrodes and interconnects.

R_2NiO_{4+x} (R=La, Pr, Nd) has been studied as cathode materials for SOFC due to their superior diffusivity of interstitial oxygen ions at high temperature.^[81] The thermal expansion coefficients

of La_2NiO_4 are compatible with yttria-stabilized zirconia (YSZ) and gadolinium-doped ceria (GDC) electrolytes, and the transport properties of this materials can be tuned by doping both La and Ni sites. Doped La, Gd, Sr, Y and Pr are the most common cathode materials used in SOFC. A brief overview of all these materials can be found in the review article presented by Wincewicz et al.^[82]

Subsequently, the most common anode materials used in SOFC with YSZ are Cu, Ru, Cu-Ni, Cu-Co, and yttria-doped ceria.^[83] Cu-GDC, Cu-Ni-GDC, Cu-CeO₂-ScSZ (scandia-stabilized zirconia-ScSZ) were also identified as potential anodes with better performance, low cost and easy synthesis techniques compare to other traditional SOFC anode materials.^[84] Despite their popularity as electrodes, their incompatibility with certain electrolytes and unfavorable redox reactions at high temperature has led to the development of alternative materials that overcome those limitations, such as perovskite-based cathode, anode and electrolyte components for SOFC.^[3]

YSZ is a state-of-art electrolyte material in SOFC because of its excellent stability in redox environments and long-life cycle. However, it suffers the drawback of low ionic conductivity and incompatibility with some cathode materials.^[75] GDC enables MIEC at low oxygen partial pressure and good compatibility with cathode materials. However, its low electron conduction at low oxygen partial pressure and mechanical instability limit its performance in SOFC applications. On the other hand, Sc-doped ZrO₂ offers significant ionic conductivity and excellent stability in reduction and oxidation environments, meaning greater cyclability. However, the cost of this material (due to the limited availability of Sc) is its greatest impediment.

1.3.2.3 Perovskite Oxides for SOFC Components

Perovskite oxides have been widely studied as cathode, anode and electrolyte components in SOFC, where most of the components contain A-site cations of rare earth (such as La, Ce, Sm) or alkaline earth (such as Ca, Sr, Ba) elements or a mixture thereof, while B-site cations are mostly 3d transition metals (such as Ti, Cr, Mn, Fe, Co, Ni, Cu).^[3, 85] For instance, La-based perovskites such as, LaCrO₃, LaMnO₃, LaFeO₃, LaCoO₃, LaNiO₃ with partial substitution of alkaline-earth cations in A-site (Mg, Ca, Sr, Ba), have been extensively studied as SOFC cathodes in the literature.^[86-89] Ohno et al.^[86] examined the electronic conductivity of R_{1-x}A_xMO₃ (R: lanthanide, A: alkaline-earth metal, M = Co, Cr, 0 < x < 1) and showed that La_{1-x}Ca_xCoO₃ exhibits the highest utility as electrodes in high-temperature SOFC. Isaacs and Olmer^[87] studied La_{0.5}Sr_{0.5}FeO₃, La_{0.8}Ba_{0.2}CoO₃ and La_{0.95}Mg_{0.05}Cr_{0.85}Al_{0.15}O₃, and identified La_{0.5}Sr_{0.5}FeO₃ as most active catalytic materials for oxygen reduction.

Accordingly, Yamamoto et al.^[88] inspected the electronic conductivity and polarization of sputtered La_{1-x}Sr_xMO₃ (M = Cr, Mn, Fe, Co) electrode on YSZ (Fig. 1.6(a)) and found La_{0.7}Sr_{0.3}MnO₃ to be the most suitable electrode at ~ 1073 K due to its high electronic conductivity, oxygen reduction capability and chemical stability with YSZ. Hammouche et al.^[90] systematically investigated the structural and thermal properties of La_{1-x}Sr_xMnO₃ (x=0 – 0.5) with varying the concentration of doped-Sr and found that the electrochemical activity of this composition improved with the increasing doping concentration. Jiang reviewed La_{1-x}Sr_xMnO₃ materials in terms of their complex function of structures, oxygen deficiencies, and interesting electrical, thermal, mechanical properties and electrochemical performances prominent for SOFC cathode.

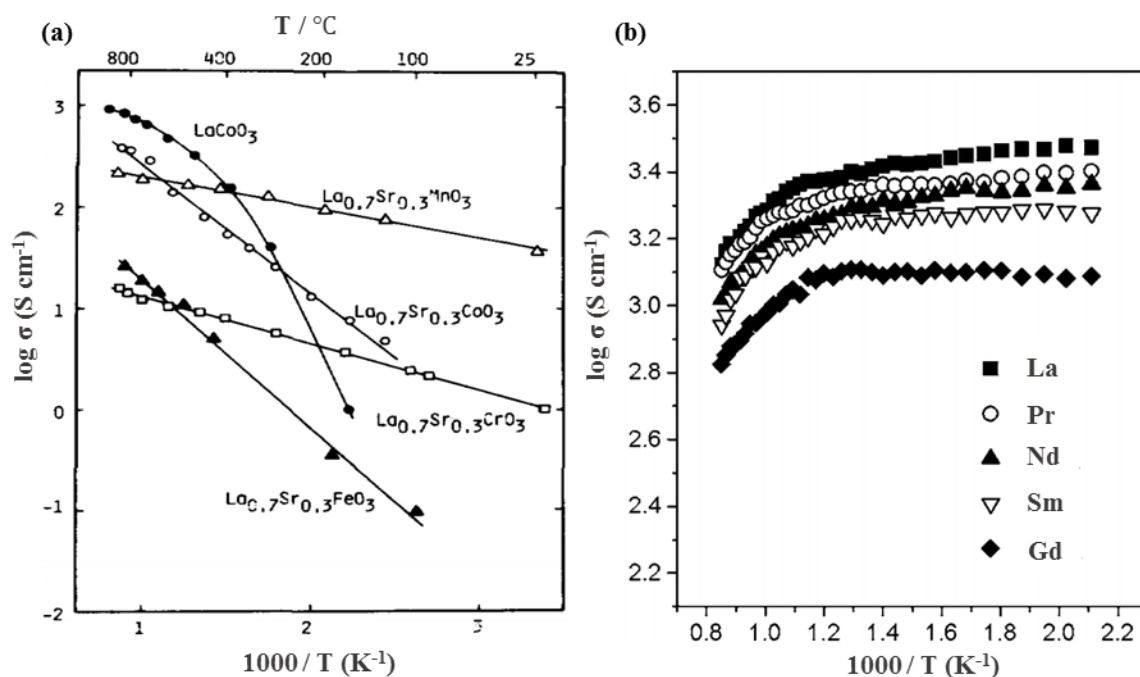


Fig. 1.6 Comparison of temperature-dependent electrical conductivity ($\sigma / \text{S cm}^{-1}$) in the open air with the combination of rare-earth and alkali-earth elements mixture of A-site cations and 3d transition metal at B-site cations: (a) LaCoO₃ and La_{0.7}Sr_{0.3}MO₃ (M = Cr, Mn, Fe, Co).^[88] Reprinted with permission from Elsevier®. (b) R_{0.6}Sr_{0.4}CoO₃ (R = La, Pr, Nd, Sm, Gd).^[89] Reprinted with permission from ECS®.

The high-performance stability of LSM materials based electrodes was attributed with the cation vacancies reduction under SOFC operating conditions which significantly enhances the sintering resistance of these materials.^[91] Although LSM has been widely used as a cathode in HT-SOFC due to its high electrical conductivity and catalytic activity in oxygen reduction reactions, high thermal stability and compatibility with common SOFC electrolytes, there are several limitations of this material. One of the main limitations of LSM is its increasing polarization resistance (<1 to $2000 \Omega \text{ cm}^2$) with decreasing temperature from 1300 to 800 K, which limits its viability for IT-

SOFC.^[83] Nevertheless, among various investigated cathode materials, till today, $\text{La}_{0.8}\text{Sr}_{0.2}\text{MnO}_3$ is considered the state-of-the-art cathode material for HT-SOFC.^[92]

Lee and Manthiram^[89] synthesized $\text{R}_{0.6}\text{Sr}_{0.4}\text{CoO}_3$ (R = La, Pr, Nd, Sm, Gd) perovskite oxides for IT-SOFC cathodes based on their ionic and electronic conductivity (Fig. 1.6(b)). They reported optimum electrocatalytic activity for $\text{Nd}_{0.6}\text{Sr}_{0.4}\text{CoO}_3$ due to opposite trends between the thermal expansion coefficients and the electrical and oxide ion conductivities from La to Gd in $\text{R}_{0.6}\text{Sr}_{0.4}\text{CoO}_3$. More recently, $\text{R}_x\text{Ba}_{1-x}\text{Co}_{0.7}\text{Fe}_{0.3}\text{O}_{3-\delta}$ (R = La, Pr, Nd, $x=0.1, 0.2$) were experimentally and theoretically characterized for IT-SOFC and found that partial doping of Ba cations by rare earth elements at A-sites, stabilize the cubic structure and enhance the catalytic activity for the oxygen reduction reaction.^[92] More recently, $\text{La}_{0.2}\text{Sr}_{0.25}\text{Ca}_{0.45}\text{TiO}_3$ was identified as a multifunctional perovskite, where all the anode, cathode and electrolyte components can be made up by this material for LT-SOFC.^[93] The multifunctionality of $\text{La}_{0.2}\text{Sr}_{0.25}\text{Ca}_{0.45}\text{TiO}_3$ as cathode, anode and electrolyte is achieved due to its variation in conducting behaviours at high and low oxygen partial pressures in oxidizing or reducing atmospheres. Intensive research has been carried out to discover high performance perovskite materials for LT-SOFC cathodes in the literatures, including $\text{La}_{0.85}\text{Sr}_{0.15}\text{Ca}_{0.85}\text{Fe}_{0.15}\text{O}_{3-\delta}$,^[94] $\text{SrCo}_{0.8}\text{Nb}_{0.1}\text{Ta}_{0.1}\text{O}_{3-\delta}$,^[95] $\text{BaCo}_{0.7}\text{Fe}_{0.22}\text{Sc}_{0.08}\text{O}_{3-\delta}$,^[96] $\text{Sr}_{0.92}\text{Fe}_x\text{Ti}_{1-x}\text{O}_{3-\delta}$ ($x=0.25, 0.30$),^[97] and $\text{SrNb}_{0.1}\text{Co}_{0.9-x}\text{Fe}_x\text{O}_{3-\delta}$.^[98]

The requirement of electronic, thermal, mechanical and electrochemical properties for SOFC anode is identical with cathode materials except the oxidizing environments replaced by reducing conditions. Among the numerous perovskite materials, SrTiO_3 is extensively characterized as a SOFC anode in the literature.^[99] The electronic properties of SrTiO_3 and its catalytic activity in reducing conditions can be tuned by partial substitution of Sr. For instance, La doping in the A-site of SrTiO_3 yields an electronic conductivity of nearly $\sim 0.01 - 500 \text{ S cm}^{-1}$ (minimum requirement

for SOFC anode $\sim 10\text{-}100\text{ S cm}^{-1}$ ^[99]) at 1100 - 1300 K with conditional oxygen partial pressure.^[100] Ruiz-Morales et al. showed that partial substitutions of A-site cation by La and B-site cations with Ga and Mn in SrTiO₃, exhibited superior catalytic performances for the oxidation of methane at high temperature competitive with state-of-the-art Ni-YSZ anodes.^[101]

Doping B-site with Al³⁺, Ga³⁺, Feⁿ⁺, Mg²⁺, Mnⁿ⁺ and Sc³⁺ within the parent perovskite La_{0.33}Sr_{0.67}Ti_{0.92}B_{0.08}O_{3- δ} , have also been investigated and claimed that dopants significantly affect the electronic conductivity, redox properties and electrocatalytic properties of this material.^[102] Multivalent cation (eg. Feⁿ⁺ or Mnⁿ⁺) doping at B-sites reduces the conductivity significantly more than single valency cations due to their reduction in preference to the Ti³⁺ cations. In addition, tailoring LaMnO₃, LaCrO₃, or La_{1-x}Sr_xCr_{1-y}M_yO₃ (M = Mn, Fe, Co, Ni) compositions can bring the best SOFC anode catalysts.^[103] For example, La_{1-x}Sr_xMn_{0.5}Cr_{0.5}O_{3- δ} (x=0, 0.2) were identified as promising SOFC anodes due to their high stability in reducing and oxidizing environment.^[8] Additionally, incorporation of other transition metals in La_{1-x}Sr_xCr_{1-y}M_yO₃ (M = Mn, Fe, Co, Ni) was found to enhance the catalytic properties in the SOFC anode.^[104] Other MIEC perovskites such as La_{0.6}Sr_{0.4}Co_{0.2}Fe_{0.8}O₃, La_{0.3}Sr_{0.7}TiO_{3- δ} , La_{0.3}Sr_{0.7}Co_{0.07}Ti_{0.97}O_{3- δ} were proposed as promising IT-SOFC anode based on their electrical and ionic conductivities.^[8, 105]

Sr- and Mn-doped LaGaO₃ have been widely investigated as SOFC electrolytes because of their high ionic and low electronic conductivity, and stability in both oxidizing and reducing environments.^[106] RGaO₃ (R = La, Pr, Nd, Sm) were systematically investigated by 10% doping of Ca with R in the A-site and found that the oxide ion conductivity is the dominant factor and have a strong dependency on A-site rare-earth cations with an order of increase, Sm < Nd < La < Pr (Fig. 1.7(a)). However, the electronic conductivity of doped LaGaO₃ was found to be dependent on A-site alkaline-earth dopants with an order of increase, Ca < Ba < Sr (Fig. 1.7(b)).^[58, 107] Al-doped

CaTiO₃ is proposed as a potential electrolyte due to its insulating character in reducing environments and high transport number.^[108] Furthermore, BaCeO₃, BaZrO₃, SrZrO₃ are identified as attractive electrolytes in SOFC applications.^[3] Nevertheless, the development of SOFC components from the view of lowering the operational temperature require a systemic investigation of temperature effects on the redox properties of potential perovskite materials for SOFC technology.

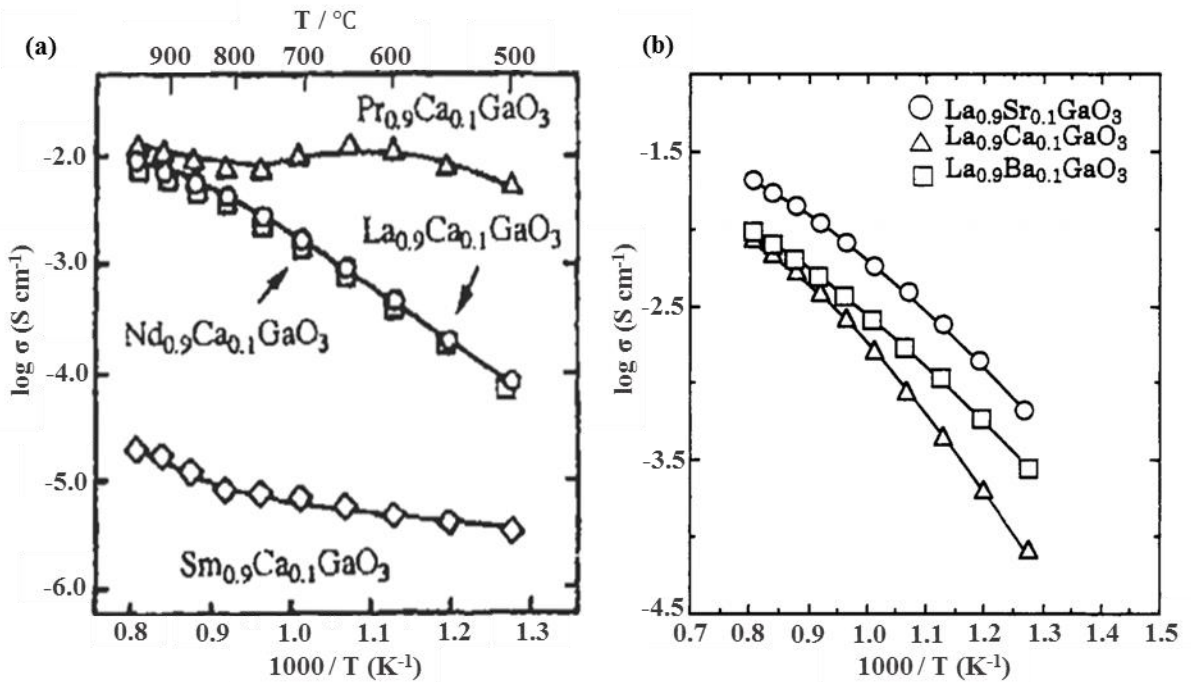


Fig. 1.7 (a) Electronic conductivity ($\sigma / \text{S cm}^{-1}$) of Ca-doped RGaO₃ (R = La, Pr, Nd, Sm).^[107] Reprinted with permission from Elsevier®. (b) Electronic conductivity ($\sigma / \text{S cm}^{-1}$) of doped LaGaO₃ by alkaline-earth cations (Sr, Ca, Ba).^[107] Reprinted with permission from Elsevier®.

1.4 First-Principles Studies of Perovskite Oxides

The high experimental cost has proved a major barrier to discover the high-temperature composition-structure-property relationships at the atomic level, considering the number of

conceivable materials based on the ABO_3 perovskite structure. Moreover, the experimental development of novel perovskites without *a priori* knowledge of redox activity could be very time-consuming. Advances in theory, computing hardware, and numerical algorithms have instead enabled new simulation-based methods for investigating the structure and properties of ABO_3 perovskites, in a relatively fast and cost-efficient manner. First-principles methods, such as density functional theory (DFT), can describe fundamental physical properties of materials at the molecular level, and domain-specific knowledge relevant to a particular application. These methods can explore thousands of potential materials via high-throughput approaches^[109] similarly to machine learning (ML) approaches.^[110] In the following sections, such first-principle approaches to the study and design of perovskite materials will be reviewed.

1.4.1 Effect of A-site and B-site Cations in ABO_3 Perovskites

Calle-Vallejo et al.^[111] used DFT (Generalized Gradient Approximation (GGA) - Revised Perdew Burke Ernzerhof (RPBE) exchange-correlation functional^[112]) to study the trends in the stability of 20 fully oxidized ABO_3 perovskites by predicting the formation energies (ΔG_f^0) of perfect crystal structures with Ba, Ca, Sr, Y and La metals at the A site, and 3d transition metals (from Ti to Cu) at the B site. Their results reveal that the ΔG_f^0 of perfect ABO_3 perovskites are linearly related to the atomic number of their B-site cation (see Fig. 1.8(a)). Further, this linear relationship was shown to depend on the oxidation state of the B-site cation, meaning that perovskites with the same oxidation states in A- and B-site cations (e.g. $LaCoO_3$) are more stable than those with mixed oxidation states (e.g. $BaCoO_3$).

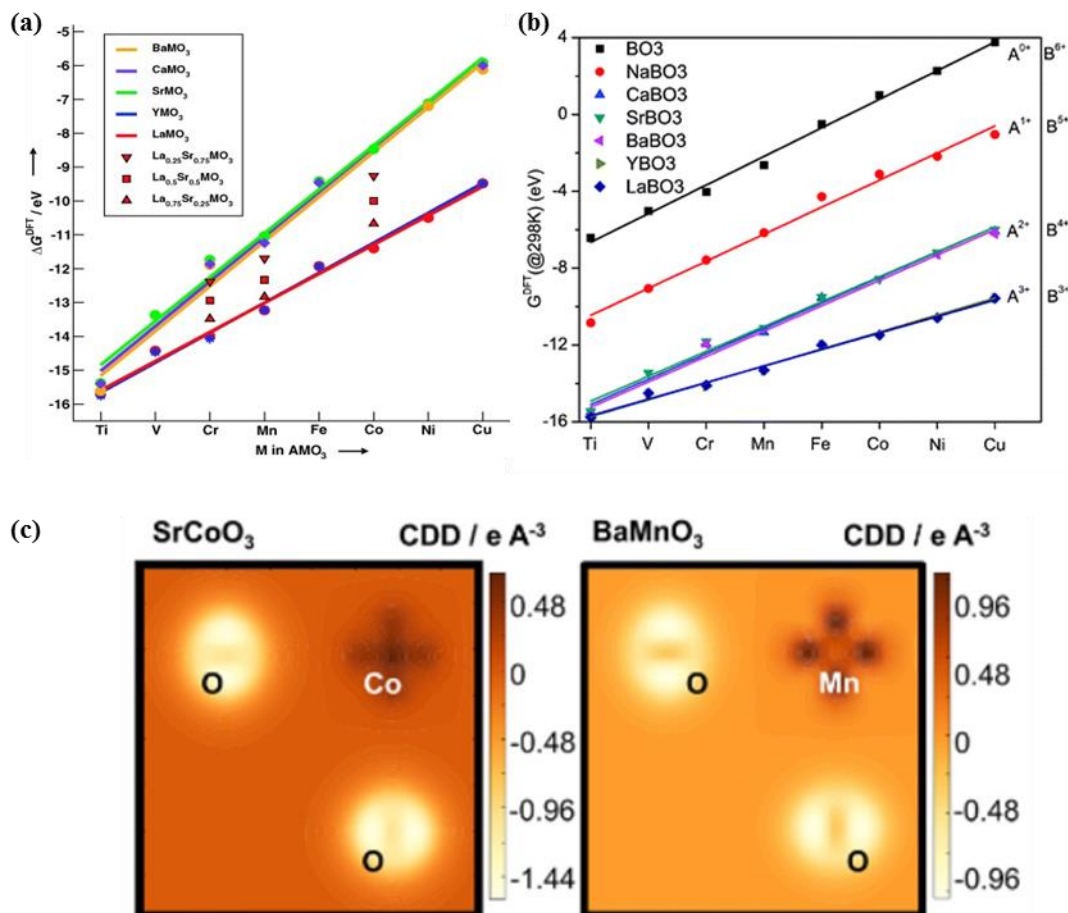


Fig. 1.8 Trends between formation energies of perovskites materials with B and A site cations: (a) with the atomic number of B-site cation,^[111] (b) with the similar B-site cations as shown in (a) and additional variation of A-site cation.^[113] Reprinted with permission from Royal Society of Chemistry[®]. (c) The difference in charge density distribution after O vacancy formation relative to the stoichiometric surface and the reference gas-phase O_2 (given at the height of the transition metal ion).^[114] Reprinted with permission from Wiley Online Library[®].

The stabilities of these perovskites also decreased more slowly along with the 3d series from Ti to Cu in B-site elements. Additionally, for a given B-site element the ΔG_f^0 in each group of

investigated perovskites remained near-independent of A. For instance, the calculated ΔG_f^0 of SrCoO₃, CaCoO₃, BaCoO₃ were almost identical. However, these qualitative trends were observed only for alkaline-earth or rare-earth metal perovskites, and whether these trends extend to other families of perovskites remain an open question. A further study by Calle-Vallejo^[110] accounted for the effect of the A-site into the ΔG_f^0 of ABO₃ consistent with his previous work.^[115] This study also showed that perovskites comprising matched oxidation state in A- and B-site cations exhibited a lower difference in ΔG_f^0 while those with different oxidation state cations (e.g. 2+ and 4+) have larger differences (see Fig. 1.8(b)). The lower oxidation state in the A-site cation yielded lower ΔG_f^0 . These trends were rationalized in terms of the A–O and B–O interactions in the ionic crystal.

Ezbiri et al.^[114] further studied the effect of the B-site and A-site bonds with oxygen, using the same method to calculate Gibbs free energies of oxygen vacancy formation (ΔG_v) of 12 perovskites (A=Sr, Ba, La; and B=Mn, Co, Ni, Cu). In contrast to the investigations of Calle-Vallejo et al., this work mostly focused on non-stoichiometric perovskites, for which more negative ΔG_v was attributed to the larger transition metal-oxygen bond length (e.g. Co-O in SrCoO_{3- δ} as compared with Mn-O in BaMnO_{3- δ}), which enables the formation of relatively stable oxygen vacancies. The performance of SrCoO_{3- δ} in this respect was additionally correlated with the charge transfer from the O-2p orbitals to the 3d orbitals of the B-site cation. Specifically, the lower gap between these states in SrCoO_{3- δ} , compared to other perovskites such as BaMnO_{3- δ} , yields higher O₂ exchange capacity (Fig. 1.8(c)). It was therefore proposed that SrCoO_{3- δ} could be an ideal material for solar thermochemical separation of O₂. However, the potential of this material for water splitting applications remains unexplored.

Li et al.^[1] employed DFT+U (GGA - Perdew-Burke-Ernzerhof (PBE) exchange-correlation functional^[116]) calculations to explore the structural stability and oxygen vacancy formation energies (E_v) of nine lanthanum based perovskites (LaMO_3 , $M = \text{Sc-Cu}$) as a function of δ for methane partial oxidation. Except for $\text{LaFeO}_{3-\delta}$, the E_v becomes less positive on moving from $\text{LaScO}_{3-\delta}$ to $\text{LaCuO}_{3-\delta}$, indicating increased reducibility. $\text{LaFeO}_{3-\delta}$ proved to be an exception here, by virtue of the stability of the d^5 configuration obtained upon reduction of Fe^{3+} , which is less than that for a Mn^{3+} B-site cation. In addition, Li et al.^[1] have done geometric energy decomposition analysis by the description of E_v as a function of two energy contributions: the removal of an oxygen from the crystal structure (ΔE_{bond}) and the relaxation of the structure in the presence of the oxygen vacancy (ΔE_{dist}). This work is also consistent with the previous works of Calle-Vallejo et al.^[111] and Zeng et al.^[113]

Similar results were predicted using DFT+U (GGA-PBE) by Brown et al.^[117] for the titanate perovskites CaTiO_3 , SrTiO_3 and BaTiO_3 . These authors found that E_v was proportional to the degree of geometrical distortion within the defective TiO_2 sublattice, and this correlates with the size of the A-site cation ($\text{Ca}^{2+} < \text{Sr}^{2+} < \text{Ba}^{2+}$). For Ca^{2+} , vacancy defects in the (001) surface yield dramatic structural distortions, whereby TiO_2 octahedra rotate toward an orthorhombic arrangement. The TiO_2 sublattice in CaTiO_3 effectively acts as a thermodynamic trap for oxygen vacancy defects, which incur prohibitively high E_v , but relatively small migration barriers. On the other hand, these results indicate that vacancy diffusion in SrTiO_3 and BaTiO_3 (which have larger A-site cations) is kinetically controlled.

1.4.2 Effect of Doping Both A-site and B-site Cations in ABO₃ Perovskites

Deml et al.^[118] used PBE+U to predict E_v of Sr_xLa_{1-x}Mn_yAl_{1-y}O_{3-δ} ((x, y)=(0.2, 0.4, 0.6, 0.8)) as a function of A-cation and B-cation substitution. Two mechanistic regimes for oxygen vacancy formation were identified: when $x_{Sr} > y_{Mn}$ (regime 1) and $x_{Sr} \leq y_{Mn}$ (regime 2). Decreasing E_v could be systematically achieved by increasing Sr content until it is equivalent to the Mn content. This led to the conclusion that the ideal material composition is Sr_{0.4}La_{0.6}Mn_{0.6}Al_{0.4}O_{3-δ} with an E_v value of 2.6 eV. A material-independent E_v range ($1.8 < E_v < 2.4$) was proposed to define suitable perovskites based on water splitting thermodynamics, with a reduction at 1623 K and $p(O_2)$ of 10^{-5} atm and oxidation at 1273 K. The selected Sr_{0.4}La_{0.6}Mn_{0.6}Al_{0.4}O_{3-δ} material has an E_v larger than 2.4 eV, which is related to the higher temperature and/or lower $p(O_2)$ required to be reduced. The E_v range proposed by Deml et al. enables high throughput pre-screening of new potential solar thermochemical water splitting based on 0 K energy calculations and neglecting explicit thermal corrections. The impact of thermal corrections relevant to redox materials operating conditions has not been explored deeply in this respect.

In a separate study, Deml et al.^[119] explored the effect of materials properties on E_v and enthalpies of formation (ΔH_f) using Green function methods (i.e. GW theory) and DFT+U. The electronic bandgap (E_g) calculated using either method enabled E_v to be predicted via two different correlations (see Fig. 1.9), however, with different margins of statistical error. If this is compared with the values expected in the allowable range presented by Deml et al. (1.8 to 2.4 eV),^[118] the deviation of this value implies an accuracy of $\pm 21.67\%$ over the lower limit and $\pm 16.25\%$ over the higher limit. In another range of values observed in Fig. 1.9, the model accurately described 98% of the oxides considered.^[120]

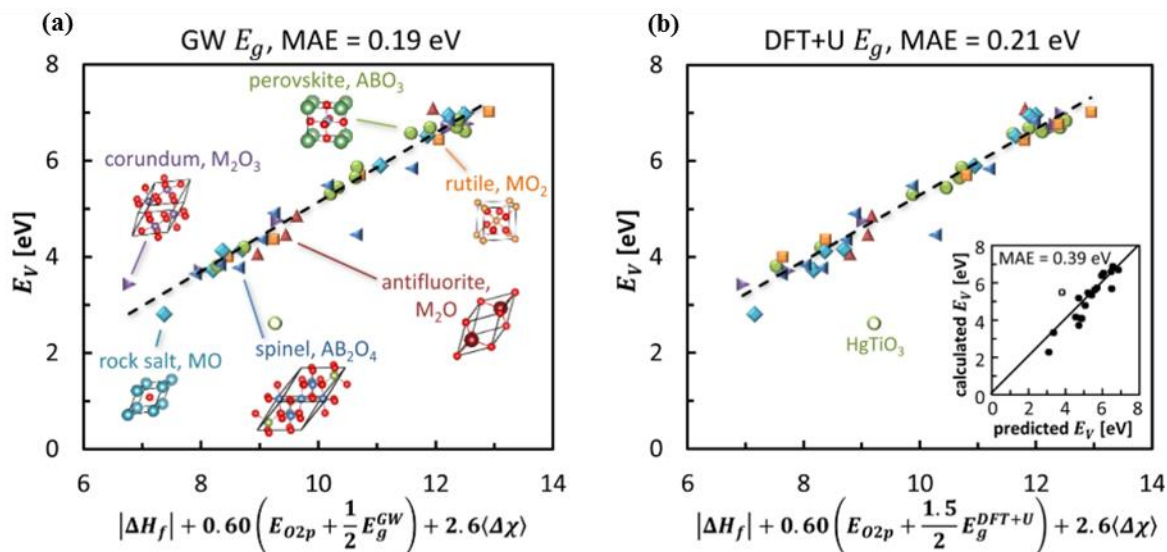


Fig. 1.9 Predicted relationship between formation energy of a neutral oxygen vacancy (E_v) and, in order of significance, oxide enthalpies of formation (ΔH_f); the midgap energy relative to the O 2p band centre (E_{O-2p}) + $(1/2)E_g$, and atomic electronegativities ($\langle \Delta\chi \rangle$). This linear correlation was shown for band gap values from both (a) GW, and (b) DFT+U calculations, reproducing calculated E_v .^[119] In the inset (b), the mean absolute error (MAE) of 0.39 eV shows the performance of E_v model resulting from a subset of 18 randomly chosen oxides (excluded from the predictive model) against 1800 oxides. (b) Reprinted with permission from ACS Publications[®].

Maiti et al.^[121] used DFT (GGA - Perdew-Wang 1991 (PW91) exchange-correlation functional^[122]) and *in-situ* X-ray diffraction (XRD) to investigate bulk and surface E_v of $La_{1-x}Sr_xFe_{1-y}Co_yO_{3-\delta}$ ($x=0.2$ or 0.5 , $y=0$ or 0.5) along (100) and (110) planes. From their analysis, it was shown that increasing the Sr content in the A-site and decreasing Fe content in the B-site reduces E_v . In particular, E_v in $La_{0.5}Sr_{0.5}CoO_{3-\delta}$ is energetically the most favourable among the selected materials within the preferred energy zone (3.36 ± 0.5 eV). However, E_v is likely site-specific, with vacancy formation in the La layer being more favourable than in the Sr layer due to

facile electron redistribution in the former sub-lattice. For the $\text{La}_{1-x}\text{Sr}_x\text{Fe}_{1-y}\text{Co}_y\text{O}_{3-\delta}$ perovskite family, comparison of CO_2 adsorption strengths across the different pure and non-stoichiometric surface terminations revealed that La-O termination surface is more effective in converting CO_2 to CO.

In a separate study, Maiti et al.^[123] employed DFT (GGA-PBE) to assess the CO_2 conversion capability for reverse water gas shift chemical looping using four major groups of perovskites: ABO_3 , $\text{AA}'\text{BO}_3$, $\text{ABB}'\text{O}_3$ and $\text{AA}'\text{BB}'\text{O}_3$ ($A = \text{La, Ca, Sr, Ba}$; $B = \text{Cr, Mn, Fe, Co, Ni, Cu, Al, Ga}$). They achieved 100% selective CO generation from CO_2 at the highest known rates ($160 \mu\text{moles min}^{-1} \text{g}^{-1}$ of perovskite) at record low process temperatures of 723–773 K using La and Ca-based perovskite oxides. They obtained a descriptor, shown in Fig. 1.10, of the E_v fitted for mixed $\text{ABB}'\text{O}_3$ and $\text{AA}'\text{BO}_3$ that helped to describe the mixed perovskites $\text{AA}'\text{BB}'\text{O}_3$ similar to the work of Deml et al.^[119] by using the enthalpy of formation and the binding energy obtained experimentally. They focus their study only on materials having an E_v of 3.36 ± 0.5 eV where they found a few compositions with promising splitting performance.

Sr- and Co-doped $\text{LaGaO}_{3-\delta}$ was evaluated as efficient redox materials by both experiments and DFT calculations.^[124] Both analyses revealed that Co doping at the B-site weakens the B-site metal-oxygen bonding, thereby enhancing the reduction reaction and hence the reduction temperature. E_v of $\text{La}_{1-x}\text{Sr}_x\text{Ga}_{1-y}\text{Co}_y\text{O}_{3-\delta}$ can also be tuned by tailoring the dopant concentration of Sr and Co content. This work aligned with the findings shown by Deml et al.^[118] in the Sr and Mn doping effects. This material showed H_2 production capacities 15 times higher than that obtained using ceria.

Mulmi et al.^[125] reported $\text{Ba}_2\text{Ca}_{0.66}\text{Nb}_{1.34-x}\text{Fe}_x\text{O}_{6-\delta}$ perovskite as a promising candidate for thermochemical CO_2 splitting compared to the state-of-the-art material ceria. They used DFT+U (GGA-PBE) analysis calculations to predict the energy required for carbon deposition and iron carbide formation, similarly to Sastre et al.^[126] with La-Fe based perovskites. The most stable configuration of 2O-C-Fe is trigonal planar while moving from that configuration required a higher E_v value. This work showed that the addition of Ca increased E_v , showing similar conclusions as observed by Cooper et al.^[66] in higher ΔH_f by the addition of Ca.

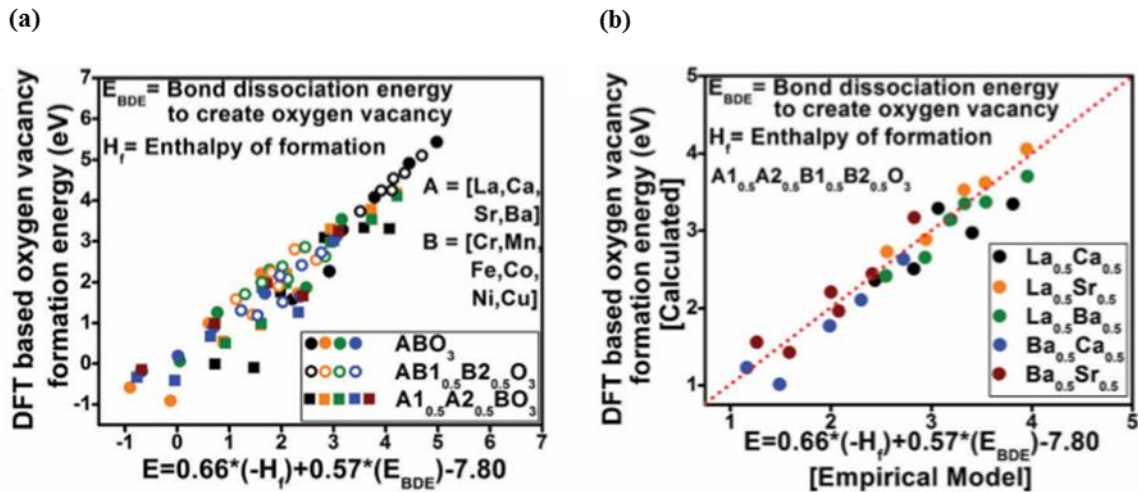


Fig. 1.10 Empirical modeling of oxygen vacancy formation energies (E_v) of the perovskite oxides. (a) FT-computed energies (E_v) for ABO_3 , and substituted as shown, were fitted to the enthalpies of formation and bond dissociation energies (E_{BDE}). (b) The fitted model of E_v was used to calculate the energies for the mixed perovskites. The DFT-calculated energies matched well with that from the empirical model.^[123] Reprinted with permission from Royal Society of Chemistry®.

1.4.3 High-Throughput Screening Studies

Meredig and Wolverton^[127] published one of the first studies to develop a thermodynamic screening technique to identify new H₂O and CO₂ splitting materials. Initially, they applied their method to 105 binary and ternary oxide cycles that failed to meet the reduction enthalpy and entropy regimes for thermodynamically favorable H₂O and CO₂ splitting. They used DFT (PW91) to compute reduction/oxidation enthalpies and entropies of four selected pair cycles: MgO-Mg, Al₂O₃-Al, SiO₂-Si, and GeO₂-Ge. Their results showed very accurate predictions with single metal oxides.

Emery et al.^[128] performed one of the most extensive high-throughput investigations using DFT/DFT+U (GGA-PBE) reported in the literature to date, by screening 5,329 cubic and distorted perovskites with two descriptors (thermodynamic stability and E_v), see Fig. 1.11. Of these, 383 perovskites were deemed to be stable, based on a threshold value of 25 meV/atom (at 0 K). The second descriptor was applied for a “shortlist” of stable compounds, resulting in the identification of 139 perovskite materials (12 cubic, 8 rhombohedral and 119 orthorhombic) for which $2.5 < E_v < 5$ eV/atom at T = 0 K. Notably, these 139 candidates included some compounds that had never been conceived or tested experimentally, such as BiVO₃, CeCoO₃, CeAgO₃, LaAgO₃, YbMoO₃, LiIrO₃.

Recently, a new tolerance factor was predicted by Bartel et al.^[129] from 576 experimentally observed stable ABX₃ oxides and halides, which they claimed as significantly better than the widely used Goldschmidt tolerance factor. Here, the oxidation state of A-site cation is considered in addition to the ionic radii-based Goldschmidt tolerance factor. This tolerance factor was used in a high-throughput to predict the probability of forming stable double perovskites. For 990 oxides

($\text{La}_2\text{BB}'\text{O}_6$) and 164 halides ($\text{Cs}_2\text{BB}'\text{Cl}_6$) the probabilities were greater than 85% and 69.6% respectively.

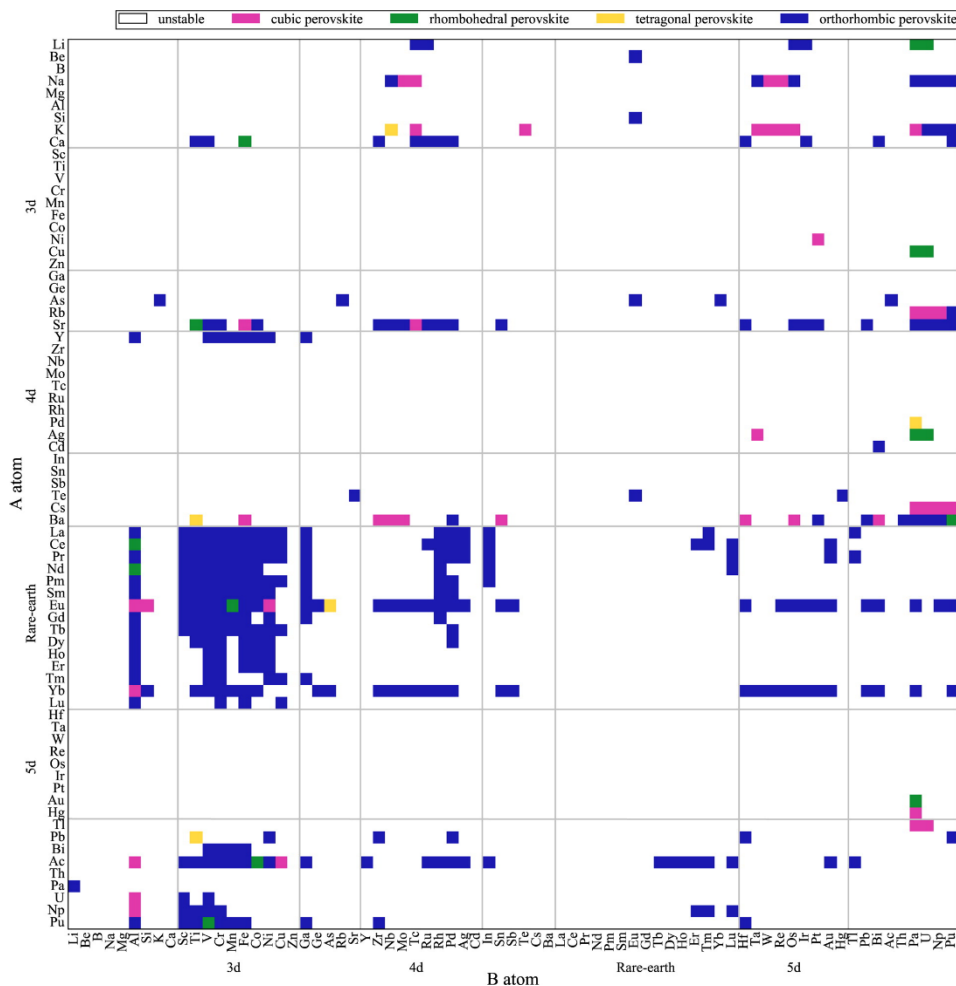


Fig. 1.11 High-throughput DFT map of predicted 389 stable ABO_3 perovskites out of 5329 stoichiometric compounds.^[128] Reprinted with permission from ACS Publications®.

Michalsky et al.^[130] investigated the thermochemical activity of 60 cubic perovskites $\text{A}_{0.5}\text{A}'_{0.5}\text{B}_{0.5}\text{B}'_{0.5}\text{O}_{3-\delta}$ (A, A' = Ca, Sr, La; B, B' = Mn, Co, Mo, W) using DFT (GGA - RPBE) along with experimental validation. Assessing the free energy of reduction (ΔG_{RR}) at high temperatures

and NH_3 production from H_2O at low temperatures, these authors concluded that the B-site element in the ABO_3 perovskite plays the vital role in tuning the redox properties, compared to the A-site cation. Perovskites containing Co or Mn at the surface, and Co-doped with Mo or W in bulk, such as CaCoO_3 -terminated $\text{La}_{0.5}\text{Ca}_{0.5}\text{Mo}_{0.5}\text{Co}_{0.5}\text{O}_3$, SrCoO_3 -terminated $\text{Sr}_{0.5}\text{La}_{0.5}\text{Co}_{0.5}\text{W}_{0.5}\text{O}_3$ and CaMnO_3 -terminated $\text{Sr}_{0.5}\text{Ca}_{0.5}\text{MnO}_3$, were proposed as promising candidates for solar-driven thermochemical ammonia production.

1.4.4 Ab-Initio Databases and Machine-Learning Approaches

As recent DFT analyses were performed based on thousands of compounds, a large effort has been done into gathering all these data in material databases. Some notable materials databases are listed here in Table 1.1. The Computational Materials Repository gathers most of the databases organized by type of material computed.^[131] This repository provides a quickly accessible way to other material databases. Automatic-FLOW for Materials Discovery (AFLOW) contains over 2,000,000 materials with more than 300,000 band-structures (BS).^[132] This is one of the few databases that includes thermochemical properties relevant to this Thesis. The Materials Project contains a database of properties such as E_v and E_g , amongst others.^[133] The Open Quantum Materials Database (OQMD), developed by the Wolverton group,^[134] contains theoretical (i.e. DFT) and experimental E_v of more than 200,000 materials. The Novel Materials Discovery Laboratory (NOMAD) maintains the largest repository for computational materials science accepted by Nature Scientific Data, and includes more than 50,000,000 total energies, 44,000,000 bulk crystal structures, 37,000,000 molecular geometries, 4,600,000 molecule/cluster geometries, ~2,000,000 BS, 276,000 surfaces and 91 phonon calculations.^[135]

Table 1.1 DFT Materials Databases

Database	Number of Compounds	Properties included	Link
The Computational Materials Repository	-	Energetics Structural Electronic Elastic Optical Thermoelectric	https://cmr.fysik.dtu.dk/
NOMAD	Over 50,000,000	Structural Energetics Electronic Optoelectric Thermoelectric	http://nomad-repository.eu
AFLOW	Over 2,000,000	Energetic Structural Electronic	http://afflowlib.org/
The Materials Project	over 600,000	Energetics Structural	https://materialsproject.org/
OQMD	over 200,000	Energetics Structural	http://oqmd.org/
National Renewable Energy Laboratory's computational materials database (NRELMatDB)	Over 30000	Structural Thermochemical Energetic Electronic Dielectric	https://materials.nrel.gov/
JARVIS-DFT	873	Energetics Structural Electronic Elastic Optical Thermoelectric	https://www.nist.gov/programs-projects/jarvis-dft

NREL MatDB (National Renewable Energy Laboratory's computational materials database) includes structures, bandgaps, absorption spectra and thermochemical properties for more than 30,000 materials relevant to renewable energy applications, such as photovoltaic materials,

materials for photo-electrochemical water splitting and thermoelectric.^[136] The JARVIS-DFT database includes the electronic, elastic, optical and thermoelectric properties of 873 materials.^[137]

The assembly of these material property databases can be used by ML approaches to predict new perovskite materials before their synthesis and characterization is attempted experimentally.^[129, 138, 139] ML algorithms “learn” from existing data which are collected from computational simulations and experimental measurements. In one of the first ML studies in this field, Hautier et al.^[140] combined the data mining structure predictor and high-throughput *ab initio* computations to predict 209 new A-B-O compounds across different chemical classes. This method is fast and efficient but has limitations. It is possible that a true ground state can be missed, and this method cannot predict a compound crystallizing in an unknown structure prototype. However, finding a new stable compound through this method, while not guaranteeing the true ground state, indicates that, in any case, there is an unknown stable compound existing in this chemical system.

A later study was developed by Balachandran et al.^[141] using two ML models. Fig. 1.12(a) represents the structural plot for stable cubic and non-cubic perovskites as a function of the Mendeleev number of A and B components developed by Balachandran et al. The first ML model (random forest) classified the 390 compounds into 254 perovskites and 136 non-perovskites with a 90% average cross-validation (CV) accuracy. The second ML model (gradient tree boosting) further classified the perovskites into 22 known cubic perovskites and 232 known non-cubic perovskites with a 94% average CV accuracy. Shannon’s ionic radii, tolerance and octahedral factors, A-O and B-O bond length and the A and B Villars’ Mendeleev numbers were the effective chemical descriptors that affected the classification of the perovskites. This work found that the new perovskites are most likely to occur when the A and B atoms are a lanthanide or actinide,

when the A atom is an alkali, alkali earth, or late transition metal atom, or when the B atom is a p-block atom. The data was validated using a DFT-based convex hull (DFT-CH) approach.

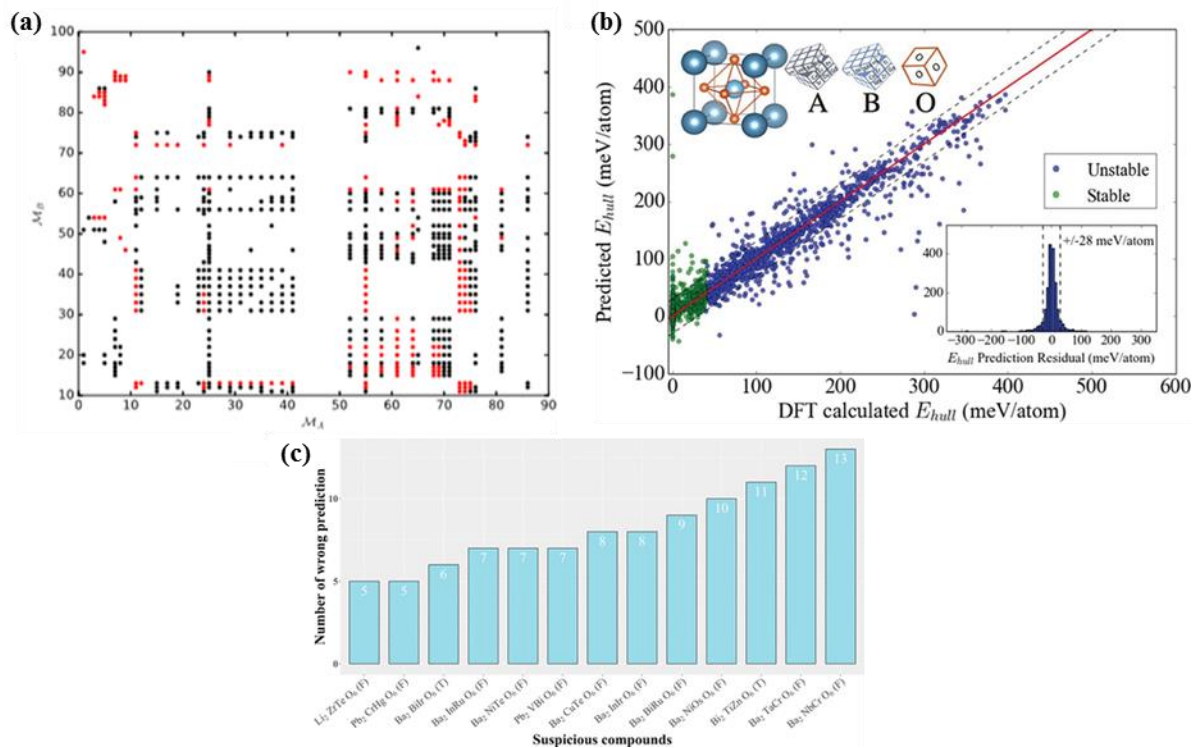


Fig. 1.12 ML example of a prediction of compounds: (a) structural map of cubic perovskites (black) and non-cubic perovskites (red); M_A and M_B represent Mendeleev number of A and B atoms. Reprinted with permission from APS Physics[®];[141] (b) prediction of perovskite stability extended from DFT calculations presented in Ref.[142] Reprinted with permission from ACS Publications[®]; and (c) number of inconsistent predictions on each $\text{A}_2\text{B}'\text{B}''\text{O}_6$ compound for 16 kinds of ML models. T means perovskite and F means non-perovskite. Reprinted with permission from Elsevier[®]. [143]

However, the ML analyses and predictions are statistical and hence are always subject to changes caused by fluctuations.[141] For instance, discrepancies were obtained for various reasons, such as

missing important entropic contributions to the free energy at finite temperatures in most of the materials used for training the ML algorithm. Thus, for several materials, the DFT-CH approach suffices but for others that are rich in structural and other phase transitions, such as perovskites, this may not be the case.

In parallel, Li et al.^[142] (Fig. 1.12(b)) checked several ML classification and regression models to predict the thermodynamic phase stability of perovskite oxides. This work used a dataset of more than 1929 DFT-calculated perovskite oxide energies. Out of 791 features, the top 70 were enough to produce the most accurate models without significant overfitting based on the CH energies of each perovskite compound, similar to Ref.^[141] This model was then validated for 15 new compounds where it was found that the model is useful to quickly identify stable and near-stable perovskite oxides when the elements frequently appear in the database. Conversely, the model should probably not be used for elements that are infrequent or not represented in the database.^[142]

Xu et al.^[143] developed a data-driven based ML model on the basis of perovskite stability data from the Materials Project database. They used a procedure to identify ABX_3 and $A_2B'B''X_6$ stability by using the crystal structure stored in this database. Importantly, they found several inconsistent predictions on each $A_2B'B''O_6$ compound for 16 kinds of ML models (Fig. 1.12(c)). 590 ABX_3 and 538 $A_2B'B''X_6$ compounds were extracted, and these results extended previous perovskite data, correcting mistakes of 11 ABO_3 compounds in Refs.^[141, 142, 144] This model can predict formability of perovskite comparable to typical DFT prediction and showed potential for reliable future ML work.

Pilania et al.^[144] constructed a ML model (support vector classification) using training sets of 185 experimentally reported ABX_3 compounds to predict the stability of 455 possible ABX_3

compounds. Of these, 40 stable ABX_3 perovskite structures were identified with an accuracy of $\geq 85\%$. They found similar descriptors as per Ref.^[141] using a set of kernel methods. They also found that to make reliable predictions of thermodynamic stability of the identified ABX_3 , and chemistries must be rigorously tested against all potential chemical combinations that may combine to form the composition of interest. Although this work is very rigorous, it was not applied to ABO_3 perovskites.

Evolutionary methods (a type of ML algorithm) have also been used for the prediction of the space group of a specific composition. Ong et al.^[145] proposed $BiVO_3$ as a redox material by generating a population of structures with randomly selected space groups. Later, each structure was optimized by DFT+U methods, and E_v calculated to yield the predicted crystal structures with the minimum energy. However, some experimental studies have found that $BiVO_3$ is not a stable structure at high temperatures.^[146] The heat treatment conditions involve phases such as metallic BiV_2O_5 , $BiVO_4$, $Bi_4V_2O_{10.5}$, and $Bi_{1.62}V_8O_{16}$, indicates that the DFT studies should pay attention to phase composition and stability at high temperatures.

The various DFT frameworks discussed above rely mostly upon GGA exchange-correlation functionals, (e.g. PBE, RPBE and PW91), for assessing or predicting key properties of perovskite materials, such as oxygen vacancy formation energies, enthalpies of formation, bond-dissociation energies, cation oxidation states, reactant adsorption energies. These parameters govern high-temperature gas splitting reactions (see Table 1.2). The choice of exchange-correlational functionals in any DFT approximation is crucial in determining the accuracy of properties derived from the electronic structure of a material. More specifically, ABO_3 perovskites invariably exhibit electron densities with highly localized regions within individual BO_6 octahedra that will present challenges to any GGA-level exchange-correlation functional.

Table 1.2 The exchange-correlation functionals used in DFT methods for characterizing the properties of perovskite oxides related to oxygen-deficient applications.

Years	GGA	Investigated materials	Materials properties	Ref
2010	RPBE	20 ABO ₃ perovskites (A = Y, La, Ca, Sr, Ba; B=Ti, V, Cr, Mn, Fe, Co, Ni, Cu)	Formation energy, stability	[111]
2013	RPBE	ABO ₃ Perovskites (A = Na, Ca, Sr, Ba, Y, La; B = Ta, W, Re, Os, Ir, Pt; Ti, V, Cr, Mn, Fe, Co, Ni, Cu), BO ₃ oxides	Formation energy, stability	[113]
2014	PBE+U	16 compositions of Sr _x La _{1-x} Mn _y Al _{1-y} O ₃ (x, y)=(0.2,0.4,0.6,0.8)	Oxygen vacancy formation energy	[118]
2015	PW91	La _{0.75} Sr _{0.25} Co _{1-y} Fe _y O _{3-δ} (y=0,0.5,0.75,1)	Adsorption energy	[147]
2015	GW/ PBE+U	ABO ₃ perovskite (A=Ba, Ca, Hg, K, Sc, Sr, Y; B= Sn, Ti, Zr, Nb, Al, Hf)	Oxygen vacancy formation energy, oxide enthalpy of formation, bandgap	[119]
2015	RPBE	ABO ₃ perovskite (A=Sr, Ba or La; and B=Mn, Co, Ni or Cu)	Oxygen exchange capacity	[114]
2016	PW91	La _(1-x) Sr _x Fe _(1-y) Co _y O _(3-δ) (x=0.2 or 0.5; y=0 or 0.5)	Oxygen vacancy formation energy, adsorption strength	[121]
2016	PBE/ PBE+U	5329 cubic and distorted ABO ₃ perovskites	Thermodynamic stability, oxygen vacancy formation energy,	[128]
2017	RPBE	60 cubic perovskites A _{0.5} A' _{0.5} B _{0.5} B' _{0.5} O _{3-δ} (A, A' = Ca, Sr, La; B, B' = Mn, Co, Mo, W)	N ₂ reduction and oxygen vacancy formation energy, Vacancy stability, Thermochemical activity	[130]
2017	PBE+U	Ba ₂ Ca _{0.66} Nb _{1.34-x} Fe _x O _{6-δ}	Oxygen vacancy formation energy,	[125]
2018	PBE	Earth-abundant perovskites A _{1-x} A' _x B _{1-y} B' _y O ₃ (A, A' = La, Ca, Sr, Ba; B, B' = Cr, Mn, De, Co, Ni, Cu, Al, Ga)	Oxygen vacancy formation energy, bonding dissociation energy	[123]
2018	PBE+U	LaMO ₃ (M = Sc, Ti, V, Cr, Mn, Fe, Co, Ni, Cu)	Oxygen vacancy formation energy	[1]
2019	PBE+U	(Ce ₂ Ti ₂ O ₇)	Oxygen vacancy formation energy, reaction energy	[148]
2019	PBE+U	La _{1-x} Sr _x Ga _{1-y} Co _y O _{3-δ}	Oxygen vacancy formation energy	[124]

For instance, the predicted ΔG_f^0 values for a range ABO₃ perovskites with 3d transition metals in B site using the RPBE exchange-correlational functional, showed a constant difference of ~0.75

eV from the respective experimental ΔG_f^0 values.^[111] This likely arises from the incorrect localization of 3d electron in the B-site cation due to the self-interaction error inherent to GGA-DFT. This error can be mitigated by applying a Hubbard Coulomb/exchange U/J corrections to the strongly-correlated electrons in the material, and particularly to the 3d and/or 4f electrons (See the theoretical overview of the Hubbard correction (§2.2.8.4) provided in Chapter 2). However, accurately reproducing experimental properties typically requires specific empirical parameterization of U/J values against some known reference value. Alternatively, there are non-empirical strategies for calculating the effective Hubbard U parameter for a specific material.^[149]

1.5 Knowledge Gap, Project Aims and Chapter Outline

The preceding literature review has pointed out that ABO_3 perovskite oxides in which A-site cations are rare-earth (such as La, Ce, Sm) or alkaline-earth (such as Ca, Sr, Ba) or a mixture thereof, and B-site cations that are mostly 3d transition metals (such as Ti, Cr, Mn, Fe, Co, Ni, Cu or their mixture) show particularly attractive potential for STWS and SOFC applications. However, it is evident that, despite a handful of investigations into undoped ABO_3 , a systematic investigation of the factors that control structural stability, electronic structure, thermochemical properties and oxygen reduction thermochemistry at STWS- and SOFC-relevant conditions has not been reported in the literature to date. Therefore, such a study is important in identifying new potential materials for these technologies, along with design parameters that will enable their generation.

This project seeks to address this knowledge gap by investigating undoped ABO_3 perovskites systematically in terms of the A-site and B-site cations to explore the fundamental origins of structural, thermochemical and reduction trends in these materials. This Thesis will pursue the following specific aims towards this overarching goal:

1. Develop an accurate DFT protocol for modelling electronic structures and, vibrational and phonon properties of $Ba^{2+}M^{4+}O_3^{2-}$ ($M = Ti - Cu$) and $R^{3+}Co^{3+}O_3^{2-}$ ($R = La, Ce, Nd, Sm$). The DFT protocol will be benchmarked against experimental data for a smaller subset of perovskite compounds available in the literature.
2. Characterize the structural, thermochemical and reduction properties of $Ba^{2+}M^{4+}O_3^{2-}$ ($M = Ti - Cu$) and $R^{3+}Co^{3+}O_3^{2-}$ ($R = La, Ce, Nd, Sm$). The effect of the B-site cation on $Ba^{2+}M^{4+}O_3^{2-}$ and the A-site cation on $R^{3+}Co^{3+}O_3^{2-}$ will also be discussed from the point of view of these electronic and vibrational properties.
3. Characterize the high-temperature thermochemistry of oxygen-deficient $Ba^{2+}M^{4+}O_3^{2-}$ ($M = Ti - Cu$) and $R^{3+}Co^{3+}O_3^{2-}$ ($R = La, Ce, Nd, Sm$) under conditions relevant to STWS and SOFC applications. The effect of temperatures and oxygen vacancies on $Ba^{2+}M^{4+}O_3^{2-}$ and $R^{3+}Co^{3+}O_3^{2-}$ will also be elucidated.

The remainder of this Thesis is outlined as follows:

- **Chapter Two** details the electronic structure methodology used throughout the remainder of this Thesis. An efficient DFT protocol is developed and validated with the available experimental data of ABO_3 perovskite containing alkaline cation at the A-site (e.g. Ba), and 4f metal (Ce), 4d metal (Zr), and 3d metal (Mn) at the B-site. (*Aim 1*)
- **Chapter Three** presents trends in structural, electronic, thermochemical and oxygen reduction properties of $Ba^{2+}M^{4+}O_3^{2-}$ ($M = Ti - Cu$) and the effects of B-site cations along with the 3d series metal series from Ti to Cu at B-site based on first-principles DFT calculations. (*Aims 2, 3*)
- **Chapter Four** investigates the role of the A-site cation in $R^{3+}Co^{3+}O_3^{2-}$ ($R = La, Ce, Nd, Sm$) systematically and provides new insight into the structural stability, electronic, thermochemical properties of oxygen-deficient $R^{3+}Co^{3+}O_3^{2-}$ based on first-principles DFT calculations. (*Aims 2, 3*)
- **Chapter Five** presents the main conclusions of the thesis and outlines avenues for potential future work.

1.6 References

1. Li Q, Deng Y-X, Zhu Y-A, et al. Structural stability of lanthanum-based oxygen-deficient perovskites in redox catalysis: a density functional theory study. *Catalysis Today*. 2018.
2. Goodenough JB. Electronic and ionic transport properties and other physical aspects of perovskites. *Rep Prog Phys*. 2004;67(11):1915-93.
3. Ishihara T. *Perovskite oxide for solid oxide fuel cells*: Springer Science & Business Media; 2009.
4. Kubicek M, Bork AH, Rupp JL. Perovskite oxides—a review on a versatile material class for solar-to-fuel conversion processes. *Journal of Materials Chemistry A*. 2017;5(24):11983-2000.
5. Carrillo RJ, Scheffe JR. Advances and trends in redox materials for solar thermochemical fuel production. *Solar Energy*. 2017;156:3-20.
6. Haeussler A, Abanades S, Jouannaux J, Julbe A. Non-stoichiometric redox active perovskite materials for solar thermochemical fuel production: a review. *Catalysts*. 2018;8(12):611.
7. Babaei A ZL, Tan SL. Pd-promoted (La, Ca)(Cr, Mn)O₃/GDC anode for hydrogen and methane oxidation reactions of solid oxide fuel cells. *Solid State Ionics*. 2010;181(25-26):1221-8.
8. Deleebeeck L, Fournier J, Birss V. Comparison of Sr-doped and Sr-free La_{1-x}Sr_xMn_{0.5}Cr_{0.5}O_{3±δ} SOFC Anodes. *Solid State Ionics*. 2010;181(25-26):1229-37.
9. El-Himri A, Marrero-López D, Ruiz-Morales JC, Pena-Martinez J, Nunez P. Structural and electrochemical characterisation of Pr_{0.7}Ca_{0.3}Cr_{1-y}Mn_yO_{3-δ} as symmetrical solid oxide fuel cell electrodes. *Journal of Power Sources*. 2009;188(1):230-7.

10. Fu C, Sun K, Zhang N, Chen X, Zhou D. Electrochemical characteristics of LSCF–SDC composite cathode for intermediate temperature SOFC. *Electrochimica Acta*. 2007;52(13):4589-94.
11. Jun A, Kim J, Shin J, Kim G. Perovskite as a cathode material: a review of its role in solid oxide fuel cell technology. *ChemElectroChem*. 2016;3(4):511-30.
12. Da Silva FS, de Souza TM. Novel materials for solid oxide fuel cell technologies: A literature review. *International Journal of Hydrogen Energy*. 2017;42(41):26020-36.
13. Hossain S, Abdalla AM, Jamain SNB, Zaini JH, Azad AK. A review on proton conducting electrolytes for clean energy and intermediate temperature-solid oxide fuel cells. *Renewable and Sustainable Energy Reviews*. 2017;79:750-64.
14. Kan WH, Thangadurai V. Challenges and prospects of anodes for solid oxide fuel cells (SOFCs). *Ionics*. 2015;21(2):301-18.
15. Atkinson A, Barnett S, Gorte R, et al. Advanced anodes for high-temperature fuel cells. *Materials For Sustainable Energy: A Collection of Peer-Reviewed Research and Review Articles from Nature Publishing Group*: World Scientific; 2011. p. 213-23.
16. Ullmann H, Trofimenko N, Naoumidis A, Stöver D. Ionic/electronic mixed conduction relations in perovskite-type oxides by defect structure. *Journal of the European Ceramic Society*. 1999;19(6-7):791-6.
17. Liu Y, Parisi J, Sun X, Lei Y. Solid-state gas sensors for high temperature applications—a review. *Journal of Materials Chemistry A*. 2014;2(26):9919-43.
18. Fergus JW. Perovskite oxides for semiconductor-based gas sensors. *Sensors and Actuators B: Chemical*. 2007;123(2):1169-79.

19. Sunarso J, Hashim SS, Zhu N, Zhou W. Perovskite oxides applications in high temperature oxygen separation, solid oxide fuel cell and membrane reactor: a review. *Progress in Energy and Combustion Science*. 2017;61:57-77.
20. Yao Y-FY. The oxidation of hydrocarbons and CO over metal oxides: IV. Perovskite-type oxides. *Journal of Catalysis*. 1975;36(3):266-75.
21. Forni L, Oliva C, Barzetti T, Selli E, Ezerets AM, Vishniakov AV. FT-IR and EPR spectroscopic analysis of $\text{La}_{1-x}\text{Ce}_x\text{CoO}_3$ perovskite-like catalysts for NO reduction by CO. *Applied Catalysis B: Environmental*. 1997;13(1):35-43.
22. Choi SO, Moon SH. Performance of $\text{La}_{1-x}\text{Ce}_x\text{Fe}_{0.7}\text{Ni}_{0.3}\text{O}_3$ perovskite catalysts for methane steam reforming. *Catalysis Today*. 2009;146(1-2):148-53.
23. Chen X, Liu Q, Khor KA, Chan S. High-performance $(\text{La}, \text{Sr})(\text{Cr}, \text{Mn})\text{O}_3/(\text{Gd}, \text{Ce})\text{O}_{2-\delta}$ composite anode for direct oxidation of methane. *Journal of Power Sources*. 2007;165(1):34-40.
24. Ermanoski I, Siegel NP, Stechel EB. A new reactor concept for efficient solar-thermochemical fuel production. *Journal of Solar Energy Engineering*. 2013;135(3).
25. Stambouli AB, Traversa E. Solid oxide fuel cells (SOFCs): a review of an environmentally clean and efficient source of energy. *Renewable and Sustainable Energy Reviews*. 2002;6(5):433-55.
26. Perkins C, Weimer AW. Likely near-term solar-thermal water splitting technologies. *International Journal of Hydrogen Energy*. 2004;29(15):1587-99.
27. Bockris J, Dandapani B, Cocke D, Ghoroghchian J. On the splitting of water. *International Journal of Hydrogen Energy*. 1985;10(3):179-201.

28. Das N, Kandimalla S. Application of perovskites towards remediation of environmental pollutants: an overview. *International Journal of Environmental Science and Technology*. 2017;14(7):1559-72.
29. Cook T, Dogutan D, Reece S, Surendranath Y, Teets T, Nocera D. Solar energy supply and storage for the legacy and nonlegacy worlds. *Chemical Reviews*. 2010;110(11):6474-502.
30. Balzani V, Credi A, Venturi M. Photochemical conversion of solar energy. *ChemSusChem*. 2008;1(1-2):26-58.
31. Steinfeld A. Solar thermochemical production of hydrogen—a review. *Solar Energy*. 2005;78:603–15.
32. Perkins C WA. Solar-thermal production of renewable hydrogen. *AIChE Journal*. 2009;55:286–93.
33. Scheffe JR, and Aldo Steinfeld. Oxygen exchange materials for solar thermochemical splitting of H₂O and CO₂: a review. *Materials Today* 2014;17(7):341–8.
34. Lewis NS. Toward cost-effective solar energy use. *Science*. 2007;315(5813)(798-801).
35. King DA. Introduction: energy for a sustainable future. *Philosophical Transactions of the Royal Society A: Mathematical, Physical and Engineering Sciences*. 2007;365(883-895).
36. Siegel NP MJ, Ermanoski I, Diver RB, Stechel EB. Factors affecting the efficiency of solar driven metal oxide thermochemical cycles. *Industrial & Engineering Chemistry Research*. 2013;52(3276–3286).
37. Cook T, Dogutan D, Reece S, Surendranath Y, Teets T, Nocera D. Solar energy supply and storage for the legacy and nonlegacy worlds. *Chemical Reviews*. 2010;110(6474-6502).
38. Edem NT LH, Le Pierrès N, Luo L. A review on long-term sorption solar energy storage. *Renewable and Sustainable Energy Reviews*. 2009;13(2385-2396).

39. Abanades S CP, Flamant G, Neveu P. Screening of water-splitting thermochemical cycles potentially attractive for hydrogen production by concentrated solar energy. *Energy*. 2006;31(14):2805-22.
40. Bilgen C, Broggi A, Bilgen E. The solar Cristina process for hydrogen production. *Solar Energy*. 1986;36(3):267-80.
41. Sakurai M, Bilgen E, Tsutsumi A, Yoshida K. Adiabatic UT-3 thermochemical process for hydrogen production. *International Journal of Hydrogen Energy*. 1996;21(10):865-70.
42. Sakurai M, Bilgen E, Tsutsumi A, Yoshida K. Solar UT-3 thermochemical cycle for hydrogen production. *Solar Energy*. 1996;57(1):51-8.
43. Roeb M, et al. Materials-related aspects of thermochemical water and carbon dioxide splitting: a review. *Materials*. 2012;11(2015-2054).
44. Bayon A, de la Calle A, Ghose KK, Page A, McNaughton R. Experimental, computational and thermodynamic studies in perovskites metal oxides for thermochemical fuel production: A review. *International Journal of Hydrogen Energy*. 2020; 45(23):12653-79.
45. Ermanoski I. Maximizing efficiency in two-step solar-thermochemical fuel production. *Energy Procedia*. 2015;69:1731-40.
46. Bulfin B, Call F, Lange M, Lubben O, Sattler C, Pitz-Paal R, et al. Thermodynamics of CeO_2 thermochemical fuel production. *Energy & Fuels*. 2015;29(2):1001-9.
47. Arifin D, Ambrosini A, Wilson SA, Mandal B, Muhich CL, Weimer AW. Investigation of Zr, Gd/Zr, and Pr/Zr-doped ceria for the redox splitting of water. *International Journal of Hydrogen Energy*. 2020;45(1):160-74.

48. Le Gal A, Abanades S, Flamant G. CO₂ and H₂O splitting for thermochemical production of solar fuels using nonstoichiometric ceria and ceria/zirconia solid solutions. *Energy & Fuels*. 2011;25(10):4836-45.
49. de la Calle A, Bayon A. Annual performance of a thermochemical solar syngas production plant based on non-stoichiometric CeO₂. *International Journal of Hydrogen Energy*. 2019;44(3):1409-24.
50. Allendorf MD, Diver RB, Miller JE, Siegel NP, editors. Thermodynamic analysis of mixed-metal ferrites for hydrogen production by two-step water splitting. ASME 2006 International Solar Energy Conference; 2006: American Society of Mechanical Engineers Digital Collection.
51. Steinfeld A. Solar hydrogen production via a two-step water-splitting thermochemical cycle based on Zn/ZnO redox reactions. *International Journal Hydrogen Energy* 2002;27(6):611-9.
52. Weidenkaff A RA, Wokaun A, Steinfeld A. Thermogravimetric analysis of the ZnO/Zn water splitting cycle. *Thermochim Acta*. 2000;359:69–75.
53. Levêque G AS, Jumas J-C, Olivier-Fourcade J. Characterization of two-step tin-based redox system for thermochemical fuel production from solar-driven CO₂ and H₂O splitting cycle. *Industrial & Engineering Chemistry Research* 2014;53(14):5668–77.
54. Muhich CL, Blaser S, Hoes MC, Steinfeld A. Comparing the solar-to-fuel energy conversion efficiency of ceria and perovskite based thermochemical redox cycles for splitting H₂O and CO₂. *International Journal of Hydrogen Energy*. 2018;43(41):18814-31.
55. Pena MA FJ. Chemical structures and performance of perovskite oxides. *Chemical Reviews*. 2001;101(7):1981-2018.

56. Demont A, Abanades S, Beche E. Investigation of perovskite structures as oxygen-exchange redox materials for hydrogen production from thermochemical two-step water-splitting cycles. *J Phys Chem C*. 2014;118(24):12682-92.
57. McDaniel AH, Ambrosini A, Coker EN, Miller JE, Chueh WC, O'Hayre R, et al. Nonstoichiometric perovskite oxides for solar thermochemical H₂ and CO production. *Energy Procedia*. 2014;49:2009-18.
58. Ishihara T, Matsuda H, Takita Y. Doped LaGaO₃ perovskite type oxide as a new oxide ionic conductor. *Journal of the American Chemical Society*. 1994;116(9):3801-3.
59. Ishihara T, Hideaki Matsuda, and Yusaku Takita. Effects of rare earth cations doped for La site on the oxide ionic conductivity of LaGaO₃-based perovskite type oxide. *Solid State Ionics* 1995;79:147-51.
60. Feng M, and J. B. Goodenough. A superior oxide-ion electrolyte. *European Journal of Solid State and Inorganic Chemistry* 1994;31(8):663-72.
61. Scheffe JR, Weibel D, Steinfeld A. Lanthanum–strontium–manganese perovskites as redox materials for solar thermochemical splitting of H₂O and CO₂. *Energy & Fuels*. 2013;27(8):4250-7.
62. McDaniel AH, Miller EC, Arifin D, Ambrosini A, Coker EN, O'Hayre R, et al. Sr- and Mn-doped LaAlO_{3-δ} for solar thermochemical H₂ and and CO production. *Energy & Environmental Science* 2013;6(8):2424-8.
63. Demont A, Abanades S, Beche E. Investigation of perovskite structures as oxygen-exchange redox materials for hydrogen production from thermochemical two-step water-splitting cycles. *The Journal of Physical Chemistry C*. 2014;118(24):12682-92.

64. Dey S, Naidu B, Rao C. Beneficial effects of substituting trivalent ions in the B-site of $\text{La}_{0.5}\text{Sr}_{0.5}\text{Mn}_{1-x}\text{A}_x\text{O}_3$ (A= Al, Ga, Sc) on the thermochemical generation of CO and H_2 from CO_2 and H_2O . Dalton Transactions. 2016;45(6):2430-5.
65. Dey S, Naidu B, Rao C. $\text{Ln}_{0.5}\text{A}_{0.5}\text{MnO}_3$ (Ln= Lanthanide, A= Ca, Sr) perovskites exhibiting remarkable performance in the thermochemical generation of CO and H_2 from CO_2 and H_2O . Chemistry—A European Journal. 2015;21(19):7077-81.
66. Cooper T, Scheffe JR, Galvez ME, Jacot R, Patzke G, Steinfeld A. Lanthanum manganite perovskites with Ca/Sr A-site and Al B-site doping as effective oxygen exchange materials for solar thermochemical fuel production. Energy Technology. 2015;3(11):1130-42.
67. Bork AH, Kubicek M, Struzik M, Rupp JL. Perovskite $\text{La}_{0.6}\text{Sr}_{0.4}\text{Cr}_{1-x}\text{Co}_x\text{O}_{3-\delta}$ solid solutions for solar-thermochemical fuel production: strategies to lower the operation temperature. Journal of Materials Chemistry A. 2015;3(30):15546-57.
68. Wang L, Al-Mamun M, Liu P, Zhong YL, Wang Y, Yang HG, et al. Enhanced thermochemical H_2 production on Ca-doped lanthanum manganite perovskites through optimizing the dopant level and re-oxidation temperature. Acta Metallurgica Sinica (English Letters). 2018;31(4):431-9.
69. Wang L, Al-Mamun M, Liu P, Wang Y, Yang HG, Zhao H. $\text{La}_{1-x}\text{Ca}_x\text{Mn}_{1-y}\text{Al}_y\text{O}_3$ perovskites as efficient catalysts for two-step thermochemical water splitting in conjunction with exceptional hydrogen yields. Chinese Journal of Catalysis. 2017;38(6):1079-86.
70. Wang L, Al - Mamun M, Zhong YL, Liu P, Wang Y, Yang HG, et al. Enhanced thermochemical water splitting through formation of oxygen vacancy in $\text{La}_{0.6}\text{Sr}_{0.4}\text{BO}_{3-\delta}$ (B= Cr, Mn, Fe, Co, and Ni) perovskites. ChemPlusChem. 2018;83(10):924-8.

71. Wang L, Al-Mamun M, Zhong YL, Jiang L, Liu P, Wang Y, et al. Ca²⁺ and Ga³⁺ doped LaMnO₃ perovskite as a highly efficient and stable catalyst for two-step thermochemical water splitting. *Sustainable Energy & Fuels*. 2017;1(5):1013-7.
72. Tu H, Stimming U. Advances, aging mechanisms and lifetime in solid-oxide fuel cells. *Journal of Power Sources*. 2004;127(1-2):284-93.
73. Huijsmans J, Van Berkel F, Christie G. Intermediate temperature SOFC—a promise for the 21st century. *Journal of Power Sources*. 1998;71(1-2):107-10.
74. Mahato N, Banerjee A, Gupta A, Omar S, Balani K. Progress in material selection for solid oxide fuel cell technology: A review. *Progress in Materials Science*. 2015;72:141-337.
75. Ivers-Tiffée E, Weber A, Herbstritt D. Materials and technologies for SOFC-components. *Journal of the European Ceramic Society*. 2001;21(10-11):1805-11.
76. Sun C, Hui R, Roller J. Cathode materials for solid oxide fuel cells: a review. *Journal of Solid State Electrochemistry*. 2010;14(7):1125-44.
77. Kawada T, Mizusaki J. "Current electrolytes and catalyst." in *Handbook of Fuel Cells: Fundamentals, Technology, Applications*, W. Vielstich, A. Lamm, and H. A. Gasteiger, Eds.: John Wiley & Sons, pp. 987-1001, . 2003.
78. Shaikh SP, Muchtar A, Somalu MR. A review on the selection of anode materials for solid-oxide fuel cells. *Renewable and Sustainable Energy Reviews*. 2015;51:1-8.
79. Singhal SC, Kendall K. *High-temperature solid oxide fuel cells: fundamentals, design and applications*, chapter-6, pp-150: Elsevier; 2003.
80. Singhal SC, Kendall K. *High-temperature solid oxide fuel cells: fundamentals, design and applications*, chapter-1, pp-7: Elsevier; 2003.

81. Kharton V, Yaremchenko A, Shaula A, Patrakeevev M, Naumovich E, Logvinovich D, et al. Transport properties and stability of Ni-containing mixed conductors with perovskite-and K_2NiF_4 -type structure. *Journal of Solid State Chemistry*. 2004;177(1):26-37.
82. Wincewicz KC, Cooper JS. Taxonomies of SOFC material and manufacturing alternatives. *Journal of Power Sources*. 2005;140(2):280-96.
83. Jacobson AJ. Materials for solid oxide fuel cells. *Chemistry of Materials*. 2009;22(3):660-74.
84. Sun C, Stimming U. Recent anode advances in solid oxide fuel cells. *Journal of Power Sources*. 2007;171(2):247-60.
85. Yattoo MA, Kawale SS, Skinner SJ. Perovskite and layered oxide materials for intermediate temperature solid oxide fuel cells. *Intermediate Temperature Solid Oxide Fuel Cells: Electrolytes, Electrodes and Interconnects*. 2019:315.
86. Ohno Y, Nagata S, Sato H. Effect of electrode materials on the properties of high-temperature solid electrolyte fuel cells. *Solid State Ionics*. 1981;3:439-42.
87. Isaacs H, Olmer L. Comparison of materials as oxygen catalytic electrodes on zirconia electrolyte. *Journal of the Electrochemical Society*. 1982;129(2):436-43.
88. Yamamoto O, Takeda Y, Kanno R, Noda M. Perovskite-type oxides as oxygen electrodes for high temperature oxide fuel cells. *Solid State Ionics*. 1987;22(2-3):241-6.
89. Lee K, Manthiram A. Comparison of $Ln_{0.6}Sr_{0.4}CoO_{3-\delta}$ ($Ln = La, Pr, Nd, Sm, \text{ and } Gd$) as cathode materials for intermediate temperature solid oxide fuel cells. *Journal of the Electrochemical Society*. 2006;153(4):A794-A8.

90. Hammouche A, Siebert E, Hammou A. Crystallographic, thermal and electrochemical properties of the system $\text{La}_{1-x}\text{Sr}_x\text{MnO}_3$ for high temperature solid electrolyte fuel cells. *Materials Research Bulletin*. 1989;24(3):367-80.
91. Jiang SP. Development of lanthanum strontium manganite perovskite cathode materials of solid oxide fuel cells: a review. *Journal of Materials Science*. 2008;43(21):6799-833.
92. Zhang W, Zhang L, Guan K, Zhang X, Meng J, Wang H, et al. Effective promotion of oxygen reduction activity by rare earth doping in simple perovskite cathodes for intermediate-temperature solid oxide fuel cells. *Journal of Power Sources*. 2020;446:227360.
93. Dong W, Yaqub A, Janjua NK, Raza R, Afzal M, Zhu B. All in one multifunctional perovskite material for next generation SOFC. *Electrochimica Acta*. 2016;193:225-30.
94. Radhika D, Kannan K, Neseraj A, Namitha R. Facile low-temperature synthesis and application of $\text{La}_{0.85}\text{Sr}_{0.15}\text{Co}_{0.85}\text{Fe}_{0.15}\text{O}_{3-\delta}$ as superior cathode for LT-SOFCs using C-TAB as surfactant. *Materials Research Innovations*. 2019:1-7.
95. Li M, Zhao M, Li F, Zhou W, Peterson VK, Xu X, et al. A niobium and tantalum co-doped perovskite cathode for solid oxide fuel cells operating below 500°C . *Nature communications*. 2017;8:13990.
96. Duan C, Hook D, Chen Y, Tong J, O'Hayre R. Zr and Y co-doped perovskite as a stable, high performance cathode for solid oxide fuel cells operating below 500°C . *Energy & Environmental Science*. 2017;10(1):176-82.
97. Javed MS, Raza R, Ahsan Z, Rafique MS, Shahzadi S, Shaikat S, et al. Electrochemical studies of perovskite cathode material for direct natural gas fuel cell. *International Journal of Hydrogen Energy*. 2016;41(4):3072-8.

98. Zhu Y, Sunarso J, Zhou W, Jiang S, Shao Z. High-performance $\text{SrNb}_{0.1}\text{Co}_{0.9-x}\text{Fe}_x\text{O}_{3-\delta}$ perovskite cathodes for low-temperature solid oxide fuel cells. *Journal of Materials Chemistry A*. 2014;2(37):15454-62.
99. Verbraeken MC, Ramos T, Agersted K, Ma Q, Savaniu CD, Sudireddy BR, et al. Modified strontium titanates: from defect chemistry to SOFC anodes. *Rsc Advances*. 2015;5(2):1168-80.
100. Marina OA, Canfield NL, Stevenson JW. Thermal, electrical, and electrocatalytical properties of lanthanum-doped strontium titanate. *Solid State Ionics*. 2002;149(1-2):21-8.
101. Ruiz-Morales JC, Canales-Vázquez J, Savaniu C, Marrero-López D, Zhou W, Irvine JT. Disruption of extended defects in solid oxide fuel cell anodes for methane oxidation. *Nature*. 2006;439(7076):568.
102. Miller DN, Irvine JT. B-site doping of lanthanum strontium titanate for solid oxide fuel cell anodes. *Journal of Power Sources*. 2011;196(17):7323-7.
103. Oh T-S, Anthony SY, Adijanto L, Gorte RJ, Vohs JM. Infiltrated lanthanum strontium chromite anodes for solid oxide fuel cells: Structural and catalytic aspects. *Journal of Power Sources*. 2014;262:207-12.
104. Sfeir J, Buffat PA, Möckli P, Xanthopoulos N, Vasquez R, Mathieu HJ, et al. Lanthanum chromite based catalysts for oxidation of methane directly on SOFC anodes. *Journal of Catalysis*. 2001;202(2):229-44.
105. Li X, Zhao H, Xu N, Zhou X, Zhang C, Chen N. Electrical conduction behavior of La, Co co-doped SrTiO_3 perovskite as anode material for solid oxide fuel cells. *International Journal of Hydrogen Energy*. 2009;34(15):6407-14.

106. Zhang L, Xiao J, Xie Y, Tang Y, Liu J, Liu M. Behavior of strontium-and magnesium-doped gallate electrolyte in direct carbon solid oxide fuel cells. *Journal of Alloys and Compounds*. 2014;608:272-7.
107. Ishihara T, Matsuda H, Takita Y. In *2nd Ionic and Mixed Conducting Ceramics*, eds. T A Ramanaryanan, W L Worrell and H L Tuller, The Electrochemical Society Proceedings, Pennington, NJ. 1994;PV92-12:85.
108. Takahashi T, Iwahara H. Ionic conduction in perovskite-type oxide solid solution and its application to the solid electrolyte fuel cell. *Energy Conversion*. 1971;11(3):105-11.
109. Alberi K, Nardelli M, Zakutayev A, Mitas L, Curtarolo S, Jain A, et al. The 2019 materials by design roadmap. *Journal of Physics D: Applied Physics*. 2018;52(1):013001.
110. Bartel CJ, Millican SL, Deml AM, Rumptz JR, Tumas W, Weimer AW, et al. Physical descriptor for the Gibbs energy of inorganic crystalline solids and temperature-dependent materials chemistry. *Nature communications*. 2018;9(1):1-10.
111. Calle - Vallejo F, Martínez JI, García - Lastra JM, Mogensen M, Rossmeisl J. Trends in stability of perovskite oxides. *Angewandte Chemie International Edition*. 2010;49(42):7699-701.
112. Hammer B, Hansen LB, Nørskov JK. Improved adsorption energetics within density-functional theory using revised Perdew-Burke-Ernzerhof functionals. *Physical Review B*. 1999;59(11):7413.
113. Zeng Z, Calle-Vallejo F, Mogensen MB, Rossmeisl J. Generalized trends in the formation energies of perovskite oxides. *Physical Chemistry Chemical Physics*. 2013;15(20):7526-33.
114. Ezbiri M, Allen KM, Gálvez ME, Michalsky R, Steinfeld A. Design principles of perovskites for thermochemical oxygen separation. *ChemSusChem*. 2015;8(11):1966-71.

115. Nair MM, Abanades S. Insights into the redox performance of non-stoichiometric lanthanum manganite perovskites for solar thermochemical CO₂ splitting. *ChemistrySelect*. 2016;1(15):4449-57.
116. Perdew JP, Burke K, Ernzerhof M. Generalized gradient approximation made simple. *Physical Review Letters*. 1996;77(18):3865.
117. Brown JJ, Ke Z, Geng W, Page AJ. Oxygen Vacancy Defect Migration in Titanate Perovskite Surfaces: Effect of the A-Site Cations. *The Journal of Physical Chemistry C*. 2018;122(26):14590-7.
118. Deml A, Stevanovi V, Holder A, Sanders M, O'Hayre R, Musgrave C. Tunable Oxygen Vacancy Formation Energetics in the Complex Perovskite Oxide Sr_xLa_{1-x}Mn_yAl_{1-y}O₃. *Chemistry of Materials*. 2014;26(22):6595-602.
119. Deml AM, Holder AM, O'Hayre RP, Musgrave CB, Stevanovi V. Intrinsic material properties dictating oxygen vacancy formation energetics in metal oxides. *The Journal of Physical Chemistry Letters*. 2015;6(10):1948-53.
120. Deml AM, Holder AM, O'Hayre RP, Musgrave CB, Stevanovi V. Intrinsic material properties dictating oxygen vacancy formation energetics in metal oxides - supplementary information. *The Journal of Physical Chemistry Letters*. 2015;6(10):1948-53.
121. Maiti D, Daza YA, Yung MM, Kuhn JN, Bhethanabotla VR. Oxygen vacancy formation characteristics in the bulk and across different surface terminations of La_(1-x)Sr_xFe_(1-y)Co_yO_(3-δ) perovskite oxides for CO₂ conversion. *Journal of Materials Chemistry A*. 2016;4(14):5137-48.
122. Perdew JP, Wang Y. Accurate and simple analytic representation of the electron-gas correlation energy. *Physical Review B*. 1992;45(23):13244.

123. Maiti D, Hare BJ, Daza YA, Ramos AE, Kuhn JN, Bhethanabotla VR. Earth abundant perovskite oxides for low temperature CO₂ conversion. *Energy & Environmental Science*. 2018;11(3):648-59.
124. Chen Z, Jiang Q, Cheng F, Tong J, Yang M, Jiang Z, et al. Sr-and Co-doped LaGaO_{3-δ} with high O₂ and H₂ yields in solar thermochemical water splitting. *Journal of Materials Chemistry A*. 2019;7(11):6099-112.
125. Mulmi S, Chen H, Hassan A, Marco JF, Berry FJ, Sharif F, et al. Thermochemical CO₂ splitting using double perovskite-type Ba₂Ca_{0.66}Nb_{1.34-x}Fe_xO_{6-δ}. *Journal of Materials Chemistry A*. 2017;5(15):6874-83.
126. Sastre D, Serrano DP, Pizarro P, Coronado JM. Chemical insights on the activity of La_{1-x}Sr_xFeO₃ perovskites for chemical looping reforming of methane coupled with CO₂-splitting. *Journal of CO₂ Utilization*. 2019;31:16-26.
127. Meredig B, Wolverton C. First-principles thermodynamic framework for the evaluation of thermochemical H₂O-or CO₂-splitting materials. *Physical Review B*. 2009;80(24):245119.
128. Emery AA, Saal JE, Kirklin S, Hegde VI, Wolverton C. High-throughput computational screening of perovskites for thermochemical water splitting applications. *Chemistry of Materials*. 2016;28(16):5621-34.
129. Bartel CJ, Sutton C, Goldsmith BR, Ouyang R, Musgrave CB, Ghiringhelli LM, et al. New tolerance factor to predict the stability of perovskite oxides and halides. *Science Advances*. 2019;5(2):693.
130. Michalsky R, Steinfeld A. Computational screening of perovskite redox materials for solar thermochemical ammonia synthesis from N₂ and H₂O. *Catalysis Today*. 2017;286:124-30.

131. Landis DD, Hummelshoj JS, Nestorov S, Greeley J, Dulak M, Bligaard T, et al. The computational materials repository. *Computing in Science & Engineering*. 2012;14(6):51-7.
132. Curtarolo S, Setyawan W, Hart GL, Jahnatek M, Chepulskii RV, Taylor RH, et al. AFLOW: an automatic framework for high-throughput materials discovery. *Computational Materials Science*. 2012;58:218-26.
133. Jain A, Ong SP, Hautier G, Chen W, Richards WD, Dacek S, et al. Commentary: The Materials Project: A materials genome approach to accelerating materials innovation. *Apl Materials*. 2013;1(1):011002.
134. Saal JE, Kirklin S, Aykol M, Meredig B, Wolverton C. Materials design and discovery with high-throughput density functional theory: the open quantum materials database (OQMD). *Jom*. 2013;65(11):1501-9.
135. Draxl C, Scheffler M. NOMAD: The FAIR concept for big data-driven materials science. *MRS Bulletin*. 2018;43(9):676-82.
136. Perkins JD, White RR, Munch K, editors. A comprehensive data ecosystem to accelerate materials research. In *ECS Meeting Abstracts 2017 Apr 15 (No. 35, p. 1686)*. IOP Publishing.
137. Choudhary K. JARVIS: Novel NIST databases to aid Material Discovery. *APS*. 2019;2019:T70-271.
138. Liu Y, Zhao T, Ju W, Shi S. Materials discovery and design using machine learning. *Journal of Materiomics*. 2017;3(3):159-77.
139. De Luna P, Wei J, Bengio Y, Aspuru-Guzik A, Sargent E. Use machine learning to find energy materials. *Nature Publishing Group*; 2017; 23-27.

140. Hautier G, Fischer CC, Jain A, Mueller T, Ceder G. Finding nature's missing ternary oxide compounds using machine learning and density functional theory. *Chemistry of Materials*. 2010;22(12):3762-7.
141. Balachandran PV, Emery AA, Gubernatis JE, Lookman T, Wolverton C, Zunger A. Predictions of new ABO_3 perovskite compounds by combining machine learning and density functional theory. *Physical Review Materials*. 2018;2(4):043802.
142. Li W, Jacobs R, Morgan D. Predicting the thermodynamic stability of perovskite oxides using machine learning models. *Computational Materials Science*. 2018;150:454-63.
143. Xu Q, Li Z, Liu M, Yin W-J. Rationalizing perovskite data for machine learning and materials design. *The Journal of Physical Chemistry Letters*. 2018;9(24):6948-54.
144. Pilania G, Balachandran PV, Kim C, Lookman T. Finding new perovskite halides via machine learning. *Frontiers in Materials*. 2016;3:19.
145. Ong M, Campbell Q, Dabo I, Jishi RA. First-principles investigation of $BiVO_3$ for thermochemical water splitting. *International Journal of Hydrogen Energy*. 2019;44(3):1425-30.
146. Dragomir M, Valant M. Synthesis peculiarities of $BiVO_3$ perovskite. *Ceramics International*. 2013;39(5):5963-6.
147. Daza YA, Maiti D, Kent RA, Bhethanabotla VR, Kuhn JN. Isothermal reverse water gas shift chemical looping on $La_{0.75}Sr_{0.25}Co_{(1-Y)}Fe_YO_3$ perovskite-type oxides. *Catalysis Today*. 2015;258:691-8.
148. Ruan C, Huang Z-Q, Lin J, Li L, Liu X, Tian M, et al. Synergy of the catalytic activation on Ni and the $CeO_2-TiO_2/Ce_2Ti_2O_7$ stoichiometric redox cycle for dramatically enhanced solar fuel production. *Energy & Environmental Science*. 2019.

149. Kulik HJ. Perspective: Treating electron over-delocalization with the DFT+ U method. The Journal of Chemical Physics. 2015;142(24):240901.

Chapter 2: First-Principles Methodology for Electronic Structures and Thermochemical Properties of ABO₃ Perovskites

2.1 Introduction

Design of new functional materials requires their composition-structure-property relationships to be understood at the atomic level. First-principles methods, such as DFT, can describe and predict fundamental physical properties of materials for this purpose and so enable the development of new materials for targeted applications. This chapter presents an overview of the electronic structure methods used in subsequent chapters of this thesis. A DFT ansatz suitable for studying the phonon dispersion and thermochemical properties of ABO₃ perovskites is also developed, notably via comparing the performance of GGA exchange-correlation functionals against experimental crystal structures, phonon dispersions, and temperature-dependent entropies, specific heats and enthalpies.

2.2 Electronic Structure Methods

2.2.1 Time-Independent Schrödinger Equation

The total energy of a molecular system of M nuclei with coordinates $\{R_1, R_2, \dots, R_M\}$ and N -electrons with coordinates $\{r_1, r_2, \dots, r_N\}$ is described by quantum mechanics via the time-independent Schrödinger equation,^[1]

$$E = \langle \psi(\mathbf{r}, \mathbf{R}) | \hat{H} | \psi(\mathbf{r}, \mathbf{R}) \rangle \quad (2.1)$$

In this eigenvalue operator equation, the Hamiltonian operator \hat{H} describes the total potential and kinetic energies of the system, and determines the form of the time-independent wave function Ψ

and its corresponding energy E . The non-relativistic form of \hat{H} for electronic $\{r_i\}$ and nuclear $\{R_I\}$ degrees of freedom is,^[2]

$$\hat{H} = \hat{T}_N(R_I) + \hat{T}_e(r_i) + \hat{V}_{eN}(r_i, R_I) + \hat{V}_{ee}(r_i) + \hat{V}_{NN}(R_I) \quad (2.2)$$

Here, $\hat{T}_N(R_I)$ and $\hat{T}_e(r_i)$ are the nuclear and electronic kinetic energy operators, respectively, and $\hat{V}_{eN}(r_i, R_I)$, $\hat{V}_{ee}(r_i)$ and $\hat{V}_{NN}(R_I)$ are the electron-nuclei, electron-electron, and nuclei-nuclei electrostatic potential operators respectively, such that,

$$\hat{T}_N(R_I) = \sum_{I=1}^M \frac{\hbar^2}{2m_I} \nabla_I \quad (2.3)$$

$$\hat{T}_e(r_i) = \sum_{i=1}^N \frac{\hbar^2}{2m_e} \nabla_i \quad (2.4)$$

$$\hat{V}_{eN}(r_i, R_I) = \sum_{I=1}^M \sum_{i=1}^N \frac{1}{4\pi\epsilon_0} \frac{Z_I e^2}{|\vec{R}_I - \vec{r}_i|} \quad (2.5)$$

$$\hat{V}_{ee}(r_i) = \frac{1}{2} \sum_{i,j,i \neq j=1}^N \frac{1}{4\pi\epsilon_0} \frac{e^2}{|\vec{r}_j - \vec{r}_i|} \quad (2.6)$$

$$\hat{V}_{NN}(R_I) = \frac{1}{2} \sum_{I,J,I \neq J=1}^M \frac{1}{4\pi\epsilon_0} \frac{Z_I Z_J e^2}{|\vec{R}_J - \vec{R}_I|} \quad (2.7)$$

where m_I is the mass of the I^{th} nucleus, R_I and R_J are the positions of the I^{th} and J^{th} nuclei, Z_I and Z_J are their nuclear charges, m_e is the mass of the i^{th} electron, r_i and r_j are the positions of the i^{th} and j^{th} electrons, and ∇_i is the Laplacian kinetic energy operator.

2.2.2 Born-Oppenheimer Approximation

The Born Oppenheimer (BO) approximation^[3] assumes that nuclei are fixed with respect to electronic motion, due to their significantly greater mass. This enables the motion of electrons and

nuclei to be treated separately in equation (2.1), which decouples the electronic and nuclear contributions to the total wave function. The total spatial function can then be expressed as a product of an electronic and nuclear wavefunction,

$$\langle \psi(\mathbf{r}, \mathbf{R}) \rangle = |\Psi_k(\mathbf{r}; \mathbf{R})\rangle |\chi_N(\mathbf{R})\rangle \quad (2.8)$$

where, $\Psi_k(\mathbf{r}; \mathbf{R})$ and $\chi_N(\mathbf{R})$ are the electronic and nuclear wavefunctions respectively, where both are functions of the electronic coordinates (\mathbf{r}) and nuclear coordinates (\mathbf{R}). $\Psi_k(\mathbf{r}; \mathbf{R})$ has a parametric dependency on nuclear positions (\mathbf{R}) expressed by the semicolon and only depends upon the electronic state k . Within the BO approximation, the nuclear kinetic energy can be neglected, and the nuclei-electron Coulombic attraction becomes constant for a given nuclear configuration. Equation (2.2) can thus be simplified to an electronic Schrödinger equation,

$$\hat{H}_e(\mathbf{r}; \mathbf{R}) |\Psi_k(\mathbf{r}; \mathbf{R})\rangle |\chi_N(\mathbf{R})\rangle = E_k |\Psi_k(\mathbf{r}; \mathbf{R})\rangle |\chi_N(\mathbf{R})\rangle \quad (2.9)$$

where the electronic Hamiltonian $\hat{H}_e(\mathbf{r}; \mathbf{R}) = [\hat{T}_e(r_i) + \hat{V}_{eN}(r_i, R_l) + \hat{V}_{ee}(r_i)]$, gives a set of normalized eigenfunctions $\Psi_k(\mathbf{r}; \mathbf{R})$ and eigenvalues E_k . By solving this electronic Schrödinger equation for a set of distinct nuclear coordinates, the electronic potential energy surface (PES) can be constructed.

2.2.3 Hartree-Fock Theory

Analytical solutions to the electronic Schrödinger equation for multiple-electron systems are not known. It is, therefore, necessary to calculate approximate solutions to equation (2.9). The standard approach was developed by Hartree and Fock (HF), who solved the “three-body problems” in multiple-electron systems using the independent electron approximation.^[4, 5] In the HF theory approximation, the N -electron wave function is represented as a Slater determinant (i.e. an antisymmetric product) of N 1-electron orthonormal spin-orbital wave functions $\varphi_i(x)$,

$$\varphi_{HF} = \frac{1}{\sqrt{N!}} \begin{vmatrix} \varphi_1(1) & \varphi_2(1) & \cdots & \varphi_N(1) \\ \varphi_1(2) & \varphi_2(2) & \cdots & \varphi_N(2) \\ \vdots & \vdots & \ddots & \vdots \\ \varphi_1(N) & \varphi_2(N) & \cdots & \varphi_N(N) \end{vmatrix} \quad (2.10)$$

where $\frac{1}{\sqrt{N!}}$ is the normalization factor. The expectation value of the electronic Hamiltonian in the Hartree product basis defines the HF energy,

$$E_{HF} = \langle \varphi_{HF} | \hat{H} | \varphi_{HF} \rangle \quad (2.11)$$

This energy and the corresponding Hartree product spin orbitals are determined variationally. This provides an optimal set of 1-electron spin orbitals and the corresponding lowest energy (the HF energy).

2.2.4 Electron Correlation Methods

HF theory is based on the independent particle approximation, and so treats the electron-electron repulsion as an average, or “mean-field”, effect arising from the average electron charge cloud experienced by one electron due to all other electrons. Importantly, this approximation ignores the instantaneous correlation between electrons and hence this shortcoming in HF theory manifests itself as an overestimation in the total electronic energy. The difference between the HF energy with a complete (infinite) basis set (E_{HF}^∞ , or the “HF-limit”), and the “true”, exact electronic energy, is defined as the electron correlation energy,

$$E_{correlation} = E_{exact} - E_{HF}^\infty \quad (2.12)$$

There are several popular routes to determine the electron correlation: self-consistent treatment of the electron correlation in DFT, perturbation theory (notably second-order Møller-Plesset Perturbation Theory), coupled-cluster theory, and configuration interaction. However, the scaling in terms of basis set size M increases from M^4 to M^{10} for these various post-HF methods, depending

on the degree of excitation included in the correlated wave function.^[6] Considering the computational costs and the size of the system, the direct self-consistent method is most commonly employed in modern computational chemistry, where the electron-correlation is modelled via the electron density instead of the wave function itself. In this formalism, the energy is recast as a functional of the electron density.

2.2.5 Thomas-Fermi and Thomas-Fermi-Dirac Models

The Thomas-Fermi (TF) model^[7] was the first to describe the electronic structure in terms of an electron density $\rho(\mathbf{r})$, as opposed to the complicated many electron wavefunction Ψ . As electrons are indistinguishable, for a system of N particles the probability of finding any electron near a point \mathbf{r} in space can be defined in terms of the electron density amplitude,

$$\rho(\mathbf{r}) = N \int |\Psi(\mathbf{r}_1, \mathbf{r}_2, \dots, \mathbf{r}_N)|^2 d\mathbf{r}_2 d\mathbf{r}_3 \dots d\mathbf{r}_N \quad (2.13)$$

The total energy of the electron system is then,

$$E_{TF}[\rho(\mathbf{r})] = C_k \int [\rho(\mathbf{r})]^{5/3} d\mathbf{r} - e \int \rho(\mathbf{r}) V_{ext.}(\mathbf{r}) d\mathbf{r} + \frac{1}{2} e^2 \int \frac{\rho(\mathbf{r})\rho(\mathbf{r}')}{|\mathbf{r}-\mathbf{r}'|} d\mathbf{r} d\mathbf{r}' \quad (2.14)$$

The first term in the right-hand side of equation (2.14) is the kinetic energy, and the second and third terms represent the Coulomb potential energy due to nuclei-electron and electron-electron interactions, respectively.

The main drawback of the TF model is that the charge distribution related to the electron itself is not excluded in the third term of equation (2.14). The TF model, therefore, neglects the Pauli exclusion principle. Dirac subsequently suggested correction for this problem by the inclusion of an explicit exchange energy E_{XC} ,^[8]

$$E_{XC}[\rho(\mathbf{r})] = -C_{\chi} \int [\rho(\mathbf{r})]^{4/3} d\mathbf{r} \quad (2.15)$$

With the inclusion of this exchange term, the total energy functional of the density is,

$$\begin{aligned} E_{TF}[\rho(\mathbf{r})] = & C_k \int [\rho(\mathbf{r})]^{5/3} d\mathbf{r} - e \int \rho(\mathbf{r}) V_{ext.}(\mathbf{r}) d\mathbf{r} \\ & + \frac{1}{2} e^2 \int \frac{\rho(\mathbf{r})\rho(\mathbf{r}')}{|\mathbf{r} - \mathbf{r}'|} d\mathbf{r}d\mathbf{r}' - C_{\chi} \int [\rho(\mathbf{r})]^{4/3} d\mathbf{r} \end{aligned} \quad (2.16)$$

However, this model oversimplified the molecular binding and not much real importance for quantitative prediction in atomic or molecular scale.^[9]

2.2.6 Hohenberg-Kohn Theorem

The Hohenberg-Kohn (HK) theorems^[10] prove that: (i) the energy is a unique functional of electron density, and (ii) the electron density yielding the minimal electronic energy (which can be calculated variationally) is the “true” electronic density. If we consider two different external potentials $v(\mathbf{r})$ and $v'(\mathbf{r})$ giving the same density $\rho(\mathbf{r})$, the two Hamiltonians H and H' will have two different normalized wave functions. The corresponding ground-state energy can be written as,

$$E_0 < \langle \psi | \hat{H} | \psi \rangle = \langle \psi | \hat{H}' | \psi \rangle + \langle \psi | \hat{H} - \hat{H}' | \psi \rangle = E'_0 + \int \rho(\mathbf{r}) [v(\mathbf{r}) - v'(\mathbf{r})] d\mathbf{r} \quad (2.17)$$

$$E'_0 < \langle \psi | \hat{H}' | \psi \rangle = \langle \psi | \hat{H} | \psi \rangle + \langle \psi | \hat{H}' - \hat{H} | \psi \rangle = E_0 - \int \rho(\mathbf{r}) [v(\mathbf{r}) - v'(\mathbf{r})] d\mathbf{r} \quad (2.18)$$

The HK energy, E_{HK} , can be rewritten as,

$$E_{HK}[\rho] = \int \rho(\mathbf{r}) v(\mathbf{r}) d\mathbf{r} + F_{HK}[\rho] \quad (2.19)$$

where

$$F_{HK}[\rho] = T[\rho] + V_{ee}[\rho] \quad (2.20)$$

2.2.7 Kohn-Sham Density Functional Theory

While the HK theorems show that the energy is a unique functional of the ground-state density, it does not provide a method to calculate it. This problem was overcome by the Kohn-Sham (KS) method, which reintroduces self-consistent field molecular orbitals into HK DFT, which enable the formation of a trial density that can be used to approximate the kinetic energy. KS DFT^[11] treats the N interacting electron system as N non-interacting particles. In this case the electronic energy can be written as the functional of ground-state electron density such that,

$$E[\rho] = T[\rho] + V^{e-N}[\rho] + V^{e-e}[\rho] \quad (2.21)$$

For any closed-shell system, the potential due to coulombic attraction between nuclei and electron can be written as,

$$V^{e-N}[\rho] = \int \rho(r)v(r)dr \quad (2.22)$$

where $v(r)$ is the external potential created by all nuclei over all electrons. In the system of N non-interacting electrons, there will be no active potential due to repulsion between electrons. The Hamiltonian for N non-interacting electrons can thus be written as,

$$\hat{H}_s = \hat{T}_s^e + \hat{V}_s^{e-N} \quad (2.23)$$

The kinetic energy functional of the system in terms of KS orbitals and the potential due to coulombic attraction can be expressed, respectively, as,

$$\hat{T}_s^e[\rho_s] = - \sum_{i=1}^{N/2} \langle \Psi_i(r) | \frac{1}{2} \Delta_i | \Psi_i(r) \rangle \quad (2.24)$$

$$\hat{V}_s^{e-N} = \int \rho_s(r)v(r)dr \quad (2.25)$$

So, for the non-interacting electrons system, the electronic energy can be written as,

$$\hat{E}_s[\rho_s] = - \sum_{i=1}^{N/2} \langle \Psi_i(r) | \frac{1}{2} \Delta_i | \Psi_i(r) \rangle + \int \rho_s(r) v(r) dr \quad (2.26)$$

For a real system, the expression of energy in terms of the non-interacting system is therefore,

$$E[\rho] = \hat{T}_s^e[\rho_s] + \Delta T[\rho_s] + V^{e-N}[\rho_s] + V_s^{e-e}[\rho_s] + \Delta V_{e-e}[\rho_s] \quad (2.27)$$

Here, $\Delta T[\rho_s]$ includes all the deviations of the real kinetic functional from the reference system. $\Delta V_{e-e}[\rho_s]$ includes a correction to electron-electron interaction once they are considered. Both corrections are grouped within the exchange-correlation functional,

$$E_{XC}[\rho] = \Delta T[\rho_s] + \Delta V_{e-e}[\rho_s] \quad (2.28)$$

and the classical electrostatic repulsion energy constitutes the Hartree term,

$$V_s^{e-e}[\rho_s] = \frac{1}{2} \int \int \frac{\rho(r_1)\rho(r_2)}{r_{12}} dr_1 dr_2 \quad (2.29)$$

In terms of equation (2.26), (2.28) and (2.29), equation (2.27) can be rewritten as,

$$E[\rho] = \hat{T}_s^e[\rho_s] + \int \rho_s(r) v(r) dr + \frac{1}{2} \int \int \frac{\rho(r_1)\rho(r_2)}{r_{12}} dr_1 dr_2 + E_{XC}[\rho] \quad (2.30)$$

2.2.8 Exchange-Correlation Functionals

Theoretically, the exchange-correlation (XC) energy in the third term of the right-hand side of equation (2.30) is a consequence of the Pauli exclusion principle, since two electrons of the same spin must be spatially separated, thereby reducing the Coulombic electron-electron repulsion energy. While there is a unique analytical form for the XC potential (and hence energy), it is unknown. Many approximations for $E_{XC}[\rho]$ have therefore been proposed. of particular relevance to this Thesis are the so-called the Local Density Approximation and the Generalized Gradient Approximation.

2.2.8.1 Local Density Approximation

The Local Density Approximation (LDA) is employed extensively in the calculation of structures and total energies of solid-state materials.^[12-14] Within the LDA, the XC energy for a density $\rho(r)$ is defined as,

$$E_{xc}^{LDA} = \int \rho(r) \epsilon_{xc}(\rho) dr \quad (2.31)$$

where $\epsilon_{xc}(\rho)$ is the XC energy per particle of a uniform electron gas of density ρ . The energy density functional $\epsilon_{xc}(\rho)$ is always treated as a sum of individual exchange and correlation contributions,

$$\epsilon_{xc}(\rho) = \epsilon_x(\rho) + \epsilon_c(\rho) \quad (2.32)$$

The first term in equation (2.32) is given by the Dirac functional,

$$\epsilon_x(\rho) = -\frac{3}{4} \left(\frac{3}{\pi}\right)^{\frac{1}{3}} \rho(r) \quad (2.33)$$

An expression for the correlation energy $\epsilon_c(\rho)$ has been determined by Quantum Monte Carlo calculations.^[15]

2.2.8.2 Local Spin Density Approximation

The Local Spin Density Approximation (LSDA) is equivalent to the LDA, however, it treats electrons with opposite spin via different spatial Kohn-Sham orbitals. The two-different XC functional for spin up and spin down can be expressed as,

$$E_{xc}^{LDA}(\rho_\alpha) = E_x^{LDA}(\rho_\alpha) + E_c^{LDA}(\rho_\alpha) \quad (2.34)$$

$$E_{xc}^{LDA}(\rho_\beta) = E_x^{LDA}(\rho_\beta) + E_c^{LDA}(\rho_\beta) \quad (2.35)$$

$E_{xc}^{LDA}(\rho_\alpha)$, $E_{xc}^{LDA}(\rho_\beta)$ and their functional derivatives can be accurately calculated as per references.^[16, 17]

2.2.8.3 Generalized Gradient Approximation

In the LDA, the functional used to approximate the energy of the true density depends only on the local density. It overestimates the exchange energy and underestimates the correlation energy, which works fairly well for covalent systems or simple metals due to the cancellation errors, however it brings several drawbacks to systems which deviate from the LDA model. The typical drawbacks of LDA functionals including overbinding tendency, overestimation of adsorption energies, cohesive energies and bulk modulus of solids, while largely underestimating the lattice parameters, diffusion barriers, spin and orbital moments, and electronic bandgaps.^[18] An improvement upon this method is to include the local gradient of the electron density in the XC functional. Perdew and Yang^[19] introduced this gradient term to the LDA functional. Here, the assumption is made that for each point in space with an electron density $\rho(r)$ and its local gradients,

$$E_{XC}[\rho] \approx \int dr f_{GGA}(\rho(r), |\nabla\rho(r)|, \nabla^2\rho(r)) \quad (2.36)$$

There are several different parametrizations of the GGA obtained from experimental data and first-principles calculations. The most popular XC functionals are that of PW91,^[20] PBE,^[21] RPBE,^[22] Perdew Burke Ernzerhof revised for solids and surfaces (PBEsol),^[23] and Becke-Lee-Yang-Parr (BLYP)^[24-27] (a combination of exchange correction of Becke's functional^[27] and correlation potential of Lee, Yang and Parr (LYP)^[24]). The various approaches to improving GGA functionals are devoted to specializing for certain classes of compounds. For instance, PW91 has been extensively used for predicting a wide range of materials properties with reasonable accuracy, including van der Waals dimers and hydrogen-bonded complexes.^[28, 29] However, due to the presence of spurious fluctuations in the XC potential at both low and high electron densities, this functional is generally less applicable for many chemical systems.^[30] On the other hand, PBE is designed to be a universal GGA functional with limited empirical dependencies. It overcomes the

previously noted problem of the PW91 functional, and thus works better with pseudopotentials. The performance of the PBE functional has been demonstrated for both molecules and solids,^[31, 32] it predicts accurately relative energies, bond lengths, and vibrational frequencies, however, it overestimates absolute bonding distances and vibrational frequencies. RPBE is a revised version of PBE, which limits the maximum possible of theoretical E_{XC} values by satisfying the Lieb-Oxford criterion.^[33] RPBE calculates adsorption energies comparatively well, however, it overestimates energy barriers. PBEsol is the solid-oriented revised version of PBE, which significantly improves the prediction of equilibrium properties of densely-packed solids and their surfaces.^[23] A series of recent studies with 18 solid groups, including five sets of ionic solids and equal sets of semiconductor, four sets of main group metals and equivalent sets of transition metals, demonstrated that PBEsol predicts lattice constants (which has greater influence on other solid properties, like bulk moduli and thermochemical properties) comparatively better than other non-empirical functionals.^[23, 31, 32] On the other hand, the empirical functionals BLYP are more accurate for organic and main group molecules, but also less accurate for larger molecules.^[34-36] Therefore, benchmark studies are required to identify an appropriate functional in predicting thermochemistry and geometries of a system.

2.2.8.4 Strong Electron Correlation and the Hubbard Correction

Both the LDA and GGA fail to accurately describe the degree of localization/delocalization in the electron density, due to the presence of the self-interaction error^[37] (a product of the non-exact treatment of the exchange energy in KS-DFT). Specifically, LDA/GGA densities are too delocalized, compared to the true density.^[38] This shortcoming produces significant errors in important catalytic properties of transition and rare-earth metal oxides (e.g. Ti – Cu, La, Ce),

including crystal lattice structures, conductivity, oxide reduction and oxidation energies.^[39-44] This problem is most acute for the strongly correlated electrons (i.e. those with high angular momentum), such as the d and f electrons present in metals. Yet it is these electrons which ultimately determine the physicochemical properties of metal oxides.

The Hubbard correction was introduced into LDA/GGA DFT to correct for such electron delocalization via two terms: an “on-site” Coulomb interaction (U), which is associated with electron-electron pairing, and an “on-site” exchange interaction (J), which describes the repulsion of opposite-spin electrons within specific orbitals.^[38, 45] These U and J corrections can be introduced into the DFT energy functional either by the method of Liechtenstein et al.^[46] where U and J corrections are applied independently, or the method of Dudarev et al.^[47] where U and J are added as an effective correction, $U_{\text{eff}} = (U - J)$. The DFT energy functional according to the Liechtenstein method takes the form,^[46]

$$E_{DFT+U}[n, \hat{n}] = E_{DFT}[n] + E_{Hub}[\hat{n}] - E_{dc}[\hat{n}] \quad (2.37)$$

where

$$E_{Hub}[\hat{n}] = \frac{1}{2} \sum_{\{\gamma\}} (U_{\gamma_1\gamma_3\gamma_2\gamma_4} - U_{\gamma_1\gamma_3\gamma_4\gamma_2}) \hat{n}_{\gamma_1\gamma_2} \hat{n}_{\gamma_3\gamma_4} \quad (2.38)$$

and

$$E_{dc}[\hat{n}] = \frac{U}{2} \hat{n}_{tot} (\hat{n}_{tot} - 1) - \frac{J}{2} \sum_{\sigma} \hat{n}_{tot}^{\sigma} (\hat{n}_{tot}^{\sigma} - 1) \quad (2.39)$$

In equation (2.37), $E_{Hub}[\hat{n}]$ is the Hubbard Hamiltonian describing the electron-electron interaction, and $E_{dc}[\hat{n}]$ eliminates double counting of the interaction energy contribution in $E_{DFT}[n]$.

In equation (2.38),

$$\hat{n}_{\gamma_1\gamma_2} = \hat{n}_{\gamma} \delta_{m_1 m_2} \quad (2.40a)$$

and

$$U_{\gamma_1\gamma_3\gamma_2\gamma_4} = \sum_k a_k(m_1, m_2, m_3, m_4) F^k \quad (2.410b)$$

where $0 \leq k \leq 2l$ and $U_{\gamma_1\gamma_3\gamma_2\gamma_4}$ can be written in terms of Slater's integrals F^0, F^2, F^4, F^6 as implemented in the Vienna *ab initio* simulation package (VASP).^[48] They are normally specified in terms of the effective on-site Coulomb interaction (U) and exchange interaction (J). The Slater integrals can be converted in the following way,

$$\text{p-electrons: } F^0 = U, F^2 = 5J \quad (2.41)$$

$$\text{d-electrons: } F^0 = U, F^2 = \frac{14}{1+0.625}J, F^4 = 0.625F^2 \quad (2.42)$$

$$\text{f-electrons: } F^0 = U, F^2 = \frac{6435}{286+195*0.668+250*0494}J, F^4 = 0.668F^2 \text{ and } F^6 = 0.494F^2 \quad (2.43)$$

Although Hubbard U/J corrections in equation (2.41–2.43) treat the electron self-interaction errors considerably better, however, inappropriate U/J values can cause artefacts in electronic structure (e.g. degeneracy of t_{2g}/e_g transition metal states).^[49] Therefore, it is necessary to determine the correct U/J potential, which can be achieved via empirically fitting of DFT+U/J properties against a known reference value, usually needed to adjust with experimental values of respective metal oxides properties such as bandgap, lattice structure, equilibrium volume, magnetic moment etc.

2.2.9 Periodicity, Plane-Wave Basis Sets and Pseudopotentials

The electronic structure of crystalline materials is most conveniently modelled by using a structural unit cell which is replicated infinitely in space via periodic boundary conditions. The unit cell of such a system can be defined by lattice vectors $\mathbf{a}_1, \mathbf{a}_2, \mathbf{a}_3$. According to Bloch's theorem for an infinite periodic system, the KS orbitals can then be expressed as,

$$|\Psi_i(\mathbf{r})\rangle = e^{(i\mathbf{k} \cdot \mathbf{r})} |u_i(\mathbf{r})\rangle \quad (2.44)$$

where \mathbf{k} is the vector which lies within the first Brillouin zone (BZ) and $u_i(\mathbf{r})$ is a periodic basis function. The basis set for a given \mathbf{k} will be discrete, and the periodic function can be expanded as follows,

$$|u_i(\mathbf{r})\rangle = \frac{1}{\sqrt{\Omega}} \sum_{\mathbf{G}} c_{i\mathbf{G}} e^{i\mathbf{G}\cdot\mathbf{r}} \quad (2.45)$$

Here, the volume of the unit cell is $\Omega = \mathbf{a}_1 \cdot (\mathbf{a}_2 \times \mathbf{a}_3)$ and \mathbf{G} is a reciprocal lattice vector.

Using equation (2.44) and (2.45), the final expression for the KS orbitals as a linear combination of basis functions can be expressed as,

$$|\Psi_i(\mathbf{r})\rangle = \sum_{\mathbf{G}} c_{i,\mathbf{k}+\mathbf{G}} e^{i(\mathbf{k}+\mathbf{G})\cdot\mathbf{r}} \quad (2.46)$$

where, $c_{i,\mathbf{k}+\mathbf{G}}$ are the coefficients for the expansion. In principle, an infinite basis set is required to expand the electronic wave function exactly. In practice, however, only those reciprocal lattice vectors yielding kinetic energies lower than predefined cutoff energy (E_{cut}) are considered and included in the basis set expansion, such that $\frac{1}{2} \|\mathbf{G}\|^2 < E_{cut}$.

In practice, most periodic DFT calculations employ plane-wave basis sets however, the major drawback of this approach is that a huge number of plane waves are required to describe some localized features of the electronic structure, for example, core orbital structure. This problem may be mitigated in part by the use of Pseudo-Potentials (PP). The PP approximation is based on the assumption that the valence electrons predominantly determine chemical bonding and chemical reactivity. Consequently, the large number of plane-wave basis functions required to reproduce core orbitals can be replaced with a single ‘PP’ that mimics the strong interaction between the nuclei and in the core region of the atom (see Fig. 2.1). This results in fewer plane waves being required to describe the KS orbitals adequately.^[50]

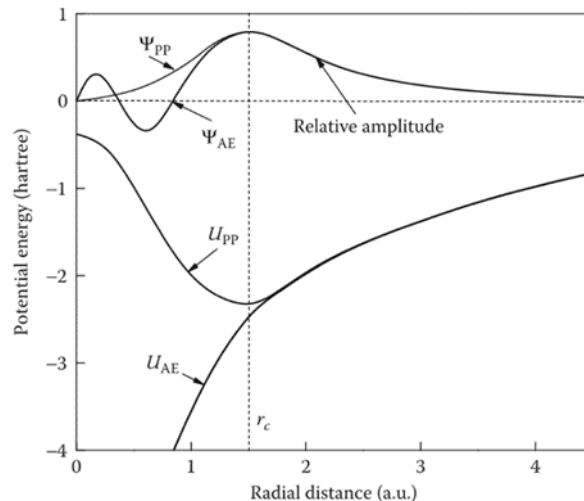


Fig. 2.1 The PP concept – the potential in the core region of an atom, which is the product of many individual basis functions for each electron, is replaced with single fictitious potential. Ψ_{PP} and Ψ_{AE} corresponds to pseudo- and all-electron wavefunctions respectively; u_{PP} and u_{AE} corresponds to pseudo- and all-electron potentials, respectively.^[51] Reprinted with permission from CCC®.

2.3 Modelling Thermochemistry with DFT via Phonon Dispersions

DFT describes the electronic structure of a crystalline material at 0 K and 0 atm. It does not account for temperature- and pressure-dependent phenomena of a material, for instance, the thermochemical properties that are the focus of this thesis, such as heat capacity, enthalpy and free energy. Calculation of these properties requires energy minimization concerning the free energy of the system, and entropic terms (electronic, ionic and configurational entropy) to be specifically treated.^[52] Typically the starting point for approximating thermochemical properties in periodic/crystalline materials using DFT is the calculation of phonon dispersions on the BO potential surface.^[53-58]

In any crystalline material, the atoms are continuously undergoing small oscillations, or vibrations, about their equilibrium position. These atomic displacements give rise to coupled, uniform vibrations throughout the crystal lattice, otherwise known as phonons.^[59-62] The energies associated with all individual atomic vibrations and phonons are governed by the temperature of the material and can be represented as a function of atomic displacements,

$$\begin{aligned} \Phi = \Phi_0 + \sum_{lk} \sum_{\alpha} \Phi_{\alpha}(lk) u_{\alpha}(lk) + \frac{1}{2} \sum_{l'l''} \sum_{kk'k''} \sum_{\alpha\beta} \Phi_{\alpha\beta}(lk, l'k') u_{\alpha}(lk) u_{\beta}(l'k') \\ + \frac{1}{3!} \sum_{l'l''k''} \sum_{kk'k''} \sum_{\alpha\beta\gamma} \Phi_{\alpha\beta\gamma}(lk, l'k', l''k'') \times u_{\alpha}(lk) u_{\beta}(l'k') u_{\gamma}(l''k'') \\ + \dots \end{aligned} \quad (2.47)$$

where $\Phi_0, \Phi_{\alpha}(lk), \Phi_{\alpha\beta}(lk, l'k')$ and $\Phi_{\alpha\beta\gamma}(lk, l'k', l''k'')$, are the zeroth, first, second, and third-order force constant, $\alpha\beta\gamma\dots$ are Cartesian indices and $u(lk)$ is the atomic displacement of the k^{th} atom in the l^{th} unit cell. The zeroth-order force constant, Φ_0 , is the 0 K energy of the system in its equilibrium geometry (i.e. that typically calculated in a standard DFT calculation). If all atoms are held fixed in their equilibrium positions, the force acting on the k^{th} atom in the α -direction is the first derivative of the potential energy with respect to atom k ,^[63, 64]

$$F_{\alpha}(lk) = -\frac{\partial\Phi}{\partial u_{\alpha}(lk)} \quad (2.48)$$

The second- and third-order force constants $\Phi_{\alpha\beta}(lk, l'k')$ and $\Phi_{\alpha\beta\gamma}(lk, l'k', l''k'')$ are,

$$\Phi_{\alpha\beta}(lk, l'k') = \frac{\partial^2\Phi}{\partial u_{\alpha}(lk)\partial u_{\beta}(l'k')} = -\frac{\partial F_{\alpha}(lk)}{\partial u_{\beta}(l'k')} \quad (2.49)$$

$$\Phi_{\alpha\beta\gamma}(lk, l'k', l''k'') = \frac{\partial^3\Phi}{\partial u_{\alpha}(lk)\partial u_{\beta}(l'k')\partial u_{\gamma}(l''k'')} = -\frac{\partial^2 F_{\alpha}(lk)}{\partial u_{\beta}(l'k')\partial u_{\gamma}(l''k'')} \quad (2.50)$$

and can be derived from lattice frequencies and perturbation theory, respectively.^[63] In the crystal system with small atomic displacements at constant volume, the second-order force constant is

calculated by the harmonic approximation using lattice frequencies, and the third-order force constants are obtained using perturbation theory. The second-order force constants define the dynamical matrix $D_{kk'}^{\alpha\beta}(\mathbf{q})$,

$$D_{kk'}^{\alpha\beta}(\mathbf{q}) = \sum_{l'} \frac{\Phi_{\alpha\beta}(0k, l'k')}{\sqrt{m_k m_{k'}}} e^{-i\mathbf{q} \cdot [r(l'k') - r(0k)]} \quad (2.51)$$

Diagonalization of the dynamical matrix yields the vibrational and phonon frequencies $\omega_{\mathbf{q}j}$ over the BZ,^[64]

$$\left| D_{kk'}^{\alpha\beta}(\mathbf{q}) - \omega_{\mathbf{q}j}^2 e_{\mathbf{q}j}^{\alpha k} \right| = 0 \quad (2.52)$$

or,

$$\omega_{\mathbf{q}j}^2 e_{\mathbf{q}j}^{\alpha k} = \sum_{\beta k'} D_{kk'}^{\alpha\beta}(\mathbf{q}) e_{\mathbf{q}j}^{\beta k'} \quad (2.53)$$

These harmonic frequencies $\omega_{\mathbf{q}j}$ can then be used to calculate the temperature-dependent internal energy (E), Helmholtz free energy (A), constant volume heat capacity (C_V) and entropy (S) within the harmonic approximation at a temperature T and constant volume V ,

$$E = \sum_{\mathbf{q}j} \hbar\omega_{\mathbf{q}j} \left[\frac{1}{2} + \frac{1}{\exp\left(\frac{\hbar\omega_{\mathbf{q}j}}{k_B T}\right) - 1} \right] \quad (2.54)$$

$$A = \frac{1}{2} \sum_{\mathbf{q}j} \hbar\omega_{\mathbf{q}j} + k_B T \sum_{\mathbf{q}j} \ln \left[1 - \exp\left(-\frac{\hbar\omega_{\mathbf{q}j}}{k_B T}\right) \right] \quad (2.55)$$

$$C_V = \sum_{\mathbf{q}j} k_B \left(\frac{\hbar\omega_{\mathbf{q}j}}{k_B T} \right)^2 \frac{\exp\left(\frac{\hbar\omega_{\mathbf{q}j}}{k_B T}\right)}{\left[\exp\left(\frac{\hbar\omega_{\mathbf{q}j}}{k_B T}\right) - 1 \right]^2} \quad (2.56)$$

$$S = \frac{1}{2T} \sum_{\mathbf{q}j} \hbar\omega_{\mathbf{q}j} \coth \left[\frac{\hbar\omega_{\mathbf{q}j}}{2k_B T} \right] - k_B \sum_{\mathbf{q}j} \ln \left[2 \sinh \frac{\hbar\omega_{\mathbf{q}j}}{2k_B T} \right] \quad (2.57)$$

Here the summations run over wave vectors \mathbf{q} and band indices j . The further conversion of (C_v) to constant pressure heat capacity (C_p) can be performed via quasi-harmonic approximations,^[65, 66]

$$C_p = C_v + \alpha^2 \beta V T \quad (2.58)$$

where, α , β , V , represent the thermal expansion coefficient, bulk modulus and volume of the system, respectively. To transform the constant volume thermodynamic variables to constant pressure thermodynamic variables, volume dependences of phonon frequencies are introduced by performing phonon calculations across a wide volume range. The temperature dependent Gibbs free energy $G(T, p)$ at constant pressure (p) can be obtained from Helmholtz free energy $A(T, V)$ through the transformation,

$$G(T, p) = \min_v [A(T, V) + pV] \quad (2.59)$$

where, the right-side terms require to find the minimum value by changing volume V . $A(T, V)$ can be approximated as,

$$A(T, V) \cong E^{DFT}(V) + A^{PHONON}(T, V) \quad (2.60)$$

where $E^{DFT}(V)$ is calculated as the total electronic energy at a volume V from DFT calculation and $A^{PHONON}(T, V)$ is the temperature-dependent phonon Helmholtz free energy at V . By using equations (2.59) and (2.60), the minimum values of $G(T, p)$ at a given temperature is obtained which simultaneously generates the respective equilibrium volumes $V(T)$. Therefore, the volumetric thermal expansion coefficient (α) is obtained from $V(T)$ and bulk modulus (β) is computed using the following equation,^[67]

$$\alpha = (1/V) \left(\frac{\partial V}{\partial T} \right)_p \quad (2.61)$$

$$\beta = -V \left(\frac{\partial P}{\partial V} \right)_T \quad (2.62)$$

2.4 Phonon Structures and Thermochemical Properties of Ba-based ABO₃ Perovskites

In order to develop an accurate DFT protocol for modelling the electronic structure of ABO₃ perovskites (considered in Chapters 3 and 4 of this thesis), DFT ansatz was first developed for representative perovskites containing alkaline cation (Ba) at A-site, and 4f metal (Ce), 4d metal (Zr) and 3d metal (Mn) at B-site. Thermochemical properties of BaCeO₃ and BaZrO₃ have been established via many independent experimental studies.^[68-70] These perovskite materials are therefore ideal candidates by which first-principles DFT predictions of thermochemical properties can be benchmarked. The following discussion presents a systematic evaluation of the lattice structure and phonon properties for these perovskites. Where possible, data is compared to exiting literature values for BaCeO₃ and BaZrO₃. A systematic evaluation of common GGA XC functionals is additionally presented for BaMnO₃, since the thermochemical properties of this perovskite have not yet been studied extensively in the literature. Analysis of the phonon structure of BaCeO₃, BaZrO₃ and BaMnO₃ perovskites calculated via Density Functional Perturbation Theory (DFPT) (equations (2.53)) is also presented. For materials shown to be thermally stable, temperature-dependent entropies, specific heats and relative molar enthalpies, calculated using DFT (i.e. equations (2.54) – (2.58)) are presented and validated against available experimental data.

2.4.1 Computational Methods

Initial structures for GGA DFT optimization were taken from experimental crystal data (see Fig. 2.2). BaCeO₃ exists in the orthorhombic phase between 0 – 675 K (space group *Pnma* between 0 – 533 K,^[71] *Imma* space group between 534 – 675 K^[72]), in the rhombohedral phase between 676 – 1153 K (space group $R\bar{3}c$),^[72] and in the cubic phase above 1153 K (space group *Pm3m*).^[73, 74] BaZrO₃ exhibits only the ideal cubic perovskite phase (*Pm3m* space group), irrespective of temperature.^[75] At ambient conditions, BaMnO₃ has been shown to exhibit both hexagonal (*P63/mmc*) and cubic phases.^[76-78] However, only the *P63/mmc* structure has been resolved experimentally; an ideal hypothetical cubic (*Pm3m*) phase was considered here since the exact crystal structure for this phase has not been reported.^[79] The ideal theoretical cubic BaMnO₃ unit cell was constructed by considering Ba atom at (0, 0, 0) in the unit cell, Mn at (1/2, 1/2, 1/2) and three O atoms at (0, 1/2, 1/2), (1/2, 1/2, 0), and (1/2, 0, 1/2) (all in terms of fractional coordinates). Initial lattice parameters were taken from existing literature for the cubic phase,^[78-81] and varied across the range of reported values (3.9, 3.96, 4.01 Å) with respect to the total energies to find an optimized GGA value.

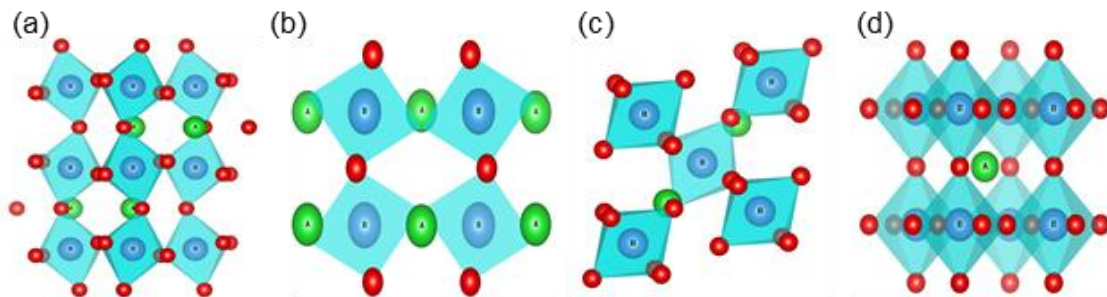


Fig. 2.2 Crystal structures of ABO₃ phases. (a) orthorhombic (*Pnma*), (b) orthorhombic (*Imma*), (c) rhombohedral ($R\bar{3}c$), (d) cubic (*Pm3m*). The green, blue and red balls represent A, B and O atoms, respectively. Aqua surfaces indicate BO₃ octahedra.

All DFT calculations reported here implemented projector augmented wave (PAW)-PP^[82] using VASP.^[48] The most universal GGA functional, PBE was employed for BaCeO₃ and BaZrO₃. Additional Hubbard U/J (9/0.9 eV) corrections (PBE+U/J) were added to the Ce metal in orthorhombic BaCeO₃ following previous examples in the literature.^[83-85] For BaMnO₃, the thermochemical properties of this perovskite have not been reported in the literature, and so these properties are examined here with multiple GGA functionals (PBE,^[21] RPBE,^[22] PBEsol,^[23]). This ensures that DFT-predicted values are consistent, but also enables any potential dependency of thermochemical properties on the choice of XC functional to be identified. For all calculations, a 500 eV plane wave cut-off was employed with Methfessel-Paxton electron smearing (0.4 eV) to alleviate potential SCF convergence issues.^[86] To sample the BZ of the unit cells, 4×4×4 Monkhorst-Pack k-point schemes were employed to the k-point mesh sampling. The total DFT energy was fully optimized with respect to ionic positions, cell shape and cell volume, using a convergence criterion 1.0×10^{-8} eV.

For cubic phase perovskites, the DFT energy was fully optimized using a Birch-Murnaghan equation of state (BM EOS).^[87] For the lower-symmetry phases, this approach is prohibitive, and so the DFT energy was minimized against all internal structural degrees of freedom (i.e. cell volume, cell shape, ionic position). Vibrational properties of the optimized unit cells were calculated using the supercell approach using a 2×2×2 extension of the optimized unit cell with the number of k points reduced accordingly. The real-space force constants of the crystallographic supercell were calculated using DFPT, as implemented in VASP, using forces on atoms calculated via finite differences (atomic displacements of 0.01 Å).^[88, 89] Phonon modes were then calculated using these force constants with the Phonopy software package,^[90] using Monkhorst-Pack grid of 48×48×48 q points for the phonon wave vectors (see equation (2.52)).

2.4.2 BaCeO₃

Optimal PBE+U/J lattice vectors were compared with experimental data, as shown in Table 2.1. All calculated lattice parameters are in excellent agreement with experimental values, deviating by at most ~2%, thereby validating PBE+U/J for structure prediction in this material.

Table 2.1 Comparison of experimental and PBE+U/J lattice parameters of orthorhombic, rhombohedral and cubic BaCeO₃.

Phase		Lattice parameters (Å)		
		a	b	c
Orthorhombic (<i>Pnma</i>)	Exp. ^[71]	6.22	6.24	8.78
	Theory	6.33	6.36	8.94
Orthorhombic (<i>Imma</i>)	Exp. ^[72]	6.26	6.23	8.79
	Theory	6.31	6.29	8.87
Rhombohedral (<i>R$\bar{3}c$</i>)	Exp. ^[72]	6.24	6.24	6.24
	Theory	6.33	6.33	6.33
Cubic (<i>Pm$\bar{3}m$</i>)	Exp. ^[74]	4.44	4.44	4.44
	Theory	4.53	4.53	4.53

The thermochemical properties of orthorhombic, rhombohedral and cubic BaCeO₃, such as entropy (S), relative molar enthalpies ($H(T)-H(298\text{ K})$) were obtained using harmonic approximation, and constant pressure specific heat (C_p) was obtained using the quasi-harmonic approximation as outlined in §2.3. The reported thermochemical properties across four phases: $Pnma$, $Imma$, $R\bar{3}c$ and $Pm\bar{3}m$ were considered for BaCeO₃ between the temperature range of 0 – 533 K, 534 – 675 K, 676 – 1153 K, and 1154 – 2000 K, respectively based on the experimentally reported phase transitions for this material.^[73] Scholten et al.^[70] have previously investigated the thermochemical properties of BaCeO₃ perovskites at low temperature by adiabatic calorimetry and at high temperature by drop calorimetry. A similar study by Ahrens et al.^[68] reported thermochemical data for BaCeO₃ between 1.6 K and room temperature by means of adiabatic calorimetry.

PBE+U/J thermochemical data for these materials calculated in this work are compared with the experimental values reported by Scholten et al. in Fig. 2.3(a-c), which showed excellent agreement with the calculated values up to 900 K. However, we have not taken into consideration of reported data above 900 K by Scholten et al., as the results were derived from smoothed thermodynamic function. Selected theoretical values of C_p , S and ($H(T)-H(298\text{ K})$) for BaCeO₃ are compared to experimental data in Table 2.2. Table 2.2 shows that, at room temperature and high temperatures the calculated C_p , S and ($H(T)-H(298\text{ K})$) are in excellent agreement with available experimental data. For example, at 298.15 K, the largest deviation between this work and experiment is less than 2 J K⁻¹ mol⁻¹ for both C_p and S . At higher temperature (900 K), this difference is 4 J K⁻¹ mol⁻¹. Additionally, ($H(T)-H(298\text{ K})$) for BaCeO₃ calculated here to be within 3 kJ mol⁻¹ of the published experimental value.

Table 2.2 Comparison of calculated PBE+U/J and experimental S and C_p values of BaCeO₃

T (K)		C_p (J K ⁻¹ mol ⁻¹)	S (J K ⁻¹ mol ⁻¹)	$H(T)-H(298.15 \text{ K})$ (kJ mol ⁻¹)
298.15	Expt. ^[68]	114.8	145.8	-
	Expt. ^[70]	111.91	144.51	-
	This work	113.12	146.94	-
900	Expt. ^[70]	131.06	280.18	74.88
	This work	133.13	284.24	71.13

The calculated S values of BaCeO₃ for both the orthorhombic phases $Pnma$ (0 – 533 K) and (534 – 675 K), and rhombohedral phase $R\bar{3}c$ (676 – 900 K) are in excellent agreement with experimental data (Fig. 2.3(a)). However, the S values of cubic phase, $Pm\bar{3}m$ (1154 – 2000 K) deviates by 81 J K⁻¹ mol⁻¹ from the rhombohedral phase $R\bar{3}c$ at phase transition temperature 1154 K. This is attributed here to the fact that distortions within the CeO₃ octahedra and a change in the coordination sphere of the A-site Ba²⁺ cation (which changes from 6- to 12-coordinate) are both associated with negative frequencies in the phonon spectra shown in Fig. 2.4(d). These vibrations of the Ba²⁺ and Ce⁴⁺ cations, which are in effect a signature of instability in the crystal lattice, become increasingly more obvious in the rhombohedral and cubic phases (see Fig. 2.4(c, d)). The variation of C_p with temperatures obeys Debye T^3 law at low temperatures, and above room temperature reaches around 125.7 J K⁻¹ mol⁻¹ at 500 K, consistent with Dulong-Petit's law ($3nR=124.7 \text{ J K}^{-1} \text{ mol}^{-1}$, $n=5$ is the number of atoms in each unit cell), while above 500 K, C_p departs from the Dulong-Petit's law due to quasi-harmonic contributions.

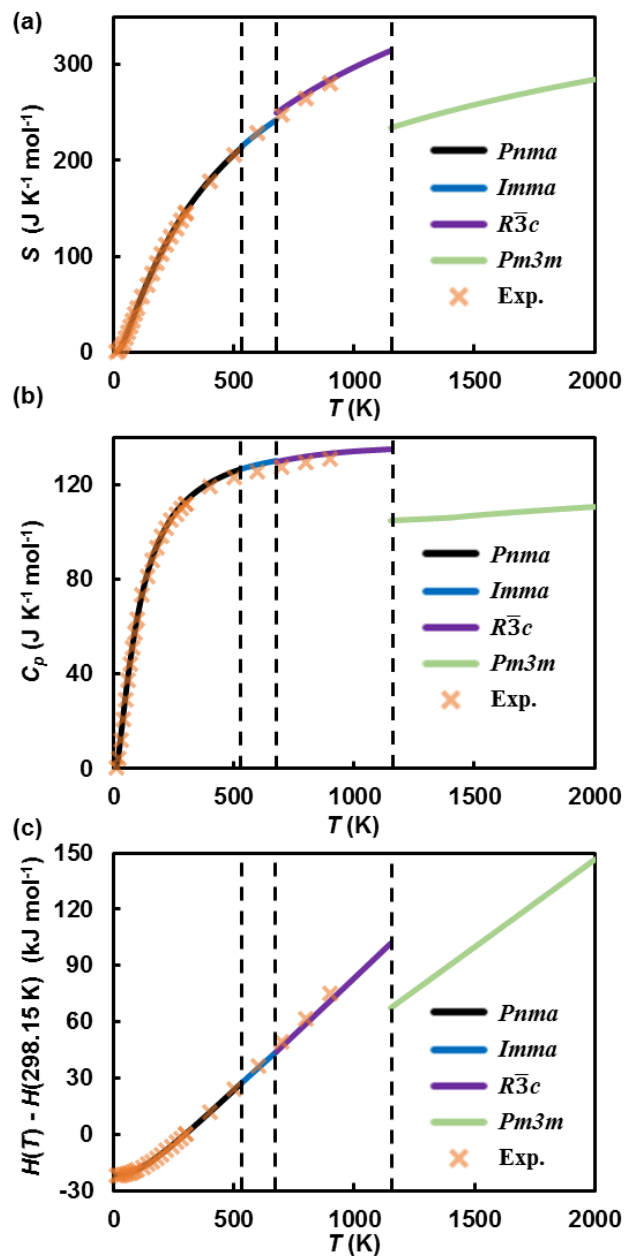


Fig. 2.3 PBE+U/J and experimental values of (a) S ($\text{J K}^{-1} \text{mol}^{-1}$); (b) C_p ($\text{J K}^{-1} \text{mol}^{-1}$) and (c) $(H(T)-H(298.15 \text{ K}))$ (kJ mol^{-1}) of BaCeO_3 . The vertical dotted lines show the phase transition point of $Pnma$ (0 – 533 K), $Imma$ (534 – 675 K), $R\bar{3}c$ (676 – 1153 K), and $Pm3m$ (1154 – 2000 K) of BaCeO_3 . Experimental data were taken from Ahrens et al.^[68] between 0 – 300 K, and Scholten et al.^[70] between 300 – 900 K.

Overall, experimental C_p data are in near-exact agreement with theoretical C_p values produced in this work up to 900 K (Fig. 2.3(b)). Similarly, calculated $(H(T)-H(298\text{ K}))$ values for BaCeO₃ (Fig. 2.3(c)) between 0 – 900 K are in very good agreement with experiment. This agreement indicates that the thermochemical properties for the cubic phase of BaCeO₃ are an accurate prediction that can be tested in future experiments.

The vibrational contributions to these thermochemical properties can be explained via analysis of phonon dispersion and vibrational density of states (VDOS). The phonon dispersions and VDOS of BaCeO₃ in the $Pnma$, $Imma$, $R\bar{3}c$, and $Pm\bar{3}m$ phases are presented along the high symmetry Γ -M-R-X- Γ -R path in Fig. 2.4(a-d). In all cases (Fig. 2.4(a-d)), the acoustic modes (below 150 cm⁻¹) in this material are predominantly governed by the motions of heavier Ba²⁺ cation, while the optical modes (above 300 cm⁻¹) are dominated by the motion of oxygen atoms. The B-site Ce⁴⁺ cation provides a substantial contribution to the intermediate-frequency regimes between 150 - 300 cm⁻¹ in BaCeO₃. There exist soft phonon modes at the M-point of the $Imma$ phase (Fig. 2.4(b)) and the Γ -point of the $R\bar{3}c$ phase (Fig. 2.4(c)), indicating the likely mechanism by which a respective $Pnma$ – $Imma$ and $Imma$ – $R\bar{3}c$ phase transition of BaCeO₃ takes place.^[73]

In contrast, cubic BaCeO₃ exhibits imaginary frequencies at Γ , M, R and X points (Fig. 2.4(d)). The unstable phonon modes at Γ -point correspond to the polar vibrational modes of Ce displacement within CeO₃ octahedral sublattice (Fig. 2.5(a)). The other unstable phonon modes at the M-point (Fig. 2.5(b)) and R-point (Fig. 2.5(c)) originate from the in-phase and out-of-phase octahedral rotation within the CeO₃ sublattices respectively, whereas instabilities at the X-point (Fig. 2.5(d)) correspond to the breathing mode within individual CeO₃ octahedra. All the imaginary phonon modes of respective crystal structure were accounted in predicting their thermodynamic properties shown in Fig. 2.3.

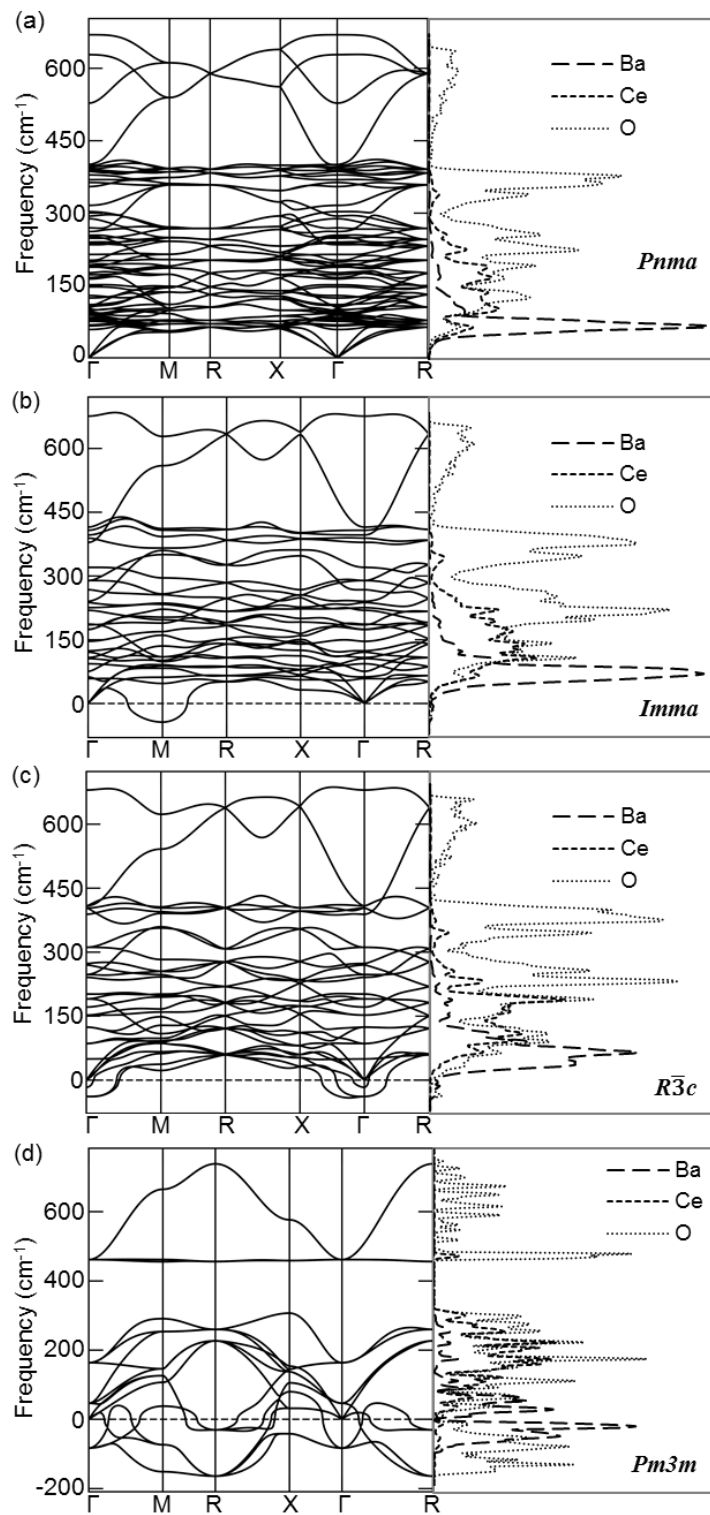


Fig. 2.4 The calculated PBE+U/J phonon dispersions (left) and VDOS (right) of BaCeO₃: (a) orthorhombic (*Pnma*), (b) orthorhombic (*Imma*), (c) rhombohedral (*R $\bar{3}c$*), (d) cubic (*Pm $\bar{3}m$*).

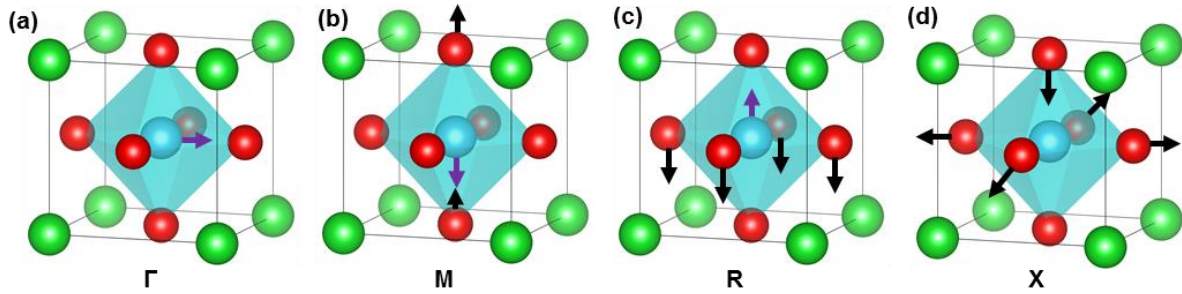


Fig. 2.5 The unstable phonon modes of cubic ($Pm3m$) $BaCeO_3$ associated with the vibration at the q-points: (a) Γ -point, (b) M-point, (c) R-point, and (d) X-point. Atom colors as per Fig. 2.2.

2.4.3 $BaZrO_3$

The experimental lattice constant of cubic $BaZrO_3$ is 4.19 Å.^[91] The theoretical lattice constant of cubic $BaZrO_3$ was optimized using the BM EOS.^[87] Lattice parameter values varied from 4 to 5 Å with an interval of 0.01 Å against the total energy of the unit cell (see Fig. 2.6). The minimum PBE ground state energy corresponds to a lattice constant of 4.23 Å. The calculated PBE lattice constant has a deviation of ~ 0.04 Å with the experimental value, but has an exact agreement with other theoretical works using the same GGA functional.^[92] Notably, the value obtained by PBE is comparably in good agreement with experimental value than other GGA functionals reported in the literature (see Table 2.3).

Table 2.3 Comparison of PBE lattice parameters ($a/\text{Å}$) of cubic ($Pm3m$) $BaZrO_3$ with experimental and other theoretical works.

	Exp. ^[75]	PBE ^{a)}	PBE ^[92]	RPBE ^[92]	PW91 ^[93]
($a/\text{Å}$)	4.19	4.23	4.235	4.269	4.25

a) This work.

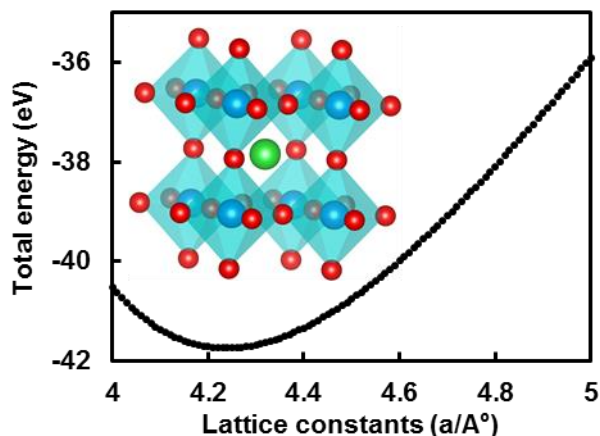


Fig. 2.6 PBE fitted BM-EOS curve of cubic ($Pm\bar{3}m$) BaZrO₃. Atom colors as per Fig. 2.2.

Thermochemical properties of BaZrO₃ have also been experimentally studied,^[68, 69] and are used here to validate the predictions obtained using the PBE functional. Table 2.4 demonstrates that calculated PBE C_p , S and $(H(T)-H(298\text{ K}))$ values for BaZrO₃ at 298.15 K and 1000 K are in close agreement with experimental data.^[68, 69] For example, at 298.15 K, the largest deviation of S and C_p values between this work and the experimental results are less than $8\text{ J K}^{-1}\text{ mol}^{-1}$ and $6\text{ J K}^{-1}\text{ mol}^{-1}$, respectively. At high-temperature (1000 K), these differences are less than $7\text{ J K}^{-1}\text{ mol}^{-1}$. Additionally, $(H(T)-H(298\text{ K}))$ for BaZrO₃ calculated here is within 4 kJ mol^{-1} of the published experimental value.^[69] Ahrens et al.^[68, 69] have previously investigated the thermochemical properties of BaZrO₃ perovskite between 1.6 K and room temperature by means of adiabatic calorimetry. A similar study by Cordfunke et al.^[69] reported high-temperature thermochemical data for BaZrO₃. The PBE thermochemical properties are compared against these experimental values in Fig. 2.7. The calculated S values of BaZrO₃ are in excellent agreement with experimental data at low- and high-temperatures (Fig. 2.7(a, b)).

The variation of C_p with temperatures obeys the Debye T^3 law at low temperatures, while above 500 K, C_p tends to the departure from the Dulong-Petit's law due to quasi-harmonic contributions.

Below 300 K (Fig. 2.7(c)), experimental C_p data are in near-exact agreement with theoretical C_p values produced in this work. A maximum discrepancy of $\sim 4.8 \text{ J K}^{-1} \text{ mol}^{-1}$ is observed between experiment and theory at temperature 1400 K. Nevertheless, calculated C_p values at high temperature show agreeable fitting with experimental C_p data, as shown in Fig. 2.7(d). Similarly, the $(H(T)-H(298 \text{ K}))$ values for BaZrO_3 (Fig. 2.7(e, f)) between 0 – 2000 K are in very good agreement with experiment, with a maximum deviation of $\sim 7\%$ at 2000 K.

Table 2.4 Comparison of PBE-PAW and experimental thermochemical properties of BaZrO_3 at 298.15 K and 1000 K.

T (K)		C_p	S	$(H(T)-H(298 \text{ K}))$
		($\text{J K}^{-1} \text{ mol}^{-1}$)	($\text{J K}^{-1} \text{ mol}^{-1}$)	(kJ mol^{-1})
	Expt. ^[68]	107	125.5	-
298.15	Expt. ^[69]	101.71	124.7	-
	This work	107.35	132.2	-
1000	Expt. ^[69]	129.72	267.76	84.74
	This work	127.58	273.6	80.0

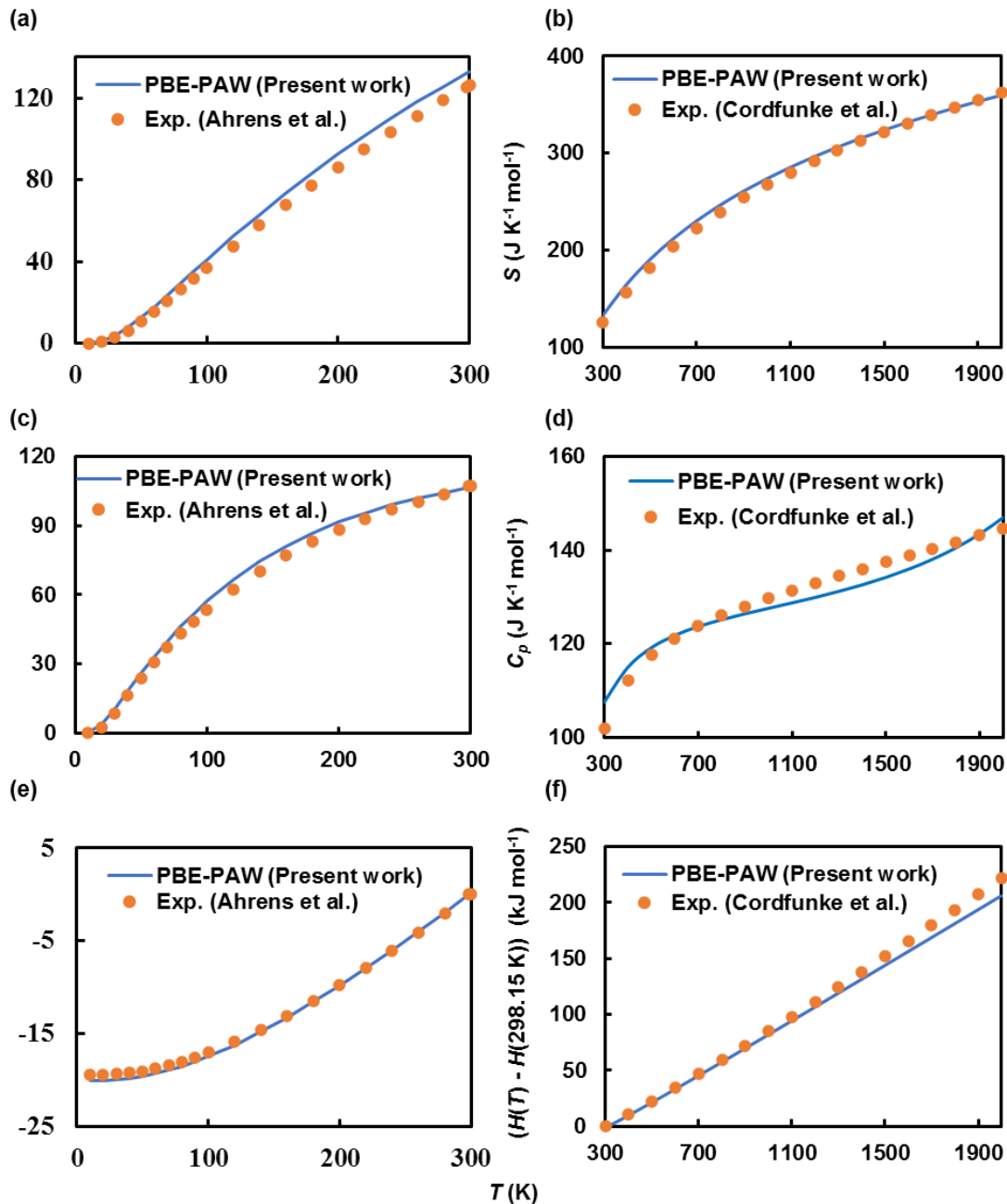


Fig. 2.7 PBE-PAW and experimental S ($\text{J K}^{-1} \text{mol}^{-1}$) of BaZrO_3 between (a) 0 – 300 K, and (b) 300 – 2000 K. PBE-PAW and experimental C_p ($\text{J K}^{-1} \text{mol}^{-1}$) of BaZrO_3 between (c) 0 – 300 K, and (d) 300 – 2000 K. PBE-PAW and experimental $(H(T)-H(298 \text{ K}))$ (kJ mol^{-1}) of BaZrO_3 between (e) 0 – 300 K, and (f) 300 – 2000 K. Experimental data were taken from Ahrens et al.^[68, 69] between 0 – 300 K, and Cordfunke et al.^[69] between 300 – 2000 K.

The PBE-PAW predicted phonon dispersion curves and VDOS of cubic BaZrO₃ along the high symmetry Γ -M-R-X- Γ -R path is shown in Fig. 2.8(left). The acoustic modes in each material are predominantly governed by the motions of heavier Ba atoms (Fig. 2.8(right)) to low-frequency regime below 150 cm⁻¹, while the optical modes are by the motion of oxygen atoms to high-frequency regime above 450 cm⁻¹. The B-site Zr in BaZrO₃ has a smaller contribution to the low-frequency regimes (Fig. 2.8(right)). This highlights the different nature of the A- and B-site vibrations. The intermediate-frequency phonon modes (e.g. $\sim 150 - 400$ cm⁻¹) for these three perovskites are generally dominated by the vibration of the Zr atoms, for the same reason. The two-regime distribution of VDOS likely comes from the mass ratio of two atoms. This is attributed to the relatively small mass of O compared to Ba and Zr.

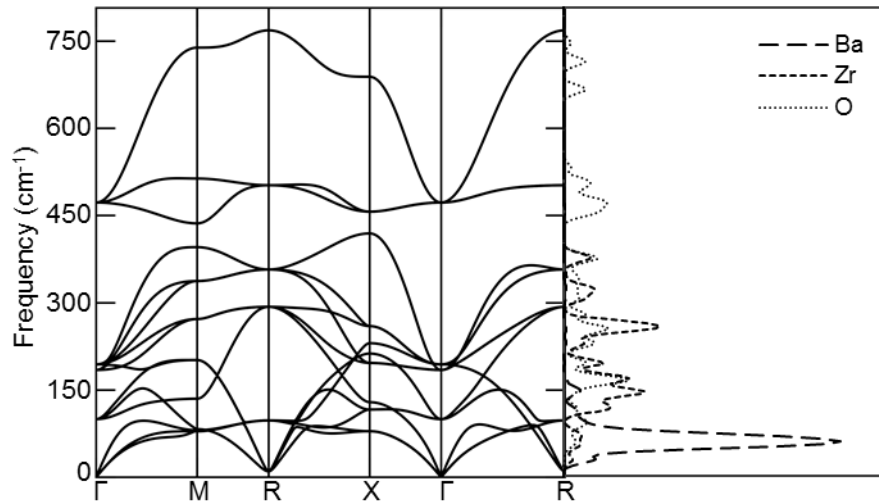


Fig. 2.8 The calculated phonon BS of cubic ($Pm3m$) BaZrO₃ by PBE functional: (a) phonon dispersions (left) and VDOS (right).

2.4.4 BaMnO₃

The experimental lattice vectors of hexagonal (*P63/mmc*) BaMnO₃^[76] were optimized using PBE, RPBE, PBEsol XC functionals by relaxing cell volume, cell shape, and ionic positions. The optimized lattice parameters are compared with experimental data in Table 2.5.

Table 2.5 Comparison of optimized lattice parameters of hexagonal (*P63/mmc*) BaMnO₃ using different GGA functionals with experimental work.

	Lattice parameters (a/Å)		
	a	b	c
Exp. ^[76]	5.70	4.94	4.82
PBE	5.76	4.98	4.93
RPBE	5.86	5.08	5.02
PBEsol	5.67	4.91	4.86

PBE and RPBE overestimate the experimental lattice vectors, while PBEsol underestimates these values. However, the deviation between the calculated and experimental values of hexagonal BaMnO₃ are within 1%. Contrary, the equilibrium structural parameter of cubic BaMnO₃ was optimized by BM EOS using PBE, RPBE and PBEsol functionals. The calculated total energies as a function of lattice constant are fitted in Fig. 2.9.

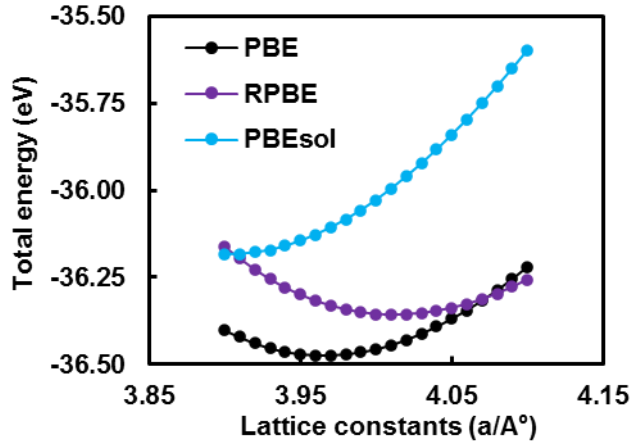


Fig. 2.9 The BM EOS of cubic ($Pm3m$) $BaMnO_3$ with calculated data and fitting curves using different GGA functionals.

The fitted BM EOS curves show considerable variation with these different GGA functionals, and the optimized lattice constants derived from the BM EOS are compared in Table 2.6. It is evident from this table that RPBE predicts the largest lattice constant, 4.01 Å, which is ~ 0.05 Å larger than that found with PBE, and 0.11 Å larger than that found with PBEsol. The latter value (obtained with PAW pseudopotentials) here has near-exact agreement with other theoretical works reported by PBE with Ultra-Soft (US)-PP^[79] and LSDA with PAW-PP.^[81] However, the PBE-PAW result presented here slightly overestimates (~ 0.02 Å) the other theoretical works,^[78] reported with the same GGA functional, but different K-points than the present work which may slightly influence the lattice parameter. Nevertheless, RPBE-PAW produces the same lattice parameter reported in the literature using identical GGA functional.^[80] This implies that the optimized lattice constant values of cubic $BaMnO_3$ presented in the current work are reliable to predict the phonon dispersion and thermochemical properties of cubic $BaMnO_3$.

Table 2.6 Comparison of optimized lattice parameters ($a/\text{\AA}$), bulk modulus (B/GPa) and its pressure derivative (B_0) of cubic BaMnO_3 using different GGA functionals and literature data.

	PBE-PAW ^{a)}	RPBE-PAW ^{a)}	PBEsol-PAW ^{a)}	PBE-PAW	RPBE-PAW	PBE-USPP, LSDA-PAW
($a/\text{\AA}$)	3.96	4.01	3.90	3.94 ^{b)}	4.01 ^{c)}	3.90 ^{d)}
B (Gpa)	143	126	169	-	-	-
B_0	4.75	4.49	5.07	-	-	-

a) This work. b) Ref.^[78] c) Ref.^[80] d) Ref.^[79, 81]

The thermochemical properties of hexagonal and cubic BaMnO_3 have not been characterized yet experimentally or theoretically. The influence of GGA-functionals is investigated here by comparing the vibrational S , C_v and ($H(T)-H(298\text{ K})$) values of BaMnO_3 between 0 – 2000 K using PBE, RPBE and PBEsol (Fig. 2.10). At an equivalent temperature, the S values calculated with the PBEsol for both hexagonal and cubic phases are marginally lower than both the PBE and RPBE values (Fig. 2.10(a, b)). For instance, at 300 K, PBE predicts the S values of hexagonal and cubic BaMnO_3 to be 117 and 110 $\text{J K}^{-1} \text{mol}^{-1}$ respectively, whereas PBEsol predicts a value of 116 and 108 $\text{J K}^{-1} \text{mol}^{-1}$ at the same temperature. By comparison, RPBE is larger than this PBEsol value by 5 and 11 $\text{J K}^{-1} \text{mol}^{-1}$ hexagonal and cubic phases, respectively. This trend remains almost identical at all temperatures up to 2000 K. Predicted C_v values of BaMnO_3 are shown in Fig. 2.10(c, d).

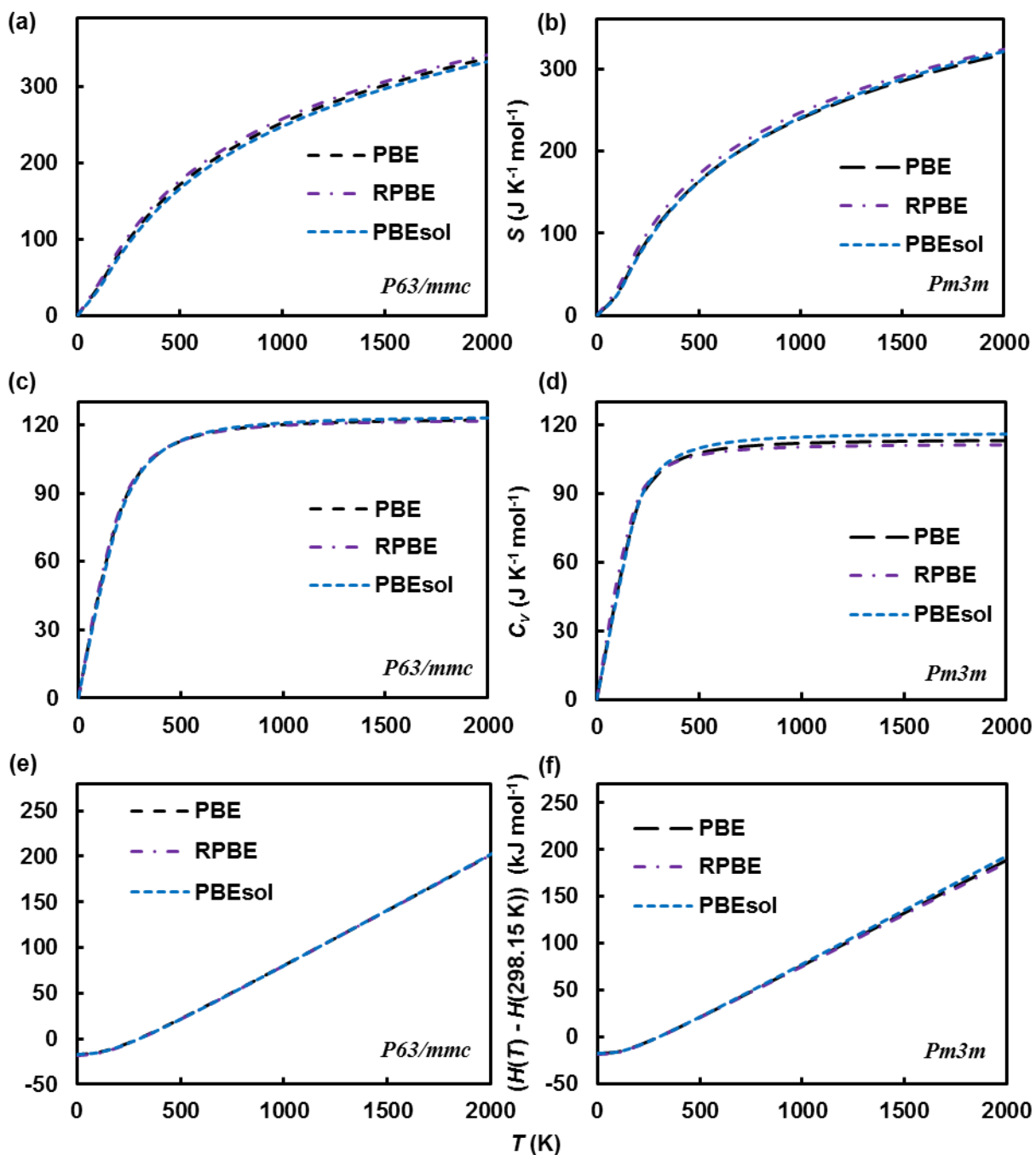


Fig. 2.10 Calculated S ($\text{J K}^{-1} \text{mol}^{-1}$) for (a) hexagonal ($P63/mmc$) and (b) cubic ($Pm3m$); calculated C_v ($\text{J K}^{-1} \text{mol}^{-1}$) for (c) hexagonal ($P63/mmc$) and (d) cubic ($Pm3m$); calculated $(H(T) - H(298 \text{ K}))$ (kJ mol^{-1}) for (e) hexagonal ($P63/mmc$) and (f) cubic ($Pm3m$) of BaMnO_3 between 0 – 2000 K using various GGA functionals.

In general, C_v varies with temperature as one would expect; at low temperatures C_v obeys Debye's T^3 law, while at temperatures above 500 K, C_v tends to be constant, approaching the classical limit of Dulong-Petit's law. This indicates that all three XC functionals provide a reliable thermochemical properties prediction using DFPT. Nevertheless, the variation in C_v with different GGA-functionals is smaller both in standard conditions and high-temperature. Interestingly, the predicted C_v values by three GGA functionals at 300 K are identical ($\sim 99 \text{ J K}^{-1} \text{ mol}^{-1}$) for both hexagonal and cubic phases, however, contrary to the entropic values, the C_v values calculated by PBEsol overestimated the PBE values at high temperature for cubic phase, while the reverse trend is observed for RPBE functional. For example, at 2000 K, PBE calculates the C_v value $\sim 113 \text{ J K}^{-1} \text{ mol}^{-1}$, which is $3 \text{ J K}^{-1} \text{ mol}^{-1}$ less than PBEsol prediction but $2 \text{ J K}^{-1} \text{ mol}^{-1}$ more than RPBE. However, C_v values of hexagonal phase by three GGA functionals at 2000 K are similar ($\sim 122 \text{ J K}^{-1} \text{ mol}^{-1}$).

Relative molar enthalpies for BaMnO_3 are shown in Fig. 2.10(e, f). Similar to the predicted C_v values, all GGA functionals considered here predict consistent relative molar enthalpies values, particularly at low temperatures, as expected. For instance, at 300 K, the predicted $(H(T)-H(298 \text{ K}))$ values predicted using these GGA functionals differ by no more than $\sim 0.18 \text{ kJ mol}^{-1}$ for both hexagonal and cubic phases. At 2000 K, this value increases by only $\sim 8 \text{ kJ mol}^{-1}$ for the cubic phase, while remaining identical for the hexagonal phase. These results, therefore, suggest that the thermochemical properties of the BaMnO_3 hexagonal and cubic phase perovskite are effectively invariable to the choice of GGA functional used.

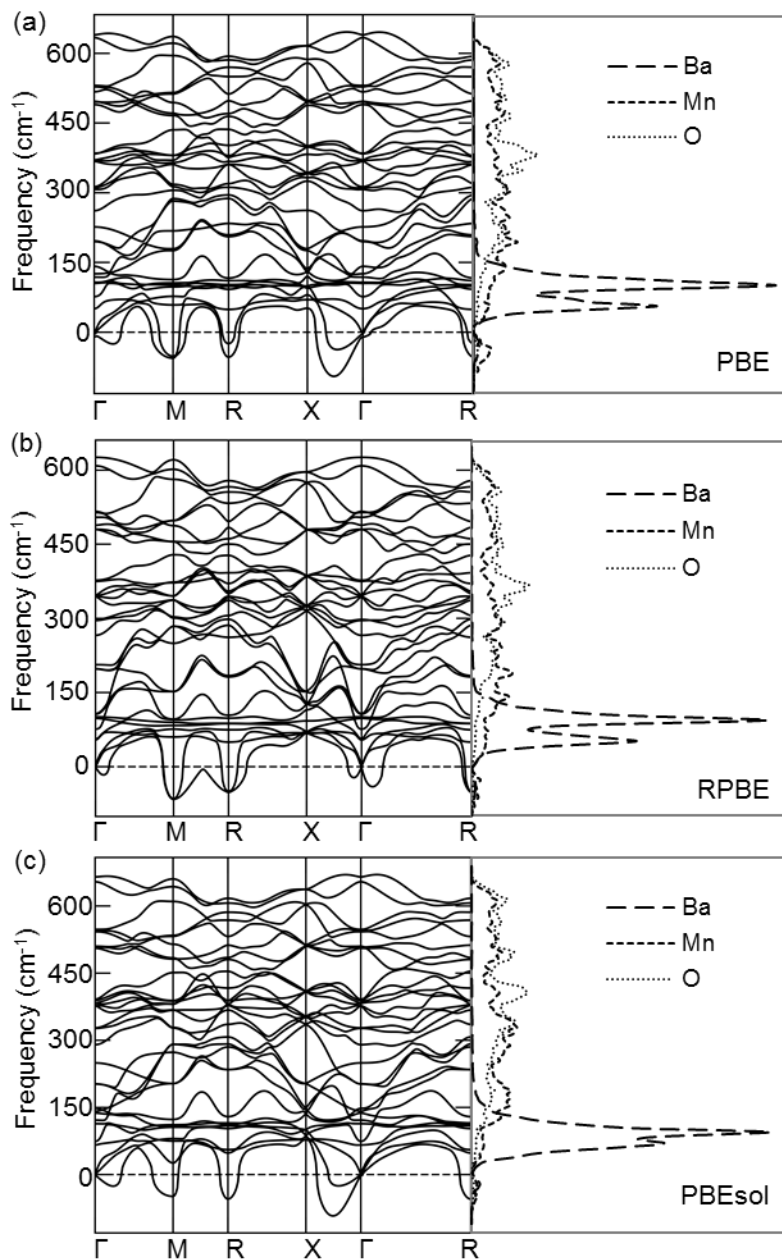


Fig. 2.11 The calculated phonon dispersions (left) and VDOS (right) of hexagonal ($P63/mmc$) BaMnO_3 using different GGA functionals: (a) PBE, (b) RPBE, (c) PBEsol.

The phonon dispersion curves of hexagonal ($P63/mmc$) and cubic ($Pm3m$) BaMnO_3 are shown along with the high symmetry directions Γ -M-R-X- Γ -R in the BZ shown in Fig. 2.11(left) and Fig. 2.12(left), respectively using PBE, RPBE and PBEsol functionals. In hexagonal BaMnO_3 , some

modes soften at M, R and between X and Γ points slightly, which can be attributed to the structural distortion of $P63/mmc$ at low temperature due to partial displacement of MnO_6 octahedra.^[76] The projected VDOS of hexagonal $BaMnO_3$ by all three GGA functionals show consistent vibrational contributions from Ba^{2+} , Mn^{4+} and O^{2-} ions. The lower frequency regimes of 0 – 200 cm^{-1} mostly dominated by Ba^{2+} ions, intermediate frequency regimes between 200 – 400 cm^{-1} associated with the vibrations of Mn^{4+} ions, and high energy level between 400 – 650 cm^{-1} mostly governed by the motion of O^{2-} ions. Noticeably, the phonon frequencies of Mn^{4+} and O^{2-} are observed both in intermediate and high energy levels due to the lower metallic masses of Mn^{4+} , compared to Zr^{4+} and Ce^{4+} discussed above.

In contrast, all three GGA functionals generate unstable phonon modes for cubic $BaMnO_3$ at the Γ , M and X points. This indicates that all three functionals predict the cubic phase of $BaMnO_3$ to be unstable, and this is consistent with a previous report.^[81] However, PBEsol shifts the phonon dispersion curves comparably to the higher energy level than two other functionals. For instance, the unstable phonon modes at Γ -point is observed at ~ -220 cm^{-1} for PBEsol (Fig. 2.12(c)), where at the same point PBE and RPBE functionals distribute the phonon bands to the lower the energy level nearby -260 cm^{-1} (Fig. 2.12(a)) and -300 cm^{-1} (Fig. 2.12(b)), respectively. This unstable mode corresponds to the axial vibration of Mn^{4+} within the MnO_3 octahedral sublattice, while O^{2-} remain largely static (Fig. 2.13(a)). Similar to the Γ -point, the negative phonon frequencies observed at the X-point by three functionals vary across energy range -200 to -300 cm^{-1} , where PBEsol shifts the phonon band to higher energy. This unstable mode arises from a symmetric O^{2-} stretch mode within the MnO_3 octahedral sublattice (Fig. 2.13(b)).

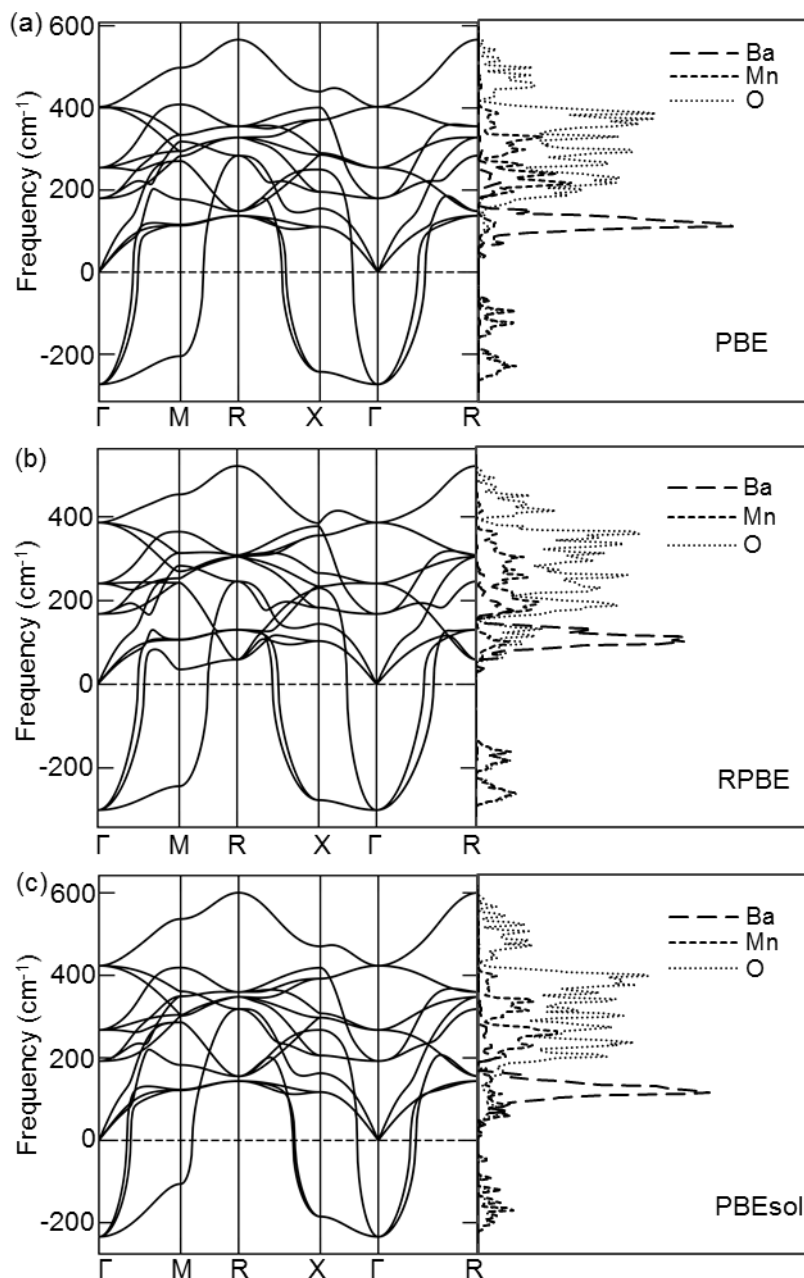


Fig. 2.12 The calculated phonon dispersions (left) and VDOS (right) of cubic ($Pm3m$) $BaMnO_3$ using different GGA functionals: (a) PBE, (b) RPBE, (c) PBEsol.

On the other hand, the negative phonon modes at M-point predicted by PBEsol are $\sim -100 \text{ cm}^{-1}$, while PBE and RPBE produce phonons down to -200 cm^{-1} and -250 cm^{-1} , respectively. This

negative frequency is governed by an antisymmetric breathing mode of the O^{2-} ions (Fig. 2.13(c)). The corresponding imaginary phonon modes of respective crystal structure were accounted in predicting their thermodynamic properties shown in Fig. 2.10. The corresponding VDOS of cubic $BaMnO_3$ obtained using the PBE, RPBE and PBEsol functionals are shown in Fig. 2.12(right). Overall, the low-frequency regime below 170 cm^{-1} is predominantly governed by the motions of heavier Ba^{2+} cations, as anticipated. Contrary, the vibrational motions of Mn^{4+} and O^{2-} correspond to the intermediate- and high-frequency regimes ($\sim 170\text{-}650\text{ cm}^{-1}$), respectively. Noticeably, PBEsol predicts slightly higher phonon energies for the O^{2-} modes ($\sim 600\text{ cm}^{-1}$), compared to both PBE ($\sim 550\text{ cm}^{-1}$) and RPBE (500 cm^{-1}).

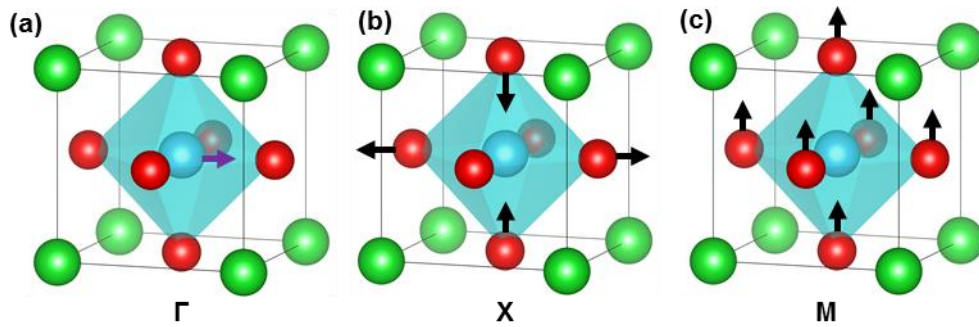


Fig. 2.13 Unstable phonon modes of cubic ($Pm3m$) $BaMnO_3$ associated with the vibrations at the q -points: (a) Γ -point, (b) X -point, and (c) M -point. Atom colors as per Fig. 2.2.

2.5 Conclusion

The choice of GGA-functionals in any DFT approximation is crucial in determining the accuracy of properties derived from the lattice structure of a material. The universal GGA functional, PBE, provides an accurate description of the phonon dispersion of cubic $BaZrO_3$, while PBE with Hubbard corrections (PBE+U/J) provides an accurate description of the orthorhombic,

rhombohedral and cubic BaCeO₃ respectively. The agreement between experimental and calculated thermochemical properties for these two perovskites are excellent. The calculated lattice parameters of hexagonal and cubic BaMnO₃ using PBE, RPBE and PBEsol are consistent with reported experimental data. In addition, the phonon dispersions and thermochemical properties of hexagonal and cubic BaMnO₃ predicted here for the first time using PBE, RPBE and PBEsol suggest that these properties are effectively invariant to the choice of GGA functional. In light of these results, the PBEsol functional, which is the solid-oriented revised version of PBE, is considered in subsequent chapters of this thesis to predict the electronic and thermochemical properties of perovskite materials.

2.6 References

1. Schrodinger E. An undulatory theory of the mechanics of atoms and molecules. *Physical Review*. 1926; 28(6)(1049–1070).
2. Szabo A, Ostlund NS. *Modern quantum chemistry: introduction to advanced electronic structure theory*: Courier Corporation; 2012.
3. Born M, Oppenheimer J. On the quantum theory of molecules. *Ann. Physik*. 1927; 84 (457).
4. Hartree DR, editor *The wave mechanics of an atom with a non-Coulomb central field. Part II. Some results and discussion*. *Mathematical Proceedings of the Cambridge Philosophical Society*; 1928; 24 (1): 111-132. Cambridge Univ Press.
5. Fock V. Näherungsmethode zur Lösung des quantenmechanischen Mehrkörperproblems. *Zeitschrift für Physik*. 1930 Jan 1;61(1-2):126-48.
6. Jensen F. *Introduction to Computational Chemistry*, chapter 4, pp. 184: Wiley; 2007.

7. Thomas LH. Proceedings of the Royal Society of London Series A, Containing Papers of a Mathematical and Physical Character 1927;114(768):561-76.
8. Dirac PA. Note on exchange phenomena in the Thomas atom. Mathematical Proceedings of the Cambridge Philosophical Society; 1930: Cambridge Univ Press.
9. Teller E. On the stability of molecules in the Thomas-Fermi theory. Reviews of Modern Physics. 1962;34(4):627.
10. Hohenberg P, Kohn W. Inhomogeneous electron gas. Physical Review. 1964;136(3B):B864.
11. Kohn W, Sham LJ. Self-consistent equations including exchange and correlation effects. Physical Review. 1965;140(4A):A1133.
12. Jones RO, Gunnarsson O. The density functional formalism, its applications and prospects. Reviews of Modern Physics. 1989;61(3):689.
13. Slater JC. The self-consistent field for molecules and solids: McGraw-Hill New York; 1974.
14. Von Barth U, Kumar V, Andersen O, Mookerjee A. Lectures on methods of electronic structure calculations. World Scientific, Singapore; 1994.
15. Vosko SH, Wilk L, Nusair M. Accurate spin-dependent electron liquid correlation energies for local spin density calculations: a critical analysis. Canadian Journal of Physics. 1980;58(8):1200-11.
16. Parr RG. Density functional theory of atoms and molecules. Horizons of Quantum Chemistry: Springer; 1980. p. 5-15.
17. Jensen F. Introduction to computational chemistry: John Wiley & Sons; 2016.

18. Lee JG. Computational materials science: an introduction, Second Edition, chapter 5: Density functional theory, pp. 156: CRC Press; 2017.
19. Perdew JP, Yue W. Accurate and simple density functional for the electronic exchange energy: Generalized gradient approximation. *Physical Review B*. 1986;33(12):8800.
20. Perdew JP, Wang Y. Accurate and simple analytic representation of the electron-gas correlation energy. *Physical Review B*. 1992;45(23):13244.
21. Perdew JP, Burke K, Ernzerhof M. Generalized gradient approximation made simple. *Physical Review Letters*. 1996;77(18):3865.
22. Hammer B, Hansen LB, Nørskov JK. Improved adsorption energetics within density-functional theory using revised Perdew-Burke-Ernzerhof functionals. *Physical Review B*. 1999;59(11):7413.
23. Perdew JP, Ruzsinszky A, Csonka GI, Vydrov OA, Scuseria GE, Constantin LA, et al. Restoring the density-gradient expansion for exchange in solids and surfaces. *Physical Review Letters*. 2008;100(13):136406.
24. Lee C, Yang W, Parr R. *Phys Rev A*. 1988;38:3098.
25. Becke AD. Density-functional thermochemistry. III. The role of exact exchange. *The Journal of Chemical Physics*. 1993;98(7):5648-52.
26. Stephens PJ, Devlin FJ, Chabalowski CF, Frisch MJ. Ab initio calculation of vibrational absorption and circular dichroism spectra using density functional force fields. *The Journal of Physical Chemistry*. 1994 Nov;98(45):11623-7.
27. Becke AD. Density-functional exchange-energy approximation with correct asymptotic behavior. *Physical Review A*. 1988;38(6):3098.

28. Tsuzuki S, Lüthi HP. Interaction energies of van der Waals and hydrogen bonded systems calculated using density functional theory: Assessing the PW91 model. *The Journal of Chemical Physics*. 2001;114(9):3949-57.
29. Wesolowski TA, Parisel O, Ellinger Y, Weber J. Comparative Study of Benzene $\odot\odot\odot$ X (X= O₂, N₂, CO) Complexes Using Density Functional Theory: The Importance of an Accurate Exchange– Correlation Energy Density at High Reduced Density Gradients. *The Journal of Physical Chemistry A*. 1997;101(42):7818-25.
30. Lee JG. *Computational materials science: an introduction*, Second Edition, chapter 5: Density functional theory, pp. 158: CRC Press; 2017.
31. Zhao Y, Truhlar DG. Construction of a generalized gradient approximation by restoring the density-gradient expansion and enforcing a tight Lieb–Oxford bound. *The Journal of Chemical Physics*. 2008;128(18):184109.
32. Staroverov VN, Scuseria GE, Tao J, Perdew JP. Tests of a ladder of density functionals for bulk solids and surfaces. *Physical Review B*. 2004;69(7):075102.
33. Lieb EH, Oxford S. Improved lower bound on the indirect Coulomb energy. *International Journal of Quantum Chemistry*. 1981;19(3):427-39.
34. Sousa SF, Fernandes PA, Ramos MJ. General performance of density functionals. *The Journal of Physical Chemistry A*. 2007;111(42):10439-52.
35. Redfern PC, Zapol P, Curtiss LA, Raghavachari K. Assessment of Gaussian-3 and density functional theories for enthalpies of formation of C1– C16 alkanes. *The Journal of Physical Chemistry A*. 2000;104(24):5850-4.

36. Grimme S. Accurate calculation of the heats of formation for large main group compounds with spin-component scaled MP2 methods. *The Journal of Physical Chemistry A*. 2005;109(13):3067-77.
37. Mori-Sánchez P, Cohen AJ, Yang W. Many-electron self-interaction error in approximate density functionals. *American Institute of Physics*; 2006.
38. Kulik HJ. Perspective: Treating electron over-delocalization with the DFT+U method. *The Journal of Chemical Physics*. 2015;142(24):240901.
39. Cramer CJ, Truhlar DG. Density functional theory for transition metals and transition metal chemistry. *Physical Chemistry Chemical Physics*. 2009;11(46):10757-816.
40. Tran F, Blaha P, Schwarz K, Novák P. Hybrid exchange-correlation energy functionals for strongly correlated electrons: Applications to transition-metal monoxides. *Physical Review B*. 2006;74(15):155108.
41. Russo TV, Martin RL, Hay PJ. Density functional calculations on first-row transition metals. *The Journal of Chemical Physics*. 1994;101(9):7729-37.
42. Wang L, Maxisch T, Ceder G. Oxidation energies of transition metal oxides within the GGA+U framework. *Physical Review B*. 2006;73(19):195107.
43. Korhonen T, Puska MJ, Nieminen RM. Vacancy-formation energies for fcc and bcc transition metals. *Physical Review B*. 1995;51(15):9526.
44. Lutfalla S, Shapovalov V, Bell AT. Calibration of the DFT/GGA+U method for determination of reduction energies for transition and rare earth metal oxides of Ti, V, Mo, and Ce. *Journal of Chemical Theory and Computation*. 2011;7(7):2218-23.
45. Verma P, Truhlar DG. Does DFT+U mimic hybrid density functionals? *Theoretical Chemistry Accounts*. 2016;135(8):182.

46. Liechtenstein A, Anisimov V, Zaanen J. Density-functional theory and strong interactions: Orbital ordering in Mott-Hubbard insulators. *Physical Review B*. 1995;52(8):R5467.
47. Dudarev S, Botton G, Savrasov S, Humphreys C, Sutton A. Electron-energy-loss spectra and the structural stability of nickel oxide: An LSDA+U study. *Physical Review B*. 1998;57(3):1505.
48. Kresse G, Furthmüller J. Vienna ab-initio simulation package (VASP). Institut für Materialphysik, Vienna. 2004.
49. Arroyo-de Dompablo M, Morales-García A, Taravillo M. DFT+U calculations of crystal lattice, electronic structure, and phase stability under pressure of TiO₂ polymorphs. *The Journal of Chemical Physics*. 2011;135(5):054503.
50. Hamann D, Schlüter M, Chiang C. Norm-conserving pseudopotentials. *Physical Review Letters*. 1979;43(20):1494.
51. Lee JG. *Computational materials science: an introduction*, Second Edition, chapter 6: Treating Solids, pp. 177: CRC Press; 2016.
52. Lee JG. *Computational materials science: an introduction*: CRC Press; 2016.
53. Alfe D, De Wijs GA, Kresse G, Gillan MJ. Recent developments in ab initio thermodynamics. *International Journal of Quantum Chemistry*. 2000;77(5):871-9.
54. Huang LF, Lu XZ, Tennesen E, Rondinelli JM. An efficient ab-initio quasiharmonic approach for the thermodynamics of solids. *Comp Mater Sci*. 2016;120:84-93.
55. Xiang SK, Xi F, Bi Y, Xu J, Geng HY, Cai LC, et al. Ab initio thermodynamics beyond the quasiharmonic approximation: W as a prototype. *Physical Review B*. 2010;81(1).
56. Zhang W, Smith JR, Wang XG. Thermodynamics from ab initio computations. *Physical Review B*. 2004;70(2).

57. Chester GV, Houghton A. Electron-phonon interaction in metals i: The harmonic approximation. *Proceedings of the Physical Society*. 1959 Apr 1;73(4):609.
58. Patterson CW. Corrections to the Born-Oppenheimer approximation for a harmonic-oscillator. *Physical Review A*. 1993;47(2):879-83.
59. Ziman JM. *Electrons and phonons: the theory of transport phenomena in solids*: Oxford University Press; 1960.
60. Dove MT. *Introduction to lattice dynamics*: Cambridge University Press; 1993.
61. Ghatak AK, Kothari LS. *An introduction to lattice dynamics*: Addison-Wesley London; 1972.
62. Srivastava GP. *The physics of phonons*: CRC Press; 1990.
63. Chaput L, Togo A, Tanaka I, Hug G. Phonon-phonon interactions in transition metals. *Physical Review B*. 2011;84(9):094302.
64. Togo A, Chaput L, Tanaka I. Distributions of phonon lifetimes in Brillouin zones. *Physical Review B*. 2015;91(9):094306.
65. Nie Y, Xie Y. Ab initio thermodynamics of the hcp metals Mg, Ti, and Zr. *Physical Review B*. 2007;75(17):174117.
66. Wang H-Y, Xu H, Huang T-T, Deng C-S. Thermodynamics of wurtzite GaN from first-principle calculation. *The European Physical Journal B*. 2008;62(1):39-43.
67. He Q, Yan ZT. Study of temperature dependence of bulk modulus and interatomic separation for ionic solids. *Physica Status Solidi (b)*. 2001;223(3):767-71.
68. Ahrens M, Maier J. Thermodynamic properties of BaCeO₃ and BaZrO₃ at low temperatures. *Thermochimica Acta*. 2006;443(2):189-96.

69. Cordfunke E, Konings R. Enthalpy increments of barium zirconate, BaZrO₃, and an assessment of its thermochemical properties. *Thermochimica Acta*. 1989;156(1):45-51.
70. Scholten M, Schoonman J, Van Miltenburg J, Cordfunke E. The thermodynamic properties of BaCeO₃ at temperatures from 5 to 940 K. *Thermochimica Acta*. 1995;268:161-8.
71. Basbus JF, Caneiro A, Suescun L, Lamas DG, Mogni LV. Anomalous X-ray diffraction study of Pr-substituted BaCeO_{3-δ}. *Acta Crystallographica Section B: Structural Science, Crystal Engineering and Materials*. 2015;71(4):455-62.
72. Knight K. Structural phase transitions, oxygen vacancy ordering and protonation in doped BaCeO₃: results from time-of-flight neutron powder diffraction investigations. *Solid State Ionics*. 2001;145(1-4):275-94.
73. Genet F, Loridant S, Ritter C, Lucazeau G. Phase transitions in BaCeO₃: neutron diffraction and Raman studies. *Journal of Physics and Chemistry of Solids*. 1999;60(12):2009-21.
74. Knight K. Structural phase transitions in BaCeO₃. *Solid State Ionics*. 1994;74(3-4):109-17.
75. Levin I, Amos TG, Bell SM, Farber L, Vanderah TA, Roth RS, et al. Phase equilibria, crystal structures, and dielectric anomaly in the BaZrO₃-CaZrO₃ system. *Journal of Solid State Chemistry*. 2003;175(2):170-81.
76. Cussen EJ, Battle PD. Crystal and magnetic structures of 2H BaMnO₃. *Chemistry of Materials*. 2000;12(p831-p838).
77. Li N, Yao K, Gao G, Zhu L, Wu Y. Surface properties of the (001) surface of cubic BaMnO₃: A density functional theory study. *Journal of Applied Physics*. 2010;107(12):123704.
78. Søndena R, Stølen S, Ravindran P, Grande T, Allan NL. Corner-versus face-sharing octahedra in AMnO₃ perovskites (A= Ca, Sr, and Ba). *Physical Review B*. 2007;75(18):184105.

79. Gökoğlu G, Yıldırım H. Electronic structure and surface properties of cubic perovskite oxide BaMnO₃. *Comp Mater Sci.* 2011;50(3):1212-6.
80. Ezbiri M, Allen KM, Gálvez ME, Michalsky R, Steinfeld A. Design principles of perovskites for thermochemical oxygen separation-Supporting Information. *ChemSusChem.* 2015;8(11):1966-71.
81. Rondinelli JM, Eidelson AS, Spaldin NA. Non-d⁰ Mn-driven ferroelectricity in antiferromagnetic BaMnO₃. *Physical Review B.* 2009;79(20):205119.
82. Blöchl P. Projector augmented-wave method. *Phys Rev B.* 1994;50(24):17953-79.
83. Shishkin M, Ziegler T. Structural, electronic, stability and reduction properties of perovskite surfaces: The case of rhombohedral BaCeO₃. *Surface Science.* 2012;606(13-14):1078-87.
84. Bennett JW, Grinberg I, Davies PK, Rappe AM. Pb-free semiconductor ferroelectrics: A theoretical study of Pd-substituted Ba(Ti_{1-x}Ce_x)O₃ solid solutions. *Physical Review B.* 2010;82(18):184106.
85. Polfus JM, Pishahang M, Bredeisen R. Influence of Ce³⁺ polarons on grain boundary space-charge in proton conducting Y-doped BaCeO₃. *Physical Chemistry Chemical Physics.* 2018;20(23):16209-15.
86. Methfessel MP, Paxton AT. High-precision sampling for Brillouin-zone integration in metals. *Physical Review B.* 1989;40(6):3616.
87. Birch F. Finite elastic strain of cubic crystals. *Physical Review.* 1947;71(11):809.
88. Giannozzi P, Gironcoli S, Pavone P, Baroni S. Ab initio calculation of phonon dispersions in semiconductors. *Physical Review B.* 1991;43(9):7231.

89. Gonze X, Lee C. Dynamical matrices, Born effective charges, dielectric permittivity tensors, and interatomic force constants from density-functional perturbation theory. *Physical Review B*. 1997;55(16):10355.
90. Togo A, Tanaka I. First principles phonon calculations in materials science. *Scripta Materialia*. 2015;108:1-5.
91. Levin I, Amos TG, Bell SM, Farber L, Vanderah TA, Roth RS, et al. Phase equilibria, crystal structures, and dielectric anomaly in the BaZrO₃–CaZrO₃ system. *Journal of Solid State Chemistry*. 2003;175(2):170-81.
92. Bjorheim TS, Arrigoni M, Gryaznov D, Kotomin E, Maier J. Thermodynamic properties of neutral and charged oxygen vacancies in BaZrO₃ based on first principles phonon calculations. *Physical Chemistry Chemical Physics*. 2015;17(32):20765-74.
93. Kang SG, Sholl DS. First principles assessment of perovskite dopants for proton conductors with chemical stability and high conductivity. *RSC Advances*. 2013;3(10):3333-41.

Chapter 3: Trends in High-Temperature Reduction Thermochemistry of BaMO₃ (M = Ti – Cu): Effects of B-site Cation

3.1 Introduction

ABO₃ perovskites with mixed oxidation states are attractive candidates for high-temperature heterogeneous catalytic applications due to their tunable geometric and electronic structures, high thermal and chemical stabilities, and low costs. Alkaline-earth and rare-earth metals ABO₃ perovskites are widely used in energy applications such as MIEC,^[1] anode and cathode materials in SOFC,^[2] high-temperature gas sensors,^[3] membrane separation,^[4] hydrocarbon oxidation,^[5] and solar thermochemical fuel production.^[6-8] All of these energy applications critically depend on the formation of oxygen vacancies and the mobility of vacancies during redox reaction under various reaction conditions. In all of these cases, the perovskite metal oxide is subjected to high-temperatures and low oxygen partial pressures to create oxygen vacancies in the material,^[9]



where O_O^\times , $\text{V}_\text{O}^{\bullet\bullet}$, e^- represent a lattice site oxide ion, a lattice site oxygen vacancy and an electron respectively (using Kröger-Vink notation). The combination of these terms can be considered as an effective quasi-chemical particle $\text{O}_2^{\text{oxide}}$, i.e. the effective oxygen molecule in the oxide.^[9] The presence of oxygen vacancies creates non-stoichiometric defects in the crystal lattice, i.e. a non-stoichiometric oxide $\text{ABO}_{3-\delta}$ is produced. Obtaining the thermochemical properties of $\text{ABO}_{3-\delta}$ perovskite materials as a function of temperature is key for evaluating their potential in oxygen deficiency applications.

A-site alkaline-earth or rare-earth metal cations, such as Ca^{2+} , Sr^{2+} , Ba^{2+} , or La^{3+} , Ce^{3+} , Nd^{3+} , Sm^{3+} and B-site cations from 3d, 4d, 5d transition metal are of technical interest due to their mixed-

valence charge states, which significantly affect the chemical and thermal stability of ABO_3 perovskites. For instance, the incorporation of the larger Ba^{2+} cation in the A-site in cubic ABO_3 promotes oxygen vacancy formation and migration by distorting the crystal structure.^[10] Introduction of oxygen vacancies in $\text{Ba}^{2+}\text{M}^{4+}\text{O}_3^{2-}$ induces facile electron transfer from the defect site into the $\text{M}^{4+} 3d^n$ subshell, thereby reducing the B-site cation.^[11]

Commonly these effects are predicted via the vacancy formation energy of the compound. The formation energies of defect-free ABO_3 perovskites with Ba, Ca, Sr, Y and La metals at the A site, and 3d transition metals (Ti – Cu) at the B site were studied by Calle-Vallejo et al.^[12] Their results reveal that the formation energies of perfect ABO_3 perovskites are linearly correlated to the atomic number of their B-site cation. The stabilities of these perovskites decreased more slowly along with the 3d series from Ti to Cu. Additionally, for a given B-site element the formation energies in each group of investigated metal perovskites remained near-independent of A (if there is an identical oxidation state in the A-site cation), such as the calculated formation energies of SrCoO_3 , CaCoO_3 , BaCoO_3 . Whether these qualitative trends in the structural stability of perfect perovskites hold for oxygen-deficient perovskites, remained an open question. In this context, Li et al.^[13] studied La-based perovskites (LaMO_3 , $\text{M} = \text{Sc} - \text{Cu}$) and found that, except for LaFeO_3 , the oxygen vacancy formation energy becomes less positive on moving from LaScO_3 to LaCuO_3 , indicating increased reducibility along B-site 3d metal cations Sc – Cu. LaFeO_3 proved to be an exception here, by virtue of the stability of the d^5 configuration obtained upon reduction of Fe^{3+} , which is less than that for a Mn^{3+} B-site cation. However, the extension of these trends to other families of perovskites have not yet been explored.

Ezbiri et al.^[14] studied the effect of the B-site and A-site bonds with oxygen, to investigate the free oxygen vacancy formation energy of 12 perovskites (A = Sr, Ba, La; and B = Mn, Co, Ni, Cu). They found that the more negative oxygen vacancies formation energy was attributed to the large transition metal-oxygen bond length (e.g. the bond length of Co-O in BaCoO_{3-δ} is 2.078 Å, where the Mn-O length in BaMnO_{3-δ} is 2.061 Å), which enables the formation of relatively stable oxygen vacancies. The vacancy formation energy was additionally correlated with the charge transfer from the O-2p orbitals to the 3d orbitals of the B-site cation. Specifically, the lower gap between these states in BaCoO_{3-δ}, compared to other perovskites such as BaMnO_{3-δ}, yields higher O₂ exchange capacity.

Although a significant number of oxygen-deficient BaMO_{3-δ} have been studied, so far no systematic theoretical work has been reported regarding trends in defect thermochemistry of BaMO_{3-δ} for 3d B-site metal cations. In the present Chapter, the trends in temperature-dependent reduction free energy of BaMO₃ (M = Ti – Cu) upon oxygen vacancy formation are presented with and without thermal corrections for single neutral oxygen defect for temperatures between 0 – 2000 K. Defect thermochemistry is characterized by phonon and electronic structure analysis. Reducibility of BaMO_{3-δ} shows a linear relation with respect to the atomic number of B-site transition metals under standard conditions. However, predicted reduction free energies at elevated temperatures exhibit significant deviations from this expected trend, due to the variation in the entropic contribution from the B-site cation to the total free energy. We elucidate the physical origins of these deviations via a phonon mode analysis and demonstrate that the inclusion of explicit thermochemical corrections is critical for high-temperature properties in these materials to be modelled accurately.

3.2 Computational Methods

3.2.1 Electronic Structure Methods

Spin-polarized DFT calculations were performed using VASP^[15] The PBEsol^[16] GGA-functional was employed with PAW-PP^[17] for BaMO₃ (M = Ti – Cu). The BZ of the unit cells were sampled using a 4×4×4 Monkhorst-Pack k-point scheme. A plane-wave basis set was used with a 500 eV cut-off criterion, and the total DFT energy was fully optimized with respect to ionic position, cell shape and cell volume, using a convergence criterion 1.0 x 10⁻⁸ eV. This method gives a very accurate total energy calculation.^[15] Electron smearing (0.4 eV) was employed using the Methfessel-Paxton scheme in order to alleviate SCF convergence issues.^[18] For pure elemental solids, the elemental ground-state structures are chosen from OQMD^[19] and energy calculations were carried out with identical set up of energy cut-off (520 eV), Gaussian smearing (0.2 eV), and Γ -centered k-points meshes with similar number of k-points per reciprocal atom. However, the electron exchange and correlation are described in the PBEsol^[16] GGA-functional with PAW-PP^[17] instead of PBE with Hubbard corrections as reliable U/J corrections are lacking in literature.^[19] The structural optimisations were performed by volume, cell shape and ionic relaxations using a convergence criterion 1.0 x 10⁻⁴ eV/atom

3.2.2 Model Cubic BaMO₃ Structures

BaMO₃ (M = Ti – Cu) is assumed to have an ideal cubic structure (space group *Pm-3m* (221)) for all results in this Chapter. The volume of each BaMO₃ unit cell was determined by fitting of total ground state energies versus molar volume curves using the BM EOS.^[20] To obtain the lowest energy geometry, additional cell shape and ionic relaxation were carried out, so that a full minimization of the internal structural degrees of freedom is given to the atoms. Optimized lattice

parameters were obtained after minimizing the stress tensor, and relaxing ionic position and cell shape at constant volume. Table 3.1 lists the calculated lattice constants with a comparison to available experimental data. The optimized lattice parameters of BaMO₃ (M = Ti – Cu) are between 3.90 to 3.99 Å. On average, the deviation between the lattice constants of BaMO₃ (M = Ti – Cu) using PBEsol functional and experimental values are less than 1%.

Table 3.1 Comparison of PBEsol-PAW and experimental lattice parameter (a/Å) of cubic BaMO₃.

(a/Å)	BaTiO ₃	BaVO ₃	BaCrO ₃	BaMnO ₃	BaFeO ₃	BaCoO ₃	BaNiO ₃	BaCuO ₃
PBEsol-PAW	3.99	3.92	3.90	3.91	3.92	3.90	3.90	3.96
Exp.	4.0 ^[21]	3.94 ^[22]	-	-	3.97 ^[23]	-	-	-

3.2.3 First-Principles Thermochemical Properties of Cubic BaMO₃ (M = Ti – Cu)

Thermochemical properties including the temperature-dependent internal energy (E), Helmholtz free energy (A), heat capacity at constant pressure (C_p) and entropy (S), were calculated using DFPT,^[24] as described in equations (2.54 – 2.58). A 2×2×2 extension of the crystallographic BaMO₃ unit cell (40 atoms) was used for all reported thermochemical properties with the number of k points reduced accordingly (see Fig. 3.1(a)). This supercell represents an ideal balance between computational efficiency and thermodynamic accuracy, as demonstrated in previous investigations^[25] showing oxygen vacancy formation energy to be converged within this supercell size. The real-space force constants of the crystallographic supercells were calculated using DFPT^[24] as implemented in VASP,^[15] using forces on atoms calculated via finite differences

(atomic displacements of 0.01 Å).^[24, 26] Phonon modes were then calculated with a Monkhorst-Pack^[27] grid of $48 \times 48 \times 48$ q points for the phonon wave vectors, using Phonopy.^[28]

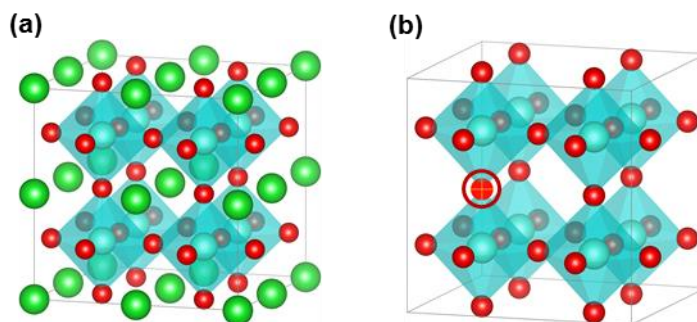


Fig. 3.1 $2 \times 2 \times 2$ supercells of (a) BaMO_3 , (b) $\text{BaMO}_{2.875}$. The green, cyan and red balls represent Ba, M and O atoms, respectively. Aqua surfaces indicate MO_3 octahedra and the red circle represents position of oxygen vacancy defect in (b). (b) omit Ba for clarity.

3.2.4 Reduction Thermochemistry of Cubic $\text{BaMO}_{3-\delta}$ ($\text{M} = \text{Ti} - \text{Cu}$)

The reduction free energies of $\text{BaMO}_{3-\delta}$ were calculated here in the manner of Deml et al.^[29] and Ezbiri et al.^[14] Single neutral oxygen vacancy was created by randomly removing one oxygen atom to afford δ values of 0.125 (i.e. 1 oxygen vacancies in the $2 \times 2 \times 2$ supercell), see Fig. 3.1(b). A number of prior reports have demonstrated that neutral oxygen vacancies, with two trapped electrons, are favored in undoped oxides under reducing conditions.^[30-33] Therefore, this investigation is limited to the formation of neutral oxygen vacancies, since the stoichiometry of the perovskite reduction reaction (equation (3.1)) requires the formation of O_2 from two neutral oxygen atoms. Here, the structures of $\text{BaMO}_{3-\delta}$ were fully optimized with cubic symmetry and under constant volume conditions, in the manner of Deml et al.^[29] and Sundell et al.^[25]

The chemical potential of BaMO_3 and $\text{BaMO}_{3-\delta}$ can be derived from DFT via,^[34]

$$\mu(T, p) = E^{DFT} + E^{ZPE} + \int_0^T C_p dT + pV - T(S^{\text{vib}}(T) - S_c) \quad (3.2)$$

where E^{DFT} is the total DFT electronic energy for the crystalline supercell with volume V , and E^{ZPE} is the DFT zero-point vibrational energy correction. The enthalpic and entropic contributions to the chemical potential (the third and fifth term, respectively) were calculated via DFPT equation (2.58) and equation (2.57) respectively. The last term S_c in equation (3.2), is the configurational entropy calculated via the standard combinatorial approximation,^[35, 36]

$$S_c = k_B \ln \left[\frac{N!}{P!(N-P)!} \right] \quad (3.3)$$

where N is the number of oxygen atoms in the BaMO₃ supercell, and P is the number of vacancy defects. The chemical potential for O₂ ($\mu(T, p_{O_2})$), is defined as,^[34]

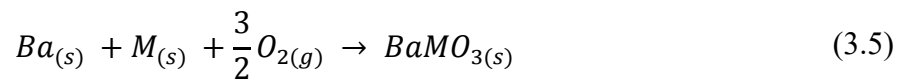
$$\mu(T, p_{O_2}) = E_i^{DFT} + E_i^{ZPE} + [H_i^\theta - H_i^0] + \int_0^T C_p dT + RT \ln(p/p_i^\theta) - TS(T, p_i^\theta) \quad (3.4)$$

The oxygen chemical potential was taken from Ref.^[37] as the total electronic energy (E^{DFT}) due to well-known issues regarding plane-wave DFT's treatment of the O₂ triplet ground state.^[38] Thermochemical corrections were taken from NIST-JANAF thermochemical tables at the specified conditions.^[39]

3.3 Results and Discussion

3.3.1 Trends in Formation Energies of Cubic BaMO₃

The chemical reaction of formation of BaMO₃ from their elementary components can be defined as,



where Ba and M atoms are in their standard solid reference states and O₂ is in the gas phase under standard conditions. The standard formation energy of BaMO₃ can be computed from the Gibbs free energy of reaction of equation (3.5),

$$\Delta G_f^0 = G_{BaMO_3}^0 - G_{Ba}^0 - G_M^0 - \frac{3}{2}G_{O_2}^0 \quad (3.6)$$

where G^0 is the standard Gibbs free energy of the substances involved in the reaction and is expressed as,

$$G^0 = E^{DFT} + ZPE - TS^0 \quad (3.7)$$

where E^{DFT} is the total energy obtained from the DFT calculations, ZPE is the zero-point energy estimated from vibration analyses, and TS^0 is the product of temperature and entropy at T=298.15 K. In case of O₂, the FERF^[40] energy was taken as the total electronic energy (E^{DFT}) due to well-known issues regarding plane-wave DFT's treatment of the O₂ triplet ground state.^[38]

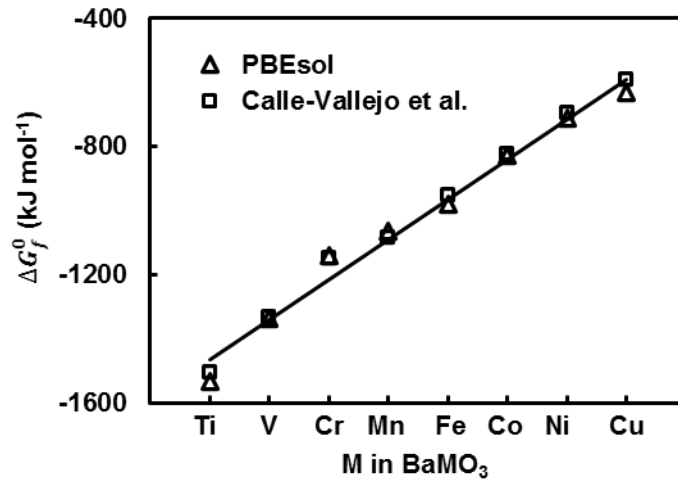


Fig. 3.2 Trends in the calculated PBEsol-PAW ΔG_f^0 values of BaMO₃ (M = Ti – Cu) at standard conditions ($p^\circ = 1$ atm, $T = 298$ K). The ΔG_f^0 values obtained by PBEsol-PAW are compared with the RPBE-USPP values at 0 K, reported by Calle-Vallejo et al.^[12].

Fig. 3.2 shows the calculated formation energies of cubic BaMO₃ (M = Ti – Cu) by PBEsol at standard conditions and compared with the reported literature data reported by Calle-Vallejo et al.^[12] who used the RPBE^[41] GGA-XC functional. Despite neglecting entropic and ZPE contribution to G^0 , formation energies reported by Calle-Vallejo et al.^[12] differ from values reported here by less than ~15 kJ mol⁻¹. The formation energies of cubic BaMO₃ exhibit a linear relationship with the atomic number of B-site cation, indicating that the structural stability of this series of compounds decreases gradually from BaTiO₃ to BaCuO₃. The origin of this linear relationship is attributed to the strength of the metal-oxygen (M–O) binding energy, which in turn is the product of the increase in energy separating the O 2p orbitals and the M d-band center moving from Ti to Cu.^[42]

3.3.2 Reduction Thermochemistry of Cubic BaMO_{3-δ} at 0 K

3.3.2.1 Oxygen Vacancy Formation Energies

The reduction thermochemistry of a perovskite depends critically on the formation and diffusion of oxygen vacancies in the material bulk. Ultimately both factors are related to the strength of the M–O bonds. The formation energy of a neutral oxygen vacancy (E_v) of BaMO_{3-δ} can be defined as,

$$E_v = E_{defect} - E_{pristine} + \mu_O^{FERE} \quad (3.8)$$

where E_{defect} , $E_{pristine}$ and μ_O^{FERE} are, respectively, the optimized 0 K DFT energy of the defective and pristine BaMO_{3-δ} supercell structures, and the chemical potential of oxygen-derived from FERRE.^[40] This approximation assumes that thermal corrections to E_{defect} and $E_{pristine}$ effectively cancel, and so does not include them explicitly, enabling high-throughput approaches to

identifying new perovskite materials for energy applications.^[29] An additional implicit assumption in equation (3.8) is that vacancy defect formation is thermodynamically, and not kinetically, controlled. For a single defect, E_v is calculated here at 0 K and reported in Fig. 3.3 and shows a linear correlation on moving from $\text{BaTiO}_{3-\delta}$ to $\text{BaCuO}_{3-\delta}$. For the first two $\text{BaMO}_{3-\delta}$ perovskites ($M = \text{Ti}, \text{V}$) in this series, the calculated E_v values are fairly high ($>430 \text{ kJ mol}^{-1}$), meaning that these two perovskites are quite difficult to reduce. BaCrO_3 has moderate E_v value of 330 kJ mol^{-1} , whereas the remaining three perovskites in this series, $\text{BaMO}_{3-\delta}$ ($M = \text{Mn}, \text{Fe}, \text{Co}$) are below 150 kJ mol^{-1} . The last two $\text{BaMO}_{3-\delta}$ perovskites ($M = \text{Cu}, \text{Ni}$) prefer to undergo reduction, indicating that even in the absence of explicit temperature corrections, these materials are intrinsically unstable in the cubic phase.

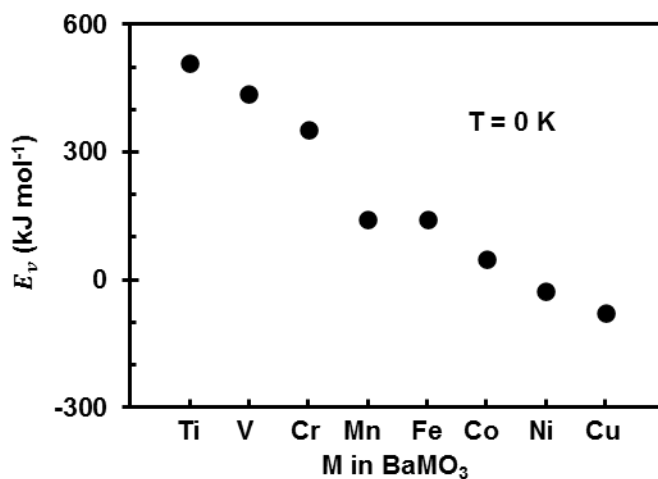


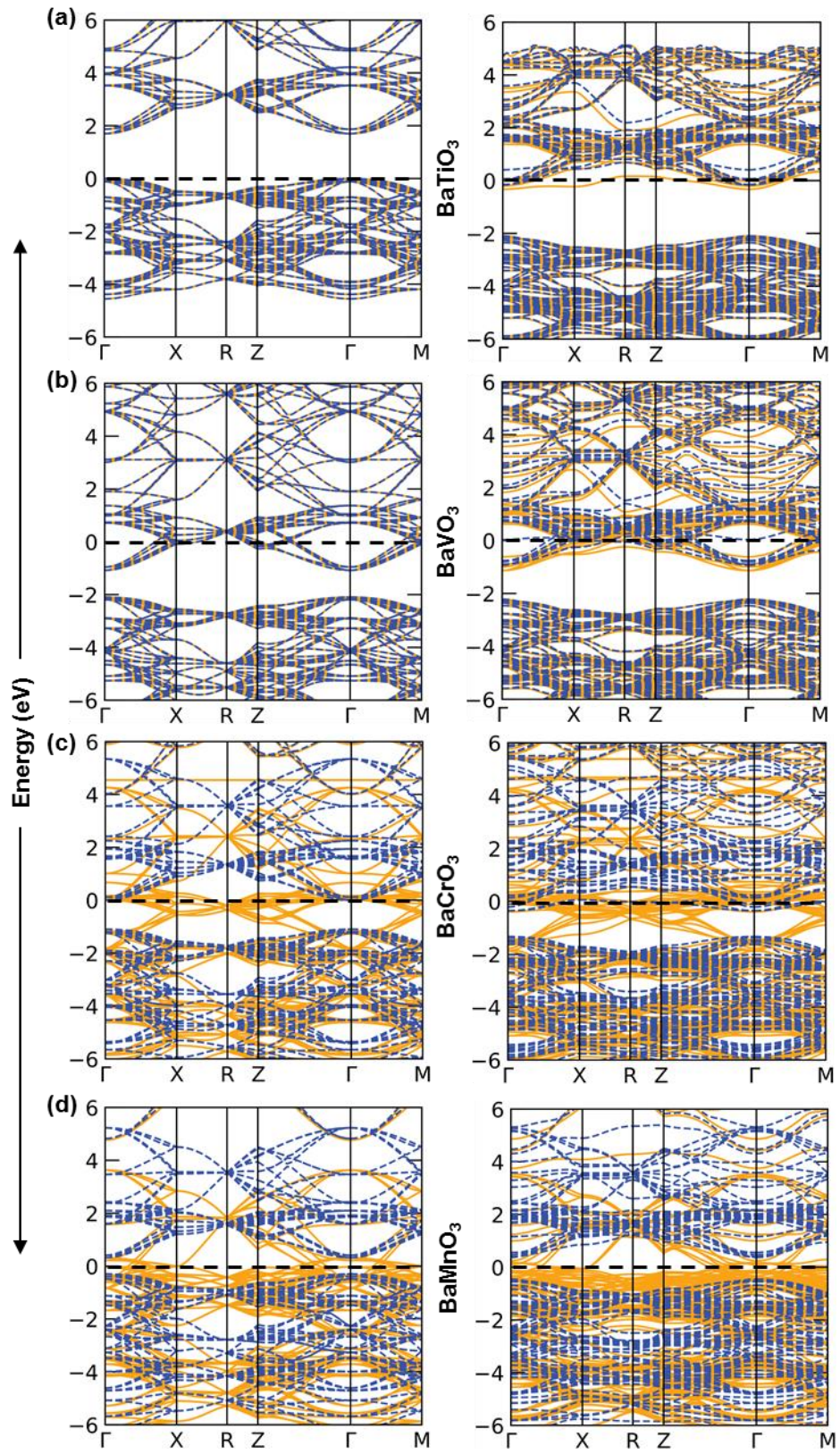
Fig. 3.3 Calculated PBEsol-PAW E_v values (kJ mol^{-1} , per single oxygen defect) of $\text{BaMO}_{3-\delta}$ ($M = \text{Ti} - \text{Cu}$).

3.3.2.2 Electronic Structures Analysis: Effect of Oxygen Vacancy and B-site Cation

We now consider analyzing the trends observed in oxygen vacancy formation energy of $\text{BaMO}_{3-\delta}$ perovskites from the electronic structure of view. In order to do electronic structure analysis, the electronic BS have to be investigated together with the corresponding partial density of states (PDOS) of $\text{BaMO}_{3-\delta}$ perovskites. Effective Bader charges analysis was done with the illustration of charge density distribution to depict the localization of vacancy site electrons to the nearby cations in $\text{BaMO}_{3-\delta}$ lattices.

The change of electronic band states upon vacancy formation, the electronic BS of pristine- and defect- $\text{BaMO}_{3-\delta}$ ($M = \text{Ti} - \text{Cu}$) are illustrated along with high symmetry directions (Γ -X-M- Γ -R-M- Γ) in the BZ in Fig. 3.4(a-h). Fig. 3.4 shows that, generally, the position of E_F gradually shifts from the bottom of the conduction band to the upper level with respect to the increasing d-electron at B-site cation moving across BaTiO_3 to BaCuO_3 . The figure shows that the pristine and defective perovskites considered here become increasingly metallic from left to right in this series. This indicates a progressive weakening of the M-O bond across the series, which in turn enhances the reduction of M^{4+} cation in the presence of a neutral vacancy defect. This observation was well established by several other studies.^[43, 44] Further, for B-site cations closer to the middle of the series, BaMO_3 are increasingly ferromagnetic. In pristine- BaTiO_3 (Fig. 3.4(a)), Ti^{4+} has a d^0 configuration, and so the material is an insulator, in accordance with experimental observations.^[45, 46] Fig. 3.4(a) shows a direct bandgap at Γ for both spin-up and -down channels. However, the presence of a single neutral oxygen vacancy in $\text{BaTiO}_{2.875}$ supercell (Fig. 3.4(a (right))) leads to the new fully occupied band below the conduction band minimum in pristine- BaTiO_3 and shifts the Fermi level (E_F) from the top of the valence band in BaTiO_3 to the bottom of the conduction band in $\text{BaTiO}_{2.875}$. Reduction of the supercell, therefore, provides electrons into the conduction band

through the spin-up channel, inducing n-type conductivity. This transition of $\text{BaTiO}_{3-\delta}$ from insulating to metallic behavior through oxygen vacancy formation has been discussed previously.^[47] Pristine- BaVO_3 (Fig. 3.4(b (left))), for which V^{4+} is found in a d^1 configuration is metallic using the selected level of theory, which is consistent with experimental observations.^[22] In the defect structure (Fig. 3.4(b (right))), E_F shifts slightly upward which reduce the bandgap for both spin-up and spin-down bands. Similar to $\text{BaTiO}_{2.875}$, there exists a direct bandgap at Γ -points in both pristine and defect structure of $\text{BaVO}_{3-\delta}$, and the spin-up bands dominate below the Fermi level in defect structure. However, $\text{BaVO}_{2.875}$ shows a slight half-metallic character. In BaCrO_3 , (Fig. 3.4(c)) the Cr^{4+} B-site cation has a d^2 configuration, and this half-metallic character is far more pronounced for both the pristine and defect supercells. Although the spin-down channel present a bandgap in both pristine and defect structures, the spin-up channel is metallic and populated below the fermi level in both structures, yielding a metallic state.^[48] Conductivity is thus largely attributed to spin-up channel in both pristine- BaCrO_3 and defective- $\text{BaCrO}_{2.875}$. Similar ferromagnetic behavior is observed in the pristine and defective $\text{BaMnO}_{3-\delta}$ BS (Fig. 3.4(d)), except here E_F lies at the middle of bandgap between spin-down bands, while in case of $\text{BaCrO}_{3-\delta}$ E_F is located just below the conduction band minima. However, in both materials conductivity can clearly be attributed to a single spin channel. This is not the case for BaFeO_3 , BaCoO_3 and BaNiO_3 , for which both spin-up and -down channels indicate metallic behavior (see Fig. 3.4(e-g)). Fig. 3.4(e) suggesting that both pristine and defective- BaFeO_3 is clearly ferromagnetic, with notable spin asymmetry near the Fermi level. Interestingly, pristine- BaCuO_3 (Fig. 3.4(h)) exhibits a direct bandgap at Γ -point, where this gap becomes narrower in its defect structure. Additionally, the spin-up and spin-down bands in this material are largely symmetric, due to the decreasing unpaired electron number in d-orbitals where the contribution of the net magnetic moment also reduced.



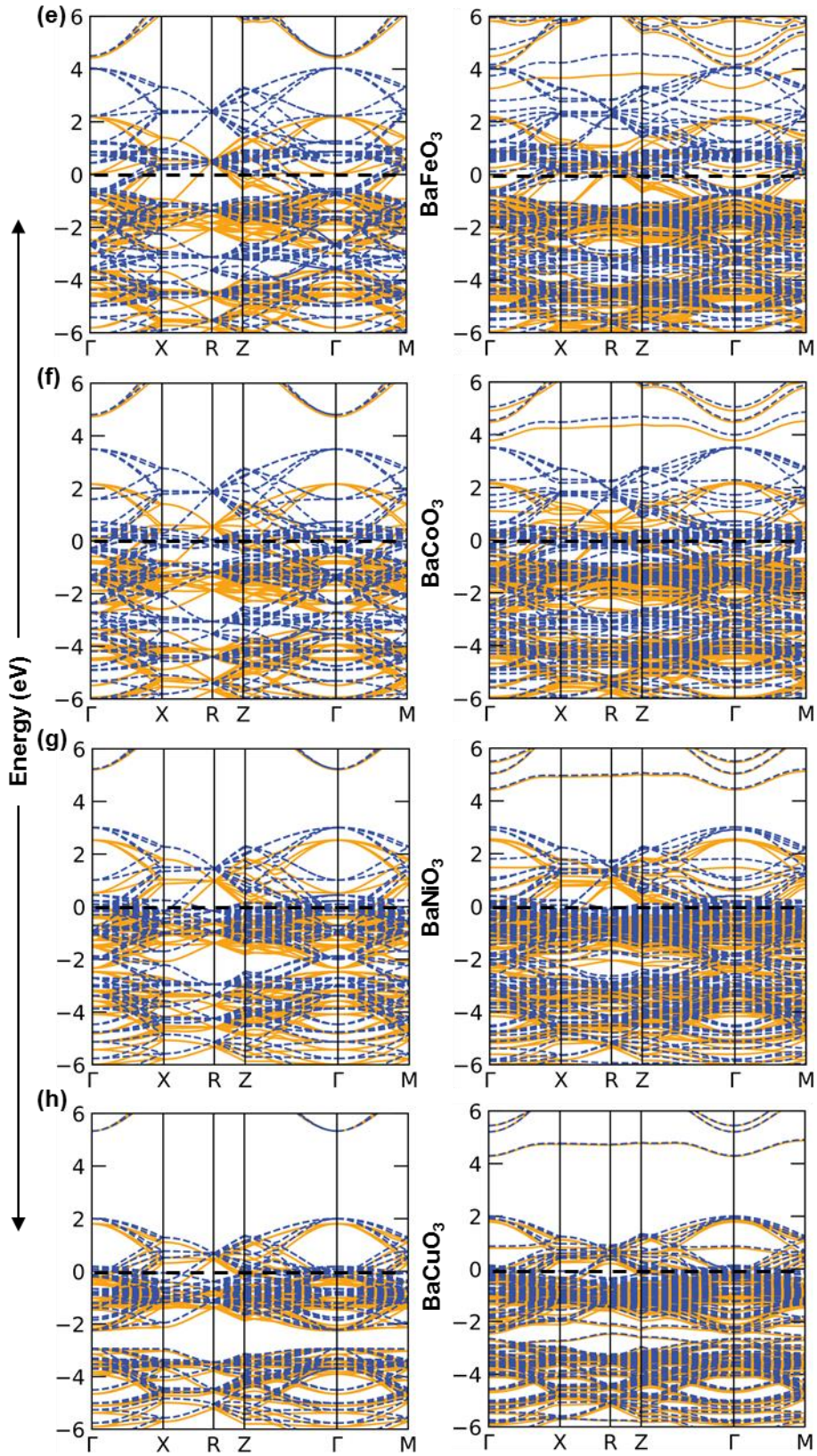


Fig. 3.4 Spin-polarized electronic BS of representative $2 \times 2 \times 2$ supercell of pristine-BaMO₃ (M = Ti – Cu) (left) and defect-BaMO_{2.875} (right) along high symmetry directions in the BZ. The solid yellow and dashed blue lines represent different spin channels (spin-up and spin-down, respectively). (a) BaTiO₃, (b) BaVO₃, (c) BaCrO₃, (d) BaMnO₃, (e) BaFeO₃, (f) BaCoO₃, (g) BaNiO₃, and (h) BaCuO₃.

This trend of magnetic moment is observed over the BaMO_{3-δ} series moving across Ti to Cu at B-site, where the asymmetric population between spin-up and spin-down is stronger between the middle four cations at the B-site from Cr to Co and coherently lowering the asymmetry in the opposite direction of both sides from the middle four cations, which reduce with respect to the decreasing unpaired electrons in d-orbitals.

In cubic BaMO₃ perovskites, the M⁴⁺ d orbitals are split into two sets: the triply-degenerate lower energy t_{2g} orbitals (d_{xy}, d_{yz} and d_{xz}), and the doubly-degenerate higher energy e_g orbitals (d_z², d_x²-y²). In order to obtain a deeper insight into the population of electronic charge among the pristine- and defect-BaMO_{3-δ} (M = Ti – Cu) electronic band compositions, the partial density of M⁴⁺-t_{2g}, -e_g and O-2p states for all BaMO₃ and BaMO_{2.875} perovskites are shown in Fig. 3.5(a-h). For pristine-BaTiO₃ (Fig. 3.5(a)), the Ti⁴⁺ t_{2g} orbitals lie ~2 eV above E_F in the conduction band. The formation of a neutral oxygen vacancy defect in the BaTiO₃ supercell results in the reduction of these orbitals. This is also the case for BaVO₃ (Fig. 3.5(b)). However, it is noted that the energy associated with the occupation of the d-t_{2g} states in BaVO_{2.875} is significantly smaller than for BaTiO_{2.875} (e.g. ~1 eV, compared to ~2 eV). In both perovskites, PDOS values of d-t_{2g}↑ and d-t_{2g}↓ show symmetric population over the conduction band energy region, however, the emergence of the ferromagnetic behavior in BaVO_{2.875} sees the V⁴⁺ d-t_{2g}↑ states shifted marginally lower in

energy than those in the down-spin channel. As anticipated, far more noticeable changes in PDOS are observed for BaCrO₃ and BaCrO_{2.875} (Fig. 3.5(c)). For the pristine supercell here, reduction of the Cr⁴⁺ cation occupies d-t_{2g}↑ orbitals exclusively. This is also true for the defective supercell, with the exception of a small d-t_{2g}↓ DOS close to E_F. Reduction of the Cr⁴⁺ cation here is incomplete, however, since O-2p↑ states at these energies are also occupied to a small extent. For BaMnO₃, conducting states again correspond to the Mn⁴⁺ d-t_{2g}↑ orbitals, and again these are the orbitals that are exclusively reduced by the formation of a neutral vacancy defect, with Mn⁴⁺ d-t_{2g}↓ spin states remaining in the conduction band. Fig. 3.5(d) shows however, that the Mn d-t_{2g}↑ and O-2p↑ states are closer in energy, and so the partial reduction of the B-site cation observed for BaCrO₃ is more significant for BaMnO₃. For both the pristine and defective-BaMnO₃ perovskite, the amplitude of d-e_g↑ spin states immediately below the Fermi level is minimal but non-zero. This indicates that Mn⁴⁺ d-e_g↑ states compete with d-t_{2g}↑ states for O-2p electrons in the presence of the neutral vacancy. The same mixing of e_g and t_{2g} is observed more prominently in pristine-BaFeO₃ (Fig. 3.5(e (left))), where a significant number of d-e_g↑ states are observed immediately below E_F with d-t_{2g}↑ states and O-2p states. This indicates a predominantly high spin configuration (t_{2g}³e_g¹) for Fe⁴⁺ cations in the pristine perovskite lattice. In defective-BaFeO_{2.875} (Fig. 3.5(e (right))), d-t_{2g}↓ states are populated below the Fermi level, where other contributions remain identical to their pristine structure, which means additional electrons in the defect structure will occupy lower d-t_{2g} energy states. PDOS for pristine- and defective-BaCoO₃ bear a strong resemblance to those for BaFeO₃ (comparing Fig. 3.5(e) and 3.5(f)), meaning that Co⁴⁺ cations also preferentially adopt a high-spin configuration (t_{2g}³e_g²). The Ni⁴⁺ in pristine-BaNiO_{2.875} (Fig. 3.5(g (left))) holds high spin configuration (t_{2g}⁵e_g²) by pushing down d-e_g energy states below the Fermi level, where the occupancy of d-e_g states remain similar in defect structure.

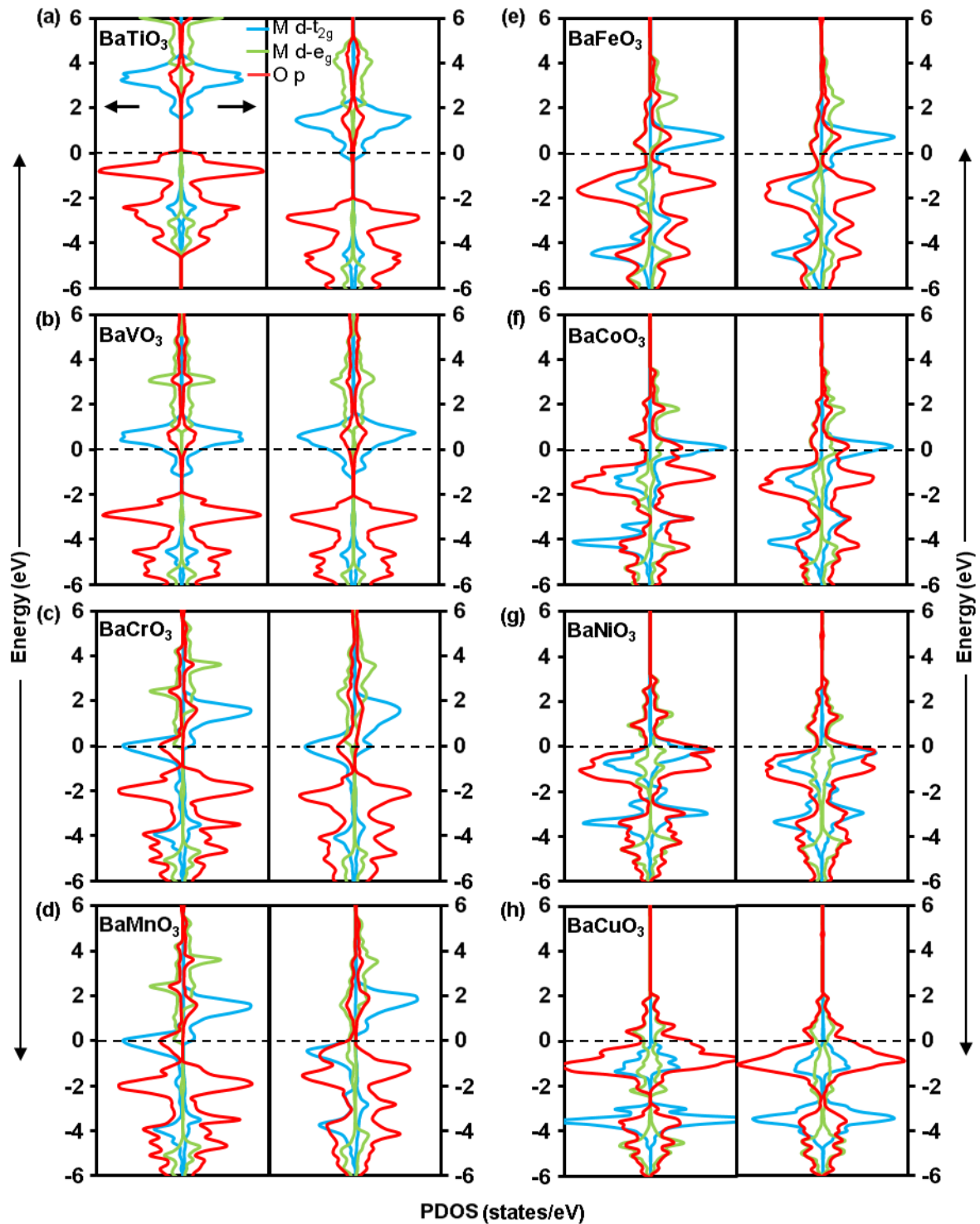


Fig. 3.5 PDOS of representative pristine-BaMO₃ (M = Ti – Cu) (left) and defect-BaMO_{3-δ} (right).

The black dashed lines represent the Fermi energy level of each perovskite set to 0 eV. The color lines – blue represents the PDOS of corresponding B-site metals of M-3d t_{2g} orbital, green

represents the PDOS of M-3d e_g orbital, and the red line represents the PDOS of O-2p orbital for respective $BaMO_3$ perovskites. The arrow in the upper left depicted PDOS values for spin-up and the upper right for spin-down. (a) $BaTiO_3$, (b) $BaVO_3$, (c) $BaCrO_3$, (d) $BaMnO_3$, (e) $BaFeO_3$, (f) $BaCoO_3$, (g) $BaNiO_3$, and (h) $BaCuO_3$.

Interestingly, the d- e_g and d- t_{2g} maintain a gap between -2 to -3 eV in pristine- $BaCuO_3$ (Fig. 3.5(h (left))), where high energy state d- e_g have a dominant nature at -2 eV. The spin configuration of Cu^{4+} in $Cu-O_6$ octahedra remain in low spin states ($t_{2g}^6 e_g^1$). The existing gap in pristine- $BaCuO_{2.875}$ is filled up by the hybridization of d- e_g and O-2p states in its defect structure.

In order to shed light on charge transfer and redistribution in defective- $BaMO_{3-\delta}$ lattice upon oxygen vacancy formation, Bader charge analysis^[49] was performed in both the pristine and defective supercell of the $BaMO_3$ series. The calculated effective Bader charges on Ba, M and O ions in pristine and oxygen-deficient $BaMO_{3-\delta}$ supercell are reported in Table 3.2. The Bader charge distribution on each species in the pristine structure suggests that, although the charge on Ba cations from $BaTiO_3$ to $BaCuO_3$ only vary between +1.55 to +1.62 e, there is a significant variation in the charges of M cations from left to the right in this series. The decrease in the positive charges of M cations from Ti to Cu follows a linear correlation with their increasing electron number in the d-shell. This implies that the degree of ionic and covalent contribution in M-O bonding from Ti to Cu vary accordingly, where Ti-O bonding has the most ionic contribution and thus less covalency, oppositely Cu-O interaction has the less ionic but most covalent contribution in this series. That is, Ti-O interaction becomes the most polarized and Cu-O interaction is the least polarized. Remarkably, the charge in Ba cation is less positive than the M cation for the first five perovskites in this series from $BaTiO_3$ to $BaFeO_3$, and more positive in the rest three

perovskites from BaCoO₃ to BaCuO₃. Therefore, the ionic contribution in Ba–O is lesser than M–O from Ti to Fe, and greater than M–O from Co to Cu, so that the degree of covalency in Ba–O follows the opposite trends among this series.

Table 3.2 Calculated Bader charges (q in e) on Ba, M and O ions in the 2×2×2 pristine- and defect-BaMO_{3-δ} supercells. Values are averaged over the number of species. q_{M1} and q_{M2} (M1 and M2 cations are marked in Fig. 3.6 (right)) represent the quantity of electronic charges of the two nearest neighbor metal cations from the vacancy site in the lattice.

	BaTiO ₃	BaVO ₃	BaCrO ₃	BaMnO ₃	BaFeO ₃	BaCoO ₃	BaNiO ₃	BaCuO ₃
Before introducing vacancy in supercell								
q_{Ba}	+1.55	+1.58	+1.59	+1.59	+1.60	+1.61	+1.62	+1.60
q_M	+2.12	+2.01	+1.90	+1.80	+1.66	+1.49	+1.36	+1.31
q_O	-1.22	-1.20	-1.16	-1.13	-1.09	-1.03	-0.99	-0.97
After the creation of oxygen vacancy in supercell								
q_{Ba}	+1.52	+1.55	+1.57	+1.56	+1.58	+1.59	+1.60	+1.58
q_M	+2.03	+1.92	+1.80	+1.74	+1.61	+1.43	+1.31	+1.26
q_{M1}	+1.79	+1.64	+1.59	+1.56	+1.40	+1.25	+1.15	+1.11
q_{M2}	+1.82	+1.67	+1.60	+1.57	+1.43	+1.26	+1.16	+1.12
q_O	-1.24	-1.21	-1.17	-1.15	-1.11	-1.05	-1.01	-0.99

The qualitative analysis of charge on O anions among these eight BaMO₃ perovskites show that, perovskite contain less negative charge on the O anion from left to right of this series.

Consequently, the energy required to break the M–O bond is reduced with respect to the weakly charged oxygen. This can be attributed to the trend of the required free energy to form an oxygen vacancy in BaMO_3 ($M = \text{Ti} - \text{Cu}$) as shown in Fig. 3.3, where BaCuO_3 (containing weakly charged oxygen) and BaTiO_3 (containing strongly charged oxygen) required the lowest and highest energy respectively to form an oxygen vacancy in this series. On the other hand, the presence of an oxygen vacancy in defective- $\text{BaMO}_{2.875}$ supercell reduces the positive charge of Ba cation slightly (1–2%) compared to the pristine lattice, but to a greater extent (4–5%) to the corresponding M cations (see Table 3.2). The Bader charges in the defect structure maintain almost identical character to their pristine structure in terms of the degree of ionic contribution and covalency in Ba–O and M–O interactions from left to right in this series of perovskites.

The quantity of electric charge transferred from the vacant oxygen site to the M cations is shown in Fig 3.6(a). The accumulation of negative charge among M cations in defect structure also has a linear correlation with their atomic number, where this correlation has negligible effects on the charge gained by Ba cation. Comparably, the proportion of negative charge gained by the Ba cations is mostly invariant irrespective of perovskites. These gained charges by M cation is related to the ionic and covalent nature of M–O interactions, where the dominant ionic environment favors greatly the localization of electrons on the ions. The percentages of negative electron charge accepted by the two nearest neighbor M cations are shown in Fig. 3.6(b). It is evident from the figure that, the total negative charge transferred from the vacant site to the M site in the lattice (Fig. 3.6(a)), is mostly distributed to the two nearest neighbor M cations (Fig. 3.6(b)), which causes these two cations to be significantly reduced. This scenario can be viewed in terms of the charge density distribution analysis in Fig. 3.7(a-h).

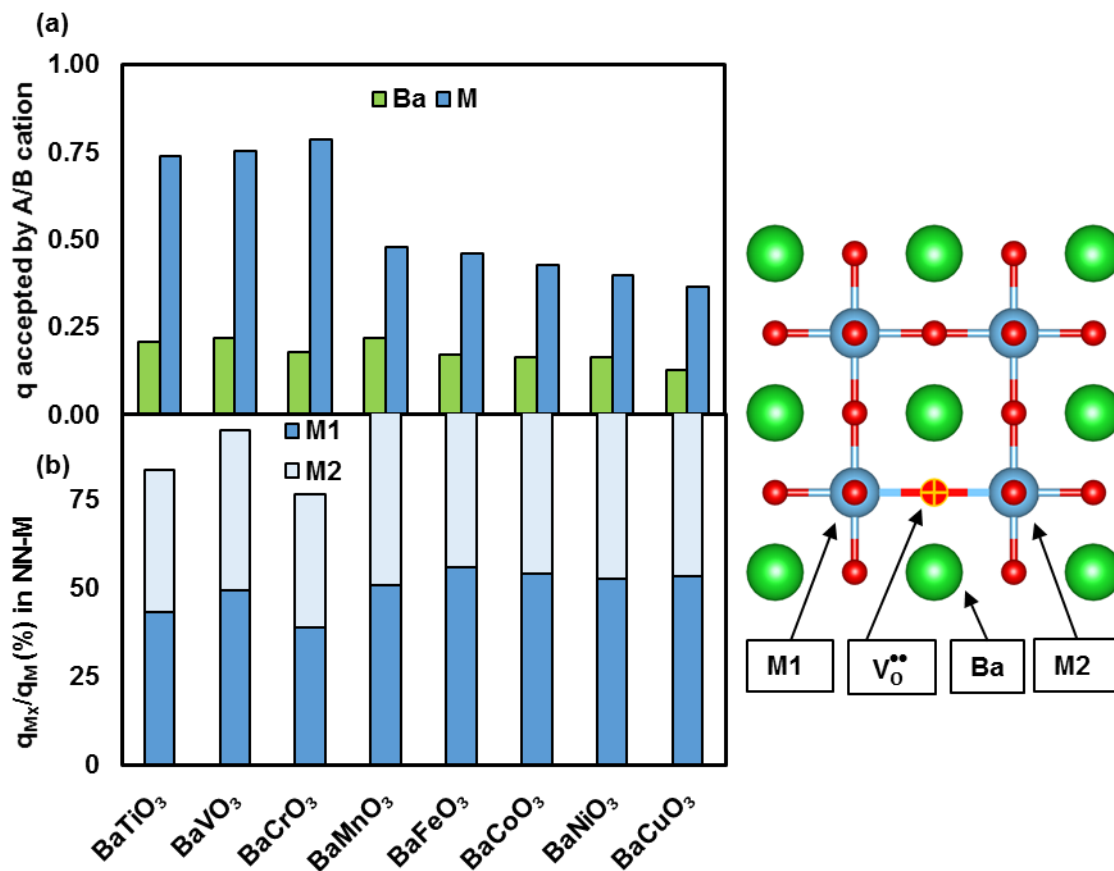


Fig. 3.6 (a) The percentage of electrons accepted by two cations (Ba and M (Ti – Cu)) in BaMO_{2.875} lattice upon oxygen vacancy formation. The green and blue bars represent the amount of Bader charges (q in e) transferred from the vacant site to Ba and metal cations (M), respectively in respective perovskite. (b) The percentage of electrons accepted by the two nearest neighbor metal (NN-M) cations (q_{M_x} , $x=1, 2$) from the total transferred charge to M (q_M) in (a). The right-side figure shows the position of two NN-M cations - M1 and M2, oxygen vacancy ($V_O^{\bullet\bullet}$) and Ba cation in BaMO_{2.875} lattice.

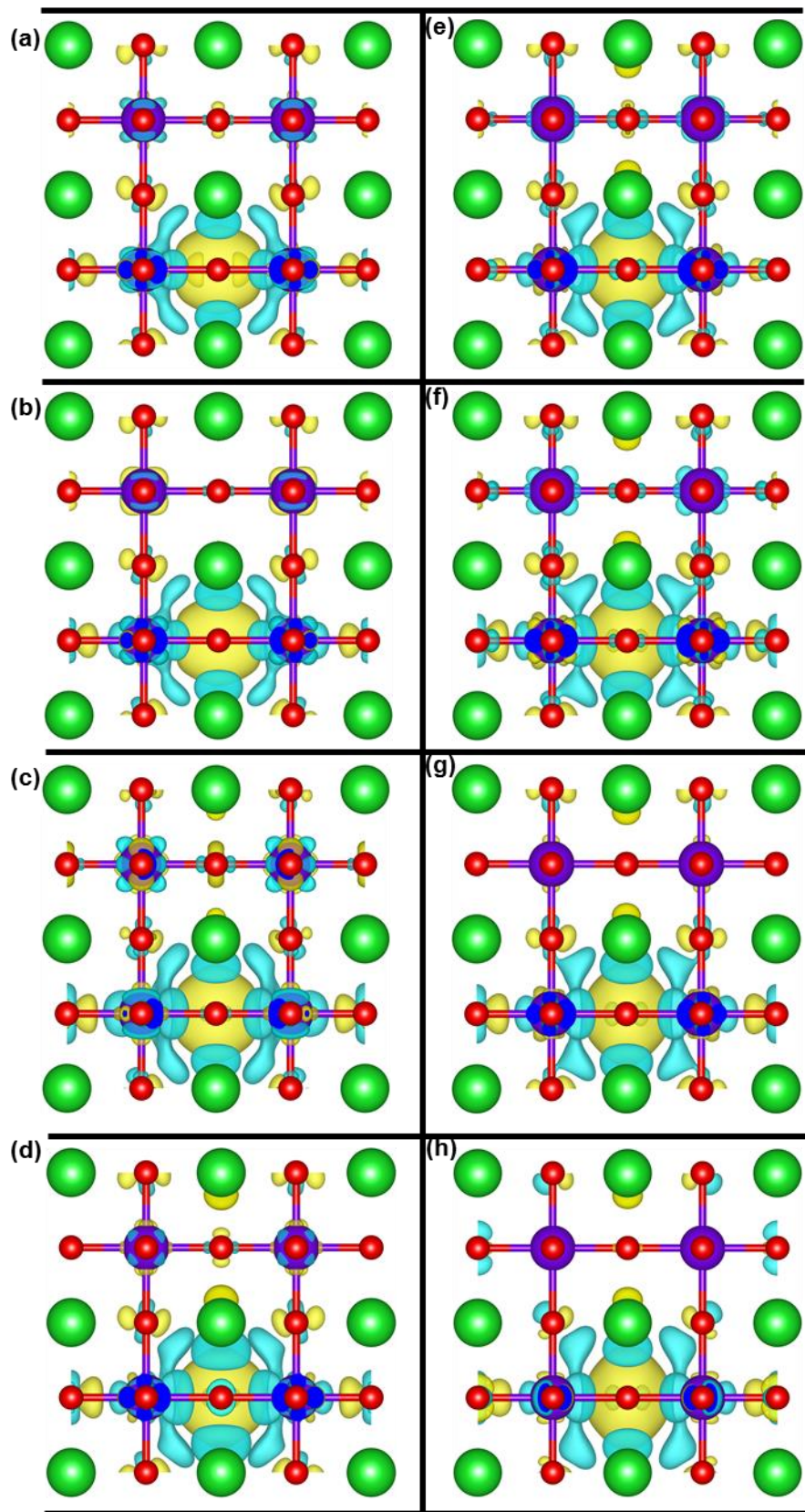


Fig. 3.7 Electronic CDD of representative (a) BaTiO_{2.875}, (b) BaVO_{2.875}, (c) BaCrO_{2.875}, (d) BaMnO_{2.875}, (e) BaFeO_{2.875}, (f) BaCoO_{2.875}, (g) BaNiO_{2.875}, and (h) BaCuO_{2.875}. Green, violet and red spheres represent Ba, M and O atoms, respectively. For the CDD analysis, 2×2×2 pristine BaMO₃ (M = Ti – Cu) is taken as the reference density in all cases with oxygen vacancy in the neutral charge state. CDD isosurfaces are drawn with a threshold of 0.002 e au⁻³; yellow/blue isosurface represents charge depletion/accumulation.

3.3.3 Reduction Thermochemistry of Cubic BaMO_{3-δ} with Thermal Corrections

3.3.3.1 Temperature-Dependent Reduction Free Energies

To consider how the incorporation of explicit DFPT thermochemical corrections influence these trend at high-temperature, the Gibbs free energies of reduction (ΔG_{RR}) of BaMO_{2.875} (i.e. BaMO₃ → BaMO_{2.875} + 1/2O₂) at temperature T and pressure p can be calculated as,

$$\Delta G_{RR}(T, p) = \mu_{BaMO_{2.875}}(T, p) - \mu_{BaMO_3}(T, p) + \frac{1}{2} \mu(T, p_{O_2}) \quad (3.9)$$

Table 3.3 lists ΔG_{RR} at standard conditions and selected temperatures (relevant for a high-temperature process such as STWS) for the production of a single vacancy defect, i.e. 8BaMO₃ → 8BaMO_{2.875} + 1/2O₂. At standard conditions, there is very good agreement between E_V and ΔG_{RR} values trends across the BaMO₃ series. However, thermochemical corrections to E_V for BaMO₃ can no longer be ignored even at minimal temperatures relevant to some oxygen deficiency applications (e.g. ~1200 K). At these temperatures, thermal corrections lead to the BaMO₃ reduction energy changing by ~300 kJ mol⁻¹. Further, ΔG_{RR} values for different B-site cation in BaMO₃ begin to deviate noticeably from each other.

Table 3.3 Calculated PBEsol-PAW ΔG_{RR} values of cubic BaMO₃ at standard conditions and at the selected temperatures for solar-to-fuel conversion applications.

T (K)	BaTiO ₃	BaVO ₃	BaCrO ₃	BaMnO ₃	BaFeO ₃	BaCoO ₃	BaNiO ₃	BaCuO ₃
	kJ mol ⁻¹							
298.15	428.12	371.75	274.36	76.975	88.55	-7.90	-78.06	-127.36
1200	188.27	192.49	60.87	-179.75	-49.71	-160.92	-176.23	-245.23
1800	9.62	75.85	-97.07	-372.12	-142.31	-260.76	-228.95	-322.89

The loss of the linear correlation at high-temperature, shown in Fig 3.8(a), suggests that the trends in the reduction free energy cannot be rationalized simply in terms of the atomic number of the B-site cation. For instance, ΔG_{RR} for the reduction of pristine BaTiO₃ to BaTiO_{2.875} is 188 kJ mol⁻¹ at 1200 K, a value 300 kJ mol⁻¹ less endothermic than the 0 K value, while at the same temperature difference, the ΔG_{RR} value differs by 240 kJ mol⁻¹ for the reduction of BaVO₃ to BaVO_{2.875}. At higher temperature, these deviations in ΔG_{RR} values increase further for all perovskites in this series. For instance, a maximum decrease of ~480 kJ mol⁻¹ is observed between 0 K and 1800 K for BaTiO₃, as reported in Table 3.3. These trends can be attributed to the change in temperature-dependent entropic contributions of pristine and defect structures on the individual BaMO_{2.875} free energy (see Fig. 3.9(a, b)). For example, the entropic contributions between BaTiO₃ and BaVO₃ (containing two nearest neighbor M cations) differ by 234 kJ mol⁻¹, while this difference is only 98 kJ mol⁻¹ between the last two perovskites in the series, BaNiO₃ and BaCuO₃.

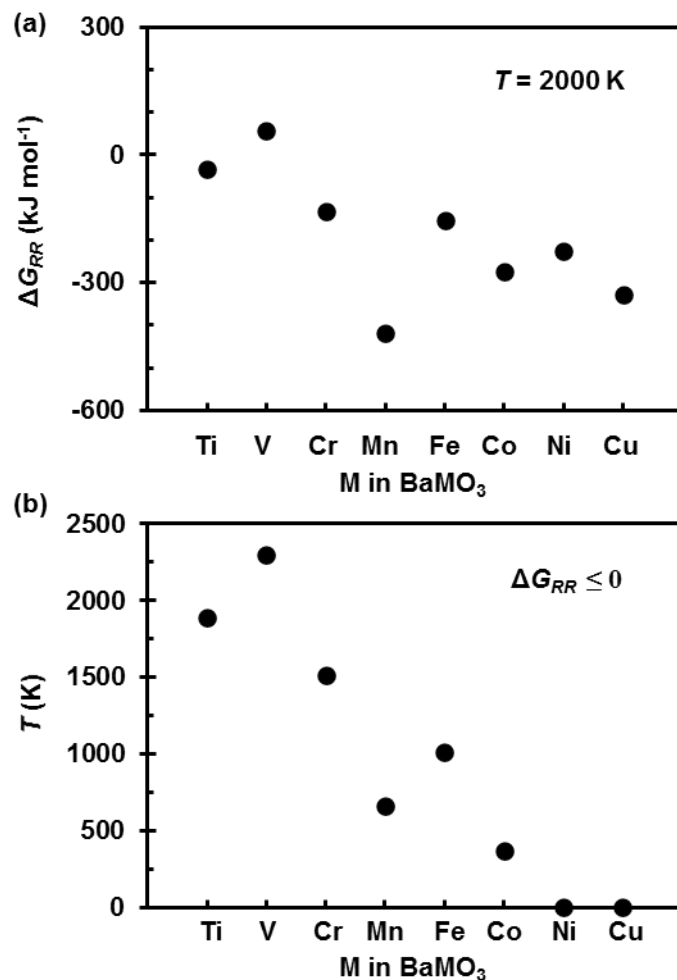


Fig. 3.8 (a) Calculated PBEsol-PAW ΔG_{RR} values (kJ mol⁻¹, per single oxygen defect) (equation (3.9)) for BaMO_{3-δ} (M = Ti – Cu) at temperatures between 0 – 2000 K and $p^{\circ} = 1$ atm. (b) Symbols indicate the minimum spontaneous reduction temperature for BaMO_{3-δ}. All ΔG_{RR} values at $P_{O_2} = 10^{-6}$ atm.

Fig. 3.8(b) presents the spontaneous reduction temperature of these BaMO_{3-δ} perovskites. This figure shows that the most stable perovskite in the series is BaVO₃, which only undergoes reduction at 2200 K. This perovskite has almost identical energetic as observed in BaZrO₃ and so could be expected to exhibit similar thermochemistry and hence potential in HT-SOFC

technology.^[50-52] BaTiO₃ and BaCrO₃ reduce at 1850 and 1450 K, respectively, and so both perovskites are in the favorable reduction temperature range for solar-to-fuel conversion applications (1100 – 1900 K).^[53] This result for BaTiO₃ is consistent with experiments demonstrating it to be a thermally stable perovskite at high temperature yielding good performance as an anode for the conversion of methane in HT-SOFC.^[54, 55] Experimental synthesis of BaCrO₃ shows the formation of an oxygen deficiency at ~1473 K. This perovskite has also been identified as a potential SOFC anode material due to its high oxide ion conductivity.^[56]

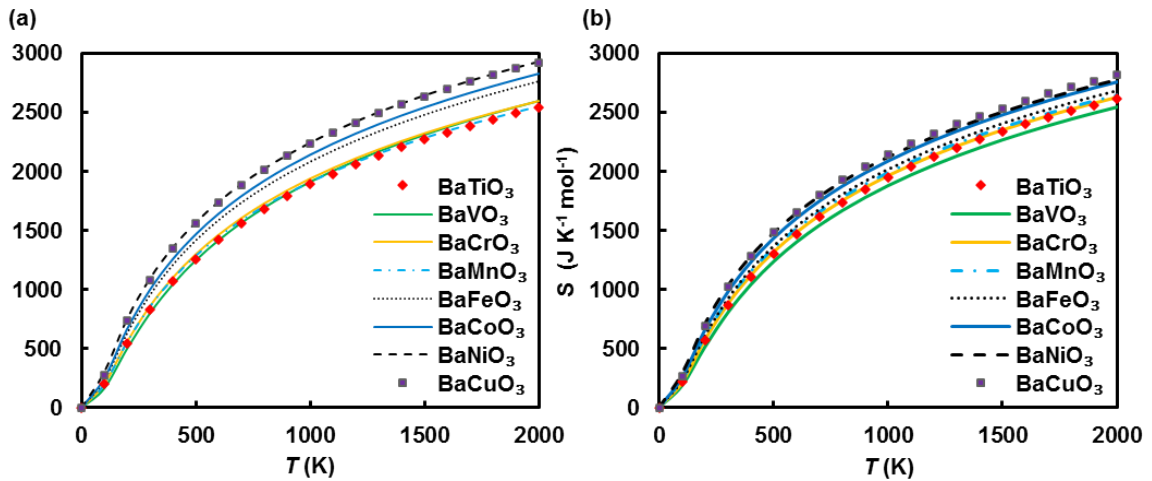


Fig. 3.9 Calculated PBEsol-PAW entropy, S ($\text{J K}^{-1} \text{mol}^{-1}$) of (a) pristine-BaMO₃ and (b) defective-BaMO_{2.875} between 0 – 2000 K using $2 \times 2 \times 2$ supercells.

By comparison, BaMnO₃ and BaFeO₃ reduce below 1100 K, suggesting their potentiality to be used in IT-SOFC applications. It is therefore not surprising that BaMnO₃ is highly active in IT-SOFC applications for NO decomposition.^[57, 58] Similarly, Xian et al.^[59, 60] experimentally demonstrated that BaFeO₃ is an efficient NO absorber. The remaining three BaMO₃ perovskites considered here ($M = \text{Co, Ni, Cu}$) are predicted to reduce below 400 K. This is in good agreement with the observation of Ezbiri et al.^[14] who found low reduction free energy for these three

perovskites. These perovskite oxides are therefore promising as ORR/OER materials in SOFC, due to the weaker M–O bond. The latter facilitates the easier formation of oxygen vacancies within the lattice, fast oxygen ion diffusion in bulk and facile surface oxygen exchange reactions.^[61, 62]

3.3.3.2 Phonon Analysis: Effect of B-site Cation and Oxygen Vacancy

The influence of B-site cations on the vibrational structure of $\text{BaMO}_{3-\delta}$ are shown in Fig. 3.10(a-f), which compares the VDOS of representative $\text{BaMO}_{2.875}$ structures for $M = \text{Ti} - \text{Cu}$. Fig. 3.10(a) shows that the range of phonon frequencies associated with A-site cations in BaMO_3 occurs between $0\text{-}200\text{ cm}^{-1}$, with the principle vibrational mode observed at $\sim 100\text{ cm}^{-1}$. There is no shift in either of these vibrational frequencies with the change of metal cation in the B-site. However, the amplitude of Ba^{2+} vibrations varies among different B-site atoms. For instance, the peak amplitude of Ba^{2+} vibrations reaches an energetic maximum in BaCuO_3 , where it drops to the minimum in BaTiO_3 among the BaMnO_3 series. Overall, the amplitude of Ba vibrations increases gradually moving across the pristine structure of BaTiO_3 to BaCuO_3 . Interestingly, there is a large decrease in the VDOS of these vibrations (Fig. 3.10(b)) in defective $\text{BaMO}_{2.875}$ as the A-site cations become less energetic. This indicates that neutral oxygen vacancies in the $\text{BaMO}_{2.875}$ lattice constrict the vibrational motion of the A-site cation in these perovskites. The introduction of neutral vacancy defects in $\text{BaMO}_{2.875}$ has similar, but more limited, effects on the B-site cations VDOS, shown in Fig. 3.10(c, d). Notably, the amplitudes of frequencies between $\sim 150 - 500\text{ cm}^{-1}$ decrease for all $\text{BaMO}_{2.875}$, but the frequency ranges shift from higher to lower scale with respect to the metallic mass of B-site cations. Fig. 3.10(e, f) shows the VDOS associated with O^{2-} vibrations in the pristine- BaMO_3 (Fig. 3.10(e)) and defective- $\text{BaMO}_{2.875}$ (Fig. 3.10(f)) lattice.

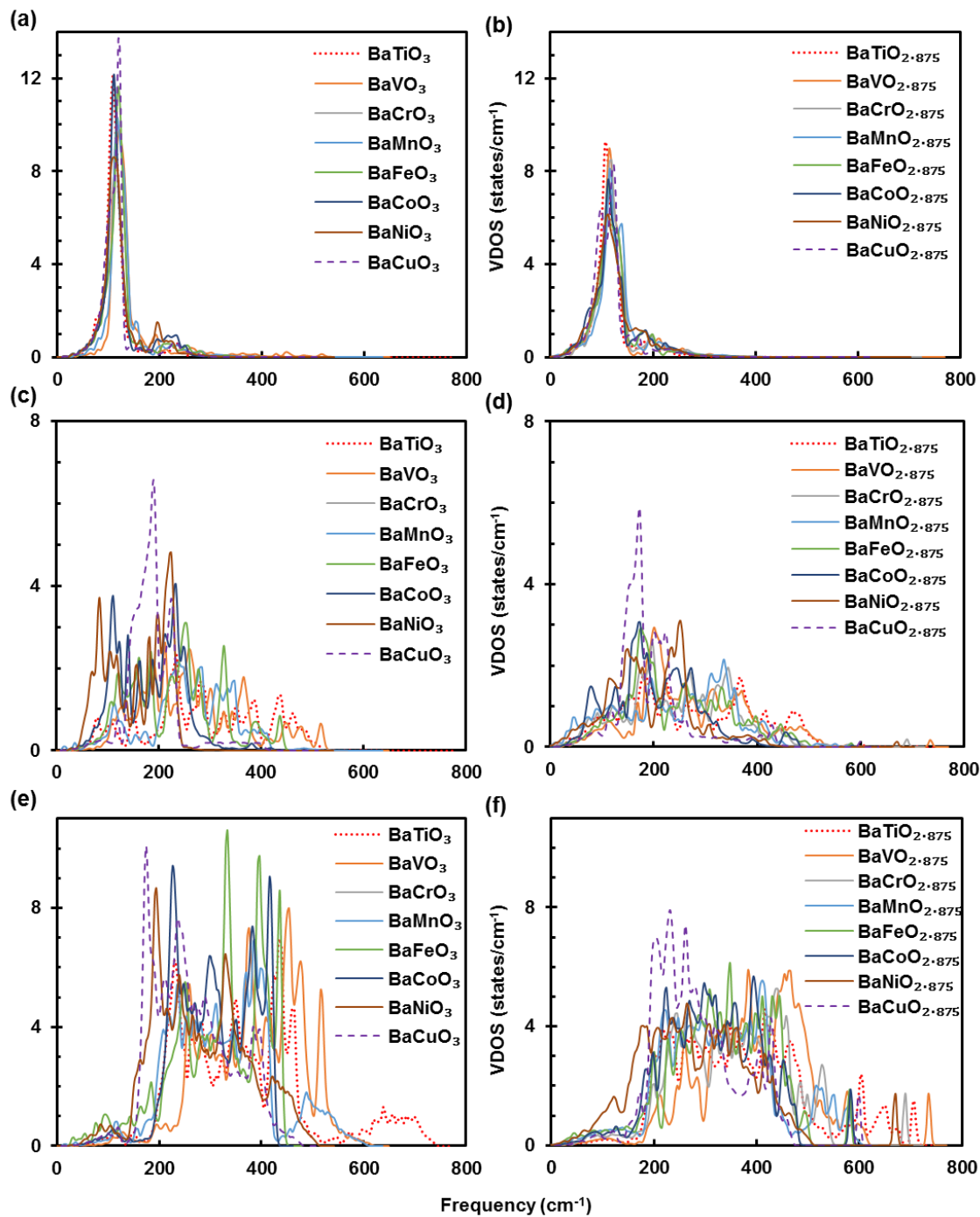


Fig. 3.10 VDOS of Ba²⁺ cations in (a) pristine-BaMO₃ and (b) defect-BaMO_{2.875}; VDOS of M⁴⁺ cations in (c) pristine-BaMO₃ and (d) defect-BaMO_{2.875}; VDOS of O²⁻ anions in (e) pristine-BaMO₃ and (f) defect-BaMO_{2.875}, calculated using PBEsol-PAW.

As for Ba^{2+} and M^{4+} , the introduction of neutral vacancy defects in $\text{BaMO}_{2.875}$ decreases the VDOS in both regions of the phonon spectrum for O^{2-} . The most noticeable change in the VDOS of O^{2-} vibrations in the defective structure is that the principal phonon modes shift towards a higher frequency range than their pristine structure. For instance, the principal phonon modes associated with O^{2-} vibrations in pristine BaCuO_3 is observed at $\sim 180 \text{ cm}^{-1}$, while for a defective structure it shifts at $\sim 250 \text{ cm}^{-1}$. Similar trends are observed among all other defective $\text{BaMO}_{2.875}$. Overall, the phonon vibration of $\text{BaMO}_{2.875}$ becomes more energetic, moving across $\text{BaTiO}_{2.875}$ to $\text{BaCuO}_{2.875}$, consistent with the reducibility of corresponding perovskite oxides.

3.3.4 Thermochemical Properties and Phonon Dispersions of Cubic BaMO_3

3.3.4.1 Effect of B-site Cation on Thermochemical Properties

Vibrational S , C_p and $(H(T)-H(298.15))$ of BaMO_3 ($\text{M} = \text{Ti} - \text{Cu}$) calculated using DFPT are reported in Table 3.4 at standard conditions and shown in Fig. 3.11(a-c) from 0 K to 2000 K. The variation on thermochemical properties among BaMO_3 perovskites along this 3d series is directly proportional to the B-site cation mass; a more massive B-site cation leads to a larger contribution to the perovskite's phonon modes, and therefore thermochemical properties. For instance, the S value of BaTiO_3 (the lowest mass of B-site atoms between $\text{Ti} - \text{Cu}$) is $103.67 \text{ J K}^{-1} \text{ mol}^{-1}$ at standard conditions while for BaCuO_3 (the highest mass of B-site atoms between $\text{Ti} - \text{Cu}$) it is $134.43 \text{ J K}^{-1} \text{ mol}^{-1}$, a difference of $\sim 30 \text{ J K}^{-1} \text{ mol}^{-1}$. With increasing temperature, the S values of all BaMO_3 perovskites have smoother curves with respect to temperature in Fig. 3.11(a).

The temperature dependence C_p of BaMO_3 are reported in Fig. 3.11(b) from 0 to 2000 K. The quasi-harmonic contributions of BaMO_3 arising from thermal expansion coefficient, bulk modulus and volume changes with temperature are provided in Appendix (Fig. 6.1). The variation of C_p

with temperature obeys the Debye T^3 law at low temperature below 500 K, whereas it departs from the classic limit of Dulong-Petit's law due to quasi-harmonic contributions at higher temperatures. Nevertheless, trends in C_p values among this series of BaMO_3 perovskites are determined by the mass of the B-site cation. For instance, BaCuO_3 has the C_p value of $113.96 \text{ J K}^{-1} \text{ mol}^{-1}$ which drops to $99.08 \text{ J K}^{-1} \text{ mol}^{-1}$ in case of BaTiO_3 at standard conditions, reported in Table 3.4 (a change of $\sim 14 \text{ J K}^{-1} \text{ mol}^{-1}$). This change of C_p values gradually increases along with the 3d series from Ti to Cu, however, with increasing temperature this difference drops to be zero at 2000 K irrespective of B-site atoms. Notably, three BaMO_3 perovskites ($M = \text{Ti, Cr, Mn}$) slightly underestimate the C_p values due to their imaginary phonon frequency at certain high symmetry points arising from their unstable cubic phase at low temperature.

Table 3.4 Calculated PBEsol-PAW S and C_p values of cubic BaMO_3 at standard condition.

($\text{J K}^{-1} \text{ mol}^{-1}$)	BaTiO_3	BaVO_3	BaCrO_3	BaMnO_3	BaFeO_3	BaCoO_3	BaNiO_3	BaCuO_3
S	103.67	99.40	107.03	106.54	118.94	124.41	136.43	134.63
C_p	99.08	103.06	102.53	100.86	108.62	110.95	113.05	113.96

The calculated $(H(T)-H(298.15))$ of BaMO_3 as a function of temperature is depicted from 0 to 2000 K in Fig. 3.11(c). It is found that the relative molar enthalpies of all BaMO_3 perovskites increase linearly with temperature. At a given temperature the values of relative molar enthalpies among BaMO_3 perovskites are similar. For instance, at 300 K temperature the difference between $(H(T)-H(298.15))$ values of BaTiO_3 and BaCuO_3 is found to be $\sim 0.02 \text{ kJ mol}^{-1}$, while at 2000 K it increases up to 6 kJ mol^{-1} . These trends remain identical for all BaMO_3 perovskites, while $(H(T)-H(298.15))$ values fractionally increase with temperature among BaMO_3 perovskites along 3d series from Ti to Cu.

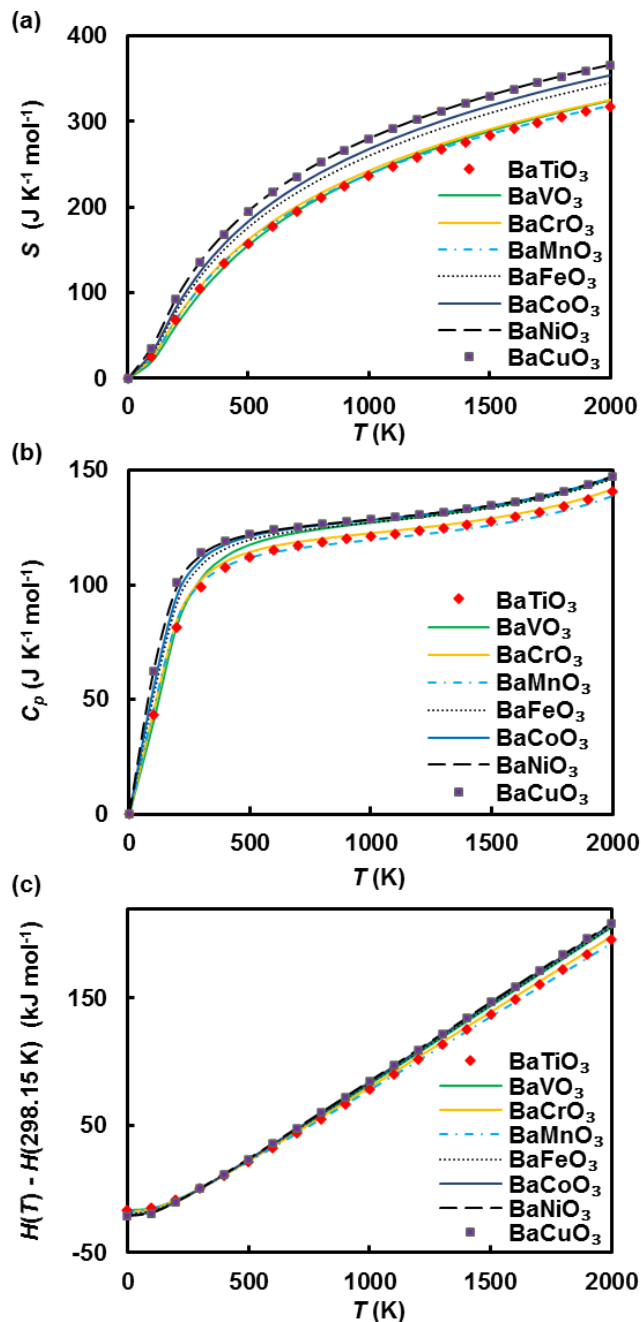


Fig. 3.11 Calculated PBEsol-PAW (a) S ($\text{J K}^{-1} \text{mol}^{-1}$), (b) C_p ($\text{J K}^{-1} \text{mol}^{-1}$), and (c) $(H(T) - H(298.15 \text{ K}))$ (kJ mol^{-1}) of the primitive unit cell of BaMO_3 ($M = \text{Ti} - \text{Cu}$) between 0 – 2000 K. Note the difference between these entropies and those presented in Fig. 3.9 is due to the size of the periodic cell used in each case.

3.3.4.2 Effect of B-site Cation on Phonon Dispersions and VDOS

The origin of vibrational contributions to the entropy, specific heat and relative molar enthalpy can be described in terms of phonon BS and projected VDOS. The cubic phonon dispersion curves of BaMO_3 ($M = \text{Ti} - \text{Cu}$) are calculated along the high symmetry directions Γ -M-R-X- Γ -R in the BZ, as shown in Fig. 3.12(a-h). Among them BaVO_3 , BaCoO_3 , BaNiO_3 and BaCuO_3 exhibit stable phonon modes at all high-symmetry points in BZ (Fig. 3.12(b, f, g, h)), while BaTiO_3 , BaCrO_3 , BaMnO_3 and BaFeO_3 have lattice instabilities at some points (Fig. 3.12(a, c, d, e), respectively). For instance, BaTiO_3 and BaMnO_3 exhibit imaginary unstable phonon modes at Γ , M and X, while BaCrO_3 shows imaginary modes at Γ and X, and BaFeO_3 shows imaginary modes at R point. For BaTiO_3 and BaMnO_3 , this is anticipated based on previous reports.^[63, 64]

The most unstable high-symmetry instabilities of these two perovskites are at Γ points with an imaginary frequency around -200 and -220 cm^{-1} for BaTiO_3 and BaMnO_3 respectively, which both correspond to a polar vibrational mode consisting predominantly of Ti (Fig. 3.13(a (left))) and Mn (Fig. 3.13(b (left))) displacement within the MO_3 octahedral sublattice, while octahedra oxygen atoms remain largely frozen. The other unstable modes at the M-point (Fig. 3.13(a (center))) and X-point (Fig. 3.13(a (right))) of BaTiO_3 correspond to the branches of Ti-dominated transverse optic modes. These structural instabilities in BaTiO_3 cause the cubic structure to undergo several phase transitions at high temperature, to phases including tetragonal, orthorhombic and rhombohedral (which is the most stable).^[65] In contrast, the imaginary frequency at X-point for BaMnO_3 arises from the breathing of oxygen octahedra associated with the vibrational movement of two adjacent oxygens towards the Mn cation, while two others move against Mn (Fig. 3.13(b (center))). However, the instability at M-point is dominated by the displacement of apical oxygen atoms rather than oxygen octahedral rotation (Fig. 3.13(c (right))).

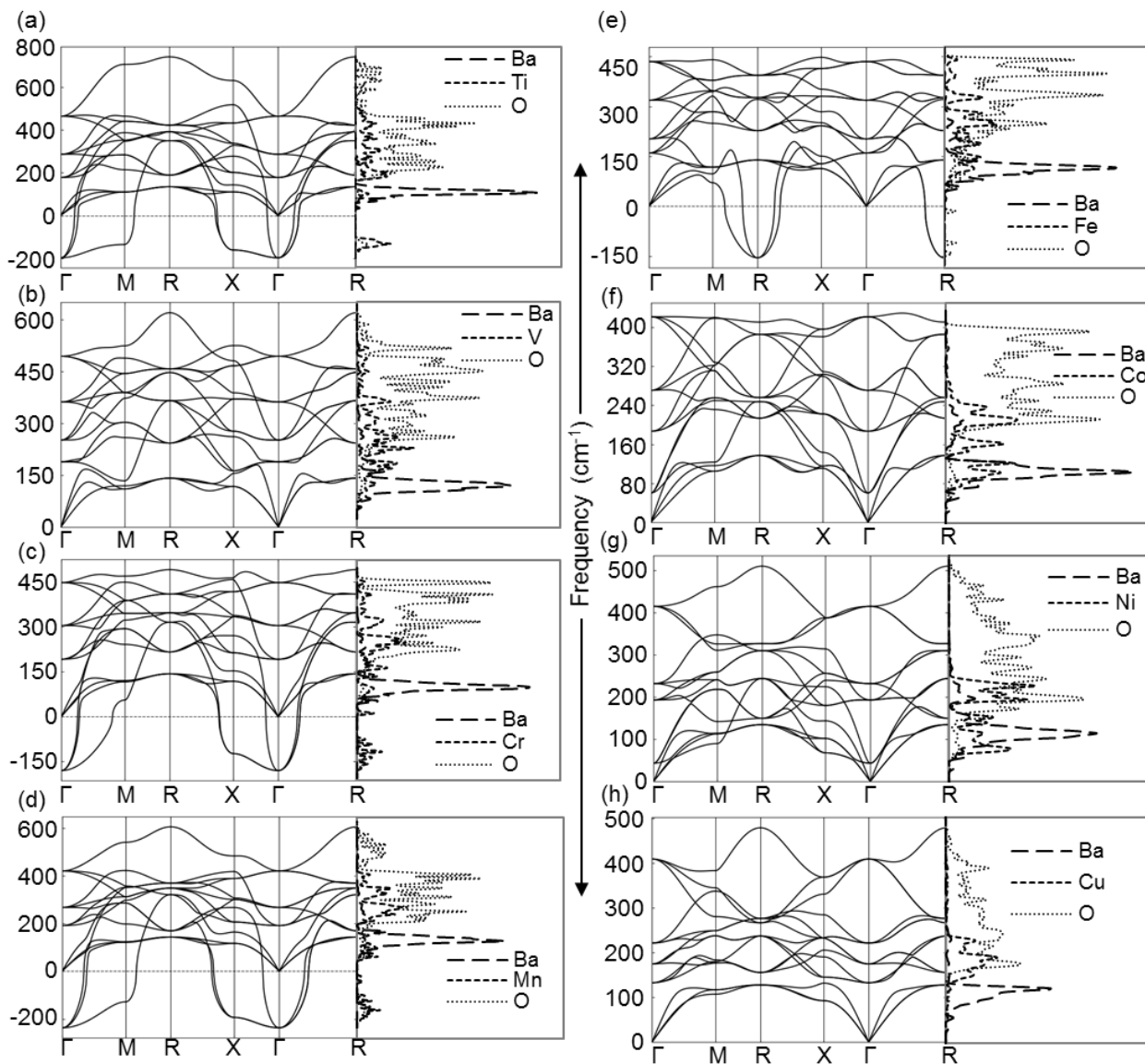


Fig. 3.12 Calculated PBEsol-PAW phonon dispersion curves (left) and VDOS (right) for the cubic unit cells of (a) BaTiO₃, (b) BaVO₃, (c) BaCrO₃, (d) BaMnO₃, (e) BaFeO₃, (f) BaCoO₃, (g) BaNiO₃, (h) BaCuO₃.

On cooling the temperature, Mn–O bond length and Mn–O–Mn bond angle can be displaced which results in structural distortion in BaMnO₃, and consequently the cubic structure (stable at high temperature) transforms to a hexagonal structure at lower temperatures via several phase

transitions.^[66] On the other hand, for BaCrO₃ the imaginary mode (-170 cm⁻¹) at Γ is dominated by the Cr–O displacement (Fig. 3.13(c (left))), while that at X corresponds to the rotation of CrO₃ octahedra (Fig. 3.13(c (right))). Finally, BaFeO₃ shows an imaginary frequency of -150 cm⁻¹ at R, due to oxygen anions vibrating towards and against Fe (Fig. 3.13(d)). The corresponding imaginary phonon modes of the respective crystal structure were accounted for predicting their thermodynamic properties shown in Fig. 3.11.

The corresponding VDOS of BaFeO₃ (Fig. 3.12(e (right))) confirms the vibrational frequency of oxygen anions in this range. The projected VDOS of cubic BaMO₃ (M = Ti – Cu) shown in Fig. 3.12(a-h (right)) can be categorized into three different frequency regimes: low-, intermediate- and high-frequency. The lower-frequency regime consists of 0 – 200 cm⁻¹, dominated by the vibrational motion of heavier metallic mass cation Ba²⁺, while the intermediate-frequency range between 200 – 400 cm⁻¹, associated with the respective 3d M⁴⁺ metal cation in individual perovskite of BaMO₃ and the optic modes between 200 – 400 cm⁻¹ frequency range mostly governed by the motion of oxygen anions. This is consistent with the respective masses of Ba²⁺, M⁴⁺ and O²⁻ ions.

Comparing all the A-site and B-site cationic VDOS contributions and the oxygen anion vibration in BaMO₃ moving across Ti to Cu at B-site, it can be clearly seen in Fig. 3.12(a-h (right)) that the amplitude of all ionic phonon frequencies gradually increase along the 3d series. That is, lattices become more energetic from BaTiO₃ to BaCuO₃. This can be attributed to the relative mass of B-site cations to A-site cations as they remain the same irrespective of metal at B-site in BaMO₃. The principle vibrational mode of Ba²⁺ is observed at ~100 cm⁻¹, where no frequency shifting is observed from BaTiO₃ to BaCuO₃. However, the phonon frequency of B-site cations and oxygen anions slowly shift from a higher to lower regime across Ti to Cu at B-site in BaMO₃ due to the

same reason of metallic masses (heavier atoms vibrate to low-frequency regimes with higher amplitude). Notably, the principle modes of B-site cations are observed at $\sim 200\text{ cm}^{-1}$.

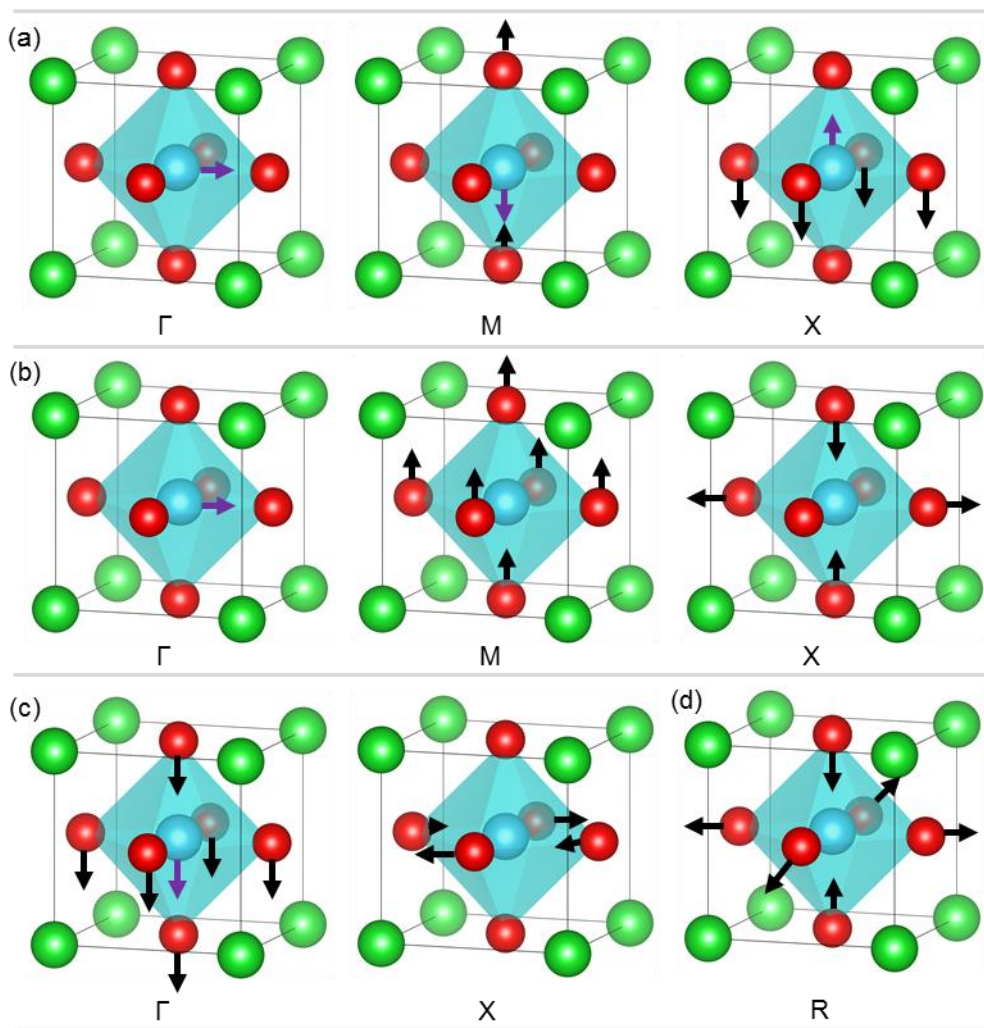


Fig. 3.13 Representation of unstable phonon modes associated with the vibration of (a) BaTiO₃ at the q-points of Γ (left), M (center) and X (right); (b) BaMnO₃ at the q-points of Γ (left), M (center) and X (right); (c) BaCrO₃ at the q-points of Γ (left) and X (right); (d) BaFeO₃ at the q-points of R. Atom colors as per Fig. 3.1.

3.4 Conclusion

In this Chapter, general trends in the calculated formation energies and reducibility of Ba-based perovskites with 3d transition metal B-site cations were characterized. These trends are attributed to the atomic number of the B-site cation and their corresponding valence electrons. Analysis of oxygen vacancy formation energies with thermal corrections demonstrated here that the first three perovskites $\text{BaMO}_{3-\delta}$ ($M = \text{Ti, V, Cr}$) reduce at very high temperature ($>1400 \text{ K}$), where the middle two $\text{BaMnO}_{3-\delta}$ and $\text{BaFeO}_{3-\delta}$ reduce under mild conditions ($<1100 \text{ K}$), and the remaining three $\text{BaMO}_{3-\delta}$ ($M = \text{Co, Ni, Cu}$) perovskites reduced below 400 K , which defines the degree of reducibility moving across $\text{BaTiO}_{3-\delta}$ to $\text{BaCuO}_{3-\delta}$.

The energy required to transfer liberated electrons from an oxygen vacancy to the 3d subshell of transition metals collectively determines the reduction free energy of $\text{BaMO}_{3-\delta}$ ($M = \text{Ti} - \text{Cu}$). The variation in entropic contributions of an individual perovskite to the reduction free energy, which can be attributed to their corresponding phonon contributions, leads the deviation of high-temperature reduction free energy trends from standard conditions. Analysis of phonon spectra and corresponding VDOS of eight $\text{BaMO}_{3-\delta}$ ($M = \text{Ti} - \text{Cu}$) cubic structures demonstrates the stability of BaVO_3 , BaCoO_3 , BaNiO_3 and BaCuO_3 structures, and the origin of instabilities among the other four structures of BaTiO_3 , BaCrO_3 , BaMnO_3 and BaFeO_3 . The variation in vibrational contributions among these lattices is attributed to their corresponding B-site atoms due to their metallic masses.

Thermochemical properties of $\text{BaMO}_{3-\delta}$ such as entropies, specific heats and relative molar enthalpies at low- and high-temperatures show consistency moving across BaTiO_3 to BaCuO_3 over the temperature range $0 - 2000 \text{ K}$. From the quantitative prediction of thermochemical properties, it is evident that the higher masses of the B-site cation have comparatively higher entropic

contributions. Additionally, the vibrational contributions become significant along the 3d series of $\text{BaMO}_{3-\delta}$; thus, their corresponding lattices have gradually higher internal energies.

This work provides valuable insight about the structural stability, thermochemical properties and reduction free energies of $\text{BaMO}_{3-\delta}$. Nevertheless, the overall DFT predicted reduction thermochemistry of $\text{BaMO}_{3-\delta}$ ($M = \text{Ti} - \text{Cu}$) with the thermal correction at high-temperature gives sufficient insight both qualitatively and quantitatively towards their use in temperature-dependent energy conversion applications.

3.5 References

1. Ullmann H, Trofimenko N, Naoumidis A, Stöver D. Ionic/electronic mixed conduction relations in perovskite-type oxides by defect structure. *Journal of the European Ceramic Society*. 1999;19(6-7):791-6.
2. Ishihara T. *Perovskite oxide for solid oxide fuel cells*: Springer Science & Business Media; 2009.
3. Liu Y, Parisi J, Sun X, Lei Y. Solid-state gas sensors for high temperature applications—a review. *Journal of Materials Chemistry A*. 2014;2(26):9919-43.
4. Sunarso J, Hashim SS, Zhu N, Zhou W. Perovskite oxides applications in high temperature oxygen separation, solid oxide fuel cell and membrane reactor: a review. *Progress in Energy and Combustion Science*. 2017;61:57-77.
5. Yao Y-FY. The oxidation of hydrocarbons and CO over metal oxides: IV. Perovskite-type oxides. *Journal of Catalysis*. 1975;36(3):266-75.
6. Kubicek M, Bork AH, Rupp JL. Perovskite oxides—a review on a versatile material class for solar-to-fuel conversion processes. *Journal of Materials Chemistry A*. 2017;5(24):11983-2000.

7. Carrillo RJ, Scheffe JR. Advances and trends in redox materials for solar thermochemical fuel production. *Solar Energy*. 2017;156:3-20.
8. Haeussler A, Abanades S, Jouannaux J, Julbe A. Non-stoichiometric redox active perovskite materials for solar thermochemical fuel production: a review. *Catalysts*. 2018;8(12):611.
9. Chizhik SA, Nemudry AP. Nonstoichiometric oxides as a continuous homologous series: linear free-energy relationship in oxygen exchange. *Physical Chemistry Chemical Physics*. 2018;20(27):18447-54.
10. Merkle R, Mastrikov YA, Kotomin EA, Kuklja MM, Maier J. First principles calculations of oxygen vacancy formation and migration in $Ba_{1-x}Sr_xCo_{1-y}Fe_yO_{3-\delta}$ perovskites. *Journal of The Electrochemical Society*. 2011;159(2):B219-B26.
11. Goodenough JB. Electronic and ionic transport properties and other physical aspects of perovskites. *Reports on Progress in Physics*. 2004;67(11):1915.
12. Calle-Vallejo F, Martínez JI, García-Lastra JM, Mogensen M, Rossmeisl J. Trends in stability of perovskite oxides. *Angewandte Chemie International Edition*. 2010;49(42):7699-701.
13. Li Q, Deng Y-X, Zhu Y-A, Li Y, Sui Z-J, Chen D, et al. Structural stability of lanthanum-based oxygen-deficient perovskites in redox catalysis: a density functional theory study. *Catalysis Today*. 2018.
14. Ezbiri M, Allen KM, Gálvez ME, Michalsky R, Steinfeld A. Design principles of perovskites for thermochemical oxygen separation. *ChemSusChem*. 2015;8(11):1966-71.
15. Kresse G, Furthmüller J. Vienna ab-initio simulation package (VASP). Institut für Materialphysik, Vienna. 2004.

16. Perdew JP, Ruzsinszky A, Csonka GI, Vydrov OA, Scuseria GE, Constantin LA, et al. Restoring the density-gradient expansion for exchange in solids and surfaces. *Physical Review Letters*. 2008;100(13):136406.
17. Blöchl P. Projector augmented-wave method. *Phys Rev B*. 1994;50(24):17953-79.
18. Methfessel M, Paxton A. High-precision sampling for Brillouin-zone integration in metals. *Physical Review B*. 1989;40(6):3616.
19. Kirklin S, Saal JE, Meredig B, Thompson A, Doak JW, Aykol M, et al. The Open Quantum Materials Database (OQMD): assessing the accuracy of DFT formation energies. *Computational Materials*. 2015;1(1):1-15.
20. Birch F. Finite elastic strain of cubic crystals. *Physical Review*. 1947;71(11):809.
21. Nakatani T, Yoshiasa A, Nakatsuka A, Hiratoko T, Mashimo T, Okube M, et al. Variable-temperature single-crystal X-ray diffraction study of tetragonal and cubic perovskite-type barium titanate phases. *Acta Crystallographica Section B: Structural Science, Crystal Engineering and Materials*. 2016;72(1):151-9.
22. Nishimura K, Yamada I, Oka K, Shimakawa Y, Azuma M. High-pressure synthesis of BaVO₃: A new cubic perovskite. *Journal of Physics and Chemistry of Solids*. 2014;75(6):710-2.
23. Hayashi N, Yamamoto T, Kageyama H, Nishi M, Watanabe Y, Kawakami T, et al. BaFeO₃: a ferromagnetic iron oxide. *Angewandte Chemie International Edition*. 2011;50(52):12547-50.
24. Gonze X, Lee C. Dynamical matrices, Born effective charges, dielectric permittivity tensors, and interatomic force constants from density-functional perturbation theory. *Physical Review B*. 1997;55(16):10355.

25. Sundell PG, Björketun ME, Wahnström G. Thermodynamics of doping and vacancy formation in BaZrO₃ perovskite oxide from density functional calculations. *Physical Review B*. 2006;73(10):104112.
26. Giannozzi P, Gironcoli SD, Pavone P, Baroni S. Ab initio calculation of phonon dispersions in semiconductors. *Physical Review B*. 1991;43(9):7231.
27. Monkhorst H, Pack J. Special points for Brillouin-zone integrations. *Physical Review B*. 1976;13(12):5188.
28. Togo A, Tanaka I. First principles phonon calculations in materials science. *Scripta Materialia*. 2015;108:1-5.
29. Deml A, Stevanović V, Holder A, Sanders M, O’Hayre R, Musgrave C. Tunable Oxygen Vacancy Formation Energetics in the Complex Perovskite Oxide Sr_xLa_{1-x}Mn_yAl_{1-y}O₃. *Chemistry of Materials* 2014;26(22):6595–602.
30. Zhukovskii YF, Kotomin EA, Evarestov RA, Ellis DE. Periodic models in quantum chemical simulations of F centers in crystalline metal oxides. *International Journal of Quantum Chemistry*. 2007;107(14):2956-85.
31. Popov A, Kotomin E, Maier J. Basic properties of the F-type centers in halides, oxides and perovskites. *Nuclear Instruments and Methods in Physics Research Section B: Beam Interactions with Materials and Atoms*. 2010;268(19):3084-9.
32. Zacherle T, Schriever A, De Souza R, Martin M. Ab initio analysis of the defect structure of ceria. *Physical Review B*. 2013;87(13):134104.
33. Bjorheim TS, Arrigoni M, Gryaznov D, Kotomin E, Maier J. Thermodynamic properties of neutral and charged oxygen vacancies in BaZrO₃ based on first principles phonon calculations. *Physical Chemistry Chemical Physics*. 2015;17(32):20765-74.

34. Jackson AJ, Walsh A. Oxidation of GaN: An ab initio thermodynamic approach. *Physical Review B*. 2013;88(16):165201.
35. Hayes W, Stoneham AM. *Defects and defect processes in nonmetallic solids*: Courier Corporation; 2012.
36. Allnatt AR, Lidiard AB. *Atomic transport in solids*: Cambridge University Press; 2003.
37. Kirklin S, Saal JE, Meredig B, Thompson A, Doak JW, Aykol M, et al. The Open Quantum Materials Database (OQMD): assessing the accuracy of DFT formation energies. *Computational Materials*. 2015;1:15010.
38. Rossmeisl J, Logadottir A, Nørskov JK. Electrolysis of water on (oxidized) metal surfaces. *Chemical Physics*. 2005;319(1-3):178-84.
39. Chase Jr M, Davies C, Downey Jr J. *JANAF Thermochemical Tables Third Edition Part II, Cr-Zr*, American Institute of Physics. Inc, New York. 1986:1243-5.
40. Steva V, Lany S, Zhang X, Zunger A. Correcting density functional theory for accurate predictions of compound enthalpies of formation: Fitted elemental-phase reference energies. *Physical Review B*. 2012;85(11):115104.
41. Hammer B, Hansen LB, Nørskov JK. Improved adsorption energetics within density-functional theory using revised Perdew-Burke-Ernzerhof functionals. *Physical Review B*. 1999;59(11):7413.
42. Martinez JI, Hansen HA, Rossmeisl J, Nørskov JK. Formation energies of rutile metal dioxides using density functional theory. *Physical Review B*. 2009;79(4):045120.
43. Nørskov JK, Bligaard T, Rossmeisl J, Christensen CH. Towards the computational design of solid catalysts. *Nature Chemistry*. 2009;1(1):37.

44. Hammer B, Norskov JK. Why gold is the noblest of all the metals. *Nature*. 1995;376(6537):238-40.
45. Seuter A. *Philips Res Rep Suppl* 1974;3.
46. Kolodiaznyi T, Tachibana M, Kawaji H, Hwang J, Takayama-Muromachi E. Persistence of ferroelectricity in BaTiO₃ through the insulator-metal transition. *Physical Review Letters*. 2010;104(14):147602.
47. Kolodiaznyi T. Insulator-metal transition and anomalous sign reversal of the dominant charge carriers in perovskite BaTiO_{3-δ}. *Physical Review B*. 2008;78(4):045107.
48. Zhu Z, Rueckert F, Budnick J, Hines W, Jain M, Zhang H, et al. Magnetic and electronic structure of the film-stabilized Mott insulator BaCrO₃. *Physical Review B*. 2013;87(19):195129.
49. Bader R, Nguyen-Dang TT, Tal Y. A topological theory of molecular structure. *Reports on Progress in Physics*. 1981;44(8):893.
50. Ghose KK, Bayon A, Hinkley J, Page AJ. Electronic structure and high-temperature thermochemistry of BaZrO_{3-δ} perovskite from first-principles calculations. *Physical Chemistry Chemical Physics*. 2019;21(23):12468-76.
51. Balachandran J, Lin L, Anchell JS, Bridges CA, Ganesh P. Defect genome of cubic perovskites for fuel cell applications. *The Journal of Physical Chemistry C*. 2017;121(48):26637-47.
52. Mahmood Q, Ali S, Hassan M, Laref A. First principles study of ferromagnetism, optical and thermoelectric behaviours of AVO₃ (A= Ca, Sr, Ba) perovskites. *Materials Chemistry and Physics*. 2018;211:428-37.

53. Bork AH, Povoden-Karadeniz E, Rupp JL. Modeling Thermochemical Solar-to-Fuel Conversion: CALPHAD for Thermodynamic Assessment Studies of Perovskites, Exemplified for (La, Sr) MnO₃. *Advanced Energy Materials*. 2017;7(1):1601086.
54. Liu D, Yan Y, Zhou H. Synthesis of Micron-Scale Platelet BaTiO₃. *Journal of the American Ceramic Society*. 2007;90(4):1323-6.
55. Li J-H, Fu X-Z, Luo J-L, Chuang KT, Sanger AR. Application of BaTiO₃ as anode materials for H₂S-containing CH₄ fueled solid oxide fuel cells. *Journal of Power Sources*. 2012;213:69-77.
56. Arévalo-López AM, Attfield JP. High-pressure BaCrO₃ polytypes and the 5H-BaCrO_{2.8} phase. *Journal of Solid State Chemistry*. 2015;232:236-40.
57. Iwakuni H, Shinmyou Y, Yano H, Matsumoto H, Ishihara T. Direct decomposition of NO into N₂ and O₂ on BaMnO₃-based perovskite oxides. *Applied Catalysis B: Environmental*. 2007;74(3-4):299-306.
58. Bu Y-F, Ding D, Gan L, Xiong X-H, Cai W, Tan W-Y, et al. New insights into intermediate-temperature solid oxide fuel cells with oxygen-ion conducting electrolyte act as a catalyst for NO decomposition. *Applied Catalysis B: Environmental*. 2014;158:418-25.
59. Xian H, Zhang X, Li X, Li L, Zou H, Meng M, et al. BaFeO_{3-x} perovskite: An efficient NO_x absorber with a high sulfur tolerance. *The Journal of Physical Chemistry C*. 2010;114(27):11844-52.
60. Xian H, Li F-L, Li X-G, Zhang X-W, Meng M, Zhang T-Y, et al. Influence of preparation conditions to structure property, NO_x and SO₂ sorption behavior of the BaFeO_{3-x} perovskite catalyst. *Fuel Processing Technology*. 2011;92(9):1718-24.

61. Hayashi H, Inaba H, Matsuyama M, Lan N, Dokiya M, Tagawa H. Structural consideration on the ionic conductivity of perovskite-type oxides. *Solid State Ionics*. 1999;122(1-4):1-15.
62. Ishihara T. Structure and properties of perovskite oxides. *Perovskite oxide for solid oxide fuel cells*: Springer; 2009. p. 1-16.
63. Ghosez P, Cockayne E, Waghmare U, Rabe K. Lattice dynamics of BaTiO₃, PbTiO₃, and PbZrO₃: A comparative first-principles study. *Physical Review B*. 1999;60(2):836.
64. Rondinelli JM, Eidelson AS, Spaldin NA. Non-d⁰ Mn-driven ferroelectricity in antiferromagnetic BaMnO₃. *Physical Review B*. 2009;79(20):205119.
65. Ghosez PSH, Gonze X, Michenaud J-P. Ab initio phonon dispersion curves and interatomic force constants of barium titanate. *Ferroelectrics*. 1998;206(1):205-17.
66. Satapathy S, Singh M, Pandit P, Gupta P. Relaxor ferroelectric behavior of BaMnO₃ (2H) at room temperature. *Applied Physics Letters*. 2012;100(4):042904.

Chapter 4: Trends in High-Temperature Reduction Thermochemistry of RCoO_3 ($\text{R} = \text{La}, \text{Ce}, \text{Nd}, \text{Sm}$): Effects of A-site Cation

4.1 Introduction

Chapter 3 studied the effect of the B-site cation into the structural, thermochemical and reduction properties of perovskite materials. This chapter discusses the variation of the A-site composition on the properties of the perovskites with rare earth element (R^{3+}) as A-site cation and transition metal (e.g. Co^{3+}) as B-site. From the B-site metals studied in Chapter 3, Co has been selected for the study of A-site element. The reason behind the investigation of Co at B-site is, Co^{3+} in an octahedral coordination environment can exist either in a low-spin state (LS, $t_{2g}^6 e_g^0$, $S = 0$), an intermediate-spin state (IS, $t_{2g}^5 e_g^1$, $S = 1$), or even a high-spin state (HS, $t_{2g}^4 e_g^2$, $S = 2$) depending on temperature.^[1-4] These temperature-dependent electronic properties and the stability under both high temperature and oxidizing conditions make cobalt lanthanide-based RCoO_3 perovskites excellent candidates for electrocatalytic applications (such as ORR and OER) at intermediate temperature (900 – 1200 K),^[3, 5-7] and as catalyst precursors for the conversion of methane to synthesis gas.^[8] In addition, Emery et al.^[9] demonstrated that RCoO_3 ($\text{R} = \text{La}, \text{Ce}, \text{Nd}, \text{Pm}, \text{Sm}, \text{Tb}, \text{Ac}$) display reduction free energies (at 0 K) close to the state-of-art solar thermochemical water splitting material CeO_2 .

Perovskites with a rare earth element (R^{3+}) as A-site cation and transition metal (e.g. Co^{3+}) as B-site cation can form identical valance charge (III-III) in their A-/B-site in RCoO_3 , and exhibit high electronic conductivity.^[10] RCoO_3 perovskites show temperature-induced insulator-to-metal and non-magnetic transitions, arising from the different electron configurations available to the Co^{3+} d^6 cation. Bhide et al.^[5, 6] studied LS-to-HS transitions in LaCoO_3 across the temperature range

from 4.2 K up to 1200 K, and reported that at temperatures below 200 K, LS Co^{3+} dominates over HS. With increasing temperature, the population of Co^{3+} start to decrease from e_g state and completely disappears at 1210 K. The spin-state equilibria in RCoO_3 were also studied between 110 – 550 K by Bose et al.^[11] and found the coexistence of both LS and HS states. The structural, electrical and thermal conductivity of LaCoO_3 were studied by Raccah and Goodenough,^[3] reporting a first-order phase change at 1210 K and a higher-order transition in temperature interval between 398 – 648 K and 923 K. Furthermore, NdCoO_3 exhibits high Seebeck coefficients at room temperature, making it a potential thermoelectric material.^[12] Also, SmCoO_3 exhibits excellent abilities as a gas-sensing material, as well as in proton SOFC electrode and methanol fuel cell applications.^[13-15]

The above discussions suggest that a rare-earth cation at A-site along with Co at B-site have the highest potentiality for use in high-temperature energy applications. Similar to the BaMO_3 perovskites studied in Chapter 3, the influence of the A-site element in the temperature-dependent thermochemical and reduction properties of $\text{RCoO}_{3-\delta}$ has not been deeply investigated before. Chapter 4 reports the effect of the modification of the A-site element on the structural, thermochemical and reduction properties of RCoO_3 ($\text{R} = \text{La}, \text{Ce}, \text{Nd}, \text{Sm}$) cobalt lanthanide-based perovskites. We limited our investigation with these elements considering the nearest-neighbor A-site atomic number in this series suggested by Emery et al.^[9] discarding Pm for their radioactive nature. The effect of the atomic number of R into electrical and thermochemical properties is shown here. Notably, cubic RCoO_3 perovskites are considered here as perovskites are normally cubic at elevated temperature related to STWS and SOFC applications.^[16]

4.2 Computational Methods

Cubic RCoO_3 ($Pm\bar{3}m$) ($R = \text{La, Ce, Nd, Sm}$) unit cells were constructed by considering R atom at center point (0, 0, 0), Co at the point (1/2, 1/2, 1/2) and three O atoms located at (0, 1/2, 1/2), (1/2, 1/2, 0), and (1/2, 0, 1/2) sites. The unit cells were optimized with spin-polarized DFT calculations using VASP.^[17] All DFT calculations reported here were performed using the PBEsol^[18] functional with PAW-PP.^[19] BZ sampling was performed using a $4 \times 4 \times 4$ Monkhorst-Pack k-point scheme. The plane-wave basis set used a 500 eV cut-off criterion, and the total DFT energy was fully optimized with respect to ionic positions, cell shape and cell volume, using a convergence criterion of 1.0×10^{-8} eV. The equilibrium cell volumes of cubic RCoO_3 were obtained through lattice optimization by calculating the ground state energies with respect to the corresponding cell volume of perovskites and fitting the data to the BM EOS.^[20] Additional lattice optimizations were carried out with fixed equilibrium volume by relaxing cell shape and ion, so that a full minimization of the internal structural degrees of freedom is given to the atoms. The pure elemental ground-state structures are chosen from OQMD^[21] and energy calculations were with the similar set up as described in Chapter 3 §3.2.1.

A $2 \times 2 \times 2$ RCoO_3 supercell was used with the number of k points reduced accordingly to predict the thermochemical properties of RCoO_3 and $\text{RCoO}_{3-\delta}$ via DFPT,^[22] which defines S , C_v , E and A as described in equations (2.54 – 2.57). C_p is then calculated using quasi-harmonic approximations as described in equation (2.58). This $2 \times 2 \times 2$ supercell represents an ideal balance between computational efficiency and thermodynamic accuracy, as demonstrated in previous investigations^[23] showing oxygen vacancy formation energy to be converged within this supercell size. The real-space force constants of the crystallographic supercells were calculated via finite differences (atomic displacements of 0.01 Å).^[22, 24] Phonon modes were then calculated with a

Monkhorst-Pack^[25] grid of $48 \times 48 \times 48$ q points for the phonon wave vectors, using Phonopy.^[26] The reduction free energies of $\text{RCoO}_{3-\delta}$ were calculated using the methodologies described in Deml et al.^[27, 28] and Ezbiri et al.^[29] Single neutral oxygen vacancies were created by randomly removing one oxygen atom to afford $\delta=0.125$ (i.e. a single oxygen vacancy in the $2 \times 2 \times 2$ supercell). The structures of $\text{RCoO}_{3-\delta}$ were fully optimized with cubic symmetry and under constant-volume conditions.^[23, 28]

4.3 Results and Discussion

4.3.1 Trends in Lattice Structures and Formation Energies of Cubic RCoO_3

The optimized lattice constants are compared with available experimental data in Table 4.1. It is found that the equilibrium lattice parameters of cubic RCoO_3 ($\text{R} = \text{La}, \text{Ce}, \text{Nd}, \text{Sm}$) perovskites using PBEsol functionals are between 3.69 to 3.79 Å, which are within 1% of the experimental results. Notably, the optimized lattice parameters of cubic RCoO_3 show a linear correlation with the atomic number of A-site cation, whereas the values decrease with respect to the increasing atomic number of A-site cation. However, LaCoO_3 and CeCoO_3 exhibit identical theoretical lattice constants, while the experimental values differ by 0.02 Å.

Table 4.1 Comparison of calculated and experimental lattice parameter of cubic ($Pm\bar{3}m$) RCoO_3 .

(a/Å)	LaCoO_3	CeCoO_3	NdCoO_3	SmCoO_3
PBEsol-PAW	3.79	3.79	3.76	3.72
Exp.	3.82 ^[30, 31]	3.80 ^[30]	3.77 ^[30, 31]	3.75 ^[31]

The standard formation energy of cubic RCoO_3 perovskites was calculated from their elementary components using equations (3.5 – 3.7) and illustrated in Fig. 4.1. In contrast with the results presented in Chapter 3 for BaMO_3 ($M = \text{Ti} - \text{Cu}$), where formation energies decrease linearly with the atomic number of B-site cation, here the formation energies of RCoO_3 increase with the atomic number of the A-site cation. The energy difference across the A-site series of RCoO_3 is between $\sim 2 - 30 \text{ kJ mol}^{-1}$, meaning that perovskites with identical oxidation state (+III) at A and B-site (RCoO_3 ; $R = \text{La, Ce, Nd, Sm}$) exhibit comparable formation energy, while mixed oxidation states between A and B sites (+II and +IV), like in BaMO_3 ($M = \text{Ti} - \text{Cu}$) exhibit larger differences, $\sim 80 - 200 \text{ kJ mol}^{-1}$, but ordered formation energies. These trends in formation energy were also observed by Calle-Vallejo et al.^[32] for $(\text{Ca, Sr, Ba})\text{MO}_3$ with mixed A/B-site oxidation states, and $(\text{La, Y})\text{CoO}_3$ with identical A/B-site oxidation states. This is in agreement with the CeCoO_3 , NdCoO_3 and SmCoO_3 perovskites showed in this work.

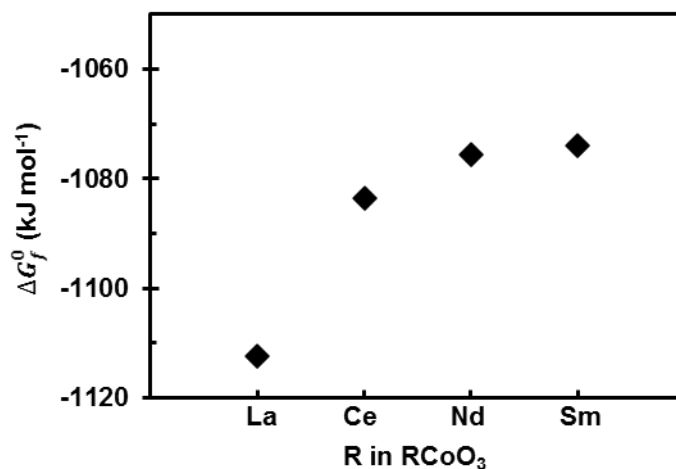


Fig. 4.1 Trends in calculated PBEsol-PAW ΔG_f^0 values of RCoO_3 ($R = \text{La, Ce, Nd, Sm}$) at standard conditions ($p^\circ = 1 \text{ atm}$, $T = 298 \text{ K}$).

4.3.2 Reduction Thermochemistry of Cubic $\text{RCoO}_{3-\delta}$ at 0 K

4.3.2.1 Oxygen Vacancy Formation Energies

The oxygen vacancy formation energies (E_v) of $\text{RCoO}_{3-\delta}$ for single neutral oxygen defect at 0 K is shown in Table 4.2. Comparing the E_v values of $\text{RCoO}_{3-\delta}$, it is clear that there exist two distinct scales of reduction free energies among the investigated perovskites. For instance, $\text{LaCoO}_{3-\delta}$ and $\text{CeCoO}_{3-\delta}$ exhibit E_v values exceeding 330 kJ mol^{-1} , while $\text{NdCoO}_{3-\delta}$ and $\text{SmCoO}_{3-\delta}$ have E_v values some 100 kJ mol^{-1} lower ($< 230 \text{ kJ mol}^{-1}$). The lower E_v values here correspond to lower temperature thermal reduction. These results suggest that CeCoO_3 is the most stable compound at 0 K of those considered, while SmCoO_3 is substantially easier to be found in a reduced form at 0 K. With $\text{CeCoO}_{3-\delta}$ as an exception, the calculated E_v values of $\text{RCoO}_{3-\delta}$ become less positive with increasing A-site cation atomic number.

For the series studied in this thesis (Chapter 3 and Chapter 4), these trends in reduction free energy of ABO_3 perovskites without thermal corrections can be described in terms of their A/B-site cation atomic numbers. The reducibility of BaMO_3 and RCoO_3 at 0 K increase with the increasing atomic number of A/B-site cations from left to right in the periodic table. The difference between the E_v values of first two compounds in RCoO_3 series, i.e. $\text{LaCoO}_{3-\delta}$ and $\text{CeCoO}_{3-\delta}$ is 31 kJ mol^{-1} , whereas, between the last two compounds, $\text{NdCoO}_{3-\delta}$ and $\text{SmCoO}_{3-\delta}$ is 16 kJ mol^{-1} , which are very minimal compared to the nearest neighbor compounds in $\text{BaMO}_{3-\delta}$ series discussed in Chapter 3. Thus, in general, it implies that the A-site atomic number have comparably less impact on reduction free energy than the B-site atomic number in ABO_3 perovskites, at least for the investigated materials here.

Table 4.2 Calculated PBEsol-PAW E_v (kJ mol⁻¹) of cubic RCoO_{3-δ} without thermal corrections.

T (K)	LaCoO ₃	CeCoO ₃	NdCoO ₃	SmCoO ₃
0	336.18	367.38	227.82	211.74

4.3.2.2 Electronic Structures Analysis: Effect of Oxygen Vacancy and A-site Cation

Electronic structure analysis allows us to examine more closely the trends observed in oxygen vacancy formation energy of RCoO_{3-δ} perovskites in terms of chemical bonding between R, Co and O. This section systematically investigates the electronic properties of all pristine and defect RCoO_{3-δ} (R = La, Ce, Nd, Sm) structures through the electronic BS of perovskites and their corresponding PDOS. The charge partitioning of each cation and anion in respective perovskite is also characterized by effective Bader charges analysis and the localization vacancy site electrons to cations are shown by charge density distribution analysis.

To understand the electronic occupation over energy states, the electronic BS of pristine- and defect-RCoO_{3-δ} are illustrated over BZ as shown in Fig. 4.2(a-d). The PBEsol predicted BS of pristine-LaCoO₃ gives a metallic state in accordance with the local spin density approximation,^[33] where no bandgap is found in both spin-up and spin-down channels (Fig. 4.2(a)). However, the experimentally observed BS of LaCoO₃ is found in the semiconducting state.^[34] This is a well-known factor that DFT underestimates the electronic band gap due to poor treatment of energy splitting between occupied and empty states,^[35-39] yet generates the basic electronic structure to rationalize the electronic contributions of each species.

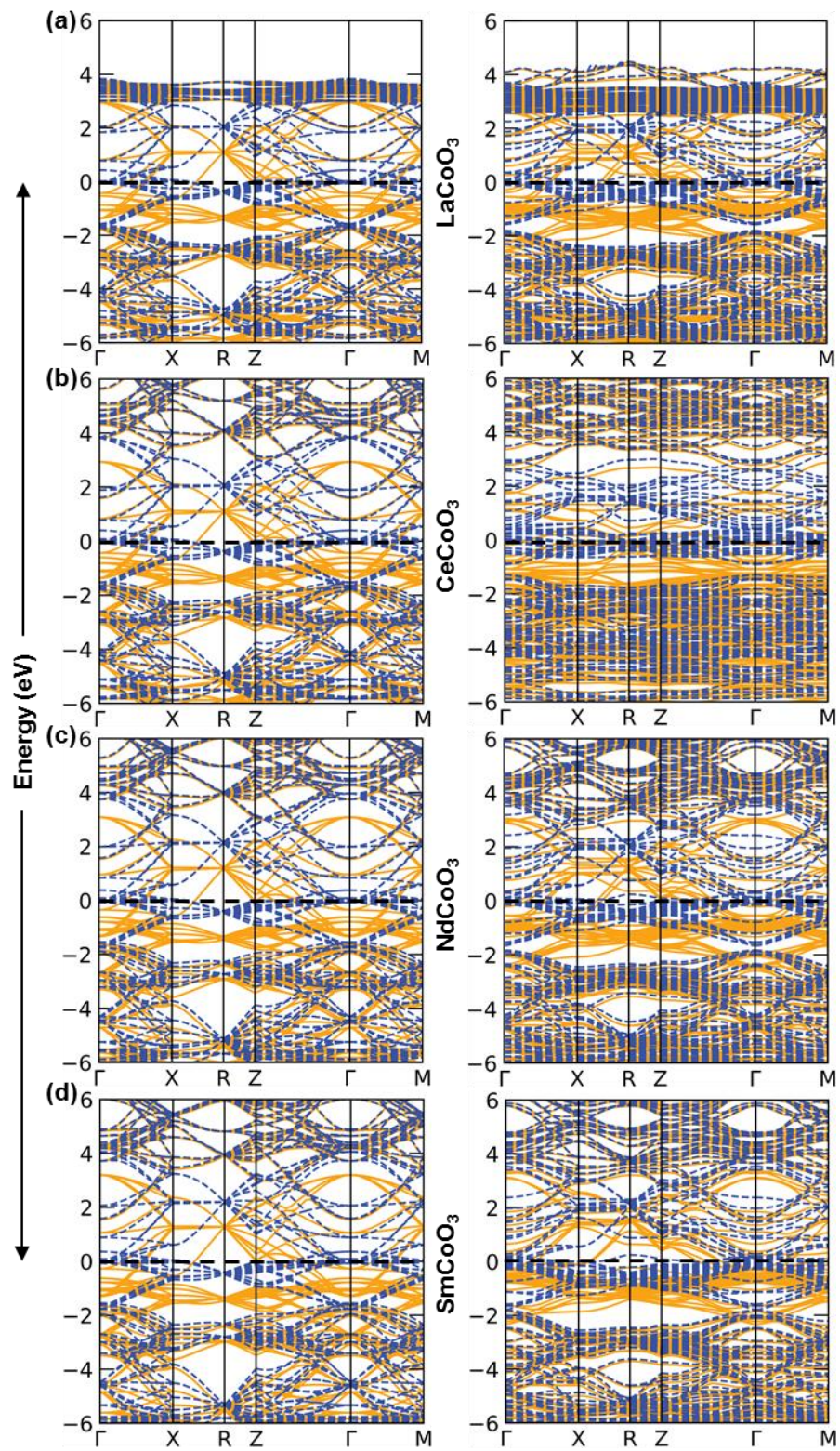


Fig. 4.2 Spin polarized electronic BS of representative $2 \times 2 \times 2$ supercell of pristine- RCoO_3 (R = La, Ce, Nd, Sm) (left) and defect- $\text{RCoO}_{2.875}$ (right): (a) LaCoO_3 , (b) CeCoO_3 , (c) NdCoO_3 , (d) SmCoO_3 , along high symmetry directions in the BZ. The solid yellow and the dashed blue lines represent different spin channels (spin-up and spin-down, respectively). The black dashed lines represent the Fermi energy level of each perovskite set to 0 eV.

Contrary, in defect supercell the spin-down channel presents a small bandgap still, the spin-up channel is metallic. The BS of CeCoO_3 (Fig. 4.2(b)) is very similar to LaCoO_3 bands, except that higher energy states above 4 eV are occupied due to Ce-4f bands. Furthermore, in defect- $\text{CeCoO}_{2.875}$ electronic structure, the bandgap between spin-down channels slightly shift up towards the Fermi level, indicating spin-up channels have dominating metallic behavior.

In the pristine- NdCoO_3 (Fig. 4.2(c)) and - SmCoO_3 (Fig. 4.2(d)) electronic structures, both the spin-up and the spin-down channels indicate metallic behavior. Interestingly, the defect- $\text{NdCoO}_{2.875}$ exhibit a bandgap at Γ -point for spin-down bands, but the defect- $\text{SmCoO}_{2.875}$ has no gap in between both channels. In all four cubic RCoO_3 perovskites structures, Co^{3+} is a d^6 center coordinated with O^{2-} anions in octahedral coordination. The spin configuration of Co^{3+} in CoO_6 octahedra can exhibit LS ($t_{2g}^6 e_g^0$, $S=0$) ground state phase to a HS ($t_{2g}^4 e_g^2$, $S=2$) via an IS ($t_{2g}^5 e_g^1$, $S=1$) due to its unusual magnetic behavior, where the stabilization of intermediate-spin state depends on the hybridization of Co-3d and O-2p orbitals.^[40-42] Thus, the projection of the wavefunction on the localized states are shown here only for Co-site with 3d- t_{2g} states (d_{xy} , d_{yz} and d_{xz}), 3d- e_g states (d_z^2 , $d_x^2-y^2$), and O-2p states.

The PDOS of pristine- LaCoO_3 show that (Fig. 4.3(a)), the occupation of $d-t_{2g}\uparrow$ and $d-t_{2g}\downarrow$ have the asymmetric population, where the peak DOS of $d-t_{2g}\uparrow$ and $d-t_{2g}\downarrow$ states are apparent near to the

Fermi level and below the Fermi level (~ 1 eV), respectively. On the other hand, the defect-LaCoO₃ reflects that the O-2p DOS become narrower over the energy range considered here. The d-p-d hybridization at the bottom edge of d-t_{2g} \uparrow and d-t_{2g} \downarrow states become weakened, which is an indication of Co-O bonds broken.

The PDOS of pristine-CeCoO₃ (Fig. 4.3(b)) has an almost similar occupation of states as observed in pristine-LaCoO₃; however, the oxygen vacancy impacts the overall O-2p DOS in the defective-CeCoO₃. Comparing the PDOS of pristine- and defect-CeCoO₃, it can be observed that, the O-2p DOS at spin-up channel lose its energy, but again gain that lost energy in Co-d-t_{2g} \uparrow states at the same energy level. Contrary, the band center of down-spin channel O-2p shifted upward to E_F and lose hybridization at the bottom edge of d-t_{2g} \downarrow states. This can be rationalized with the energetic redistribution of O-2p electron density upon forming the oxygen vacancy.

The pristine-NdCoO₃ (Fig. 4.3(c)) and -SmCoO₃ (Fig. 4.3(d)) have almost identical distributions of PDOS over the energy ranges, whereas the d-band center has slightly downshift from E_F in SmCoO₃ compared to NdCoO₃. On the other hand, the PDOS of O-2p shrink in defect structure for both perovskites, and the d-p-d hybridization becomes weak at the bottom edge of d-t_{2g} states in the both up-/down-spin channels. The above results strongly suggest the reduction of Co³⁺ in all four defect structures occurred due to the loss of energy in Co-O bonding overlapping (d-p-d hybridization) point.

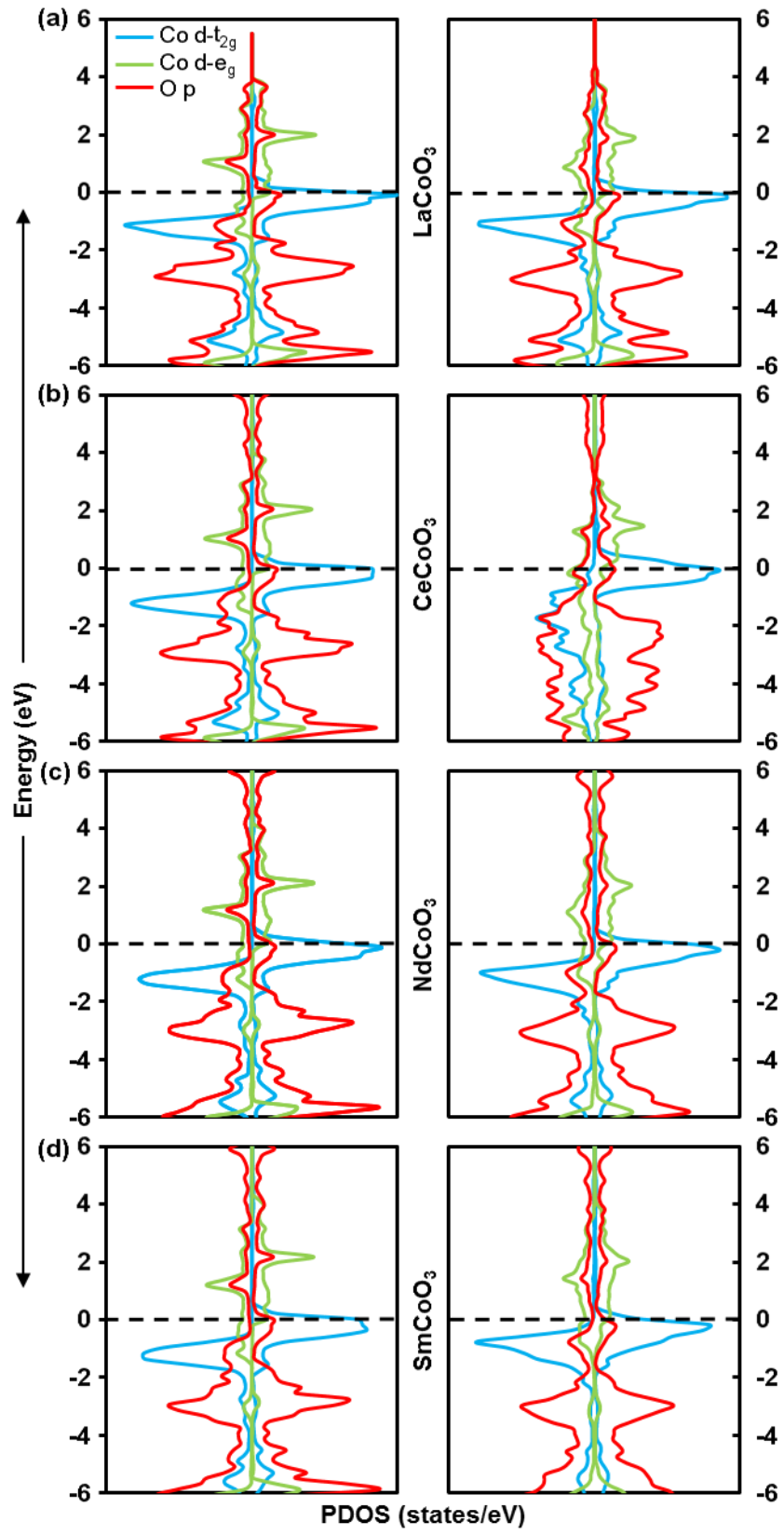


Fig. 4.3 PDOS of representative $2 \times 2 \times 2$ supercell of pristine- RCoO_3 ($\text{R} = \text{La, Ce, Nd, Sm}$) (left) and defect- $\text{RCoO}_{3-\delta}$ (right): (a) LaCoO_3 , (b) CeCoO_3 , (c) NdCoO_3 , (d) SmCoO_3 . The black dashed lines represent the Fermi energy level of each perovskite set to 0 eV. The color lines – blue, green and red represents the PDOS of corresponding Co-3d t_{2g} , Co-3d e_g and O-2p orbitals for respective RCoO_3 perovskites. The arrow in the upper left/right depicted PDOS values for spin-up/spin-down, respectively.

Bader charge analysis^[43] was performed in both pristine and defective supercells to compare and analyze the charge transfer and redistribution among ions in lattice from the vacancy site. The average charge partitioning schemes on cations and anions in pristine and defect- $\text{RCoO}_{3-\delta}$ supercells are reported in Table 4.3. The charge accumulation from vacant site to the two nearest neighbor Co^{3+} cations are also included here. Comparing the charge distribution on each species in pristine cell, it is evident that the charge on A-site cations vary significantly (+1.99 to +2.21 e) among different compounds in $\text{RCoO}_{3-\delta}$ but found an almost identical charge on B-site cations irrespective of A-site cations (La, Ce, Nd) in $\text{RCoO}_{3-\delta}$. That is, the identity of A-site cation has an insignificant effect on the assigned charge to B-site cation.

Similar trends are observed on the partitioned charge of cations and anions in defect cells for all these three perovskites. The single exception from this trend are observed in $\text{SmCoO}_{3-\delta}$, with a discrepancy of ~11% more positive charge assigned to B-site cation compare to other three perovskites. This difference could occur due to the average Co-O bond covalency accompanying different A-site cations, whereas substitution of smaller ion leads Co-O bond length compression. This is well justified in the PDOS of Co-3d and O-2p states of respective perovskites.

Table 4.3 Bader charge partitioning on R, Co and O (q in e) in the $2 \times 2 \times 2$ pristine- and defect- $\text{RCoO}_{3-\delta}$ supercell. All values (q_R , q_{Co} , q_O) are averaged over the number of species, where q_{Co1} and q_{Co2} represent the values for individual nearest neighbor B-site cations from vacancy site.

	Pristine cell			Defect cell				
	q_R	q_{Co}	q_O	q_R	q_{Co}	q_O	q_{Co1} (NN)	q_{Co2} (NN)
LaCoO_3	+1.99	+1.42	-1.14	+1.97	+1.34	-1.5	+1.09	+1.1
CeCoO_3	+2.21	+1.42	-1.21	+2.18	+1.33	-1.22	+1.09	+1.08
NdCoO_3	+2.12	+1.43	-1.18	+2.10	+1.34	-1.19	+1.08	+1.1
SmCoO_3	+2.06	+1.58	-1.21	+2.04	+1.47	-1.22	+1.16	+1.18

On the other hand, for a given $\text{RCoO}_{3-\delta}$ perovskite the charges on A-site cations have little decrement ($\sim 1\%$) from pristine to defect cells, whereas this decrease is substantial ($\sim 6\text{-}7\%$) for B-site cations. Moreover, the two nearest neighbor B-site cations accumulated most of the transferred charge assigned to the Co^{3+} cations in defect cell, where these two NN-Co cations (Co1 and Co2 as marked in Fig. 4.4(right)) mostly reduced than the other non-nearest neighbor B-site cations (see Table 4.3). Remarkably, the charge assigned to O anions in all pristine- and defect- $\text{RCoO}_{3-\delta}$ reveals that the negative charge on O anion increases only by 1% from their pristine cell. This implies that the charge from vacancy site mostly assigned to the B-site cations in $\text{RCoO}_{3-\delta}$.

Fig 4.4(a) shows the proportion of electric charge accepted by A- and B-site cations in defect- $\text{RCoO}_{3-\delta}$ supercell from the vacant oxygen site. The charge transferred to A-site cation varies between 0.17 to 0.22 e in $\text{RCoO}_{3-\delta}$, where Ce cation in $\text{CeCoO}_{3-\delta}$ has dominant feature. On the

other hand, the B-site cation in $\text{SmCoO}_{3-\delta}$ accumulated the maximum quantity of charge ($\sim 0.84 e$) in defect cell, where the quantity of charges remain almost invariant ($\sim 0.69 \pm 0.01 e$) for other three perovskites. It seems from the figure that the identity of A-site cation has very little impact on charge accumulation from the vacant site.

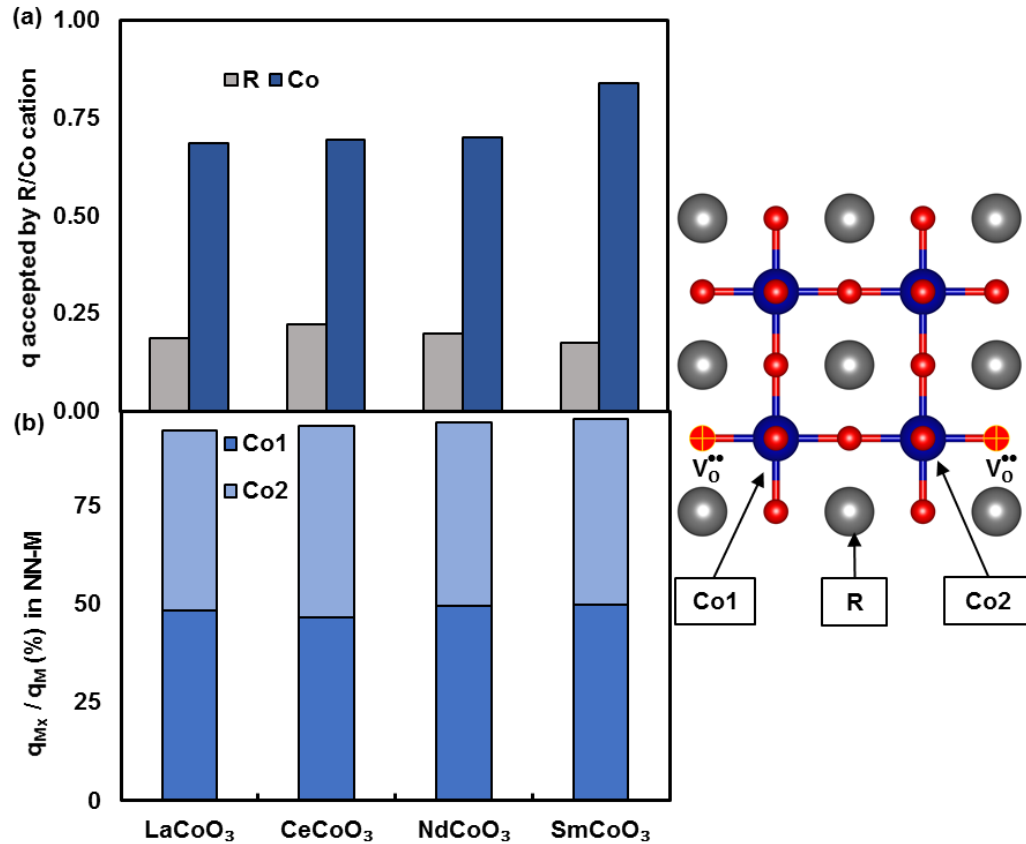


Fig. 4.4 (a) The proportion of electrons accumulated by A/B-site cations in the defect- $\text{RCoO}_{3-\delta}$ lattices. The grey and blue bars represent the amount of Bader charges (q in e) transferred from the vacant site to R and Co cations, respectively, in corresponding perovskites. (b) The percentage of electrons accepted by the two nearest neighbor Co^{3+} cations (position indicated in right side figure) from the total transferred charge to B-site cation in (a).

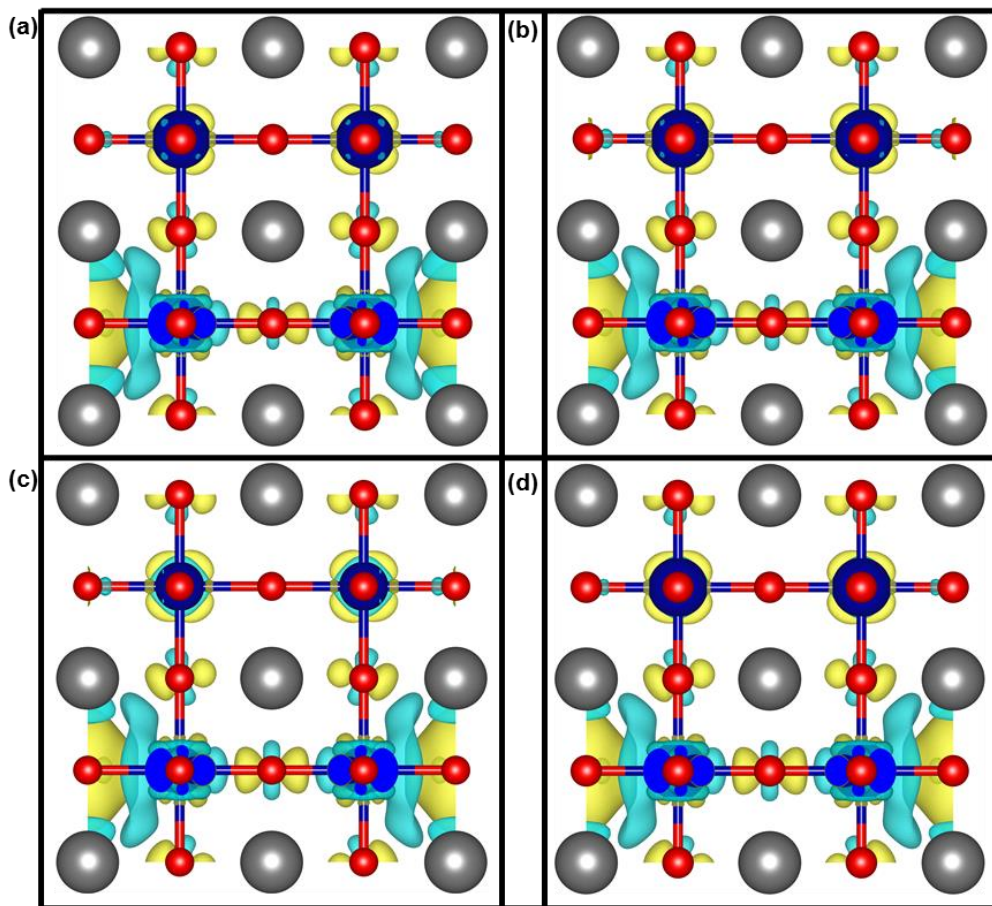


Fig. 4.5 Electronic CDD of representative (a) $\text{LaCoO}_{3-\delta}$, (b) $\text{CeCoO}_{3-\delta}$, (c) $\text{NdCoO}_{3-\delta}$, (d) $\text{SmCoO}_{3-\delta}$. The grey, blue and red spheres represent R (R = La, Ce, Nd, Sm), Co and O atoms, respectively. For the CDD analysis, $2 \times 2 \times 2$ pristine- RCO_3 is taken as the reference density in all cases with an oxygen vacancy in the neutral charge state. CDD isosurfaces are drawn with a threshold of 0.002 e au^{-3} ; yellow/blue isosurface represents charge depletion/accumulation.

Fig. 4.4(b) represents the percentage of electron charges accepted by the two nearest neighbor Co^{3+} cations in each defect cell of $\text{RCO}_3-\delta$ perovskites. Comparably, the total negative charges transferred from the vacant site to the B-site cations in the lattice (Fig. 4.4(a)), are mostly redistributed ($\sim 93\text{-}95\%$) to their nearest neighbor Co^{3+} cations, where the rest $\sim 5\text{-}7\%$ charge

distributed to the non-nearest neighbor Co^{3+} cation. This reflects that the nature of charge delocalization from vacant site to the B-site cations generates the reduction of two NN-Co cations upon oxygen vacancy formation. In order to study the charge delocalization, a CDD analysis is performed and shown in Fig. 4.5, which has an exact agreement with the Bader charge analysis.

4.3.3 Reduction Thermochemistry of Cubic $\text{RCoO}_{3-\delta}$ with Thermal Corrections

4.3.3.1 Temperature-Dependent Reduction Free Energies

The reduction free energies of cubic $\text{RCoO}_{3-\delta}$ with thermal corrections are discussed here at standard conditions and high-temperature. Table 4.4 shows that the inclusion of temperature-dependent thermal corrections to E_v values of $\text{RCoO}_{3-\delta}$ significantly impact their Gibbs free energies of reduction (ΔG_{RR}), even under standard conditions. At standard conditions, the reducibility of $\text{RCoO}_{3-\delta}$ increases almost 20% from their 0 K energy.

Table 4.4 Calculated PBEsol-PAW ΔG_{RR} (kJ mol^{-1}) of cubic $\text{RCoO}_{3-\delta}$ at standard condition.

T (K)	LaCoO ₃	CeCoO ₃	NdCoO ₃	SmCoO ₃
298.15	268.95	305.31	175.71	179.69

Fig. 4.6 shows the ΔG_{RR} with the variation of temperature between 0 – 1800 K. Within this range of temperature all four $\text{RCoO}_{3-\delta}$ perovskites are predicted to undergo spontaneous reduction reactions ($\Delta G_{RR} \leq 0$) (Fig. 4.6), however, the spontaneous reduction temperature varies with respect to the change of A-site cations. For instance, the reduction of LaCoO₃ to LaCoO_{2.875} is 36 kJ mol^{-1} less endothermic than the reduction of CeCoO₃ to CeCoO_{2.875} at standard conditions, whereas the reduction of SmCoO₃ is unexpectedly 4 kJ mol^{-1} more endothermic than the reduction of NdCoO₃. Though the reduction of SmCoO₃ shows a significant deviation in ΔG_{RR} values at high

temperatures from its standard conditions. For example, the ΔG_{RR} value of $\text{SmCoO}_{3-\delta}$ is 93 kJ mol^{-1} at 1000 K , differs by 59 kJ mol^{-1} more than the nearest neighbor compounds $\text{NdCoO}_{3-\delta}$ and most surprisingly 21 kJ mol^{-1} more endothermic than $\text{LaCoO}_{3-\delta}$. This suggests that SmCoO_3 is comparably more stable at high temperature than LaCoO_3 and NdCoO_3 . $\text{SmCoO}_{3-\delta}$ is found to be undergone spontaneous reduction reaction at a maximum temperature of $\sim 1640 \text{ K}$.

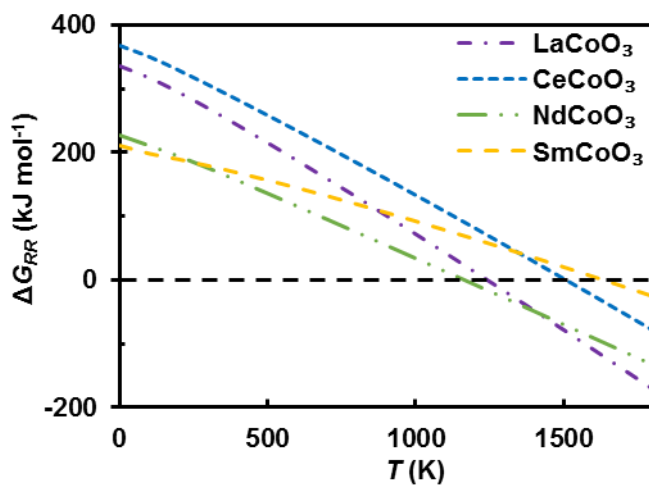


Fig. 4.6 Calculated PBEsol-PAW ΔG_{RR} values (kJ mol^{-1} , per single oxygen defect) (equation (3.9)) for $\text{RCoO}_{3-\delta}$ ($\text{R} = \text{La}, \text{Ce}, \text{Nd}, \text{Sm}$) with thermal corrections between $0 - 1800 \text{ K}$ and $p^\circ = 1 \text{ atm}$. Below the straight horizontal dashed line, all $\Delta G_{RR} < 0$ at $P_{\text{O}_2} = 10^{-6} \text{ atm}$.

On the other hand, $\text{NdCoO}_{3-\delta}$ is observed to be $\Delta G_{RR} \leq 0$ states at the minimal temperature ($\sim 1160 \text{ K}$) in this $\text{RCoO}_{3-\delta}$ series, where $\text{LaCoO}_{3-\delta}$ has negative ΔG_{RR} value above 1240 K . Besides, the loss of ΔG_{RR} values for $\text{CeCoO}_{3-\delta}$ increase significantly with temperature and endured $\Delta G_{RR} \leq 0$ states at 1510 K , a loss of 306 kJ mol^{-1} from its standard conditions. The spontaneous reduction of $\text{RCoO}_{3-\delta}$ with thermal corrections at high-temperature follow the trends with an order of increasing temperature: $\text{NdCoO}_{3-\delta} < \text{LaCoO}_{3-\delta} < \text{CeCoO}_{3-\delta} < \text{SmCoO}_{3-\delta}$. This vibrational contributions have significant impact at high-temperature on the ΔG_{RR} values of respective $\text{RCoO}_{3-\delta}$, For example, at

1500 K the entropic contributions of $\text{LaCoO}_{3-\delta}$ on ΔG_{RR} values is 40 kJ mol^{-1} higher than $\text{CeCoO}_{3-\delta}$, which leads $\text{LaCoO}_{3-\delta}$ to undergo spontaneous reduction earlier than $\text{CeCoO}_{3-\delta}$. In contrast, the entropic contributions of $\text{SmCoO}_{3-\delta}$ is 57 kJ mol^{-1} less than $\text{NdCoO}_{3-\delta}$ (Fig. 4.7(a, b)). As a result, LaCoO_3 and NdCoO_3 achieve negative ΔG_{RR} values at lower temperatures than CeCoO_3 and SmCoO_3 , respectively.

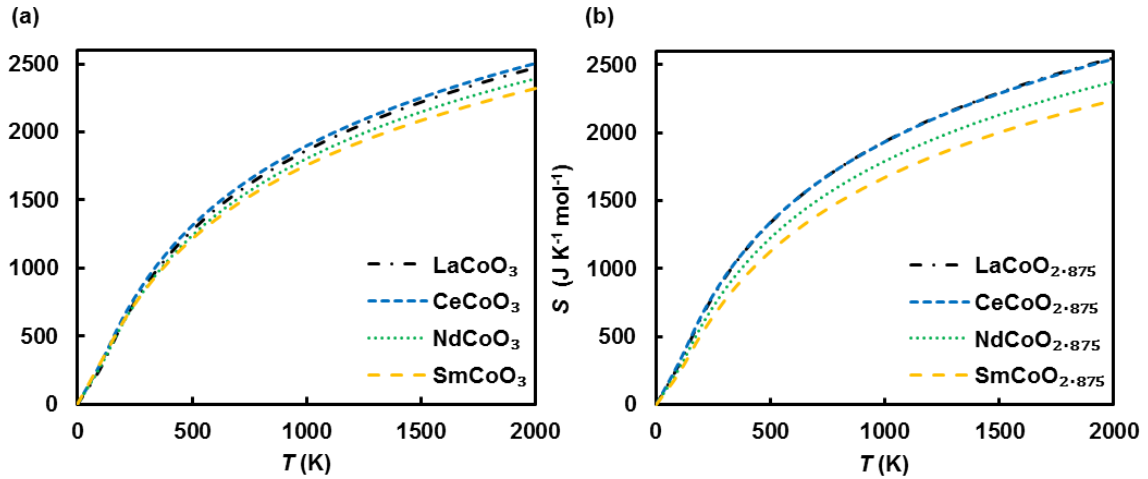


Fig. 4.7 Calculated PBEsol-PAW entropy, S ($\text{J K}^{-1} \text{mol}^{-1}$) of (a) pristine- RCoO_3 and (b) defective- $\text{RCoO}_{3-\delta}$ between 0 – 1800 K using $2 \times 2 \times 2$ supercells.

The negative ΔG_{RR} values observed in $\text{RCoO}_{3-\delta}$ perovskites within the temperature range 1100 – 1700 K, make them ideal candidates for solar-to-fuel conversion applications.^[44] Indeed, LaCoO_3 , CeCoO_3 , NdCoO_3 and SmCoO_3 have been recommended for solar thermal water splitting applications in literature based on the oxygen vacancy formation energies at 0 K,^[9] which hold true at high temperature with the thermal corrections. Furthermore, these perovskites have been widely investigated for SOFC cathodes,^[45-52] where LaCoO_3 is considered as one of the best cathode materials for HT-SOFC applications and NdCoO_3 show its potentiality as IT-SOFC cathode.

4.3.3.2 Phonon Analysis: Effect of A-site Cation and Oxygen Vacancy

The VDOS of representative pristine- and defect- $\text{RCoO}_{3-\delta}$ structures ($\text{R} = \text{La}, \text{Ce}, \text{Nd}, \text{Sm}$) are compared in Fig. 4.8(a-f). From the figures, it is clear that the oxygen vacancy substantially reduces the amplitude of phonon frequencies in low-, intermediate- and high-energy levels associated with cations and anions vibrations in defect- $\text{RCoO}_{3-\delta}$ structures. For instance, the phonon frequencies associated with A-site cation in pristine- $\text{RCoO}_{3-\delta}$ occurs between $0\text{--}150\text{ cm}^{-1}$ (Fig. 4.8(a)), whereas the principle modes are observed between $70\text{--}110\text{ cm}^{-1}$. The amplitude of A-site cations gradually increases but shifts from higher to lower energy ranges between La^{3+} to Sm^{3+} with respect to their decreasing mass of ionic radii. On the other hand, the opposite trends are observed in defect- $\text{RCoO}_{3-\delta}$ structures (Fig. 4.8(b)), where there is a sharp fall on vibrational amplitudes of A-site cations. Notably, the peak amplitude of phonon frequencies related to the Ce^{3+} cation dominates the La^{3+} . This indicates that the neutral oxygen vacancy in $\text{RCoO}_{3-\delta}$ lattice constricts the vibration motions of A-site cations.

Contrary, Co^{3+} cations in pristine- $\text{RCoO}_{3-\delta}$ lattices oscillate mostly between $200\text{--}400\text{ cm}^{-1}$ and with a distinct gap vibrate between $600\text{--}700\text{ cm}^{-1}$ (Fig. 4.8(c)). Remarkably there are two peak points (at ~ 250 and $\sim 350\text{ cm}^{-1}$) of Co^{3+} VDOS between $200\text{--}400\text{ cm}^{-1}$ for all perovskites, where additional VDOS peak is observed at high energy levels between $580\text{--}670\text{ cm}^{-1}$. The peak point of phonon amplitude reduces moving across $\text{LaCoO}_{3-\delta}$ to $\text{SmCoO}_{3-\delta}$, and corresponding phonon frequencies shifted to higher energy level from left to right in this series.

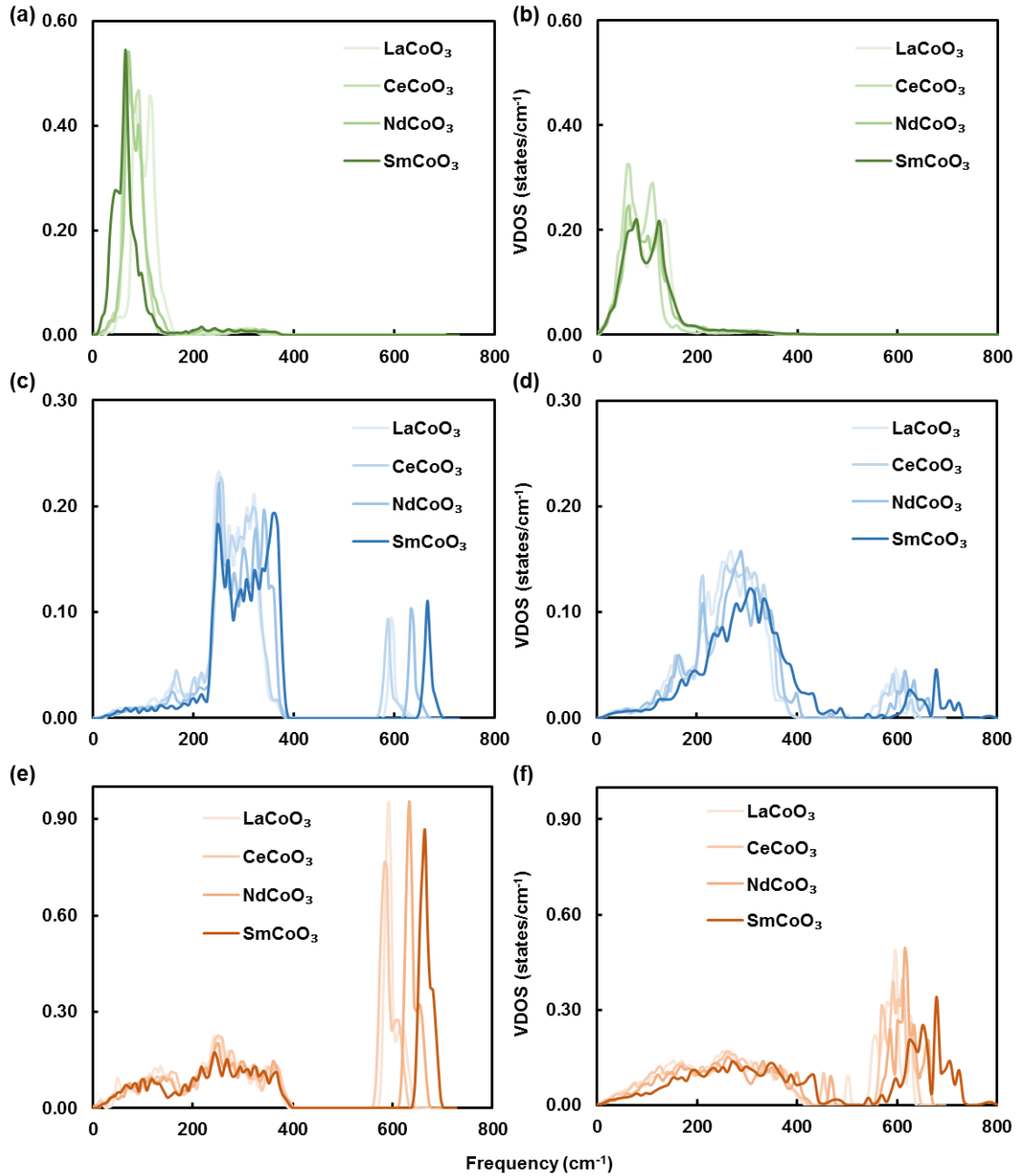


Fig. 4.8 VDOS of R³⁺ cations in (a) pristine-RCoO₃ and (b) defect-RCoO_{3-δ}; VDOS of Co³⁺ cations in (c) pristine-RCoO₃ and (d) defect-RCoO_{3-δ}; VDOS of O²⁻ anions in (e) pristine-RCoO₃ and (f) defect-RCoO_{3-δ}, calculated using 2 × 2 × 2 supercells by PBEsol functional.

On the other hand, there is a dramatic change in phonon modes of Co^{3+} cations in their defect structures. The principle phonon modes in defect structures are observed at $\sim 300 \text{ cm}^{-1}$ with a lesser extent of amplitude than the pristine VDOS for all four perovskites, and the phonon energy gap substantially reduce between $400 - 600 \text{ cm}^{-1}$ (Fig. 4.8(d)). Additionally, the VDOS associated with O^{2-} vibrations in pristine and defect- $\text{RCoO}_{3-\delta}$ lattice oscillate almost within identical frequency ranges to that of Co^{3+} cations, where the principles modes are also observed between $580 - 670 \text{ cm}^{-1}$ (Fig. 4.8(e, f)). This indicates that the introduction of neutral vacancy defect impacts the overall defective CoO_3^{2-} breathing modes, where the net amplitude decreases considerably.

To sum up, altering the A-site cations by rare-earth elements in $\text{RCoO}_{3-\delta}$ have the following consequence on phonon DOS: In pristine $\text{RCoO}_{3-\delta}$ lattices, (I) the phonon frequencies related to R^{3+} cations shift from higher to lower energy ranges with the increasing atomic number of A-site cations but follow the reverse trends with the phonon frequencies related to the Co^{3+} cations and O^{2-} anions, (II) the net amplitude of R^{3+} phonon frequencies increases from left to right in this series but decrease for Co^{3+} cations and O^{2-} anions; In defect- $\text{RCoO}_{3-\delta}$ lattices, (III) all the phonon frequencies associated with two cations, and O^{2-} anions shift from lower to higher energy level moving across $\text{LaCoO}_{3-\delta}$ to $\text{SmCoO}_{3-\delta}$ lattices, (IV) the amplitude of phonon frequencies for all cations and anions decreases from La to Sm at A-site with the exception that Ce dominates La. Since the DOS energetic of respective perovskite are originating from the individual contribution of elementary ions, thus these trends can be rationalized in terms of their energy requirement to form oxygen vacancy reported in Table. 4.2.

4.3.4 Thermochemical Properties and Phonon Dispersions of Cubic RCoO₃

4.3.4.1 Effect of A-site Cation on Thermochemical Properties

To understand the existing trends in thermochemical properties of cubic RCoO₃ (R = La, Ce, Nd, Sm), the S , C_p and $(H(T)-H(298.15))$ values are compared in Fig. 4.9(a-c) between 0 – 1800 K. Corresponding values at standard conditions are reported in Table 4.5. At room temperature, S values decrease with decreasing ionic radius of A-site cation, with the single exception of CeCoO₃. Interestingly, the S value of CeCoO₃ is 5 J K⁻¹ mol⁻¹ higher than LaCoO₃ at standard conditions.

Table 4.5 Calculated PBEsol-PAW S and C_p values of cubic RCoO₃ at standard condition.

(J K ⁻¹ mol ⁻¹)	LaCoO ₃	CeCoO ₃	NdCoO ₃	SmCoO ₃
S	110.28	115.62	108.52	106.30
C_p	92.32	92.49	87.99	83.12

This difference of S between LaCoO₃ and CeCoO₃ is maintained over the whole temperature range considered here (Fig. 4.9(a)). For instance, the difference between S values among LaCoO₃ and CeCoO₃ remains ~5 J K⁻¹ mol⁻¹, even at 1800 K, whereas the entropy of both perovskites increases by ~187 J K⁻¹ mol⁻¹ from their respective standard condition values. Conversely, the S values of NdCoO₃ and SmCoO₃ exhibit a difference of ~181 and ~172 J K⁻¹ mol⁻¹ respectively, at 1800 K from their room temperature. At standard conditions, the C_p values differ fractionally between LaCoO₃ and CeCoO₃ but in a general decrease from left to right in RCoO₃ series (Table 4.5), which hold the equal trend of S values. The variation of C_p values of RCoO₃ perovskites with temperature is presented in Fig. 4.9 (b) from 0 to 1800 K. In general, C_p curves follow Debye T^3 law at low temperature below 500 K and increase monotonically with increasing temperature.

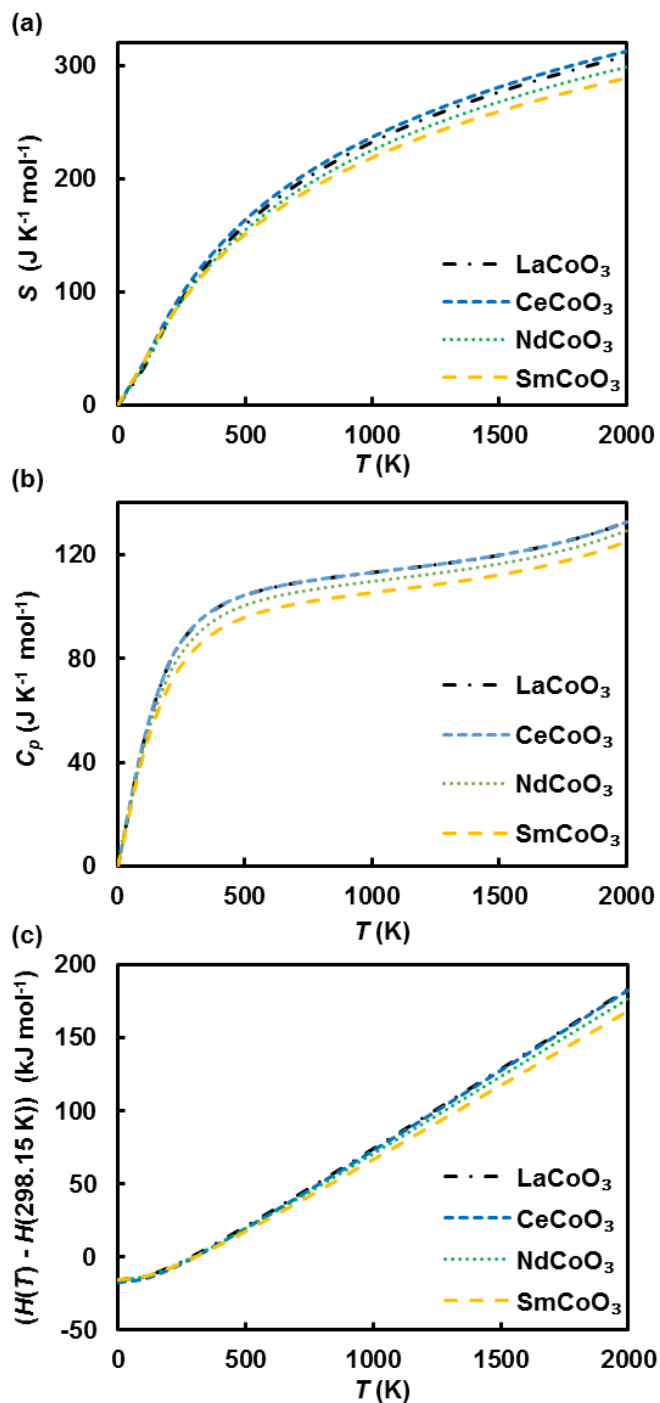


Fig. 4.9 Calculated PBEsol-PAW (a) S ($\text{J K}^{-1} \text{mol}^{-1}$), (b) C_p ($\text{J K}^{-1} \text{mol}^{-1}$), and (c) $(H(T) - H(298.15 \text{ K}))$ (kJ mol^{-1}) of the primitive unit cell of $R\text{CoO}_3$ ($R = \text{La, Ce, Nd, Sm}$) between 0 – 1800 K. Note the difference between these entropies and those presented in Fig. 4.7 is due to the size of the periodic cell used in each case.

However, at high temperature, quasi-harmonic effects on specific heat deviate its value by from the classical Dulong-Petit's law. Interestingly, C_p values of LaCoO_3 and CeCoO_3 are almost identical at all temperatures, consistent with the similarity in their phonon BS. The C_p values of LaCoO_3 and CeCoO_3 increase up to $126 \text{ J K}^{-1} \text{ mol}^{-1}$ at 1800 K (a difference of $34 \text{ J K}^{-1} \text{ mol}^{-1}$ from standard conditions), where for NdCoO_3 and SmCoO_3 , these values are less than 3 and $8 \text{ J K}^{-1} \text{ mol}^{-1}$, respectively from LaCoO_3 . That implies that the variation in the vibrational contribution of A-site cations influences the fluctuation in specific heat values among RCO_3 . The quasi-harmonic contributions of RCO_3 arising from thermal expansion coefficient, bulk modulus and volume changes with temperature are provided in appendix (Fig. 6.2).

The calculated $(H(T)-H(298.15))$ values of RCO_3 over the temperature range from 0 to 1800 K is shown in Fig. 4.9(c). The relative molar enthalpies increase linearly with increasing temperature, where the trend of increasing $(H(T)-H(298.15))$ values as a function of temperature maintain similar pattern in RCO_3 series as observed in S and C_p values. At 500 K, LaCoO_3 , CeCoO_3 and NdCoO_3 have almost identical $(H(T)-H(298.15))$ values of $\sim 20 \text{ kJ mol}^{-1}$. With increasing temperature, these differences become larger, where $(H(T)-H(298.15))$ value of LaCoO_3 is found around $\sim 161 \text{ kJ mol}^{-1}$ at 1800 K. At an equivalent temperature, the $(H(T)-H(298.15))$ values of CeCoO_3 and NdCoO_3 are respectively, 1 and 6 kJ mol^{-1} less than LaCoO_3 . However, $(H(T)-H(298.15))$ values of SmCoO_3 significantly differ from LaCoO_3 at high temperature. For instance, at 1800 K, the difference between SmCoO_3 with LaCoO_3 are 14 kJ mol^{-1} .

4.3.4.2 Effect of A-site Cation on Phonon Dispersions and VDOS

The phonon BS of optimized cubic RCO_3 ($R = \text{La, Ce, Nd, Sm}$) are compared in Fig. 4.10(a-d) for the high-symmetry points in BZ. All cubic structures exhibit imaginary frequencies at the M,

R and X points, and there are additional negative frequencies at Γ point for SmCoO_3 . This is likely due to the phase transition of these crystal structures in cubic structure from their stable ground structures in orthorhombic phase^[53] (See the discussion of similar phonon dispersions analysis of BaCeO_3 (§2.4.2) in Chapter 2. The origin of imaginary phonon modes due to phase transition from experimentally observed ground state orthorhombic phase to high-temperature cubic phase are shown in Fig. 2.4). In all RCoO_3 perovskite, the negative frequencies at R point below -200 cm^{-1} arise from the out-of-phase octahedral rotations (see Fig. 4.10(e)). Similarly, the more moderate instabilities at M point in each of these compounds originate from in-phase octahedral rotations within the CoO_3 sublattice. The weaker instabilities at X point below -100 cm^{-1} arise from a breathing mode within individual CoO_6 octahedra. The existence of soft modes at the Γ point ($\sim -50 \text{ cm}^{-1}$) in SmCoO_3 (Fig. 4.10(d)), corresponding to the motion of CoO_6 octahedra against the Sm^{3+} A-site cation. The corresponding imaginary phonon modes of the respective crystal structure were accounted for predicting their thermodynamic properties shown in Fig. 4.9.

The projected VDOS on each atom is given in Fig. 4.10(right) to show the detailed contribution from each component of the ionic lattice. The phonon modes relating to the La^{3+} cation in LaCoO_3 are primarily distributed over the acoustic branches in the range of $0 - 150 \text{ cm}^{-1}$, where Co^{3+} mostly propagated from 150 to 350 cm^{-1} (Fig. 4.10(a (right))). The high energy optical phonon modes are dominated by O^{2-} anions over the frequency range $575 - 650 \text{ cm}^{-1}$. The distribution of vibrational contributions of Ce^{3+} , Co^{3+} and O^{2-} in CeCoO_3 (Fig. 4.10(b (right))) have almost identical characteristics as seen for LaCoO_3 .

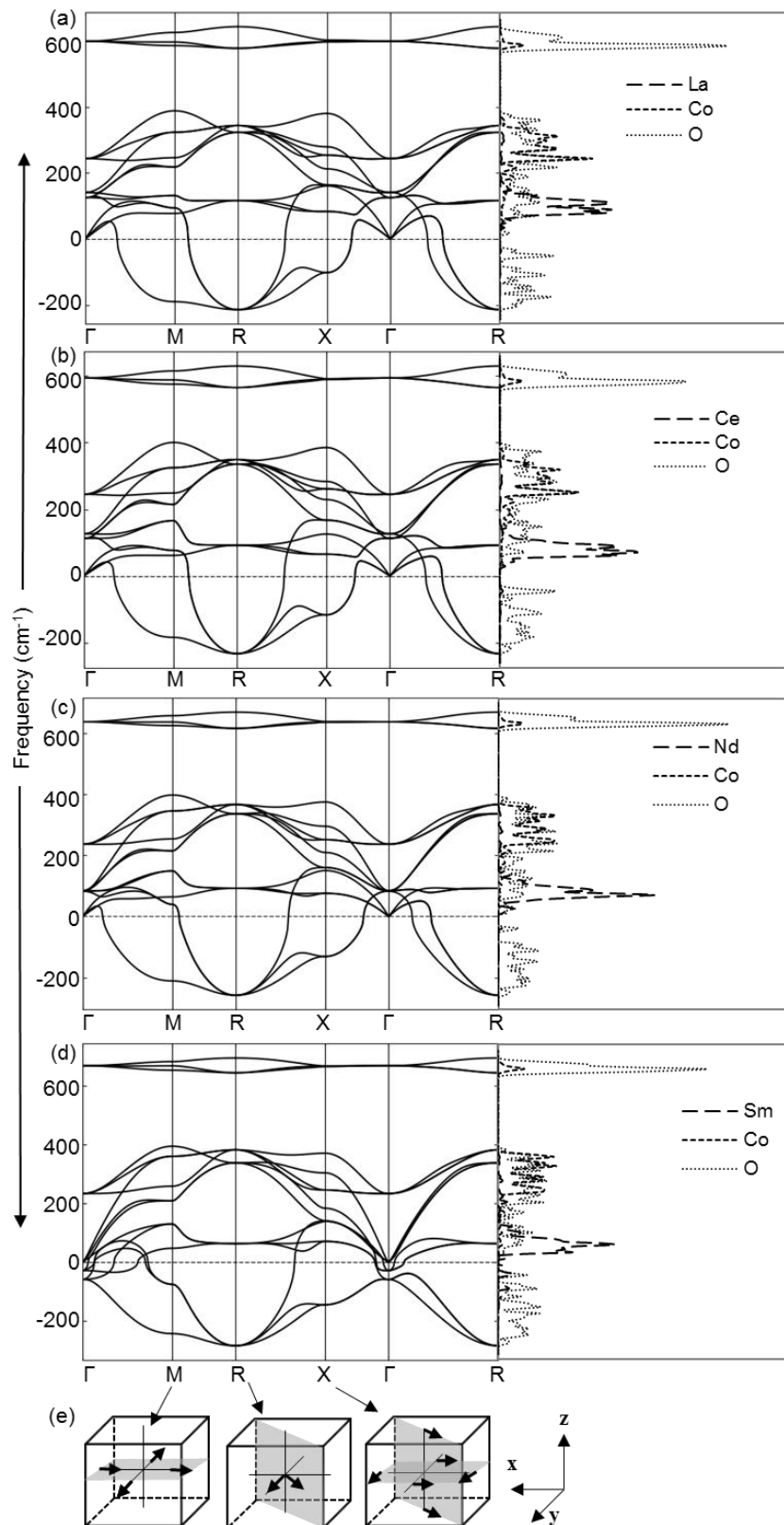


Fig. 4.10 Calculated PBEsol-PAW phonon dispersion curves (left) and VDOS (right) for the cubic unit cells of (a) LaCoO₃, (b) CeCoO₃, (c) NdCoO₃, (d) SmCoO₃; (e) depiction of unstable phonon modes at M-, R- and X-points in RCoO₃.

However, the phonon frequency of Co³⁺ and O²⁻ in NdCoO₃ (Fig. 4.10(c (right))) is higher by comparison than LaCoO₃ and CeCoO₃. For instance, the optical phonon modes governed by O²⁻ in NdCoO₃ are roughly distributed between 620 – 675 cm⁻¹, while Co³⁺ lies in the range of 200 – 375 cm⁻¹. Nevertheless, vibrational modes dominated by Nd³⁺ are observed between 0 – 150 cm⁻¹, similar to the other RCoO₃ compounds considered here (Fig. 4.10(c)). In the case of SmCoO₃, the vibration of both Co³⁺ and O²⁻ are shifted up by ~30 cm⁻¹ (Fig. 4.10(d (right))), while the Sm³⁺ cation predominantly contributes to modes between 0 – 150 cm⁻¹.

Comparing all the vibrational frequencies and amplitude of A-site, B-site cation and O²⁻ in all investigated RCoO₃ (Fig. 4.10(a-d (right))), it is evident that the vibrational amplitude of all cations and anions gradually decreases with respect to their decreasing ionic radii of the A-site cation. This is a clear indication of the reduction in lattice energy from LaCoO₃ to SmCoO₃. Notably, the principle vibrational mode of the A-site cation is observed at ~100 cm⁻¹, where there is no shift in either of these cations from La³⁺ to Sm³⁺ in RCoO₃ series. On the other hand, the principle mode of vibration associated with Co³⁺ in RCoO₃, is at ~250 cm⁻¹, while there is a secondary mode at ~350 cm⁻¹. The most noticeable change in phonon vibration is observed in the O²⁻ modes in RCoO₃, which exhibit a large shift from LaCoO₃ to SmCoO₃. However, the amplitude of these phonon modes decreases along the series, indicating a proportional relationship with the ionic radius of the A-site cation.

4.4 Conclusion

In this chapter, the existence of generalized trends in the structural, thermochemical and reduction properties of cubic RCoO_3 ($\text{R} = \text{La, Ce, Nd, Sm}$) perovskites are identified. Overall, the lattice parameters of RCoO_3 decreases with respect to the increasing atomic number of A-site cation except for CeCoO_3 . The formation energies of RCoO_3 have minor increases with the increasing atomic number of A-site cation. That is, perovskite become less stable from LaCoO_3 to SmCoO_3 . Analysis of oxygen vacancy formation energies of RCoO_3 without thermal corrections show that, LaCoO_3 and CeCoO_3 are energetically less favorable in reduction than NdCoO_3 and SmCoO_3 . The electronic structure analysis confirms the reduction of B-site cation, where the released electrons from vacancy site are primarily accepted by the two nearest neighbor B-site cations in defect $\text{RCoO}_{3-\delta}$ lattices. However, vibrational contributions at high-temperature made significant deviation in the reduction trends of RCoO_3 earlier observed at 0 K, where SmCoO_3 become the energetically least favorable and NdCoO_3 dominates all other perovskites in this series to be reduced. This can be rationalized to their corresponding entropic contributions which noticeably vary between pristine and defect structures of $\text{RCoO}_{3-\delta}$ perovskites with increasing temperature.

Analysis of pristine- and defect- $\text{RCoO}_{3-\delta}$ phonon frequencies confirm that the overall phonon amplitudes associated with cations and anions substantially decrease upon oxygen vacancy formation. In addition, oxygen vacancy has a direct impact on the propagation of phonon frequencies of cations and anions in $\text{RCoO}_{3-\delta}$ over the considered energy levels. Consequently, the thermochemical properties such as entropies, specific heats and relative molar enthalpies of pristine- and defect- RCoO_3 follow their respective phonon trends. Nevertheless, the reported reduction thermochemistry of $\text{RCoO}_{3-\delta}$ ($\text{R} = \text{La, Ce, Nd, Sm}$) with/without thermal correction gives

two general trends in an order of increasing reducibility: (i) without thermal corrections, $\text{LaCoO}_{3-\delta} < \text{CeCoO}_{3-\delta} < \text{NdCoO}_{3-\delta} < \text{SmCoO}_{3-\delta}$, and (ii) with thermal correction, $\text{SmCoO}_{3-\delta} < \text{CeCoO}_{3-\delta} < \text{LaCoO}_{3-\delta} < \text{NdCoO}_{3-\delta}$. All these generalized trends can be used to predict other perovskites in lanthanide series and their potential application in the field of SOFC and STWS applications.

4.5 References

1. Radaelli PG, Cheong S-W. Structural phenomena associated with the spin-state transition in LaCoO_3 . *Physical Review B*. 2002;66(9):094408.
2. Plakhty V, Brown P, Grenier B, Shiryaev S, Barilo S, Gavrilov S, et al. Thermal excitation of the Co^{3+} triplet spin-state in LaCoO_3 determined by polarized neutron diffraction. *J Phys Condens Matter*. 2006;18:3517-25.
3. Raccach P, Goodenough JB. First-order localized-electron collective-electron transition in LaCoO_3 . *Physical Review*. 1967;155(3):932.
4. Potze R, Sawatzky G, Abbate M. *Phys Rev B*. 1995;51:11501-06.
5. Bhide V, Rajoria D, Rao GR, Rao C. Mössbauer Studies of the high-spin-low-spin equilibria and the localized-collective electron transition in LaCoO_3 . *Physical Review B*. 1972;6(3):1021.
6. Bhide V, Rajoria D, Reddy Y, Rao GR, Rao GS, Rao C. Localized-to-itinerant electron transitions in rare-earth cobaltates. *Physical Review Letters*. 1972;28(17):1133.
7. Yamaguchi S, Okimoto Y, Tokura Y. Bandwidth dependence of insulator-metal transitions in perovskite cobalt oxides. *Physical Review B*. 1996;54(16):R11022.

8. Lago R, Bini G, Pena M, Fierrio J. Partial oxidation of methane to synthesis gas using LnCoO_3 perovskites as catalyst precursors. *Studies in Surface Science and Catalysis*. 110: Elsevier; 1997. p. 721-30.
9. Emery AA, et al. High-throughput computational screening of perovskites for thermochemical water splitting applications. *Chemistry of Materials* 2016;28(16):5621-34.
10. Ishihara T. *Perovskite oxide for solid oxide fuel cells*: Springer Science & Business Media; 2009.
11. Bose M, Ghoshray A, Basu A, Rao C. Spin-state equilibria in the LCoO_3 system from ^{59}Co NMR. *Physical Review B*. 1982;26(9):4871.
12. Moon J-W, Masuda Y, Seo W-S, Koumoto K. Influence of ionic size of rare-earth site on the thermoelectric properties of RCoO_3 -type perovskite cobalt oxides. *Materials Science and Engineering: B*. 2001;85(1):70-5.
13. Delgado E, Michel CR. CO_2 and O_2 sensing behavior of nanostructured barium-doped SmCoO_3 . *Materials Letters*. 2006;60(13-14):1613-6.
14. Michel CR, Delgado E, Santillan G, Martinez AH, Chávez-Chávez A. An alternative gas sensor material: synthesis and electrical characterization of SmCoO_3 . *Materials Research Bulletin*. 2007;42(1):84-93.
15. Martínez-Juárez A, Sanchez L, Chinarro E, Recio P, Pascual C, Jurado J. Electrical characterisation of ceramic conductors for fuel cell applications. *Solid State Ionics*. 2000;135(1-4):525-8.
16. Goodenough JB. Electronic and ionic transport properties and other physical aspects of perovskites. *Rep Prog Phys*. 2004;67(11):1915-93.

17. Kresse G, Furthmüller J. Vienna ab-initio simulation package (VASP). Institut für Materialphysik, Vienna. 2004.
18. Perdew JP, Ruzsinszky A, Csonka GI, Vydrov OA, Scuseria GE, Constantin LA, et al. Restoring the density-gradient expansion for exchange in solids and surfaces. *Physical Review Letters*. 2008;100(13):136406.
19. Blöchl P. Projector augmented-wave method. *Phys Rev B*. 1994;50(24):17953-79.
20. Birch F. Finite elastic strain of cubic crystals. *Physical Review*. 1947;71(11):809.
21. Kirklin S, Saal JE, Meredig B, Thompson A, Doak JW, Aykol M, et al. The Open Quantum Materials Database (OQMD): assessing the accuracy of DFT formation energies. *Computational Materials*. 2015;1(1):1-15.
22. Gonze X, Lee C. Dynamical matrices, Born effective charges, dielectric permittivity tensors, and interatomic force constants from density-functional perturbation theory. *Physical Review B*. 1997;55(16):10355.
23. Sundell PG, Björketun ME, Wahnström G. Thermodynamics of doping and vacancy formation in BaZrO₃ perovskite oxide from density functional calculations. *Physical Review B*. 2006;73(10):104112.
24. Giannozzi P, Gironcoli S, Pavone P, Baroni S. Ab initio calculation of phonon dispersions in semiconductors. *Physical Review B*. 1991;43(9):7231.
25. Monkhorst H, Pack J. Special points for Brillouin-zone integrations. *Physical Review B*. 1976;13(12):5188.
26. Togo A, Tanaka I. First principles phonon calculations in materials science. *Scripta Materialia*. 2015;108:1-5.

27. Deml A, Stevanovi V, Holder A, Sanders M, O'Hayre R, Musgrave C. Tunable oxygen vacancy formation energetics in the complex perovskite oxide $\text{Sr}_x\text{La}_{1-x}\text{Mn}_y\text{Al}_{1-y}\text{O}_3$. *Chemistry of Materials* 2014;26(22):6595–602.
28. Deml A, Stevano V, Muhich C, Musgrave C, O'Hayre R. Oxide enthalpy of formation and band gap energy as accurate descriptors of oxygen vacancy formation energetics. *Energy & Environmental Science*. 2014;7(6):1996–2004.
29. Ezbiri M, Allen KM, Gálvez ME, Michalsky R, Steinfeld A. Design principles of perovskites for thermochemical oxygen separation. *ChemSusChem*. 2015;8(11):1966-71.
30. Wei-Ran W, Da-Peng X, Wen-Hui S, Zhan-Hui D, Yan-Feng X, Geng-Xin S. Raman active phonons in RCoO_3 (R= La, Ce, Pr, Nd, Sm, Eu, Gd, and Dy) perovskites. *Chinese Physics Letters*. 2005;22(9):2400.
31. Wold A, Ward R. Perovskite-type oxides of cobalt, chromium and vanadium with some rare earth elements. *Journal of the American Chemical Society*. 1954;76(4):1029-30.
32. Calle-Vallejo F, Martínez JI, García-Lastra JM, Mogensen M, Rossmeisl J. Trends in stability of perovskite oxides. *Angewandte Chemie International Edition*. 2010;49(42):7699-701.
33. Nekrasov I, Streltsov S, Korotin M, Anisimov V. Influence of rare-earth ion radii on the low-spin to intermediate-spin state transition in lanthanide cobaltite perovskites: LaCoO_3 versus HoCoO_3 . *Physical Review B*. 2003;68(23):235113.
34. Sarma D, Shanthi N, Barman S, Hamada N, Sawada H, Terakura K. Band theory for ground-state properties and excitation spectra of perovskite LaMO_3 (M= Mn, Fe, Co, Ni). *Physical Review Letters*. 1995;75(6):1126.
35. Cramer CJ, Truhlar DG. Density functional theory for transition metals and transition metal chemistry. *Physical Chemistry Chemical Physics*. 2009;11(46):10757-816.

36. Tran F, Blaha P, Schwarz K, Novák P. Hybrid exchange-correlation energy functionals for strongly correlated electrons: Applications to transition-metal monoxides. *Physical Review B*. 2006;74(15):155108.
37. Russo TV, Martin RL, Hay PJ. Density functional calculations on first-row transition metals. *The Journal of Chemical Physics*. 1994;101(9):7729-37.
38. Wang L, Maxisch T, Ceder G. Oxidation energies of transition metal oxides within the GGA+U framework. *Physical Review B*. 2006;73(19):195107.
39. Korhonen T, Puska MJ, Nieminen RM. Vacancy-formation energies for fcc and bcc transition metals. *Physical Review B*. 1995;51(15):9526.
40. Hoch M, Nellutla S, Van Tol J, Choi ES, Lu J, Zheng H, et al. Diamagnetic to paramagnetic transition in LaCoO_3 . *Physical Review B*. 2009;79(21):214421.
41. Yan J-Q, Zhou J-S, Goodenough JB. Bond-length fluctuations and the spin-state transition in LCoO_3 (L= La, Pr, and Nd). *Physical Review B*. 2004;69(13):134409.
42. Korotin M, Ezhov SY, Solovyev I, Anisimov V, Khomskii D, Sawatzky G. Intermediate-spin state and properties of LaCoO_3 . *Physical Review B*. 1996;54(8):5309.
43. Bader R, Nguyen-Dang TT, Tal Y. A topological theory of molecular structure. *Reports on Progress in Physics*. 1981;44(8):893.
44. Bork AH, Povoden - Karadeniz E, Rupp JL. Modeling thermochemical solar-to-fuel conversion: CALPHAD for thermodynamic assessment studies of perovskites, exemplified for $(\text{La}, \text{Sr})\text{MnO}_3$. *Advanced Energy Materials*. 2017;7(1):1601086.
45. Skinner SJ. Recent advances in perovskite-type materials for solid oxide fuel cell cathodes. *International Journal of Inorganic Materials*. 2001;3(2):113-21.

46. Ohno Y, Nagata S, Sato H. Effect of electrode materials on the properties of high-temperature solid electrolyte fuel cells. *Solid State Ionics*. 1981;3:439-42.
47. Isaacs H, Olmer L. Comparison of materials as oxygen catalytic electrodes on zirconia electrolyte. *Journal of The Electrochemical Society*. 1982;129(2):436-43.
48. Yamamoto O, Takeda Y, Kanno R, Noda M. Perovskite-type oxides as oxygen electrodes for high temperature oxide fuel cells. *Solid State Ionics*. 1987;22(2-3):241-6.
49. Lee K, Manthiram A. Comparison of $\text{Ln}_{0.6}\text{Sr}_{0.4}\text{CoO}_{3-\delta}$ (Ln= La, Pr, Nd, Sm, and Gd) as cathode materials for intermediate temperature solid oxide fuel cells. *Journal of the Electrochemical Society*. 2006;153(4):A794-A8.
50. Elkalashy SI, Gilev A, Aksenova T, Urusova A, Cherepanov V. Phase equilibria, structure and properties of complex oxides in the $\text{NdFeO}_{3-\delta}\text{-SrFeO}_{3-\delta}\text{-SrCoO}_{3-\delta}\text{-NdCoO}_{3-\delta}$ system as potential cathodes for SOFCs. *Solid State Ionics*. 2018;316:85-92.
51. Rajasekhar M, Subramania A, Muzhumathi S. Microwave-assisted combustion synthesis of nanocrystalline NdCoO_3 cathode material for intermediate temperature solid oxide fuel cells (IT-SOFCs) application. *J Environ Nanotechnol*. 2014;3(4):86-90.
52. Lee K, Manthiram A. Characterization of $\text{Nd}_{1-x}\text{Sr}_x\text{CoO}_{3-\delta}$ ($0 \leq x \leq 0.5$) cathode materials for intermediate temperature SOFCs. *Journal of the Electrochemical Society*. 2005;152(1):A197-A204.
53. Emery AA, Saal JE, Kirklin S, Hegde VI, Wolverton C. High-throughput computational screening of perovskites for thermochemical water splitting applications. *Chemistry of Materials*. 2016;28(16):5621-34.

Chapter 5: Conclusions and Future Work

5.1 Conclusions

In this thesis, the existence of generalized trends in the structural, thermochemical and reduction properties of alkaline-earth metal oxides (BaMO_3 ; $M = \text{Ti} - \text{Cu}$) and rare-earth cobalt oxides (RCoO_3 ; $R = \text{La}, \text{Ce}, \text{Nd}, \text{Sm}$) have been established and examined using first-principles calculations. These properties are characterised with the consideration of:

- (I) the effects of B-site cation in BaMO_3 and A-site cation in RCoO_3 perovskites by systematically altering the B-site or A-site cation respectively,
- (II) the effects of cations with mixed oxidation states (BaMO_3) and identical oxidation states (RCoO_3),
- (III) the effects of oxygen vacancies on reduction properties of BaMO_3 and RCoO_3 , and
- (IV) the effects of temperature on the thermochemical properties and reduction thermochemistry of BaMO_3 and RCoO_3 .

Assessing the effects of A-site and B-site cations in these perovskites gives a general framework by which appropriate A-site and B-site cations in ABO_3 perovskites can be selected for target functionalities, via a relatively fast and cost-effective approach. This will enable rapid pre-screening of many candidate perovskite materials in future that can guide subsequent experimental investigation for related energy applications.

From the trends in formation energies of BaMO_3 and RCoO_3 , it is evident that the formation energies of ABO_3 perovskites are linearly correlated with their atomic number of A-/B-site cation, whereas it increases significantly with the increasing atomic number of B-site cation for a given period, but slightly with the increasing atomic number of A-site cation. The substantial difference

in these trends between these two groups of perovskites can be rationalised in terms of the coulombic interaction realised by A-O and B-O interactions in the ionic crystal. Perovskites with mixed oxidation state cations (i.e. BaMO_3) have a larger charge difference among different B-site cations from left to the right in the periodic table as observed from Bader charge analyses, while perovskite with cations of identical oxidation states (RCoO_3) have small charge difference among different A-site cation.

The oxygen vacancy formation energies of BaMO_3 and RCoO_3 become less positive at 0 K, moving from BaTiO_3 to BaCuO_3 and from LaCoO_3 to SmCoO_3 in the respective group of perovskites. That is, the reducibility of these perovskites increase consistently across the respective period. As observed for BaMO_3 and RCoO_3 formation energies, this trend regarding the degree of reducibility is more marked along the 3d metal series BaMO_3 ($M = \text{Ti to Cu}$) than it is for the rare-earth series RCoO_3 ($R = \text{La to Sm}$). Irrespective of these trends; however, the incorporation of thermal corrections into reduction free energies have a far more substantial effect for both groups of perovskites, where they deviate from their linear correlation at high-temperature. This deviation is ascribed to the temperature-dependent entropic contributions of individual perovskite into its reduction free energy.

The temperature-dependent thermochemical properties of defect-free BaMO_3 and RCoO_3 show that, at an equivalent temperature the entropy, specific heat and relative molar enthalpies have higher values from left to the right in BaMO_3 series, while this trend is reversed in RCoO_3 series. These two opposite trends can be attributed to their phonon contribution of respective perovskite. Analysis of the vibrational contributions of individual ion in respective perovskite among these two groups confirms that the amplitude of cations and anions gradually increase from BaTiO_3 to BaCuO_3 in BaMO_3 series, whereas the reverse trend is observed from LaCoO_3 to SmCoO_3 in

RCoO₃ series. Additionally, the phonon frequencies associated with B-site cation and O²⁻ anion shift from higher to lower energy levels from Ti to Cu at B-site in BaMO₃ series, while the opposite trend is found in RCoO₃ series from La to Sm at A-site. However, the thermochemical properties of oxygen-deficient BaMO₃ and RCoO₃ at high-temperatures do not follow these linear trends due to the inconsistent entropic contributions from defective perovskites, which ultimately influence their deviation of trends in reduction free energies at high-temperatures.

In summary, comparing the effects of A-site and B-site cations in ABO₃ perovskites, it seems that the B-site cation has dominant effects on the structural, thermochemical and reduction properties of ABO₃ perovskites for the investigated materials in this thesis.

5.2 Future Work

This thesis has established an accurate DFT protocol for modelling the lattice structure, phonon and vibrational properties of BaXO₃ (X = Ce, Zr, Mn) perovskite materials (Chapter 2) and benchmarked against experimental data where possible. Then the developed DFT protocol was applied to the calculation of electronic and phonon properties of BaMO₃ (M = Ti – Cu) and RCoO₃ (R = La, Ce, Nd, Sm), which in turn were used to predict their thermochemical properties and reduction thermochemistry properties (Chapter 3 & 4). The thermochemical properties obtained via this method showed excellent agreement with available experimental data, and so it is recommended as a facile alternative to the experimental design of new perovskite-based materials for high-temperature applications. The following possible combination of altering A/B-site cations, partial or co-doping of both cations in ABO₃ perovskite materials are recommended for future investigations.

5.2.1 Altering A- and B-site Cation in ABO₃ Perovskites

On the basis of this thesis, a study of other alkaline-earth A-site cations (e.g. Sr, Ca) with the similar 3d transition metals (Ti – Cu) at B-site, will allow trends reported in this thesis to be expanded to a generalized model mixed valence charge state (II-IV) cations in the reduction thermochemistry of these materials. Investigation of the A-site rare-earth series (La-Yb) with 3d transition metals (Ti – Cu) in the B-site would extend the present results concerning mixed-valence ions to the properties of ABO₃ perovskites with identical valence charge states (III-III). Additionally, it will also be interesting to investigate alkaline metals (Na, K) at A-site and 3d metals at B-site to identify the effects of mixed valence charge state (I-V) on these reduction properties. Moreover, substituting B-site cations with 4d and 5d metal series with all above rare-earth, alkaline-earth and alkaline metals at A-site will give a general overview of B-site cations effect in ABO₃ perovskites and to design an accurate framework for reduction thermochemistry trends existing in the periodic table related to energy applications.

5.2.2 Doping A-site Cation in ABO₃ Perovskites

A particularly relevant avenue for further research, considering recent experimental works, is the study of doped perovskites.^[1-5] For instance, doping the A-site Ba²⁺ cation with other alkaline-earth metals, e.g. Sr²⁺, in BaFeO₃ are beneficial for higher reduction extent.^[4] Thus, partial substitution of Ba²⁺ with Sr²⁺ in BaMO₃ (M = Ti – Cu) series would be interesting for investigating the reduction thermochemistry of Ba_{1-x}Sr_xMO₃ perovskites. In addition, doping lower charge cation (e.g. Ca²⁺, Sr²⁺) with higher charge cations (e.g. La³⁺) in the A-site of RCoO₃ perovskites are found very influential for maximal O₂ evolution,^[1, 3, 5] as the mixed charge at A-site increase the oxidation state of B-site, which further enhance the reduction extent. The amount of dopant

concentration will also have an impact on the reduction thermochemistry of $\text{La}_{1-x}(\text{Ca/Sr})_x\text{CoO}_3$. Therefore, the influence of these two dopants (Ca^{2+} and Sr^{2+}) with other lanthanide cations (e.g. Ce^{3+} , Nd^{3+} , Sm^{3+}) in RCO_3 series are recommended for exploration, so that trends in high-temperature oxygen reduction reaction can be elucidated.

5.2.3 Doping B-site Cation in ABO_3 Perovskites

The beneficial effect of Ce^{3+} cation substitution on B-site in BaMnO_3 has been investigated recently,^[6] and was shown to yield faster reaction kinetics and higher reduction extents due to optimized oxygen vacancy formation energy. Hence, Ce^{3+} could be considered as a B-site dopant in BaMO_3 perovskites series ($\text{M} = \text{Ti} - \text{Cu}$). On the other hand, Al^{3+} doping at B-site in LaMnO_3 perovskite stabilizes the perovskite structure by decreasing the cell volume due to stronger atomic interaction. In pure LaMnO_3 reduction, the B-site cation Mn^{4+} first reduce to Mn^{3+} which further undergoes from Mn^{3+} to energetically favorable Mn^{2+} .^[7] By contrast, the presence of Al^{3+} in LaMnO_3 promotes the reduction of Mn^{4+} to Mn^{3+} but prevents the second reduction of Mn^{3+} to Mn^{2+} , which is beneficial for releasing more O_2 during reduction.^[8] So, introducing Al^{3+} dopant at B-site in RCO_3 perovskite series is recommended for future investigations, so as to ascertain the B-site doping effects of RCO_3 .

5.2.4 The Combination of A- and B-site Doping in ABO_3 Perovskites

Substitution of Ba^{2+} with Sr^{2+} at A-site and Co^{4+} with Fe^{4+} at B-site in BaCoO_3 show increasing O_2 production rate,^[9] which can further be studied for BaMO_3 series. Similar dopant elements at A- and B-site in LaCoO_3 have also been reported to promote O_2 production.^[4] Additionally, replacing B-site Fe^{3+} dopant by Cr^{3+} in $(\text{La}, \text{Sr})\text{CoO}_3$ seems beneficial to increase reduction

extents.^[10] Ca^{2+} or Sr^{2+} dopant at A-site and Al^{3+} , Ga^{3+} , Sc^{3+} , Cr^{3+} , Fe^{3+} dopant at B-site in LaMnO_3 have also been widely investigated for oxygen reduction reaction and solar-driven fuel production.^[2, 11-16] Therefore, doping with the identical elements of +III valance charge state on the B-site and +II valance charge state on the A-site in RCoO_3 ($\text{R} = \text{La}, \text{Ce}, \text{Nd}, \text{Sm}$) perovskite series are potentially relevant materials to consider with respect to the oxygen reduction reaction, due to the fact that the mixed charged state cations must be compensated by charged vacancies or electronic defects (holes). As the oxygen vacancies prevail over electronic defects at high temperatures, mixed valance states will be balanced by oxygen vacancy.^[17, 18]

5.3 References

1. Wang L, Al-Mamun M, Liu P, Wang Y, Yang HG, Zhao H. Notable hydrogen production on $\text{La}_x\text{Ca}_{1-x}\text{CoO}_3$ perovskites via two-step thermochemical water splitting. *Journal of Materials Science*. 2018;53(9):6796-806.
2. Wang L, Al-Mamun M, Zhong YL, Jiang L, Liu P, Wang Y, et al. Ca^{2+} and Ga^{3+} doped LaMnO_3 perovskite as a highly efficient and stable catalyst for two-step thermochemical water splitting. *Sustainable Energy & Fuels*. 2017;1(5):1013-7.
3. Wang L, Al-Mamun M, Zhong YL, Liu P, Wang Y, Yang HG, et al. Enhanced thermochemical water splitting through formation of oxygen vacancy in $\text{La}_{0.6}\text{Sr}_{0.4}\text{BO}_{3-\delta}$ ($\text{B} = \text{Cr}, \text{Mn}, \text{Fe}, \text{Co}, \text{and Ni}$) perovskites. *ChemPlusChem*. 2018;83(10):924-8.
4. Nair MM, Abanades S. Experimental screening of perovskite oxides as efficient redox materials for solar thermochemical CO_2 conversion. *Sustainable Energy & Fuels*. 2018;2(4):843-54.

5. Orfila M, Linares M, Molina R, Botas JÁ, Sanz R, Marugán J. Perovskite materials for hydrogen production by thermochemical water splitting. *International Journal of Hydrogen Energy*. 2016;41(42):19329-38.
6. Barcellos DR, Sanders MD, Tong J, McDaniel AH, O'Hayre RP. $\text{BaCe}_{0.25}\text{Mn}_{0.75}\text{O}_{3-\delta}$ —a promising perovskite-type oxide for solar thermochemical hydrogen production. *Energy & Environmental Science*. 2018;11(11):3256-65.
7. Fierro J, Tascón J, Tejuca LG. Physicochemical properties of LaMnO_3 : Reducibility and kinetics of O_2 adsorption. *Journal of Catalysis*. 1984;89(2):209-16.
8. Cimino S, Lisi L, De Rossi S, Faticanti M, Porta P. Methane combustion and CO oxidation on $\text{LaAl}_{1-x}\text{Mn}_x\text{O}_3$ perovskite-type oxide solid solutions. *Applied Catalysis B: Environmental*. 2003;43(4):397-406.
9. Demont A, Abanades S, Beche E. Investigation of perovskite structures as oxygen-exchange redox materials for hydrogen production from thermochemical two-step water-splitting cycles. *The Journal of Physical Chemistry C*. 2014;118(24):12682-92.
10. Bork AH, Kubicek M, Struzik M, Rupp JL. Perovskite $\text{La}_{0.6}\text{Sr}_{0.4}\text{Cr}_{1-x}\text{Co}_x\text{O}_{3-\delta}$ solid solutions for solar-thermochemical fuel production: strategies to lower the operation temperature. *Journal of Materials Chemistry A*. 2015;3(30):15546-57.
11. McDaniel AH, Miller EC, Arifin D, Ambrosini A, Coker EN, O'Hayre R, et al. Sr- and Mn-doped $\text{LaAlO}_{3-\delta}$ for solar thermochemical H_2 and CO production. *Energy & Environmental Science*. 2013;6(8):2424-8.
12. Deml AM, Stevanovi V, Holder AM, Sanders M, O'Hayre R, Musgrave CB. Tunable oxygen vacancy formation energetics in the complex perovskite oxide $\text{Sr}_x\text{La}_{1-x}\text{Mn}_y\text{Al}_{1-y}\text{O}_3$. *Chemistry of Materials*. 2014;26(22):6595-602.

13. Ezbiri M, Takacs M, Theiler D, Michalsky R, Steinfeld A. Tunable thermodynamic activity of $\text{La}_x\text{Sr}_{1-x}\text{Mn}_y\text{Al}_{1-y}\text{O}_{3-\delta}$ ($0 \leq x \leq 1$, $0 \leq y \leq 1$) perovskites for solar thermochemical fuel synthesis. *Journal of Materials Chemistry A*. 2017;5(8):4172-82.
14. Takacs M, Hoes M, Caduff M, Cooper T, Scheffe JR, Steinfeld A. Oxygen nonstoichiometry, defect equilibria, and thermodynamic characterization of LaMnO_3 perovskites with Ca/Sr A-site and Al B-site doping. *Acta Materialia*. 2016;103:700-10.
15. Luciani G, Landi G, Aronne A, Di Benedetto A. Partial substitution of B cation in $\text{La}_{0.6}\text{Sr}_{0.4}\text{MnO}_3$ perovskites: A promising strategy to improve the redox properties useful for solar thermochemical water and carbon dioxide splitting. *Solar Energy*. 2018;171:1-7.
16. Dey S, Naidu B, Rao C. Beneficial effects of substituting trivalent ions in the B-site of $\text{La}_{0.5}\text{Sr}_{0.5}\text{Mn}_{1-x}\text{A}_x\text{O}_3$ (A= Al, Ga, Sc) on the thermochemical generation of CO and H_2 from CO_2 and H_2O . *Dalton Transactions*. 2016;45(6):2430-5.
17. Bouwmeester H, Den Otter M, Boukamp B. Oxygen transport in $\text{La}_{0.6}\text{Sr}_{0.4}\text{Co}_{1-y}\text{Fe}_y\text{O}_{3-\delta}$. *Journal of Solid State Electrochemistry*. 2004;8(9):599-605.
18. Tai L-W, Nasrallah M, Anderson H, Sparlin D, Sehlin S. Structure and electrical properties of $\text{La}_{1-x}\text{Sr}_x\text{Co}_{1-y}\text{Fe}_y\text{O}_3$. Part 2. The system $\text{La}_{1-x}\text{Sr}_x\text{Co}_{0.2}\text{Fe}_{0.8}\text{O}_3$. *Solid State Ionics*. 1995;76(3-4):273-83.

Chapter 6: Appendix

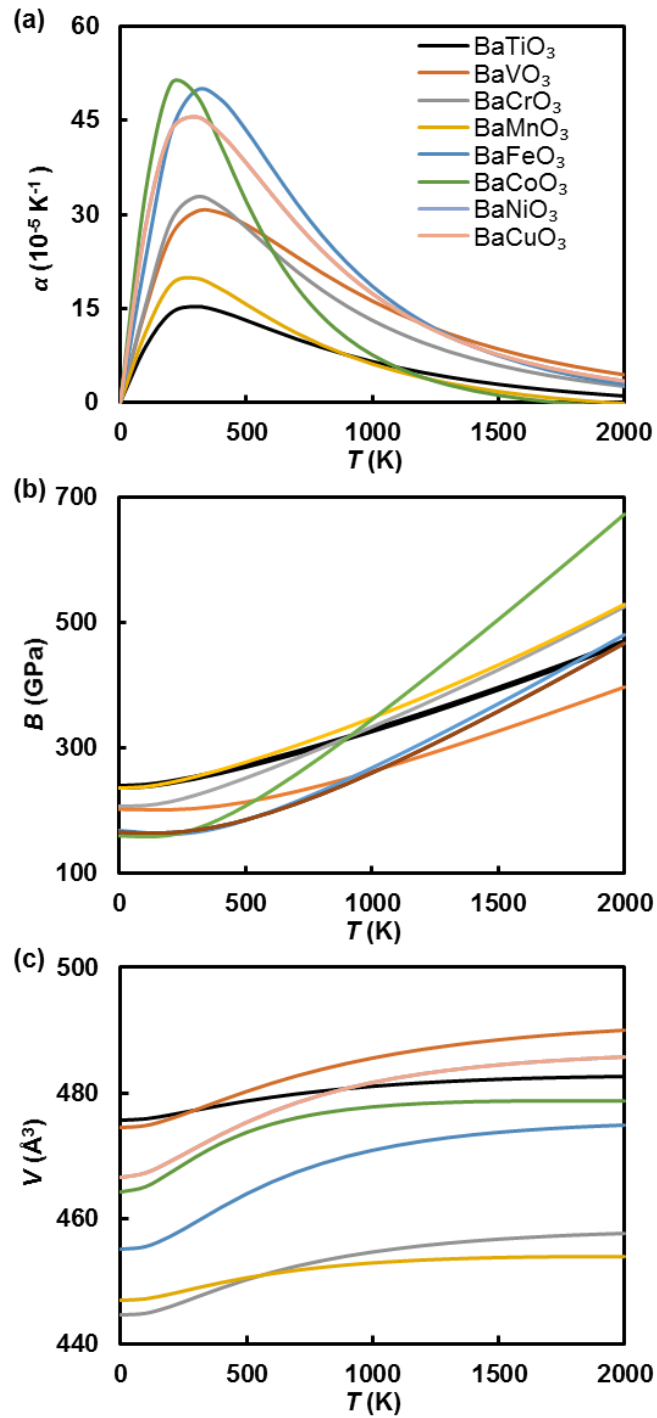


Fig. 6.1 Variation with temperature (0 – 2000 K) of the calculated BaMO₃ (M = Ti – Cu) properties from quasi-harmonic approximation: (a) thermal expansion (α/K^{-1}), (b) bulk modulus (B/GPa), (c) volume ($V/\text{\AA}^3$).

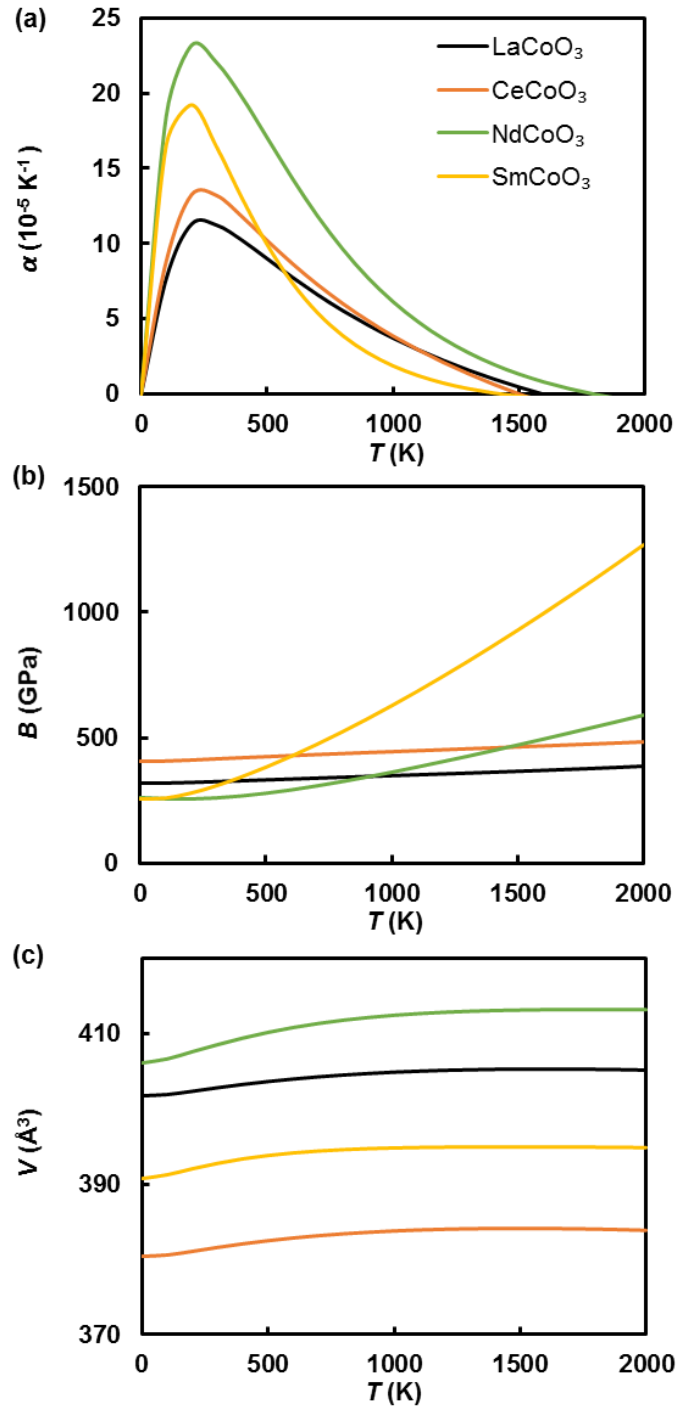


Fig. 6.2 Variation with temperature (0 – 2000 K) of the calculated RCoO₃ (R = La, Ce, Nd, Sm) properties from quasi-harmonic approximation: (a) thermal expansion (α/K^{-1}), (b) bulk modulus (B/GPa), (c) volume ($V/\text{\AA}^3$).

Chapter 7: Copyright Permissions

Fig. 1.2:

MDPI Open Access Information and Policy

All articles published by MDPI are made immediately available worldwide under an open access license. This means:

- everyone has free and unlimited access to the full-text of *all* articles published in MDPI journals;
- everyone is free to re-use the published material if proper accreditation/citation of the original publication is given;
- open access publication is supported by the authors' institutes or research funding agencies by payment of a comparatively low **Article Processing Charge (APC)** for accepted articles.

Permissions

No special permission is required to reuse all or part of article published by MDPI, including figures and tables. For articles published under an open access Creative Common CC BY license, any part of the article may be reused without permission provided that the original article is clearly cited. Reuse of an article does not imply endorsement by the authors or MDPI.

Fig. 1.4(a):

ELSEVIER LICENSE
TERMS AND CONDITIONS

Jun 05, 2020

This Agreement between Krishna Kamol Ghose ("You") and Elsevier ("Elsevier") consists of your license details and the terms and conditions provided by Elsevier and Copyright Clearance Center:

License Number	4842320220684
License date	Jun 05, 2020
Licensed Content Publisher	Elsevier
Licensed Content Publication	Energy Procedia
Licensed Content Title	Nonstoichiometric Perovskite Oxides for Solar Thermochemical H ₂ and CO Production
Licensed Content Author	A.H. McDaniel, A. Ambrosini, E.N. Coker, J.E. Miller, W.C. Chuah, R. O'Hayre, J. Tong
Licensed Content Date	Jan 1, 2014
Licensed Content Volume	49
Licensed Content Issue	n/a
Licensed Content Pages	10
Start Page	2009
End Page	2018
Type of Use	reuse in a thesis/dissertation
Portion	figures/tables/illustrations
Number of figures/tables/illustrations	1
Format	both print and electronic
Are you the author of this Elsevier article?	No
Will you be translating?	No
Title	First-Principles Investigation of Trends in High-Temperature Thermochemistry of Perovskite Metal Oxides
Institution name	The University of Newcastle, Australia
Expected presentation date	Jun 2020
Portions	Fig. 5. (a, top)
Requestor Location	Krishna Kamol Ghose University Drive SB 306 Callaghan, Callaghan, NSW 2308 Australia Attn:
Publisher Tax ID	GB 494 6272 12
Total	0.00 AUD
Terms and Conditions	

Fig. 1.4(b):



Copyright Clearance Center



RightsLink®

Home Help Email Support Krishna Kamol Ghose ▾



ACS Publications
Most Trusted. Most Cited. Most Read.

Investigation of Perovskite Structures as Oxygen-Exchange Redox Materials for Hydrogen Production from Thermochemical Two-Step Water-Splitting Cycles

Author: Antoine Demont, Stéphane Abanades, Eric Beche
Publication: The Journal of Physical Chemistry C
Publisher: American Chemical Society
Date: Jun 1, 2014

Copyright © 2014, American Chemical Society

PERMISSION/LICENSE IS GRANTED FOR YOUR ORDER AT NO CHARGE

This type of permission/license, instead of the standard Terms & Conditions, is sent to you because no fee is being charged for your order. Please note the following:

- Permission is granted for your request in both print and electronic formats, and translations.
- If figures and/or tables were requested, they may be adapted or used in part.
- Please print this page for your records and send a copy of it to your publisher/graduate school.
- Appropriate credit for the requested material should be given as follows: "Reprinted (adapted) with permission from (COMPLETE REFERENCE CITATION). Copyright (YEAR) American Chemical Society." Insert appropriate information in place of the capitalized words.
- One-time permission is granted only for the use specified in your request. No additional uses are granted (such as derivative works or other editions). For any other uses, please submit a new request.

If credit is given to another source for the material you requested, permission must be obtained from that source.

[BACK](#) [CLOSE WINDOW](#)

Fig. 1.6(a):

ELSEVIER LICENSE
TERMS AND CONDITIONS

Jun 05, 2020

This Agreement between Krishna Kamol Ghose ("You") and Elsevier ("Elsevier") consists of your license details and the terms and conditions provided by Elsevier and Copyright Clearance Center.

License Number	4842321145645
License date	Jun 05, 2020
Licensed Content Publisher	Elsevier
Licensed Content Publication	Solid State Ionics
Licensed Content Title	Perovskite-type oxides as oxygen electrodes for high temperature oxide fuel cells
Licensed Content Author	O. Yamamoto, Y. Takeda, R. Kanno, M. Noda
Licensed Content Date	Jan 1, 1987
Licensed Content Volume	22
Licensed Content Issue	2-3
Licensed Content Pages	6
Start Page	241
End Page	246
Type of Use	reuse in a thesis/dissertation
Portion	figures/tables/illustrations
Number of figures/tables/illustrations	1
Format	both print and electronic
Are you the author of this Elsevier article?	No
Will you be translating?	No
Title	First-Principles Investigation of Trends in High-Temperature Thermochemistry of Perovskite Metal Oxides
Institution name	The University of Newcastle, Australia
Expected presentation date	Jun 2020
Portions	Fig. 1
Requestor Location	Krishna Kamol Ghose University Drive SB 306 Callaghan Callaghan, NSW 2308 Australia Attn:
Publisher Tax ID	GB 494 6272 12
Total	0.00 AUD
Terms and Conditions	

Fig. 1.6(b):

1. Journal of the Electrochemical Society 0.00 AUD

Order license ID ISSN Type of Use	Pending 1945-7111 Republish in a thesis/dissertation	Publisher Portion	IOP Publishing Chart/graph/table/figure	Publisher Terms and Conditions
---	---	----------------------	--	--

[Hide Details](#)

LICENSED CONTENT

Publication Title	Journal of the Electrochemical Society	Country	United States of America
Author/Editor	Electrochemical Society.	Rightsholder	IOP Publishing, Ltd
Date	01/01/1948	Publication Type	e-Journal
Language	English	URL	http://www.scitation.org/JES

REQUEST DETAILS

Portion Type	Chart/graph/table/figure	Distribution	Worldwide
Number of charts / graphs / tables / figures requested	1	Translation	Original language of publication
Format (select all that apply)	Print, Electronic	Copies for the disabled?	Yes
Who will republish the content?	Academic institution	Minor editing privileges?	No
Duration of Use	Life of current edition	Incidental promotional use?	No
Lifetime Unit Quantity	Up to 999	Currency	AUD
Rights Requested	Main product and any product related to main product		

NEW WORK DETAILS

Title	First-Principles Investigation of Trends in High-Temperature Thermochemistry of Perovskite Metal Oxides	Institution name	The University of Newcastle
Instructor name	Krishna Kamol Ghose	Expected presentation date	2020-06-09

ADDITIONAL DETAILS

Order reference number	N/A	The requesting person / organization to appear on the license	Krishna Kamol Ghose
------------------------	-----	---	---------------------

REUSE CONTENT DETAILS

Title, description or numeric reference of the portion(s)	Figure 2	Title of the article/chapter the portion is from	The Electrochemical Society Comparison of Ln _{0.6} Sr _{0.4} CoO _{3-δ} (Ln = La, Pr, Nd, Sm, and Gd) as Cathode Materials for Intermediate Temperature Solid Oxide Fuel Cells
Editor of portion(s)	Journal of The Electrochemical Society.	Author of portion(s)	Electrochemical Society.
Volume of serial or monograph	153(4)	Issue, if republishing an article from a serial	N/A
Page or page range of portion	794-798	Publication date of portion	2006-02-24

Fig. 1.7(a):

Elsevier Science & Technology Journals - License Terms and Conditions

This is a License Agreement between Krishna Kamol Ghose ("You") and Elsevier Science & Technology Journals ("Publisher") provided by Copyright Clearance Center ("CCC"). The license consists of your order details, the terms and conditions provided by Elsevier Science & Technology Journals, and the CCC terms and conditions.

All payments must be made in full to CCC.

Order Date	30-Sep-2020	Type of Use	Republish in a thesis/dissertation
Order license ID	1066937-1	Publisher	ELSEVIER ADVANCED TECHNOLOGY
ISBN-13	9781856173872	Portion	Chart/graph/table/figure

LICENSED CONTENT

Publication Title	High-temperature solid oxide fuel cells : fundamentals, design, and applicatons	Country	United States of America
Author/Editor	Singhal, Subhash C., Kendall, Kevin, ScienceDirect (Online service)	Rightsholder	Elsevier Science & Technology Journals
Date	01/01/2003	Publication Type	Book
Language	English	URL	http://www.engineeringvillage.com/contr...

REQUEST DETAILS

Portion Type	Chart/graph/table/figure	Distribution	Worldwide
Number of charts / graphs / tables / figures requested	1	Translation	Original language of publication
Format (select all that apply)	Print, Electronic	Copies for the disabled?	Yes
Who will republish the content?	Academic institution	Minor editing privileges?	Yes
Duration of Use	Life of current edition	Incidental promotional use?	No
Lifetime Unit Quantity	Up to 999	Currency	AUD
Rights Requested	Main product and any product related to main product		

NEW WORK DETAILS

Title	First-Principles Investigation of Trends in High-Temperature Thermochemistry of Perovskite Oxides	Institution name	The University of Newcastle
Instructor name	Associate Prof. Alister Page	Expected presentation date	2020-10-01

ADDITIONAL DETAILS

Order reference number	N/A	The requesting person / organization to appear on the license	Krishna Kamol Ghose
------------------------	-----	---	---------------------

REUSE CONTENT DETAILS

Title, description or numeric reference of the portion(s)	Figure 4.17	Title of the article/chapter the portion is from	Chapter 4: Elctrolytes
Editor of portion(s)	Tatsumi Ishihara, Nigel M. Sammes and Osamu Yamamoto	Author of portion(s)	Singhal, Subhash C.; Kendall, Kevin; ScienceDirect (Online service)
Volume of serial or monograph	N/A	Issue, if republishing an article from a serial	N/A
Page or page range of portion	99	Publication date of portion	2003-01-01

Fig. 1.7(b):

Elsevier Science & Technology Journals - License Terms and Conditions

This is a License Agreement between Krishna Kamol Ghose ("You") and Elsevier Science & Technology Journals ("Publisher") provided by Copyright Clearance Center ("CCC"). The license consists of your order details, the terms and conditions provided by Elsevier Science & Technology Journals, and the CCC terms and conditions.

All payments must be made in full to CCC.

Order Date	30-Sep-2020	Type of Use	Republish in a thesis/dissertation
Order license ID	1066935-1	Publisher	ELSEVIER ADVANCED TECHNOLOGY
ISBN-13	9781856173872	Portion	Chart/graph/table/figure

LICENSED CONTENT

Publication Title	High-temperature solid oxide fuel cells : fundamentals, design, and applicatons	Country	United States of America
Author/Editor	Singhal, Subhash C., Kendall, Kevin, ScienceDirect (Online service)	Rightsholder	Elsevier Science & Technology Journals
Date	01/01/2003	Publication Type	Book
Language	English	URL	http://www.engineeringvillage.com/contr...

REQUEST DETAILS

Portion Type	Chart/graph/table/figure	Distribution	Worldwide
Number of charts / graphs / tables / figures requested	1	Translation	Original language of publication
Format (select all that apply)	Print, Electronic	Copies for the disabled?	Yes
Who will republish the content?	Academic institution	Minor editing privileges?	Yes
Duration of Use	Life of current edition	Incidental promotional use?	No
Lifetime Unit Quantity	Up to 999	Currency	AUD
Rights Requested	Main product and any product related to main product		

NEW WORK DETAILS

Title	First-Principles Investigation of Trends in High-Temperature Thermochemistry of Perovskite Oxides	Institution name	The University of Newcastle
Instructor name	Associate Prof. Alister Page	Expected presentation date	2020-10-01

ADDITIONAL DETAILS

Order reference number	N/A	The requesting person / organization to appear on the license	Krishna Kamol Ghose
------------------------	-----	---	---------------------

REUSE CONTENT DETAILS

Title, description or numeric reference of the portion(s)	Figure 4.18	Title of the article/chapter the portion is from	Chapter 4: Electrolytes
Editor of portion(s)	Tatsumi Ishihara, Nigel M. Sammes and Osamu Yamamoto	Author of portion(s)	Singhal, Subhash C.; Kendall, Kevin; ScienceDirect (Online service)
Volume of serial or monograph	N/A	Issue, if republishing an article from a serial	N/A
Page or page range of portion	100	Publication date of portion	2003-01-01

Fig. 1.8(a):

Jun 06, 2020

This Agreement between Krishna Kasmol Ghose ("You") and John Wiley and Sons ("John Wiley and Sons") consists of your license details and the terms and conditions provided by John Wiley and Sons and Copyright Clearance Center.

License Number	4842871301248
License date	Jun 06, 2020
Licensed Content Publisher	John Wiley and Sons
Licensed Content Publication	Angewandte Chemie International Edition
Licensed Content Title	Trends in Stability of Perovskite Oxides
Licensed Content Author	Jan Rossmeisl, Mogens Mogensen, Juan M. Garcia-Lastra, et al
Licensed Content Date	Sep 10, 2010
Licensed Content Volume	49
Licensed Content Issue	42
Licensed Content Pages	3
Type of use	Dissertation/Thesis
Requestor type	University/Academic
Format	Print and electronic
Portion	Figure table
Number of figures/tables	1
Will you be translating?	No
Title	First-Principles Investigation of Trends in High-Temperature Thermochemistry of Perovskite Metal Oxides
Institution name	The University of Newcastle, Australia
Expected presentation date	Jun 2020
Portions	Figure 2
Requestor Location	Krishna Kasmol Ghose University Drive SB 306 Callaghan Callaghan, NSW 2308 Australia Attn:
Publisher Tax ID	EUS26007151
Total	0.00 AUD
Terms and Conditions	

Fig. 1.8(b):



Marketplace™

Royal Society of Chemistry - License Terms and Conditions

This is a License Agreement between Krishna Kamol Ghose ("You") and Royal Society of Chemistry ("Publisher") provided by Copyright Clearance Center ("CCC"). The license consists of your order details, the terms and conditions provided by Royal Society of Chemistry, and the CCC terms and conditions.

All payments must be made in full to CCC.

Order Date	06-Jun-2020	Type of Use	Republish in a thesis/dissertation
Order license ID	1039876-1	Publisher	ROYAL SOCIETY OF CHEMISTRY
ISSN	1463-9084	Portion	Chart/graph/table/figure

LICENSED CONTENT

Publication Title	Physical chemistry chemical physics	Country	United Kingdom of Great Britain and Northern Ireland
Author/Editor	Royal Society of Chemistry (Great Britain)	Rightsholder	Royal Society of Chemistry
Date	01/01/1999	Publication Type	e-Journal
Language	English	URL	http://firstsearch.oclc.org/journal=1463-9...

REQUEST DETAILS

Portion Type	Chart/graph/table/figure	Distribution	Worldwide
Number of charts / graphs / tables / figures requested	1	Translation	Original language of publication
Format (select all that apply)	Print, Electronic	Copies for the disabled?	Yes
Who will republish the content?	Academic institution	Minor editing privileges?	No
Duration of Use	Life of current edition	Incidental promotional use?	No
Lifetime Unit Quantity	Up to 999	Currency	AUD
Rights Requested	Main product		

NEW WORK DETAILS

Title	First-Principles Investigation of Trends in High-Temperature Thermochemistry of Perovskite Metal Oxides	Institution name	The University of Newcastle
Instructor name	Associated Prof. Alister Page	Expected presentation date	2020-06-08

ADDITIONAL DETAILS

Order reference number	N/A	The requesting person / organization to appear on the license	Krishna Kamol Ghose
------------------------	-----	---	---------------------

REUSE CONTENT DETAILS

Title, description or numeric reference of the portion(s)	Figure 1	Title of the article/chapter the portion is from	Generalized trends in the formation energies of perovskite oxides
Editor of portion(s)	Phys. Chem. Chem. Phys.	Author of portion(s)	ZhenHua Zeng, Federico Calle-Vallejo, Mogens Mogensen and Jan Rossmeisl
Volume of serial or monograph	15	Issue, if republishing an article from a serial	N/A
Page or page range of portion	7526-7533	Publication date of portion	2013-03-21

Fig. 1.8(c):

JOHN WILEY AND SONS LICENSE
TERMS AND CONDITIONS

Jun 06, 2020

This Agreement between Krishna Kamol Ghose ("You") and John Wiley and Sons ("J Wiley and Sons") consists of your license details and the terms and conditions provided by John Wiley and Sons and Copyright Clearance Center.

License Number	4842880847699
License date	Jun 06, 2020
Licensed Content Publisher	John Wiley and Sons
Licensed Content Publication	ChemSusChem
Licensed Content Title	Design Principles of Perovskites for Thermochemical Oxygen Separation
Licensed Content Author	Miriam Eshiri, Kyle M. Allen, Maria E. Galvez, et al
Licensed Content Date	Apr 29, 2015
Licensed Content Volume	8
Licensed Content Issue	11
Licensed Content Pages	6
Type of use	Dissertation/Thesis
Requestor type	University/Academic
Format	Print and electronic
Portion	Figure/table
Number of figures/tables	1
Will you be translating?	No
Title	First-Principles Investigation of Trends in High-Temperature Thermochemistry of Perovskite Metal Oxides
Institution name	The University of Newcastle, Australia
Expected presentation date	Jun 2020
Portions	Figure 3 (c)
Requestor Location	Krishna Kamol Ghose University Drive SB 306 Callaghan, Callaghan, NSW 2308 Australia Attn:
Publisher Tax ID	EUS26007151
Total	0.00 AUD

Fig. 1.9:

 **RightsLink**[®]  Home  Help  Email Support  Krishna Kamol Ghose ▾

Intrinsic Material Properties Dictating Oxygen Vacancy Formation Energetics in Metal Oxides

Author: Ann M. Deml, Aaron M. Holder, Ryan P. O'Hayre, et al
Publication: Journal of Physical Chemistry Letters
Publisher: American Chemical Society
Date: May 1, 2015

Copyright © 2015, American Chemical Society

PERMISSION/LICENSE IS GRANTED FOR YOUR ORDER AT NO CHARGE

This type of permission/license, instead of the standard Terms & Conditions, is sent to you because no fee is being charged for your order. Please note the following:

- Permission is granted for your request in both print and electronic formats, and translations.
- If figures and/or tables were requested, they may be adapted or used in part.
- Please print this page for your records and send a copy of it to your publisher/graduate school.
- Appropriate credit for the requested material should be given as follows: "Reprinted (adapted) with permission from (COMPLETE REFERENCE CITATION). Copyright (YEAR) American Chemical Society." Insert appropriate information in place of the capitalized words.
- One-time permission is granted only for the use specified in your request. No additional uses are granted (such as derivative works or other editions). For any other uses, please submit a new request.

If credit is given to another source for the material you requested, permission must be obtained from that source.

BACK CLOSE WINDOW

Fig. 1.10:

			
Royal Society of Chemistry - License Terms and Conditions			
This is a License Agreement between Krishna Kamol Ghose ("You") and Royal Society of Chemistry ("Publisher") provided by Copyright Clearance Center ("CCC"). The license consists of your order details, the terms and conditions provided by Royal Society of Chemistry, and the CCC terms and conditions.			
All payments must be made in full to CCC.			
Order Date	06-Jun-2020	Type of Use	Republish in a thesis/dissertation
Order license ID	1039878-1	Publisher	RSC Publishing
ISSN	1754-5706	Portion	Chart/graph/table/figure
LICENSED CONTENT			
Publication Title	Energy & environmental science	Country	United Kingdom of Great Britain and Northern Ireland
Author/Editor	Royal Society of Chemistry (Great Britain)	Rightsholder	Royal Society of Chemistry
Date	01/01/2008	Publication Type	e-Journal
Language	English	URL	http://www.rsc.org/Publishing/Journals/E...
REQUEST DETAILS			
Portion Type	Chart/graph/table/figure	Distribution	Worldwide
Number of charts / graphs / tables / figures requested	1	Translation	Original language of publication
Format (select all that apply)	Print, Electronic	Copies for the disabled?	Yes
Who will republish the content?	Academic institution	Minor editing privileges?	No
Duration of Use	Life of current edition	Incidental promotional use?	No
Lifetime Unit Quantity	Up to 999	Currency	AUD
Rights Requested	Main product		
NEW WORK DETAILS			
Title	First-Principles Investigation of Trends in High-Temperature Thermochemistry of Perovskite Metal Oxides	Institution name	The University of Newcastle
Instructor name	Associate Prof. Alister Page	Expected presentation date	2020-06-08
ADDITIONAL DETAILS			
Order reference number	N/A	The requesting person / organization to appear on the license	Krishna Kamol Ghose
REUSE CONTENT DETAILS			
Title, description or numeric reference of the portion(s)	Fig. 7	Title of the article/chapter the portion is from	Earth abundant perovskite oxides for low temperature CO2 conversion
Editor of portion(s)	Energy & Environmental Science	Author of portion(s)	Maiti, Debtanu, Bryan J. Hare, Yolanda A. Daza, Adela E. Ramos, John N. Kuhn, and Venkat R. Bheethanabotla
Volume of serial or monograph	11(3)	Issue, if republishing an article from a serial	N/A
Page or page range of portion	648-659	Publication date of portion	2008-01-01

Fig. 1.11:

Copyright Clearance Center | RightsLink®

Home | Help | Email Support | Krishna Kamol Ghose

High-Throughput Computational Screening of Perovskites for Thermochemical Water Splitting Applications

Author: Antoine A. Emery, James E. Saal, Scott Kirklín, et al
Publication: Chemistry of Materials
Publisher: American Chemical Society
Date: Aug 1, 2016
Copyright © 2016, American Chemical Society

PERMISSION/LICENSE IS GRANTED FOR YOUR ORDER AT NO CHARGE

This type of permission/license, instead of the standard Terms & Conditions, is sent to you because no fee is being charged for your order. Please note the following:

- Permission is granted for your request in both print and electronic formats, and translations.
- If figures and/or tables were requested, they may be adapted or used in part.
- Please print this page for your records and send a copy of it to your publisher/graduate school.
- Appropriate credit for the requested material should be given as follows: "Reprinted (adapted) with permission from (COMPLETE REFERENCE CITATION). Copyright (YEAR) American Chemical Society." Insert appropriate information in place of the capitalized words.
- One-time permission is granted only for the use specified in your request. No additional uses are granted (such as derivative works or other editions). For any other uses, please submit a new request. If credit is given to another source for the material you requested, permission must be obtained from that source.

[BACK](#) [CLOSE WINDOW](#)

Fig. 1.12(a):



06-Jun-2020

This license agreement between the American Physical Society ("APS") and Krishna Kamol Ghose ("You") consists of your license details and the terms and conditions provided by the American Physical Society and SciPris.

Licensed Content Information

License Number: RNP/20/JUN/026609
License date: 06-Jun-2020
DOI: 10.1103/PhysRevMaterials.2.043802
Title: Predictions of new AB_3O_3 perovskite compounds by combining machine learning and density functional theory
Author: Prasanna V. Balachandran et al.
Publication: Physical Review Materials
Publisher: American Physical Society
Cost: USD \$ 0.00

Request Details

Does your reuse require significant modifications: No
Specify intended distribution locations: Worldwide
Reuse Category: Reuse in a thesis/dissertation
Requestor Type: Student
Items for Reuse: Figures/Tables
Number of Figure/tables: 1
Figure/Tables Details: FIG. 4
Format for Reuse: Print and Electronic
Total number of print copies: Up to 1000

Information about New Publication:

University/Publisher: The University of Newcastle
Title of dissertation/thesis: First-Principles Investigation of Trends in High-Temperature Thermochemistry of Perovskite Metal Oxides
Author(s): Krishna Kamol Ghose
Expected completion date: Jun. 2020

License Requestor Information

Name: Krishna Kamol Ghose
Affiliation: Individual
Email Id: k.ghose.bd@gmail.com

Fig. 1.12(b):

ELSEVIER LICENSE
TERMS AND CONDITIONS

Jun 06, 2020

This Agreement between Krishna Kamol Ghose ("You") and Elsevier ("Elsevier") consists of your license details and the terms and conditions provided by Elsevier and Copyright Clearance Center.

License Number	4842890931796
License date	Jun 06, 2020
Licensed Content Publisher	Elsevier
Licensed Content Publication	Computational Materials Science
Licensed Content Title	Predicting the thermodynamic stability of perovskite oxides using machine learning models
Licensed Content Author	Wei Li,Ryan Jacobs,Dane Morgan
Licensed Content Date	Jul 1, 2018
Licensed Content Volume	150
Licensed Content Issue	n/a
Licensed Content Pages	10
Start Page	454
End Page	463
Type of Use	reuse in a thesis/dissertation
Portion	figures/tables/illustrations
Number of figures/tables/illustrations	1
Format	both print and electronic
Are you the author of this Elsevier article?	No
Will you be translating?	No
Title	First-Principles Investigation of Trends in High-Temperature Thermochemistry of Perovskite Metal Oxides
Institution name	The University of Newcastle, Australia
Expected presentation date	Jun 2020
Portions	Graphical abstract
Requestor Location	Krishna Kamol Ghose University Drive SB 306 Callaghan Callaghan, NSW 2308 Australia Ann:
Publisher Tax ID	GB 494 6272 12
Total	0.00 AUD

Fig. 1.12(c):

HomeHelpEmail SupportKrishna Kamol Ghose ▾



Rationalizing Perovskite Data for Machine Learning and Materials Design
Author: Qichen Xu, Zhenzhu Li, Miao Liu, et al
Publication: Journal of Physical Chemistry Letters
Publisher: American Chemical Society
Date: Dec 1, 2018
Copyright © 2018, American Chemical Society

PERMISSION/LICENSE IS GRANTED FOR YOUR ORDER AT NO CHARGE

This type of permission/license, instead of the standard Terms & Conditions, is sent to you because no fee is being charged for your order. Please note the following:

- Permission is granted for your request in both print and electronic formats, and translations.
- If figures and/or tables were requested, they may be adapted or used in part.
- Please print this page for your records and send a copy of it to your publisher/graduate school.
- Appropriate credit for the requested material should be given as follows: "Reprinted (adapted) with permission from (COMPLETE REFERENCE CITATION). Copyright (YEAR) American Chemical Society." Insert appropriate information in place of the capitalized words.
- One-time permission is granted only for the use specified in your request. No additional uses are granted (such as derivative works or other editions). For any other uses, please submit a new request.

If credit is given to another source for the material you requested, permission must be obtained from that source.

[BACK](#) [CLOSE WINDOW](#)

Fig. 2.1:

			
Taylor & Francis Group LLC - Books - License Terms and Conditions			
<p>This is a License Agreement between Krishna Kamol Ghose ("You") and Taylor & Francis Group LLC - Books ("Publisher") provided by Copyright Clearance Center ("CCC"). The license consists of your order details, the terms and conditions provided by Taylor & Francis Group LLC - Books, and the CCC terms and conditions.</p> <p>All payments must be made in full to CCC.</p>			
Order Date	06-Jun-2020	Type of Use	Republish in a thesis/dissertation
Order license ID	1039882-1	Publisher	Taylor and Francis; Taylor and Francis
ISBN-13	9781498749732	Portion	Chart/graph/table/figure
LICENSED CONTENT			
Publication Title	Computational Materials Science : An Introduction, Second Edition	Country	United States of America
Author/Editor	Lee, June Gunn	Rightholder	Taylor & Francis Group LLC - Books
Date	12/15/2016	Publication Type	Book
Language	English		
REQUEST DETAILS			
Portion Type	Chart/graph/table/figure	Distribution	Worldwide
Number of charts / graphs / tables / figures requested	1	Translation	Original language of publication
Format (select all that apply)	Print, Electronic	Copies for the disabled?	No
Who will republish the content?	Academic institution	Minor editing privileges?	No
Duration of Use	Life of current edition	Incidental promotional use?	No
Lifetime Unit Quantity	Up to 999	Currency	AUD
Rights Requested	Main product		
NEW WORK DETAILS			
Title	First-Principles Investigation of Trends in High-Temperature Thermochemistry of Perovskite Metal Oxides	Institution name	The University of Newcastle
Instructor name	Associate Prof. Alister Page	Expected presentation date	2020-06-08
ADDITIONAL DETAILS			
Order reference number	N/A	The requesting person / organization to appear on the license	Krishna Kamol Ghose
REUSE CONTENT DETAILS			
Title, description or numeric reference of the portion(s)	Figure 6.3	Title of the article/chapter the portion is from	Chapter six: Treating solids
Editor of portion(s)	N/A	Author of portion(s)	Lee, June Gunn
Volume of serial or monograph	N/A	Issue, if republishing an article from a serial	N/A
Page or page range of portion	177	Publication date of portion	2016-12-15
PUBLISHER TERMS AND CONDITIONS			
<p>Taylor and Francis Group and Informa healthcare are division of Informa plc. Permission will be void if material exceeds 10% of all the total pages in your publication and over 20% of the original publication. This includes permission granted by Informa plc and all of its subsidiaries.</p>			